UNIVERSITÀ DEGLI STUDI DI ROMA "TOR VERGATA"

FACOLTA' DI SCIENZE MATEMATICHE FISICHE NATURALI

DOTTORATO DI RICERCA IN
ASTRONOMIA

XXI CICLO

Theory and Observations of Neutron Star X-ray Binaries: from wind to disk accretors.

Enrico Bozzo

A.A. 2008/2009

Relatore: Prof. Luigi Stella

Coordinatore: Prof. Pasquale Mazzotta

SUMMARY

X-ray binaries are among the brightest X-ray sources in our Galaxy, and were the first extrasolar X-ray sources discovered in the early '60s. The first pioneristic observations of these sources were made by using rocket flights; however, in the brief interval in which rockets operated it was hard to get sufficient information to understand the nature of these sources. Only about ten years later the first generation of X-ray satellites established that most bright X-ray sources in the Galaxy are in fact binary systems containing either a neutron star (NS) or a black hole orbiting a companion star. Most of the X-ray emission of these sources is due to the accretion of matter onto the compact object.

This thesis focuses on X-ray binaries hosting neutron stars.

The presence of NSs in X-ray binaries is often inferred from pulsations in their X-ray flux. These occur because of the so called "lighthouse" effect, that is due to the combination of the NS rotation and misaligned intense magnetic field, which funnels the accreting matter onto the star's magnetic poles. In these sources the inferred NS magnetic fields can be as high as about 1,000 billion times that on the earth, and are thus the strongest magnetic fields known in the universe. Not all NS systems have such intense magnetic fields: in many NS X-ray binaries the field is much weaker. In these cases the flow of material onto the NS is not always channeled towards the magnetic poles and sometimes only transient pulsations are observed. Many of these low magnetic field systems also show fast quasi-periodic oscillations in their X-ray flux that originate from the interaction of the NS with the surrounding accretion disk. In some cases the accreted material (mostly hydrogen and helium) accumulating on the NS surface reaches a critical mass, at which a thermonuclear explosion takes place and the source undergoes an X-ray burst. The emission properties that characterize an accreting NS in a binary system thus depend mainly on the NS physical parameters (e.g. spin period and magnetic field strength).

On the contrary, the mode in which mass transfer takes place, as well as the geometry of the accretion flow, depends on the nature of the companion star. In low mass X-ray binaries the companion star has a typical age of $\sim 10^8$ yr, and its mass is similar to or less than that of our sun. In these systems the transfer of mass takes place through the so called Roche Lobe Overflow, which usually leads to the formation of an accretion disk around the compact object. If the companion star is much younger ($\sim$few$\times 10^6$ yr) and massive ($\gg 1$ $M_\odot$), then the system is a high mass X-ray binary, and mass transfer occurs through the wind capture by the compact star. In fact, donor stars in high mass X-ray binaries are typically blue O or B stars whose intense wind can be easily captured by the NS to release X-rays.

During the past years, the operation of the present generation of X-ray satellites, such as *RXTE*, *XMM-Newton*, *Chandra*, *Swift*, and *INTEGRAL*, has opened a new era in the discovery and study of for X-ray binaries. This provided several breakthroughs as well as surprising new questions on these sources.

In this phD thesis we consider both high and low mass NS binaries, and analyze several observational and theoretical aspects of these sources. We use data obtained with the modern X-ray telescopes available on board the present generation satellites in order to investigate the accretion processes in these sources. In particular, we study both disk and wind accretion, and compare the observational results with theoretical expectations. Some improvements in the theory of disk and wind accretion are presented.

In Chapter 1 we provide a brief and comprehensive introduction on NS X-ray binaries; all other chapters are based on our original findings. We divided these chapters in two

groups.

In the first group (Chapters 2,3, 4, 5, and 6), we concentrate on studies of low mass X-ray binaries. In particular, chapter 2 summarizes the magnetic threaded disk model, that is the most widely accepted model to describe the interaction between a magnetized NS and its surrounding accretion disk. By using quasi-periodic oscillations in X-ray binaries, we present a new method to test the threaded disk model against observations of slow quasi-periodic oscillations in accreting X-ray pulsars contained in high as well as low mass X-ray binaries (Bozzo, E., Stella, L., Vietri, M., et al. 2008, A&A, in press [astro-ph/0811.0049]). We also discuss some improvements on the threaded disk model that we will develop in a future publication. In Chapter 3 we propose the "recycling magnetosphere model" to explain the spin-up/spin-down behaviour of some low mass X-ray binaries that cannot be interpreted within the magnetic threaded disk scenario (Perna, R., Bozzo, E., Stella, L. 2006, ApJ, 639, 363). This model involves an in-depth analysis of the so called propeller mechanism, which is also discussed in more detail in Chapter 4 (Falanga, M., Bozzo, E., Stella, L., et al. 2007, A&A, 464, 807). Chapters 5 and 6 focus on X-ray observations of two low mass X-ray binaries, 4U 2129+47 and XTE J1701-407. In the case of 4U 2129+47 we present the results of two *XMM-Newton* observations. Our analysis of these data revealed a delay of $\sim$190 s measured across two eclipses separated by $\sim$22 days. We show that this delay can be naturally explained as being due to the orbital motion of the binary with respect to the center of mass of a triple star and is thus probably the first X-ray signature of the triple nature of an X-ray binary (Bozzo, E., Stella, L., Papitto, A., et al. 2007, A&A, 476, 301). In the case of XTE J1701-407 we report on the first type I X-ray burst observed from this source and discuss the results of the data analysis in the context of the modern theories of nuclear burning on the NS surface (Falanga, M., Cumming, A., Bozzo, E., et al. 2008, A&A, in press [astro-ph/0901.0314]).

In the second part of this thesis (Chapters 7, 8) we concentrate on high mass X-ray binaries. In Chapter 7 we analyze in-depth the accretion process in wind-accreting binaries and apply this scenario to interpret the behaviour of a newly discovered subclass of high mass X-ray binaries, collectively termed supergiant fast X-ray transients. We suggest that these sources might host ultra-magnetized ("magnetar") NSs, and can thus provide the very first opportunity to detect and study magnetars in binary systems (Bozzo, E., Falanga, M., Stella, L. 2008, ApJ, 683, 1031). In Chapter 8 we report on an *XMM-Newton* observation of the supergiant fast X-ray transient IGR J16479-4514. The timing, spectral and spatial analysis of this observation revealed a complex phenomenology that could be interpreted in terms of an eclipse by the supergiant companion, with some residual X-ray flux during the eclipse resulting from both scattering local to the source and by an interstellar dust halo along the line of sight to IGR J16479-4514 (Bozzo, E., Stella, L., Israel, G., et al. 2008, MNRAS, 391, L108).

Finally, we provide a briefly outline of the possible future development in the research fields of this thesis.

RIASSUNTO

Le binarie a raggi-X sono tra le sorgenti piú brillanti in banda X nella nostra Galassia, e furono le prime sorgenti cosmiche in banda X ad essere scoperte all'inizio degli anni 60. Le prime osservazioni pionieristiche di queste sorgenti venivano realizzate utilizzando dei razzi; tuttavia, nel breve tempo in cui questi razzi operavano era impossibile raccogliere le informazioni necessarie per comprendere la vera natura di queste sorgenti. Soltanto circa 10 anni piú tardi, con l'avvento della prima generazione di satelliti per osservazioni in banda X fu possibile stabilire che queste sorgenti erano effettivamente dei sistemi di stelle binarie, contenenti una stella di neutroni o un buco nero in orbita intorno alla stella compagna. La gran parte dell'emissione in raggi X in queste sorgenti é dovuta all'accrescimento di materia della stella compagna sull'oggetto compatto.

In questa tesi ci concentriamo sui sistemi binari contenenti stelle di neutroni.

La presenza di stelle di neutroni nelle binarie a raggi X é in genere dedotta dalle pulsazioni osservate nel flusso in banda X proveniente da queste sorgenti. Queste pulsazioni sono dovute al cosiddetto "effetto-faro", che é il risultato dell'azione combinata della rotazione e del campo magnetico della stella di neutroni. Quest'ultimo incanala la materia in accrescimento verso i poli magnetici della stella di neutroni, e puó avere un intensitá pari a circa 1.000 bilioni di volte quella della Terra; é perció il campo magnetico piú intenso che si conosca nell'Universo.

Non tutte le stelle di neutroni hanno peró un campo magnetico cosí elevato, e in alcune di esse sembra che possa essere molto piú debole. In questi casi, il flusso di materia in accrescimento non é sempre incanalato dal campo magnetico verso i poli della stella di neutroni e talvolta vengono osservate soltanto delle pulsazioni transienti. Molte di queste sorgenti con campi deboli mostrano anche delle rapide oscillazioni quasi-periodiche che sono il risultato dell'interazione tra la stella di neutroni ed il disco di accrescimento. In alcuni casi la materia in accrescimento, costituita per lo piú da idrogeno ed elio, si accumula sulla superficie della stella di neutroni, e raggiunge una certa massa critica al di sopra della quale si innescano delle esplosioni termonucleari, dette burst in raggi-X. Questo ci mostra dunque che, in generale, le proprietá dell'emissione di una stella di neutroni dipendono dai parametri fisici della stella stessa (come, ad esempio, il suo periodo di spin e l'intensitá del campo magnetico).

Al contrario, la natura della stella compagna determina la modalitá con cui ha luogo il trasferimento di materia tra le due stelle.

Nelle binarie a raggi-X di piccola massa, le stelle compagne hanno tipicamente un etá di $\sim 10^8$ anni, e una massa simile o inferiore a quella solare. In questi sistemi il trasferimento di massa avviene a mezzo del cosiddetto "Roche Lobe Overflow", che in genere porta alla formazione di un disco di accrescimento intorno alla stella di neutroni. Nel caso in cui la stella compagna sia molto piú giovane ($\gtrsim 10^6$ anni) e piú massiva ($\gg 1$ $M_\odot$), allora il sistema prende il nome di sistema binario di grande massa, e il trasferimento di materia tra le due stelle avviene a mezzo della cattura del vento stellare. Infatti, tipicamente le compagne delle binarie di grande massa sono stelle O o B il cui intenso vento stellare puó facilmente esser catturato dalla stella di neutroni per emettere in raggi X.

Nel corso degli ultimi anni, il lancio di molti satelliti per osservazioni in banda X, come *RXTE*, *XMM-Newton*, *Chandra*, *Swift*, e *INTEGRAL*, ha aperto nuove possibilitá per lo studio delle binarie a raggi X, fornendo sempre maggiori dettagli e mostrando comportamenti che ancora necessitano di uno studio approfondito e di una corretta interpretazione.

In questa tesi ci occupiamo sia della binarie di piccola massa che di quelle di grande

massa, e analizziamo diversi aspetti di queste sorgenti sia da un punto di vista osservativo che teorico. In particolare, utilizzando i dati raccolti grazie ai telescopi a bordo dei satelliti X della generazione attuale, studiamo in dettaglio i processi di accrescimento da disco e da vento che hanno luogo nei sistemi binari. Confrontiamo poi i risultati ricavati dall'analisi dei dati con quelli aspettati dai modelli teorici, e discutiamo anche gli avanzamenti nella teoria dell'accrescimento da disco e da vento che abbiamo sviluppato nel corso di questa tesi.

Nel capitolo 1 presentiamo un'introduzione generale sulle binarie a raggi X, mentre in tutti gli altri capitoli che seguono descriviamo i risultati originali ottenuti durante lo svolgimento di questa tesi. Suddividiamo questi capitoli in due parti.

Nella prima parte (Capitoli 2,3, 4, 5, e 6) ci concentriamo sulle binarie X di piccola massa. In particolare, nel capitolo 2 riassumiamo il "magnetic threaded disk model", ovvero il modello ormai largamente accettato che spiega l'interazione tra una stella di neutroni magnetizzata e il suo disco di accrescimento. Utilizzando le oscillazioni quasi-periodiche, presentiamo un nuovo metodo sviluppato per testare questo modello rispetto alle osservazioni delle QPO da binarie di grande e piccola massa (Bozzo, E., Stella, L., Vietri, M., et al. 2008, A&A, in press [astro-ph/0811.0049]). Discutiamo anche alcuni miglioramenti che intendiamo apportare al magnetic threaded disk model e che svilupperemo in una successiva pubblicazione. Nel capitolo 3 proponiamo invece il modello della "recycling magnetosphere" per spiegare il comportamento di spin-up e spin-down di alcune sorgenti che non puó essere interpretato nell'ambito del "magnetic threaded disk model" (Perna, R., Bozzo, E., Stella, L. 2006, ApJ, 639, 363). Il modello della recycling magnetosphere prevede una trattazione dettagliata del cosiddetto "effetto-propeller", che viene discusso anche in maggior dettaglio nel capitolo 4 (Falanga, M., Bozzo, E., Stella, L., et al. 2007, A&A, 464, 807). Nei capitoli 5 e 6, ci concentriamo invece sulle osservazioni di due binarie X di piccola massa, 4U 2129+47 e XTE J1701-407. Della prima sorgente riportiamo i risultati dell'analisi di due osservazioni *XMM-Newton*, che ci ha permesso di misurare un ritardo di circa 190 s tra due eclissi distanti 22 giorni. Nella discussione del capitolo 6 mostriamo come questo ritardo possa esser naturalmente spiegato come l'effetto del moto della binaria intorno al centro di massa con una terza stella; questa misura costituisce dunque la prima prova diretta in raggi X dell'appartenenza di un sistema binario a raggi X ad un sistema triplo di stelle (Bozzo, E., Stella, L., Papitto, A., et al. 2007, A&A, 476, 301). Nel caso della sorgente XTE J1701-407 ci occupiamo invece di analizzare i dati relativi al primo burst di tipo I in raggi X osservato da questa sorgente e discutiamo i risultati di questa analisi in merito ai piú recenti modelli di bruciamento termonucleare sulla superficie di una stella di neutroni (Falanga, M., Cumming, A., Bozzo, E., et al. 2008, A&A, in press [astro-ph/0901.0314]).

Nella seconda parte di questa tesi (capitoli 7 e 8) ci concentriamo sulle binarie a raggi X di grande massa. Nel capitolo 7 analizziamo in dettaglio il processo di accrescimento da vento stellare, e applichiamo questo scenario al caso delle "supergiant fast X-ray transients" (SFXT), una nuova sottoclasse di binarie X di grande massa scoperte recentemente con *INTEGRAL*. In particolare, noi suggeriamo che queste binarie possano contenere delle "magnetar", ovvero delle stelle di neutroni con un campo magnetico eccezionalmente elevato ($\sim 10^{14}$-10^{15} G). In questo caso, le sorgenti SFXT sarebbero il primo esempio di sistemi binari contenti magnetar, e fornirebbero dunque una preziosa occasione per poter osservare e studiare questi oggetti peculiari (Bozzo, E., Falanga, M., Stella, L. 2008, ApJ, 683, 1031). Nel capitolo 8 riportiamo invece i risultati di un osservazione *XMM-Newton* della sorgente IGR J16479-4514. L'analisi temporale, spettrale e spaziale di questa osser-

vazione ha rivelato una fenomenologia molto complessa che é stata interpretata in termini di un eclissi della sorgente X da parte della stella compagna. Inoltre, il flusso X residuo durante l'eclissi si é potuto spiegare come dovuto all'effetto di scattering della radiazione X per mezzo sia di un gas parzialmente ionizzato posto vicino alla sorgente, che di un alone di polvere interstellare situato lungo la linea di vista tra noi e la sorgente IGR J16479-4514 (Bozzo, E., Stella, L., Israel, G., et al. 2008, MNRAS, 391, L108).

Infine descriviamo brevemente i possibili sviluppi futuri dei campi di ricerca trattati in questa tesi.

Acknowledgements

The research projects described in this thesis were carried out mainly at the Observatory of Rome (Monte Porzio Catone, Rome, Italy), and were supported by an Italian phD fellowship of the University of Rome, "Tor Vergata".

I would like to thank first Prof. Luigi Stella, my advisor, for his time and patience in following my research during the past three years, and for his advices on the right way of "doing science". I thank Prof. Roberto Buonanno and Pasquale Mazzotta, my phD coordinators.

Special thanks goes to my colleague Maurizio Falanga and to Patricia, for their kind hospitality during my (many) visiting collaborations in Paris (France).

I wish to thank Rosalba Perna, who gave me the very precious opportunity to spend several months in Boulder, Colorado (USA), and sheared with me a lots of interesting scientific ideas.

I also thank all my colleagues, who collaborated with me during the development of my thesis: M. Vietri (Scuola Normale Superiore di Pisa, Italy); G. Israel (INAF osservatorio astronomico di Roma, Italy); D. Lazzati (Jila, University of Colorado at Boulder, USA); A. Papitto (INAF osservatorio astronomico di Roma, Italy); S. Campana (INAF osservatorio astronomico di Brera, Italy); P. Ghosh (Tata Institute of Fundamental Research, India); L. Burderi (INAF Istituto di Astrofisica Spaziale e Fisica Cosmica Palermo, Italy); T. di Salvo (Universit di Palermo, Italy); L. Sidoli (INAF Istituto di Astrofisica Spaziale e Fisica Cosmica Milano, Italy); P. Romano (INAF Istituto di Astrofisica Spaziale e Fisica Cosmica Palermo, Italy); V. Mangano (INAF Istituto di Astrofisica Spaziale e Fisica Cosmica Palermo, Italy); R. Rampy (University of California, Santa Cruz, USA); D. Smith (University of California, Santa Cruz, USA); I. Negueruela (University of Alicante, Spain); M. I. van Adelsberg (University of Colorado at Boulder, USA).

Finally I would thank all the persons I met at the observatory of Rome (OAR), CEA-Saclay, AstroParticule et Cosmologie (APC, Univeristé Paris 7 Denis Diderot), and University of Colorado at Boulder and JILA for their kind hospitality during part of this thesis.

Last but not least, I thank my collegues and friends B. Viticchié, C. di Giulio, and M. Martini; another step done, guys!

Refereed Publications:

- Perna, R., Bozzo, E., Stella, L. (2006), On the spin-up/spin-down transitions in accreting X-ray binaries, ApJ, 639, 363.
- Falanga, M., Bozzo, E., Stella, L., Burderi, L., Di Salvo, T., Perna, R. (2007), On the maximum efficiency of the propeller mass-ejection mechanism, A&A, 464, 807
- Bozzo, E., Falanga, M., Papitto, A., Stella, L., Perna, R., Lazzati, D., Israel, G., Campana, S., Mangano, V., di Salvo, T., Burderi, L. (2007), X-ray eclipse time delays in 4U 2129+47, A&A, 476, 301
- Bozzo, E., Falanga, M., Stella, L. (2008), Are There Magnetars in High Mass X-ray Binaries? The Case of SuperGiant Fast X-Ray Transients, ApJ, 683, 1031
- Bozzo, E., Stella, L., Israel, G., Falanga, M., Campana, S. (2008), IGRJ 16479-4514: the first eclipsing supergiant fast X-ray transient?, MNRAS, 391, L108
- Bozzo, E., Stella, L., Vietri, M., Ghosh, P. (2008), Can disk-magnetosphere interaction models and beat frequency model for quasi-periodic oscillation in accreting X-ray pulsars be reconciled?, A&A, in press (astro-ph/0811.0049)
- Falanga, M., Cumming, A., Bozzo, E., Chenevez, J. (2008), The new intermediate long bursting source XTE J1701-407, A&A, in press (astro-ph/0901.0314)
- Bozzo, E., Falanga, M., Stella, L. (2008), Hunting for Magnetars in High Mass X-ray Binaries. The Case of SuperGiant Fast X-Ray Transients, submitted (astro-ph/0811.0995)

Non Refereed Publications:

- ATCA non-detection at 8.7 GHz of the Millisecond X-ray Pulsar SWIFT J1756.9-2508, Possenti, A.; Murgia, M.; Reynolds, J.; Camilo, F.; Burderi, L.; Salvo, T. Di; Antonelli, A.; Bozzo, E.; Burgay, M.; D'Amico, N.; and 6 coauthors 2007, Astr. Tel. 1128
- Possible IR counterpart of the newly discovered X-ray MSP SWIFT J1756.9-2508, Burderi, L.; Testa, V.; Menna, M. T.; Israel, G. L.; Salvo, T. Di; Papitto, A.; Riggio, A.; Antonelli, A.; Bozzo, E.; Burgay, M.; and 4 coauthors 2007, Astr. Tel., 1132
- Chandra non-detection of the newly discovered Millisecond X-ray Pulsar SWIFT J1756.9-2508, Papitto, A.; Salvo, T. Di; Burderi, L.; Gallo, E.; Menna, M. T.; Riggio, A.; Krauss, M. I.; Chakrabarty, D.; Antonelli, A.; Bozzo, E.; and 5 coauthors 2006, Astr. Tel. 1133
- Observing Supergiant Fast X-ray Transients in quiescence, Bozzo, E. 2007, XMM-Newton Proposal ID #05547202
- XMM-Newton & SWIFT observations of the Supergiant Fast X-ray transient SAX J1818.6-1703, Bozzo, E.; Campana, S.; Stella, L.; Falanga, M.; Israel, G.; Rampy, R.; Smith, D.; Negueruela, I. 2008, Astr. Tel. 1493

Conference participations:

- III CNOC, 9-11 December 2003, Monte Porzio Catone (Rome, Italy)
- Interacting Binaries, 4-10 July 2004, Cefal, Sicilia (Italy)
- IV CNOC, 23 - 25 November 2005, Padova (Italy) (Poster: A Model of Spin-Up/Spin-Down transitions in accreting X-ray Binaries)
- The Multicolored Landscape of Compact Objects and their Explosive Origins: Theory vs Observation, Cefal', Sicily (Italy), June 11-24 2006 (Oral Contribution: On the propeller effect of rapidly rotating magnetic neutron star: a new limiting condition)
- V CNOC, 11-14 September 2007, San Vito lo Capo (TP, Italy) (Oral Contribution: X-ray eclipse time delays in 4U 2129+47)
- The X-ray Universe, Granada (Spain), May 27-30 2008 (Oral Contribution: X-ray eclipse time delays in 4U 2129+47, grant support by ESA and ESA education)
- 7th INTEGRAL Workshop, Copenhagen, Sept. 8-11 2008 (Oral Contribution: Are there Magnetars in HMXBS? The case of Supergiant Fast X-ray Transients, grant support by DTU and IASF-INAF)

PhD Schools, Collaborations, & Seminars:

- 01/02/2006 – 28/02/2006 Scientific collaboration with Rosalba Perna at University of Colorado at Boulder - Boulder, Colorado, 80309, USA
- 10/02/2006 Some details of disk accretion on magnetized neutron stars (Seminar at University of Colorado at Boulder, USA)
- 20/11/2006 1/12/2006 Scientific collaboration with Maurizio Falanga (at CEA Service D'Astrophysique, Saclay, Paris- France)
- 30/11/2007 On the propeller effect of magnetic neutron stars (Seminar at CEA Service D'Astrophysique, Saclay, Paris- France)
- 15/01/2007 – 15/05/2007 Scientific collaboration with Rosalba Perna at University of Colorado at Boulder - Boulder, Colorado, 80309, USA
- National school of Astrophysics: Fundamental physics using compact objects and pulsars science with ALMA: the cool side of the Universe, May 20-27 2007 (Italy)
- 08/07/2007 – 14/07/2007 Scientific collaboration with Maurizio Falanga (at CEA Service D'Astrophysique, Saclay, Paris- France)
- 07/10/2007 – 16/10/2007 Scientific collaboration with Maurizio Falanga (at CEA Service D'Astrophysique, Saclay, Paris- France)

- 10/03/2008 – 16/03/2008 Scientific collaboration with Maurizio Falanga (at CEA Service D'Astrophysique, Saclay, Paris- France)
- 21/04/2008 – 24/04/2008 Scientific collaboration with Prof. Sandro Mereghetti and Dot. Sidoli Lara at IASF-CNR Milan (Italy)

A mio padre, mia madre e mia sorella
per il loro immancabile, indiscutibile e prezioso supporto.

A mio nonno Silvio, ai miei zii,
a mio zio Giulio e a mia cugina Elisa,
per avermi accompagnato in questi anni.

Ai miei amici Stefano, Valentina e Dario,
per il loro affetto ed il loro sostegno.

"L'uomo [...] redento dell'astronomia, penserá e agirá sempre nobilmente,
non cercherá piú che il giusto e il vero, disprezzerá gli dei falsi e bugiardi,
si sentirá veramente cittadino del cielo, e noi tutti,
che abbiamo comune l'origine e comune il destino,
formeremo una sola fraterna e armoniosa famiglia,
perché siamo tutti figli dell'infinito."
(Camillo Flammarion)

Contents

Chapter 1

Introduction

"They are only about 10 miles in diameter, yet they are more massive than the Sun. One sugar cube of neutron star material weighs about 100 million tons, which is about as much as a mountain[1]*."*
"They cram more mass than that of the sun into a sphere as wide as a city[2]*."*
"The intense magnetic fields of neutron stars exceed those produced on Earth a billion-fold, and the densities and pressures dwarf the realm of Earth-bound matter by a factor of a trillion or more [3]*."*

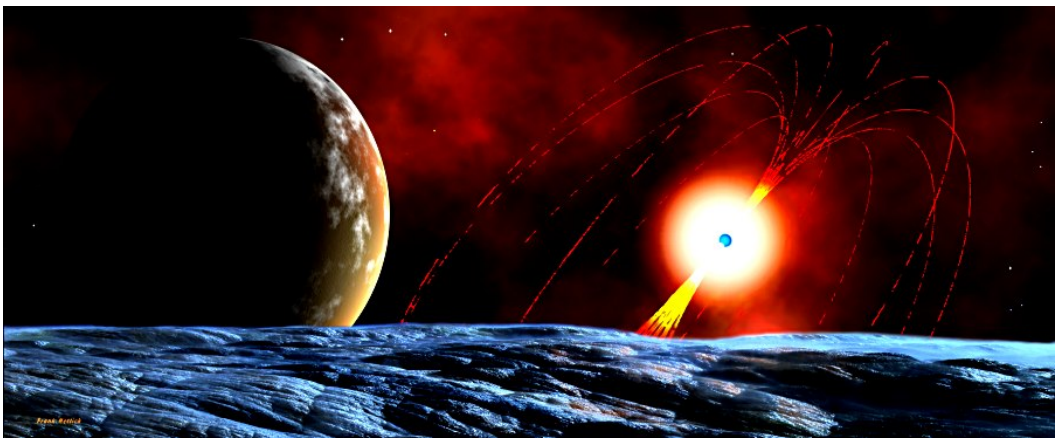

Figure 1.1: An artist impression of a magnetized neutron star

Exotic though Neutron Stars (NS) may be, the fascinating process of the formation and evolution of these stars, where the state of the matter and the strengths of the magnetic fields are anything but ordinary, involves a great deal of interest since decades. The existence of NSs was proposed first by Walter Baade and Fritz Zwicky in the early 30's (Baade & Zwicky 1934), when they were seeking an explanation for the origin of supernovae. They claimed that NSs form when a massive star of about 8-25 solar masses explodes as a supernova: the explosion ejects the star external layers into the interstellar medium while the core collapses, amplifying the magnetic field up to trillions of Gauss and

[1] http://imagine.gsfc.nasa.gov/docs/science/know_l1/neutron_stars.html
[2] Cowen, R., Science News, November 9, 2002
[3] http://www.physics.ubc.ca/ heyl/ns2005/prospectus.html

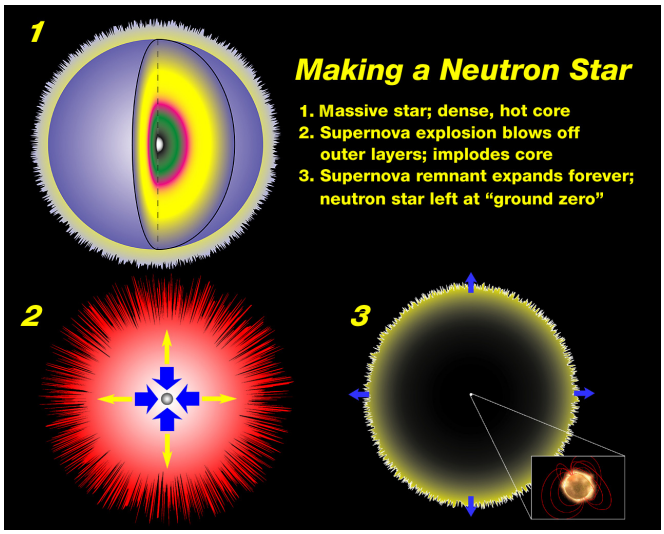

Figure 1.2: The Neutron Star recipe: making neutron stars from scratch.

compressing matter up to nuclear densities (see Fig. 1.2); protons combine with electrons to form neutrons, and hence the name "*neutron star*".

What Baade and Zwicky could not have imaged, however, was the potential of neutron stars for research in modern Astrophysics. Since the discovery of the first radio pulsar in 1967 (Hewish *et al.* 1968), a variety of astrophysical sources have then been associated with NSs. Today we know that these stars can appear as isolated object as well as members of binary systems; they can be observed as rapidly pulsing radio sources, as well as quietly cooling stars; some are persistent bright X-ray sources, whereas other are emitters of incredibly bright bursts detectable up to γ-ray energies.

Furthermore, the launch of X-ray telescopes of the present generation and the dramatic improvement of ground-based facilities in the past few years lead to even new breakthroughs regarding NSs. Among these, the discovery of "Magnetars", namely NSs with an exceptionally high magnetic field ($>10^{15}$ G), opened a new era for the study of the effects of extraordinarily intense magnetic fields on matter and radiation (see Sect. 1.4).

Neutron stars provide a unique laboratory to verify our understanding of nature at the extreme.

This PhD thesis focuses on NSs in binary systems. In particular, we will deal with the emission mechanisms and properties of these objects in the X-ray band: we will concentrate on *NS X-ray Binaries*.

Despite current estimation says that only about 5% of the total population of NSs might be hosted in binary system, these sources have provided so far an important contribution to our understanding of the evolution of NS and other stars in general.

1.1 Neutron Star X-ray Binaries

The simplest definition of a NS X-ray binary is that it is a binary system hosting a NS and emitting (mainly) in the X-ray band. It has been largely demonstrated that NS X-ray binary systems emit radiation also in the IR, Optical, UV, Gamma-ray and sometimes they show also radio emission and radio jets. Observations of these sources in different energy bands has provided crucial information to understand their nature and physical

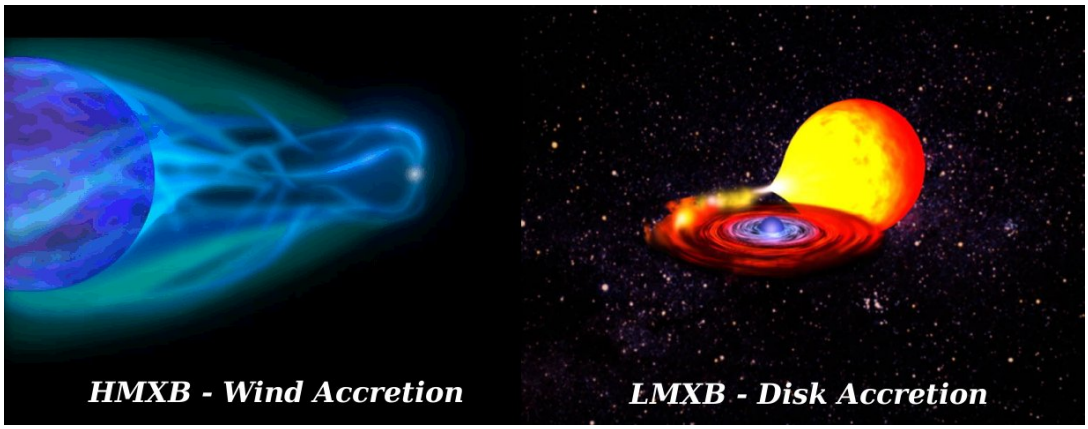

Figure 1.3: A representation of a NSHMXB and a NSLMXB. The typical geometries of wind and disk accretion are also shown.

properties. In particular it was recognized that, beside the NS, a NSXB might contain either a low ($M \leq 1\ M_\odot$) or a high ($M \gg 1\ M_\odot$) mass companion star.

At first, the discovery that NSs might be hosted in binary systems was a big surprise. Theories of binary evolution, developed until the early 60's, recognized that the more massive star in these systems should evolve first and explode as supernova (SN). However, it was argued that, at this stage, the binary system should be disgregated as a consequence of the large ejection of matter due to the explosion. It was soon realized that the survival of NS binaries was due to the effect of a huge mass transfer process, from the more to the less massive component, that must take place well before the SN explosion.

At the stage in which the first NS has formed in a binary, the less evolved companion starts to transfer mass toward the NS, and the system turns on as an X-ray binary. This mass transfer from the companion star to the NS leads to "*accretion*", and constitutes the main energy source for the X-ray emission from the system. The X-ray radiation originates from the hot plasma that descends deeply into the NS gravitational potential well: the temperature of this inflowing material increases to very large values because of the release of a large amount of gravitational energy, and easily reaches temperatures in the ∼keV range. In the X-ray band NSXBs are among the most luminous sources of our Galaxy. At present, about ∼200 sources in this class are known.

The emission properties that characterize an accreting NS in a binary system depend mainly on some of the NS physical parameters, *i.e.*, especially spin period and magnetic field. A NS with a strong magnetic field ($\sim 10^{12}$ G) possesses a magnetosphere extended for several hundred NS radii that obstructs material inflowing from the companion star and funnels it onto the NS magnetic poles. Here most of the gravitational energy of the accreting matter is released and liberated as X-ray radiation. Furthermore, if the magnetic and rotation axes are misaligned, the X-ray emission might display pulsations every time the radiation beam from the NS crosses our line of sight. This is less likely to happen for low magnetic fields ($\sim 10^{8}$ G), whose dynamical influence onto the inflowing mass is much reduced or absent. In the latter case, a boundary layer forms close to the NS surface and here most of the high energy emission is produced. Accumulation of matter in the boundary layer, as well as closer to the NS surface, has been recognized as the cause for thermonuclear bursts, which are described in detail in Sect. 1.3.

Instead, the mode with which mass transfer takes place, as well as the geometry of

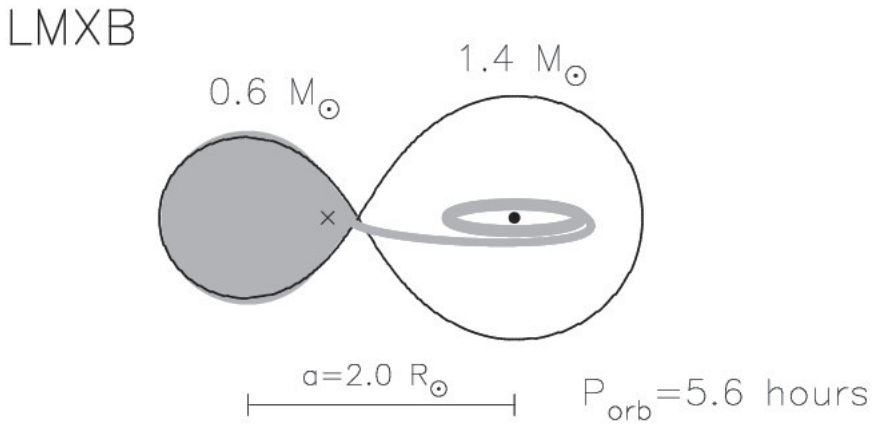

Figure 1.4: A typical NSLMXB. The NS in a LMXB is surrounded by an accretion disk which is fed by matter from the companion star overflowing through the Roche Lobe. Typical masses, orbital period and orbital separation are also indicated.

the accretion flow, is regulated by the nature of the companion star. In the following we will consider either the cases in which the companion star is an old star, typically later than type A, and the cases in which it is a O or B type star, thus younger and much more massive. In the first case, the mass of the companion star (in this case the secondary star) is <1 $M_\odot$, and the system is a low mass X-ray binary (LMXB). In these sources mass transfer occurs through the Roche Lobe overflow and an accretion disk is usually formed around the NS. When the companion star is much more massive than the NS (and is thus the primary star), the systems is a high mass X-ray binary (HMXB), and mass transfer occurs through the strong wind of the OB companion. These stars typically have very strong and fast winds that remove up to 10^{-5} $M_\odot$ yr^{-1} with terminal velocities of $\sim$1000 km s^{-1}. A NS that is orbiting close to an OB star, captures a substantial fraction of the wind, which provides the reservoir of fuel to feed the accretion process and thus the X-ray emission from the system. Only in some of these systems, incipient Roche Lobe overflow supplements the total mass transfer rate.

The accretion processes that occur in HMXBs and LMXBs take place under different physical conditions, and therefore we will threat them separately in next sections. We will first give a general description of LMXBs and HMXBs, and then discuss the theory of wind and disk accretion. Some specific topics related to these subjects will be presented in later chapters. Each of these chapter constitutes part of the original work developed in this thesis.

1.1.1 Neutron star low mass X-ray binaries

Neutron star low mass X-ray binaries are binary systems where the secondary star is later than type A, and its mass is $M \lesssim 1$ $M_\odot$ (for a review see e.g. Lewin *et al.* 1995). In some cases the secondary star can be even a white dwarf. A recent catalog of these sources has been published by Liu *et al.* (2001).

NSLMXBs are typically very old systems, with ages in the range 10^8-10^9 yr, and their spatial distribution is mostly concentrated toward the Galactic center. Their orbital

periods range from 11.4 min for 4U 1820-30 (Stella *et al.* 1987) to 16.6 d for Cir X-1 (Kaluzienski *et al.* 1976). Mass transfer to the NS occurs through an accretion disk that forms as a consequence of the Roche Lobe overflow (RLO, some details of this process are provided in Sect. 1.2.1, see also Fig. 1.4). The very short period systems (<3 hr) are expected to have degenerate dwarf mass companions and the occurrence of the RLO is guaranteed by the orbital period decay caused by gravitational radiation. In systems with orbital periods ($P_{\rm orb}$) in the range 3 hr$<P_{\rm orb}<$1 d the RLO is maintained by magnetic breaking, whereas in longer orbital period systems is the expansion of the donor star that keeps the star in touch with its Roche Lobe and regulates the transfer of mass toward the NS.

Only few NSLMXBs show X-ray eclipses, and thus most of their known orbital periods have been determined by using optical observations. In fact, despite the companion stars in these systems are intrinsically faint and difficult to observe, an optical emission modulated on the orbital period of the system is provided by the reprocessing of a fraction of the NS X-ray photons in the accretion disk and on the irradiated surface of the companion star.

Modulations in the X-ray band can be observed only for a restricted number of systems, i.e. those that are viewed almost edge-on. In all these cases, eclipses by the companion star and/or periodic absorption ("dips") by material at the outer rim of the accretion disk allowed the determination of the orbital period of the binary.

In most NSLMXBs eclipses are only partial, due to the presence of a Compton-thick highly ionized corona above and below the accretion disk (ADC, accretion disk corona, see e.g. White & Holt 1982). This corona scatters the X-rays in a region that is much more extended than the compact star where they are produced, and this region cannot be completely obscured when the companion passes in front of the NS, during an eclipse. Even if not in eclipse, ADC sources are usually less bright than other LMXBs ($\sim 10^{35}$ erg s^{-1} at the most). In fact, the presence of the scattering corona hides the central NS and only a small fraction ($\sim$1%) of the intrinsic X-ray luminosity of the source can be observed.

The origin of ADCs is still debated, but it is believed that these are generated through evaporation of matter due to the X-ray irradiation of the accretion disk surface from the central source. If this matter does not escape from the system, then it might corotate above and below the disk as a corona. Evidences for ADCs have been found in a number of NSLMXBs, and in some cases the orbital X-ray light curves also showed a sinusoidal modulation, with a minimum preceding the partial eclipse. This is usually ascribed to the partial occultation of the accretion disk corona (ADC), by a bulge at the rim of the disk caused by the incoming gas stream ("dip", see e.g. White & Holt 1982).

Generally, the observed properties of NSLMXBs depend on the viewing angle. At low inclination (<70°), no X-ray eclipses and no dips are observed, and the orbital period can be measured only from the optical light curve. At intermediate inclinations, dips can be seen as the results of (quasi-stable) structures at the edge of the accretion disk. High inclination systems (>80°) usually show partial X-ray eclipses, with residual X-ray emission due to the scattering by the ADC. In Fig. 1.6 we show the case of the X-ray binary X 1822-371, which is one of the rare eclipsing NSLMXBs, in which both optical and X-ray orbital modulations have been detected.

In some NSLMXBs orbital period changes with time have also been measured, but the results were found not to be in agreement with evolutionary expectations. While different explanations have been suggested, one of the most intriguing possibility is that, in some cases, the observed changes in period might be driven by the presence of a third star, when the binary is part of a triple system. In Chapter 5 we discuss the case of 4U 2129+47, a

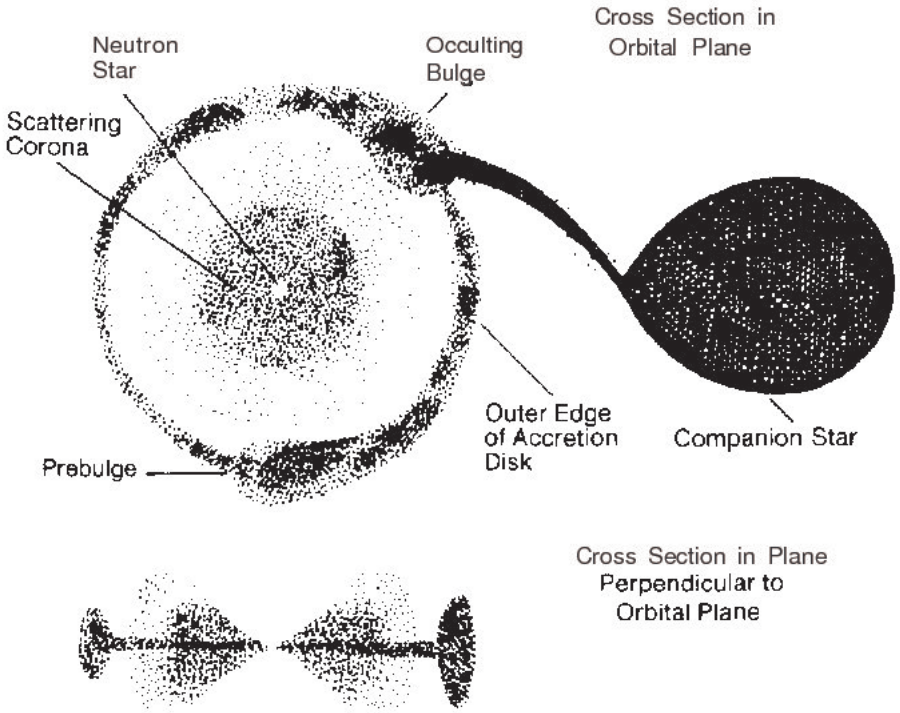

Figure 1.5: Accretion flow and system geometry in a NSLMXB with an accretion disk corona. Matter lost by the companion star through Roche Lobe overflow forms an accretion disk around the NS. The ADC is generated by evaporation of matter from the surface of the accretion disk due to the strong X-ray irradiation coming from the compact star. The bulge at the external rim of the accretion disk, where matter from the companion star impacts, is also represented. Both the ADC and the external disk rim contribute in oscurating the NS X-ray emission and generate dips and eclipses that are useful tools to measure the orbital period of the system (see also Fig. 1.6).

NSLMXBs which displays both an ADC and periodic dips and, in some cases, provides evidence for a hierarchical triple system.

NSLMXBs are very seldom X-ray pulsars. This is thought to be due to the decay of their magnetic field, which usually reaches values of $\sim 10^8$-10^9 G in $\sim 10^8$ yr. According to theory, the magnetic field of a NS is initially generated in the outer crust of the star by, e.g. thermomagnetic effects. The evolution of this field with time is then calculated from the induction equation by taking into account the structure of the NS crust, which determines the electrical conductivity, and a model for the cooling of the star, which in turns describes the temperature profile of the crust. The results obtained with these calculations show that the current distribution, which is responsible for the magnetic field, migrates inward as a result of diffusion and enters the highly conducting parts of the NS. In this region the NS is a superconductor and thus the magnetic field remains stable forever frozen at a certain residual value. The effect of ohmic dissipation results in final magnetic fields that are compatible with observations (see, e.g. Bhattacharya 2002, for some alternative models of the magnetic field decay).

Magnetic fields of the order $\sim 10^8$-10^9 G are unlikely to funnel matter toward the NS

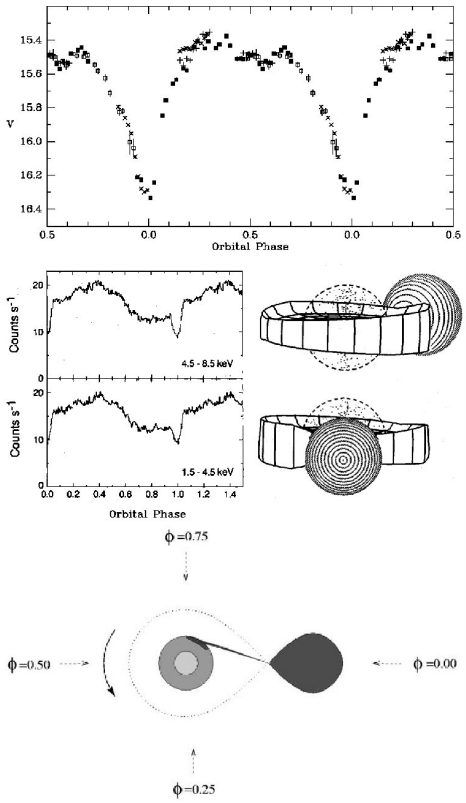

Figure 1.6: The X-ray binary X 1822-371 is one of the few NSLMXBs in which both optical and X-ray modulations on the orbital period have been detected. The apparent X-ray luminosity while not in eclipse is 3×10^{35} erg s^{-1} (thought to be about ∼1% of the intrinsic X-ray luminosity due to the effect of the scattering ADC). X 1822-371 has an orbital period of 5.57 hr, a companion star of ∼0.4 $M_\odot$ (White & Holt 1982). Pulsations at 0.6 s have been discovered (Jonker & van der Klis 2001), confirming that the compact star is a rotating NS. Studies of the X-ray and optical light curves showed that the observed modulations are due to a combination of a partial eclipse by the secondary star and obscuration by thickened outer disk rim (caused by the incoming gas stream). Panel A shows the optical lightcurve in the V band (Cowley & Schmidtke 1993), where the partial eclipse is clearly visible. The X-ray lightcurve in panel B (*EXOSAT* data) displays both an eclipse and a dip preceding it that has been attributed to the presence of a thicker outer disk rim (Hellier & Mason 1989). Panel C shows a schematic representation of the system, with the companion star, the NS and the ADC, which shape has been calculated in order to reproduce the shape of the optical and X-ray lightcurves. Finally, panel D shows a global representation of the system seen from the above, where the orbital phases are illustrated (Cottam *et al.* 2001).

magnetic poles at large distances, and in these cases accretion occurs along an equatorial bound at the NS surface, where the boundary layer between the accretion disk and the star forms. In this case X-ray pulsations are not expected. Some of the few pulsating NSLMXBs have shown alternating episodes of spin-up and spin-down. The observed spin-

up and spin-down rates are consistent with accretion torques due to an accretion disk, and have been explained by the theory of the NS magnetosphere-accretion disk interaction. This will be discussed further in Sect. 1.2.1.

On the other hand, NSLMXBs show X-ray bursts. These bursts are the results of sudden thermonuclear fusion of accreted matter at the NS surface, and we will discuss them in greater detail in Sect. 1.3.

Many NSLMXBs are transient sources that undergo transitions between outburst and quiescence over timescales that ranges from days to hundreds of days. During the first few weeks of their outbursts these sources might be among the most bright in the sky, then they fade away with a variation in the bolometric luminosity that easily reaches factor of thousands or more. These transients episodes are believed to result from instabilities in the accretion disk or in the NS magnetosphere, and the study of these sources allows models for the accretion processes and high energy emissions to be tested over a large range of mass accretion rates. Some of these models will be discussed in Chapters 3 and 4.

The X-ray spectrum of NSLMXBs is basically soft, with values of kT in exponential fits less than $\sim$10 keV. In some cases also a non thermal component has been detected up to hundreds of keV (Fiocchi *et al.* 2006). The soft thermal emission is usually interpreted as the X-ray emission generated from the NS surface and from the hot innermost region of the accretion disk. The hard X-ray emission is generally believed to derive from the reprocessing of the soft X-ray emission in the compton-thick corona above and below the surface of the accretion disk. Hard X-rays can also be produced by Comptonisation by synchrotron emission in the jet (Fender *et al.* 2004).

Often spectral changes are observed at different values of the X-ray luminosity, together with a considerable X-ray variability on a wide range of time scales, from tens of seconds down to milliseconds. Since most of the X-rays are produced due to the accretion of matter close to the NS surface, it is expected that this variability reflects variation in the mass accretion rate, likely due to inhomogeneities and instabilities within the accretion flow. Timing and spectral properties of these sources can thus be used to probe the accretion flow dynamics very close to the NS. A milestone in the understanding of these spectral and "timing" variability has been the introduction of X-ray colour-colour diagrams (XCCDs, see e.g., Hasinger & van der Klis 1989).

An X-ray color is a hardness ratio between the photon counts in two different energy bands. By calculating two X-ray colours as a function of time, the spectral variation of a source can be represented on a plane, i.e. on a XCCD. We will discuss a practical example of a XCCD for a NSLMXB in Chapter 6. The tracks that NSLMXBs trace in their XCCDs have been used to identify different subclasses of these systems: the so called "Atoll" and "Z" sources (see e.g. van der Klis 1989, 1995; Strohmayer *et al.* 1996). An example of a XCCD of an atoll and a Z source is represented in Fig. 1.7. It is commonly believed that Atoll and Z sources differ for the mean value of the mass accretion rate, as well as for the strength of their magnetic field and spin period. In the tracks of atoll sources different branches were identified. Each branch represents a different spectral state, and presumably occurs at a different mass accretion rate (Hasinger & van der Klis 1989). The "island" branch corresponds to a hard spectral state, where the soft emission is much reduced and the spectrum extends to high energies (up to 200 keV); in the "banana" branch the spectrum is softer, and most of the energy is emitted below 20 keV (see e.g., Barret 2001; Gierliski & Done 2002). The track on the XCCD usually can be completed in a time scale ranging from days to weeks. In a Z source XCCD three different branches can

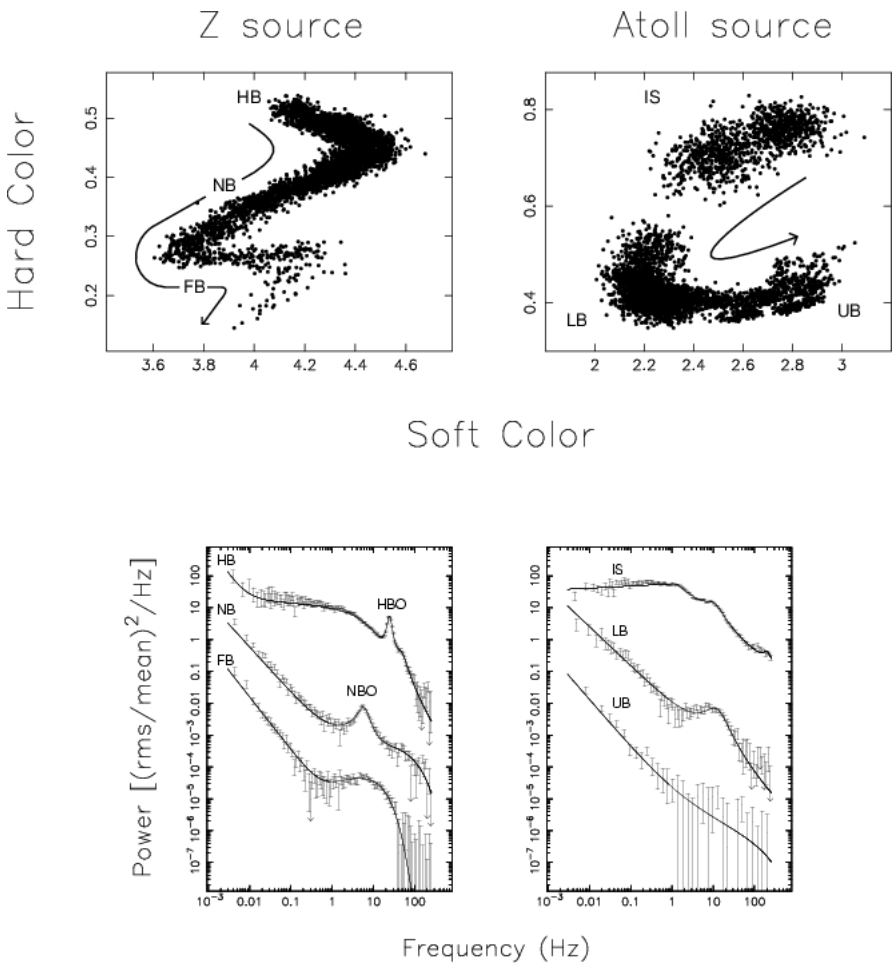

Figure 1.7: X-ray colour-colour diagrams (upper panels) and power spectra (lower panels) of a typical atoll (right panels) and Z (left panels) source. The arrows represent the direction along which the mass accretion rate increases, according to the most recent interpretations. The soft colour corresponds to (3-5)/(1-3) keV, whereas the hard colour is calculated as (6.5-18)/(5-6.5) keV (van der Klis 1995). For the Z source, the position of the horizontal, normal and flaring branches is indicated with HB, NB, and FB, respectively. For the atoll source IS, LB and UB corresponds to the island state, the lower and the upper banana, respectively. QPOs in the power spectra are clearly visible.

be identified: the "horizontal branch", the "normal branch" and the "flaring branch"; the sequence of these branches corresponds to increasing mass accretion rates. The Z sources are generally characterized by larger luminosities than those of Atoll sources, have higher magnetic fields ($\sim 10^9$ G), and complete their path in the XCCD in a time scale ranging from hours to days.

Both atoll and Z sources display several timing features that characterize their power spectra and vary in fairly continuous fashion when the sources move along their XCCDs. Among these features, the so called "Quasi-Periodic Oscillations (QPOs)" constitute one of the most interesting example. These are finite-width peaks in the power spectrum of a source. QPOs with frequencies from mHz to hundreds of Hz have been detected in many atoll and Z sources during different spectral states. Among all the observed

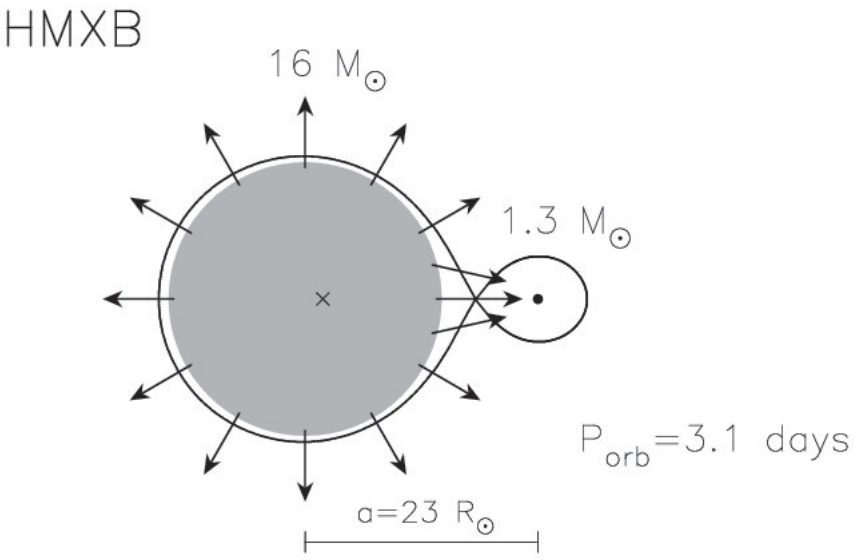

Figure 1.8: A typical NSHMXB. The NS in a HMXB is generally fed by the strong high velocity wind of the supergiant companion. Typical masses, orbital period and orbital separation are also indicated.

QPOs, kHz QPOs have drawn a lot of attention, as their fast variability time scale reflects phenomena occurring close to the NS surface and can be used to investigate the condition of the accretion flow under the effect of a strong gravitational field. In fact, different models have been developed to interpret KHz QPOs in NSLMXBs which involve mainly general-relativistic frequencies of motions close to the compact object. Millihertz QPOs in NSLMXBs are instead mostly interpreted within the "beat-frequency model" (BFM), which predicts that QPO frequencies are produced by beating orbital frequencies with the spin frequency of the NS. This requires a spin-orbit interaction that might result from: a) a periodic illumination of an orbiting blob in the disk by the NS beam sweeping around at the star's spin velocity; b) some instability at the inner disk radius that modulates the mass accretion rate. We will discuss further the beat frequency model applied to mHz QPOs in Chapter 2.

1.1.2 Neutron star high mass X-ray binaries

Besides the collapsed object, a neutron star high mass X-ray binary contains, a companion star (in this case the primary star) with a mass $\gg$1 $M_{\odot}$. Optical emission of HMXBs is dominated by the primary component, which is not, in general, strongly influenced by the presence of the X-ray source.

Typically, two subclasses of NSHMXBs are distinguished (Liu *et al.* 2001). The first class is that of permanent X-ray sources. Their optical counterparts are supergiant OB stars (I luminosity class), with roughly circular orbits, and orbital periods P_{orb}<10 d (see Fig. 1.8). Their X-ray emission is persistent, with $L_X \leq 10^{37}$ erg s^{-1}. Instead, the second class, which comprises most of the known NSHMXBs, is that of transient sources. These have Be primary stars (luminosity classes ranging between V and III), eccentricity of the orbits $0.2 \leq e \leq 0.5$, and orbital periods P_{orb}>10 d (see Fig. 1.9). Their X-ray emission is

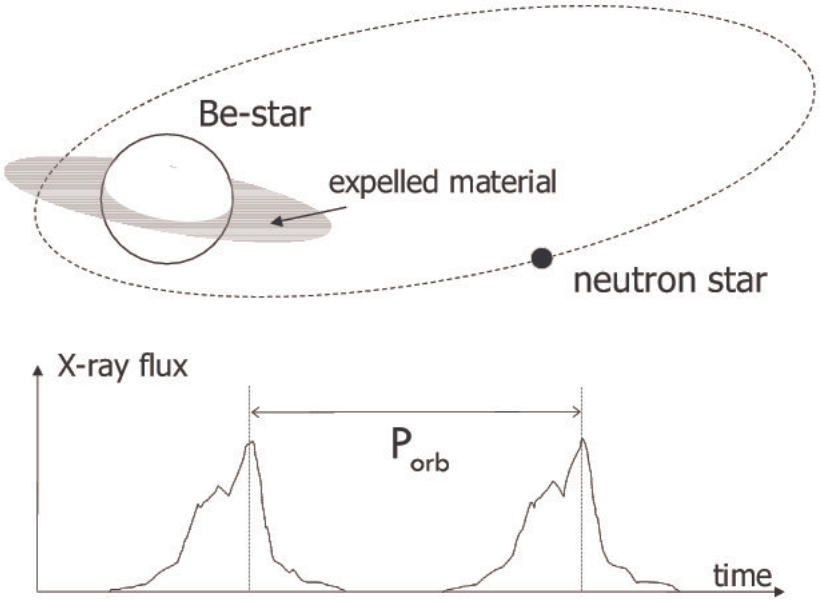

Figure 1.9: A typical NSHMXB with a Be star companion. In these systems the NS moves in an eccentric orbit around the companion, which is not filling its Roche-lobe. Near the periastron passage the NS accretes the circumstellar matter ejected from the rotating companion; this gives rise to periodic X-ray bursts lasting several days.

extremely variable, with $L_X \sim 10^{34}$-10^{39} erg s^1, with a maximum to minimum luminosity ratio of $\geq 10^2$. In several NSHMXBs were observed both low-luminosity (Type I) outbursts recurring close to periastron and, at different times, high-luminosity (Type II) outbursts that last for several orbital cycles and display little (if any) X-ray flux variations associated to the orbital phase. Some of the observed spin-up rates are consistent with accretion torques from an accretion disk, and thus it was suggested that the formation of a temporary accretion disk around the collapsed object is not unlikely during outburst phases (Rappaport 1981).

OB and Be NSHMXBs also differ because of the different origin of the mass transfer mechanism toward the NS[4]. In the first class, the mass loss process occurs via a strong stellar wind and sometimes might be sustained also through "incipient" Roche lobe overflow. In the second class, the mass transfer due to the stellar wind is not as strong as in the previous case; instead, a large mass transfer is triggered by the rapid rotation of the primary star through shell ejection episodes or build up of matter around the resonant orbits in the slow equatorial wind component (van den Heuvel 2005).

All HMXBs are relatively young sources, with ages of few$\times 10^6$ yr, and are concentrated on the galactic plane within a band of $\sim 3.9°$. The NS magnetic field in these systems has not decayed significantly, and is typically in the range 10^{11}-10^{13} G. At odds with

[4]We note that these classes can also be distinguished thanks to a known relationship between the orbital period of NSHMXBs and the spin period of the X-ray pulsars hosted in these systems (Corbet 1986). According to this relation OB and Be systems have $P_{\rm spin} \propto P_{\rm orb}^{4/7}$ and $P_{\rm spin} \propto P_{\rm orb}^{2}$, respectively.

NSLMXBs, the NS in these systems thus have large magnetospheres (typically ∼100 NS radii) that funnel the inflowing matter at large distances from the star and give rise to strong pulsations in the X-ray flux. The first pulsating HMXB, Cen X-3, was discovered by Uhuru on 7 May 1971 (Giacconi *et al.* 1971). The X-ray light curve of this source showed a clear 4.8 s modulation that has later been interpreted as the spin period of the NS hosted in this system (see Fig. 1.10).

Such strong magnetic fields have been directly measured through cyclotron lines detected in the X-ray spectra of NSHMXBs (see Fig. 1.11). In fact, when the strength of the magnetic field is below the critical quantum value $B_{crit} = m^2c^3/e\hbar \simeq 4.4 \times 10^{13}$ G, the energy spacing between the first two Landau levels[5] is equal to the cyclotron energy $E \simeq \hbar\Omega_B \sim 12$ keV$\cdot(B/10^{12})$ G. Here $\Omega_B = eB/m$ is the electron cyclotron frequency, m is the electron mass, e the electron charge, and B the strength of the magnetic field. Since in the atmosphere of an X-ray pulsars $kT < \hbar\Omega_B$, electrons are mainly confined in the ground Landau state (in a 1D distribution). Moreover, since the rate of collisional excitation to higher Landau states is much less than the cyclotron de-excitation rate from excited states, the population of the levels is far from thermal equilibrium and cyclotron line emission regulates the cooling of the atmosphere. It has been demonstrated that for $B > 10^{12}$ G, the electron temperature can be maintained at few times $\hbar\Omega_B$, whereas for $B < 10^{12}$ G, the ion temperature is high enough to excite the electron Landau levels via collisions and the electron temperature becomes enough high ($\sim 10^9$ K) to produce X-rays (Harding 1994). The spectrum that emerges from the NS atmosphere is practically a Doppler broadened cyclotron line, with a small contribution from the bremsstralhung emission to the continuum. The detection of a line due to cyclotron resonance scattering (CRS) in the X-ray spectrum can provide a very reliable estimation of the NS magnetic field strength. To date, cyclotron lines have been observed in the X-ray spectra of many NSHMXBs (such as Her X-1, 4U 0115+63, 4U 153852, X0331+53, Vela X-1, 4U 1907+09, and GX 3012; see e.g. Nagase 1994, and the references therein), and the energies measured are in the range 7-40 keV. These correspond to magnetic field strengths of $(0.6\text{-}3.5)\times 10^{12}$ G.

The spectrum of NSHMXBs is generally much harder than the spectrum of NSLMXBs, with values of kT in exponential fits larger than ∼15 keV. In some cases a cutoff energy (E_C) have been measured around ∼18-20 keV. From the analysis of these spectra, an empirical relation has also been proposed between the fundamental resonance energy (E_B) and the cutoff energy (E_C) of the power spectrum: $E_B \simeq 2E_C$. This relation suggested that the cutoff of the spectrum at high energies could be a good indicator of the cyclotron energy and then of the magnetic field intensity for those pulsars from which the CRS line is not detectable; however, this did not receive any secure confirmation and the validity of this assumption for pulsar with no detected CRS line is still a matter of debate.

Besides spectral features, high magnetic field NS in HMXBs also show features in their power spectra: in fact, in several of these sources mHz QPOs have been detected a factor $\sim 10^2$ below the spin frequency. In most of these observations the QPO frequency can be well explained by using the beat-frequency model (see Sect. 1.1). In Chapter 2 we will show how these features can be used to probe the accretion flow at the inner disk radius.

X-ray observations of NSHMXBs provides also a very useful tool to probe and study the winds of massive stars. On one hand, the continuous change in our line of sight during the orbital motion of the NS around its companion allows for a measurement of

[5] These are energy levels of conduction electrons which occur in a material subjected to a magnetic field. The Landau levels are quantized because of the quantization of the electron motion perpendicular to the field.

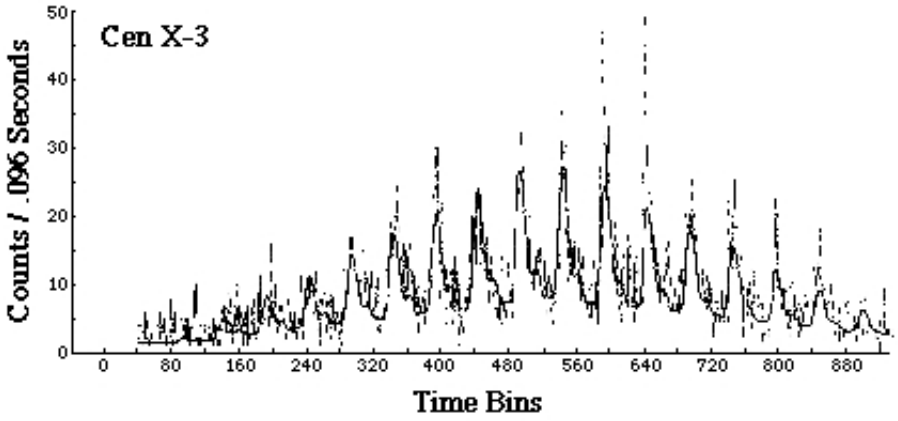

Figure 1.10: Discovery of the first pulsating X-ray source by Uhuru satellite on 7 May 1971 (Giacconi *et al.* 1971). This source was called Cen X-3 and hosts a 4.8 s spinning NS. The modulation of the X-ray emission from this source on this spin period is clearly seen.

the distribution of the X-ray absorbing gas in the system; in these cases the X-ray spectra show substantial absorption at low energies, caused by the increasing absorption cross-section of the medium-Z elements, such as Nitrogen, Oxygen and Carbon. This results in K and L absorption edges in the spectra, and emission lines from fluorescence and/or recombination. Some of these spectral features will be discussed further in Chapter 8. On the other hand, the typical X-ray variability on different time scales that characterize most of NSHMXBs, offers a unique opportunity to study how these radiatively-driven winds interacts with the compact object over a wide range of mass loss rates. This will be discussed further in Chapter 7.

1.2 Accretion processes onto NSs

The idea that the X- and γ-ray emission form compact objects could be powered by the extraction of gravitational potential energy from material accreting onto the compact objects was first suggested by Zeldovich & Guseynov (1966). The energy released from the accretion of a mass m onto a star with mass M and radius R is approximately

$$\Delta E_{\rm acc} = GMm/R, \tag{1.1}$$

where G is the gravitational constant. If the accreting star is a NS, then $M{\simeq}1.4$ M$_\odot$, $R{\simeq}10$ km, and $\Delta E{\simeq}10^{20}$ erg for each gram of accreted mass. If all this energy is released as electromagnetic radiation, then the luminosity produced by the accretion process is directly proportional to the rate at which matter reaches the NS surface, i.e. $L_{\rm acc}{=}dE_{\rm acc}/dt{\propto}\dot{M}$.

If the accretion flow has a spherical symmetry and is composed mainly by fully ionized hydrogen, then it is possible to estimate a maximum value for the mass accretion rate $\dot{M}$. This value corresponds to the rate at which the radiation pressure force, due to the electromagnetic emission from the NS, equals the gravitational force acting on a pair of

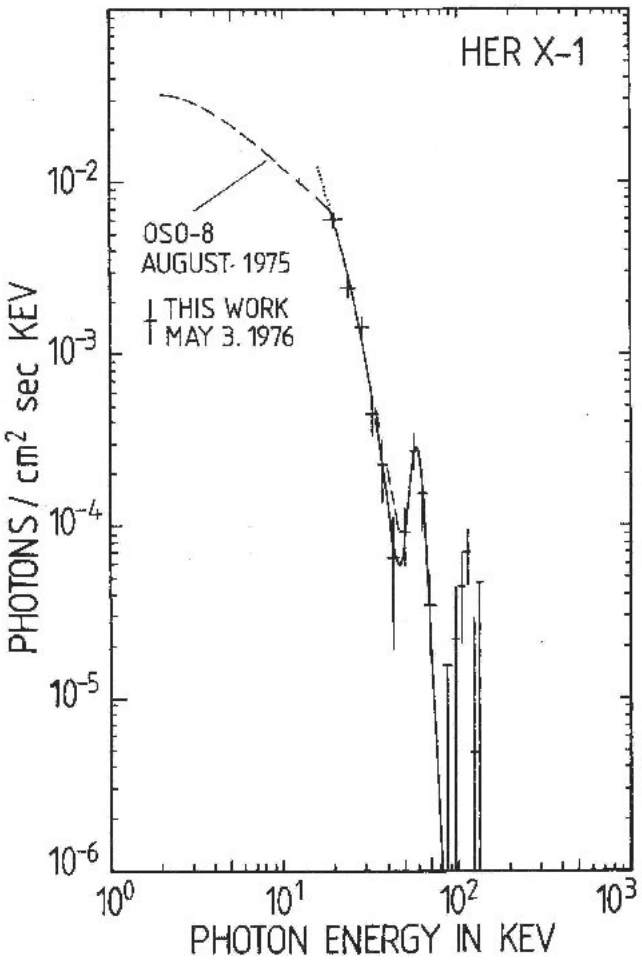

Figure 1.11: The X-ray spectrum of Her X-1 as obtained in a balloon observation in 1975, constituting the first detection of a cyclotron line (Truemper *et al.* 1978).

one electron and one proton in the close surrounding of the accreting star:

$$\frac{GM}{R^2} = \frac{L\sigma_{el}}{4\pi R^2 m_{\rm p} c}. \tag{1.2}$$

Here R is the radial distance from the star, $m_{\rm p}$ is the proton mass, and $\sigma_{\rm el}$ is the Thompson (electron) scattering cross section. The Eddington Luminosity is the maximum luminosity attainable for a spherical and steady mass accretion flow, and can be written as

$$L_{Edd} = 4\pi GMm_p c/\sigma_{el} \simeq 1.3 \times 10^{38}\ (M/M_\odot)\ erg\ s^{-1} \tag{1.3}$$

Since $L_{\rm acc}$=$GM\dot{M}/R$, the above equation also defines a maximum value of the mass accretion rate, that is

$$\dot{M}_{Edd} = 1.5 \times 10^{-8}(R/10^6)M_\odot\ yr^{-1} \tag{1.4}$$

For a NS, the typical accretion luminosity is

$$L_{acc} = 1.3 \times 10^{36}\dot{M}_{16}(M/M_\odot)(10\ km/R)\ erg\ s^{-1} \tag{1.5}$$

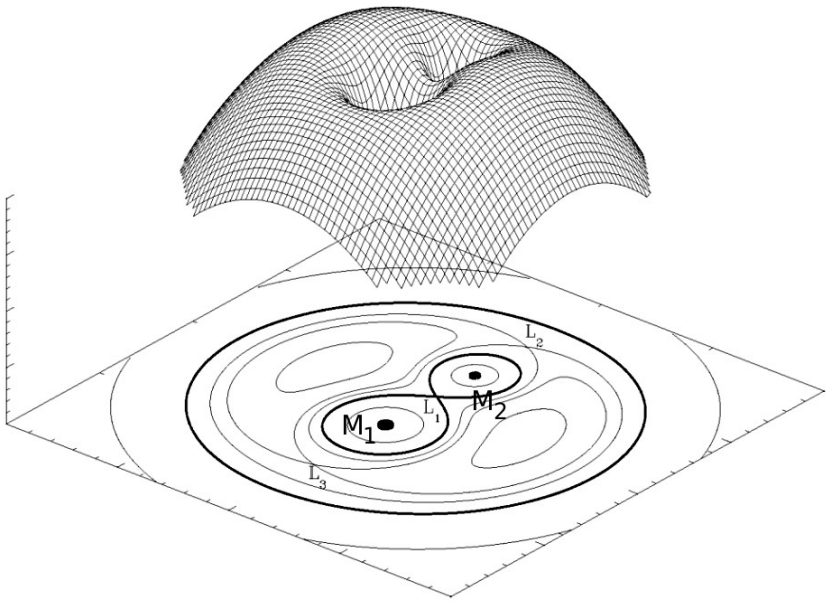

Figure 1.12: A three-dimensional representation of the Roche potential in a binary star with a mass ratio of 2. The figures at the bottom are called the Roche lobes of each star. L1, L2 and L3 are the points of Lagrange where forces cancel out. Mass can flow through the saddle point L1 from one star to its companion, if the star fills its Roche lobe.

($\dot{M}_{16}$ is the mass accretion rate in unit of 10^{16} g s^{-1}) and is generally lower than the limit imposed by Eq. 1.3. The case of accretion at rates above the Eddington limit will be discussed briefly in Sect. 1.3.

In the following we review some of the basic aspects of the accretion theory onto a NS in both the cases in which this star is interacting with an accretion disk or with the wind of the companion star.

1.2.1 Roche Lobe overflow and disk accretion

The Roche Lobe overflow (RLO) mechanism takes place in binary systems with relatively small orbital separations. In the system of reference where the two stars are fixed, the effective gravitational potential is:

$$\Phi(\vec{R}) = -\frac{GM_1}{|\vec{R}-\vec{R}_1|} - \frac{GM_2}{|\vec{R}-\vec{R}_2|} - \frac{1}{2}(\vec{\Omega}\wedge\vec{R})^2, \tag{1.6}$$

where Ω is the orbital angular velocity, $\vec{R}_1$ and $\vec{R}_2$ are the position vectors of the centers of the two stars with masses M_1 and M_2, and $\vec{R}$ is the position vector of a reference point with respect to the angular momentum axis through the barycenter of the binary systems. The equipotential surfaces are represented in Fig. 1.12. The point L_1 is called inner Lagrangian point, and connects the so called Roche Lobe surfaces. If the initially more massive star fills its Roche Lobe, then the external envelopes close to L_1 are no longer confined by the star's gravitational field and mass transfer toward the NS is initiated. The Roche Lobe radius is defined as the radius of the sphere with the closest volume to that

of the lobe, and can be approximated by (Eggleton 1983):

$$R_{\rm L}/a = 0.49q^{2/3}/(0.6q^{2/3} + ln(1 + q^{1/3})). \quad (1.7)$$

Here a is the orbital separation, and q is the mass ratio between the donor and the compact star mass. At the beginning of its evolution, a binary is in the "detached" phase, during which both the primary and the secondary stars are within their Roche Lobe. When the more massive star evolves toward the giant branch, its envelope expands ("semi-detached" phase) and RLO begins. The further evolution of the system depends on the nature of the donor star. The RLO can be sustained until the donor star fills its Roche Lobe. As a consequence of the removal of mass at L_1, the donor star is perturbed and it falls out of hydrostatical and thermal equilibrium. Therefore, in order to reestablish the equilibrium, the star will either grow or shrink; similar changes also occur for the Roche Lobe radius. A stable mass transfer can be realized only if, starting with a configuration in which the donor star fills its Roche Lobe, the changes in size of the Roche Lobe and of the star itself grow and shrink in a similar way. Calculations by Tauris & Savonije (1999) show that all NSLMXBs with donor stars $M_2 \lesssim 1.8$ $M_\odot$ generally have a stable mass transfer. On the contrary, systems with heavy donors ($q \gtrsim 1.5$) have catastrophic episodes of RLO, during which most of the mass of the donor star is transferred to the RL of the compact object. For this reason, mass transfer in NSHMXBs occurs preferably through the wind of the donor star rather than through the RLO.

Matter from the donor star acquires a supersonic velocity when passes through the inner lagrangian point; therefore, beyond L_1 the gravitational acceleration of the compact star overtakes the pressure force induced by the envelope of the donor star. Matter inside L_1 follows an elliptic trajectory, whose characteristics are determined only by the NS gravitational field and the angular momentum of this matter. The latter can be expressed as

$$l = \Omega(a - R_{\rm L})(a - \lambda R_{\rm L}), \quad (1.8)$$

where λ is the ratio of the angular velocities of the rotational motion of the companion and of the orbital motion of the NS, respectively. Once inside the Roche Lobe of the compact object, the flow of matter wraps itself up in a spiral, dissipates its kinetic energy through friction, and settles down in a Keplerian orbit at the so called circularization radius

$$R_{\rm circ}/a = (1 + q)(R_1/a)^4 \quad (1.9)$$

This ring of matter at $R_{\rm circ}$ ($\gg R_{\rm NS}$) will then spread radially due to viscosity, and a Keplerian accretion disk is formed around the NS[6].

The general theory of Keplerian accretion disks was reviewed by Pringle (1981). In his seminal paper about the initial development of the theory of accretion disk in Astrophysics, this author says: "if we put a particle in a circular orbit around a central gravitating body, it will stay in that orbit. If we extract energy and angular momentum from the particle we may allow it to spiral slowly inwards. The amount of energy that can be extracted by such a process is equal to the binding energy of the innermost accessible orbit. For orbits around sufficiently compact objects a reasonable fraction of the particle's rest mass energy can be extracted. For example, of order of 10 percent of the rest mass can be obtained from orbits around a NS, and up to 40 percent for orbits around a black hole. Thus the

[6] In Sect. 1.2.2 we will also analyze the situation in which $R_{circ} \gg R_{\rm NS}$ and matter can accrete directly onto the NS.

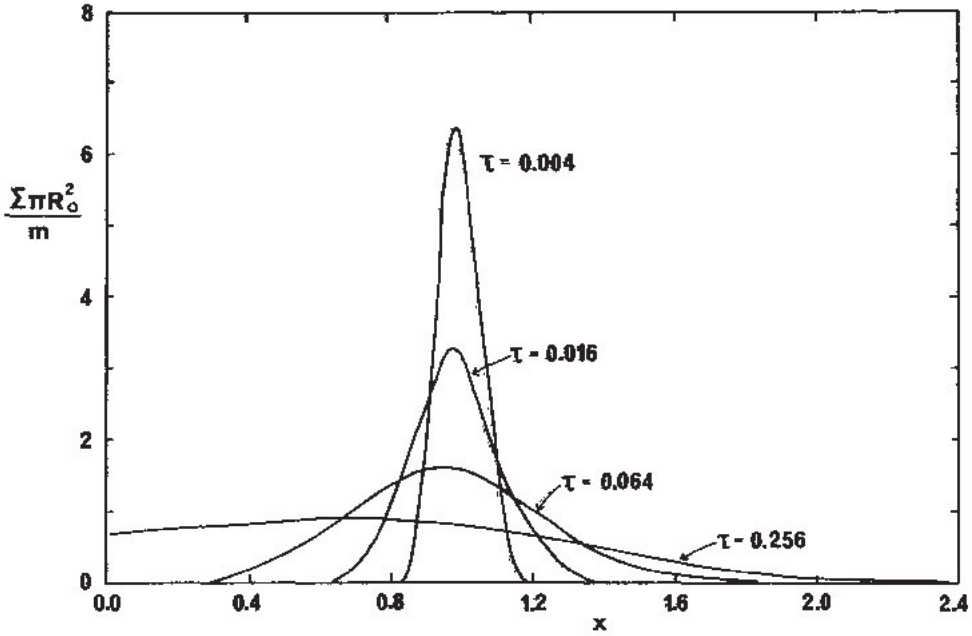

Figure 1.13: The viscous evolution of a ring of matter m. By using a constant viscosity ν in Eq. 1.10, the surface density Σ is found to be a function of the parameter $x{=}R/R_0$ only, where R_0 is the initial radius of the ring. $\tau{=}12\nu t/R_0^2$ is the dimensionless time.

accretion process can be an efficient converter of rest mass to radiation. The problem is to set up the process that can extract the energy and the angular momentum."

By approximating the accretion disk as a sequence of concentric annuli, it was suggested that the mechanism to extract energy and angular momentum is the friction between neighboring annuli, i.e. the viscosity: "if there is any viscosity present in the gas, or if there is any other process present that acts in a similar dissipative manner to dump out shearing motion, the energy of the shearing motion is dissipated in the fluid as heat, and thence radiated away. Thus, viscosity causes the gas to loose energy. Since the only energy source is the gravitational potential, this means that the gas sinks deeper in the potential well. Thus, viscosity converts gravitational potential energy into radiation in an efficient manner."

By using the equations of mass, energy and angular momentum conservation, Pringle (1981) obtained the well known diffusion equation for the surface density of the disk, Σ:

$$\frac{\partial \Sigma}{\partial t} = \frac{3}{R}\frac{\partial}{\partial R}\{R^{\frac{1}{2}}\frac{\partial}{\partial R}[\nu \Sigma R^{\frac{1}{2}}]\}. \tag{1.10}$$

Here R is the radial distance from the central point mass that generates the gravitational field, t is the time, and ν is the viscosity coefficient, which is generally a function of Σ, R, and t. The spread in time of the annulus of matter created by the Roche Lobe overflow at $R{=}R_{\rm circ}$, depends on the viscosity coefficient. If ν is a constant, then the Eq. 1.10 can be solved analytically and a representation of the solution is given in Fig. 1.13.

A physically plausible theory of the underlying causes of disc viscosity was suggested first by Shakura & Sunyaev (1973; hereafter, SS73). These authors argued that magnetic fields are the likely way in which a disc flow with a differential rotation transports angular momentum from its inner to the outer regions. Without entering the details of this physical

process, they suggested the so called α-prescription for the viscosity

$$\nu = \alpha c_s H. \tag{1.11}$$

Here $\alpha \leq 1$ is a parameter that encloses all the poorly known physics of the processes that determines the viscosity. This parametrization thus does not take into account self-consistently the dependence of ν from R and Σ (there is no a priori reason to consider $\alpha \leq 1$ and constant over the whole radial extension of the disk). However, the α prescription permits to solve analytically the equations of the structure of a Keplerian disk and encouraging results were obtained when comparing this solution with some observational data. A more physical support to the α prescription was provided by Balbus & Hawley (1991). These authors demonstrated the existence of a MHD instability, the so-called magnetorotational instability (MRI), that generates the necessary feedback to maintain a magnetic dynamo in the accretion disc and gives rise to the required transport of energy and angular momentum.

Once the α prescription is considered, the steady-state solution of SS73, i.e. the so called "standard model", can be obtained from the conservation equations reported, e.g., in Pringle (1981), by assuming a geometrically thin disk in which the heating and cooling processes are locally in equilibrium. SS73 distinguished three different regions of an accretion disk:

- Region A: this is the closest region of the disk to the central star, and thus the temperature in the disk is higher with respect to other regions. The dominant contribution to the pressure in the disk is that due to the radiation. Photon scattering on free electrons is the main source of opacity.
- Region B: this region is farther away from the central object with respect to region A. The temperature is lower and the dominant contribution to the pressure is due to the thermal pressure of the disk plasma. Electron scattering is the main source of opacity.
- Region C: this is the outermost region of the accretion disk. The temperature is still lower than in region B and the main source of opacity is the electron scattering.

The solution for the quantities that define the structure of the accretion disk are given below for each region (see e.g., Vietri 2008).

- REGION A:

$$\begin{aligned}
\Sigma &= 9.2 \times 10^4 g cm^{-2} \alpha^{-4/5} \dot{m}^{7/10} m^{1/5} \eta^{-7/10} x^{-3/4} R(x)^{7/10} \\
H &= 2.1 \times 10^3 cm \alpha^{-1/10} \dot{m}^{3/20} m^{9/10} \eta^{-3/20} x^{9/8} R(x)^{3/20} \\
\rho &= 43.5 g cm^{-3} \alpha^{-7/10} \dot{m}^{11/20} m^{-7/10} \eta^{-11/20} x^{-15/8} R(x)^{11/20} \\
T_c &= 8.1 \times 10^7 K \alpha^{-1/5} \dot{m}^{3/10} m^{-1/4} \eta^{-3/10} x^{-3/4} R(x)^{3/10} \\
\tau &= 58 \alpha^{-4/5} \dot{m}^{1/5} m^{1/5} \eta^{-1/5} R(x)^{1/5} \\
v_R &= 8.5 \times 10^5 cm s^{-1} \alpha^{4/5} \dot{m}^{3/10} m^{-1/5} \eta^{-3/10} x^{-1/4} R(x)^{-7/10}
\end{aligned} \tag{1.12}$$

- REGION B:

$$\begin{aligned}
\Sigma &= 7.08 \times 10^4 g cm^{-2} \alpha^{-4/5} \dot{m}^{3/5} m^{1/5} \eta^{-3/5} x^{-3/5} R(x)^{3/5} \\
H &= 3.5 \times 10^3 cm \alpha^{-1/10} \dot{m}^{1/5} m^{11/10} \eta^{-1/5} x R(x)^{1/5} \\
\rho &= 10.3 g cm^{-3} \alpha^{-7/10} \dot{m}^{2/5} m^{-7/10} \eta^{-2/5} x^{-33/20} R(x)^{2/5} \\
T_c &= 3.5 \times 10^8 K \alpha^{-1/5} \dot{m}^{2/5} m^{-1/5} \eta^{-2/5} x^{-9/10} R(x)^{2/5} \\
\tau &= 3.1 \times 10^3 \alpha^{-4/5} \dot{m}^{3/5} m^{1/5} \eta^{-3/5} x^{-3/5} R(x)^{3/5} \\
v_R &= 1.1 \times 10^6 cm s^{-1} \alpha^{4/5} \dot{m}^{2/5} m^{-1/5} \eta^{-2/5} x^{-2/5} R(x)^{-3/5}
\end{aligned} \tag{1.13}$$

- REGION C:

$$\begin{aligned}
&\Sigma = 4.2 g cm^{-2} \alpha^{-1} \dot{m}^{-1} \eta x^{3/2} R(x)^{-1} \\
&H = 2.1 \times 10^{5} cm \dot{m} m \eta^{-1} x R(x) \\
&\rho = 9.5 \times 10^{-6} g cm^{-3} \alpha^{-1} \dot{m}^{-2} m^{-1} \eta^{2} x^{3/2} R(x)^{-2} \\
&T_c = 3.1 \times 10^{7} K \alpha^{-1/4} m^{-1/4} x^{-3/8} \\
&\tau = 1.7 \alpha^{-1} \dot{m}^{-1} \eta x^{3/2} R(x)^{-1} \\
&v_R = 1.5 \times 10^{1} 0 cm s^{-1} \alpha \dot{m} \eta^{-1} x^{-5/2} R(x)
\end{aligned} \tag{1.14}$$

In all these equations: ρ is the disk density, h the disk height, $T_{\rm c}$ is the disk temperature in Kelvin (K), v_r the radial velocity due to the viscosity, $m = M/M_{\odot}$ is the NS mass in units of $1 M_{\odot}$, $\dot{m}$=$\dot{M}/\dot{M}_{\rm E}$ is the mass accretion rate in units of the Eddington rate, $x = R/R_{\rm s}$, $R(x) = (1 - x^{-1/2})$, $\dot{M}_E$=$1.4 \times 10^{18} (M/M_{\odot})$ g s^{-1} is Eddington mass accretion rate, and $R_{\rm s} = \frac{GM}{c^2}$ is the gravitational radius of the central compact object.

An interesting property of the SS73 solution is that all the quantities that define the structure of the thin disk (e.g., ρ, h, $T_{\rm c}$, ...) have a rather weak dependence on α. Therefore, our ignorance on the angular momentum transport process, that is enclosed in α, is not an obstacle for practical application of this simple picture.

We will show an application of the SS73 equations and discuss further the problem of poorly known parameters in the theory of accretion disks around compact objects in Chapter 2.

The accretion disk depicted by the SS73 theory was mainly developed for those cases in which the central compact object is a black hole, and therefore the problem of the interaction between the accretion disk and the magnetic field of the compact object was not taken into account. In particular, the solution discussed above assumes that all the inflowing matter is accreted at the inner disk radius. This requirement is satisfied only if the central compact object does not posses an extended magnetosphere. In Sect. 1.2.3 we discuss some details of the theory of accretion disks in the particular case in which the central compact object is a magnetized NS.

1.2.2 Wind accreting systems

As discussed in Sect. 1.1, HMXBs have companion stars of early spectral type. These stars are usually more massive than $\sim$15 M$_{\odot}$, and lose mass in the form of a stellar wind. The mass loss rate $\dot{M}_{\rm w}$ can be as high as $\sim 10^{-5}$ M$_{\odot}$ yr^{-1}, and the wind velocity is typically

$$v_{\rm w} \sim v_{\rm esc} = \sqrt{2GM_{\rm w}/R_{\rm w}} \simeq 1000 \ km \ s^{-1}. \tag{1.15}$$

Here $M_{\rm w}$ and $R_{\rm w}$ are the mass and radius of the companion star, and $v_{\rm esc}$ is the escape velocity from its surface. Since $v_{\rm esc} \gg c_{\rm s}$, where $c_{\rm s} \sim 10 ({\rm T}/10^4 \ {\rm K})$ km/s, the accreting matter is far from being in hydrostatic equilibrium. If a NS is moving with velocity $v_{\rm rel}$=$v_{\rm orb}$+$v_{\rm w}$ through a medium with sound speed $c_{\rm s}$, then Bondi (1952) demonstrated that the NS captures mass from this environment from a roughly cylindrical volume with a radius

$$R_{\rm acc} = 2GM_{\rm NS}/(v_{\rm rel}^2 + c_{\rm s}^2). \tag{1.16}$$

This is the so called "accretion radius". In the equations above $M_{\rm NS}$ is the mass of the NS and $v_{\rm orb}$=$G(M_{\rm NS}$+$M_{\rm w})/a$ its orbital velocity. The mass accretion rate onto the NS is

$$\dot{M}_{\rm w} = \pi R^2 \rho v_{\rm rel} \tag{1.17}$$

where ρ is the wind density close to the accretion radius and can be calculated by using the continuity equation

$$\dot{M}_{\rm acc} = 4\pi a^2 \rho v_{\rm w}. \tag{1.18}$$

Therefore, we have

$$\dot{M}_{\rm acc}/\dot{M}_{\rm w} = (1 + M_{\rm w}/M_{\rm NS})^{-1}(v_{\rm orb}/v_{\rm w})^4(1 + (v_{\rm orb}/v_{\rm w})^2)^{-3/2}, \tag{1.19}$$

where we introduced the approximation $c_{\rm s}/v_{\rm rel} \ll 1$. For typical wind parameters, the ratio $\dot{M}_{\rm acc}/\dot{M}_{\rm w}$ is usually in the range 10^{-4}-10^{-5}, and thus only a small fraction of the mass loss rate from the companion star can be accreted onto the NS. Hence, in order to have the accretion rate required to power the observed X-ray luminosity of wind accreting HMXBs ($\dot{M}_{\rm acc} \gtrsim 10^{-12}$ $M_\odot$ yr^{-1}), one needs $\dot{M}_{\rm w} \gtrsim 10^{-8}$ $M_\odot$ yr^{-1}, which is characteristic of main-sequence stars more massive than about 20-25 $M_\odot$ and blue supergiants of mass 15-20 $M_\odot$.

In the wind accretion scenario the net amount of specific angular momentum carried by the gas stream and captured by the accreting object is mainly due to the asymmetry of the accretion. It is possible to demonstrate that a density and velocity gradient is always present on the cylindrical surfaces because of a different amount of particles is captured at the far-side and at the near-side surface (Shapiro & Lightman 1976). Taking into account only the radial density gradient in the spherically symmetric stationary expansion of the stellar wind, the captured angular momentum J with respect to the NS is approximately given by

$$J = 1/2 \Sigma_{\rm orb} R_{\rm acc}^2. \tag{1.20}$$

This angular momentum is a factor $\sim (a/R_{\rm acc})^2$ smaller than the angular momentum of matter coming from the RLO of the companion star, and thus the formation of an accretion disk is much less likely than in the RLO scenario. In fact, in the wind accretion scenario the circularization radius is $R_{\rm circ}{=}{R_{\rm acc}}^4/8{\Omega_{\rm orb}}^2/(G\ M_{\rm NS})$, and is comparable to the NS radius for typical wind parameters: matter coming form the companion star can thus accrete almost radially onto the NS.

1.2.3 Accretion onto magnetized NSs

If a NS in a binary system possesses a strong magnetic field, then the dynamics of the gas flow in the vicinity of the NS can be largely affected by the presence of an extended magnetosphere, no matter whether the flow is nearly spherically symmetric or in the form of an accretion disk. The details of the interaction that takes place between the inflowing matter and the NS magnetosphere are far from being completely understood and a comprehensive theory is still to be developed. However, some useful concepts are derived by using the so called free-fall approximation. We assume that the infalling matter is quasi-spherical and that the NS magnetic field is purely dipolar, i.e. $B({\rm R}){=}\mu R^{-3}$. Here $\mu{=}B(R_{\rm NS})R_{\rm NS}^3$ is the magnetic dipole moment, a constant quantity that defines the strength of the NS magnetic field. In this approximation the magnetic pressure is given by

$$P_{\rm mag}(R) = B^2(R)/(8\pi) = \mu^2/(8\pi R^6); \tag{1.21}$$

this pressure increases steeply closer to the NS surface. The NS magnetic field starts to affect strongly the accretion flow where the magnetic pressure becomes larger than the total pressure of the gas, that is

$$P_{\rm ram} = \rho v_{\rm ff}^2 = (2GM)^{1/2}\dot{M}/(4\pi R_{\rm M}^{5/2}) \tag{1.22}$$

By equating these two pressures we derive the position of the so called magnetospheric radius, i.e.

$$R_{\rm M} = 5.1 \times 10^8 \dot{M}_{16}^{-2/7} m^{-1/7} \mu_{30}^{4/7} cm, \tag{1.23}$$

where $\dot{M}_{16}$ is the mass accretion rate in units of 10^{16} g s^{-1}, μ_{30} is the magnetic dipole moment μ in units of 10^{30} G cm^{-3}, and R_6=$R_{\rm NS}/10^6$ cm. It is generally believed that the flow of matter within this radius is forced to move along the magnetic field lines, and then accreted onto the NS.

The expression of the magnetospheric radius indicated in Eq. 1.23 holds strictly only when the accretion flow has a quasi-spherical symmetry, and therefore in general is better suited for wind accretion rather than for RLO accretion. However, refined theories showed that the value derived with the above simple estimate is correct within a factor of few, and is of practical use in almost all the common applications. We will discuss in Chapters 2 and 7 some cases in which this approximation fails and we will introduce the required refinements for both the wind and disk accretion geometry.

Once matter has arrived at the magnetospheric radius, accretion onto the NS can take place only if the centrifugal force, due to the rotational velocity of the NS magnetosphere, is smaller than the gravitational force. In other words, the "effective" gravity must point toward the NS. This condition is satisfied only if $R_{\rm M}$<$R_{\rm co}$, where

$$R_{co} = (GM_{\rm NS}\Omega_{\rm NS}^2)^{1/3} = 1.5 \times 10^8 m^{1/3} P_{\rm spin}^{2/3} \tag{1.24}$$

is the corotation radius. If $R_{\rm M}$<$R_{\rm co}$ then matter attached to the magnetic field lines transfers its angular momentum to the star, thus accelerating it ("spin-up"), and is then accreted onto the NS magnetic poles ("polar caps"), where releases (most of) its gravitational energy. The NS is thus in the so called "accretion regime". The lower temperature in the accreting region of the NS is of the order $\sim$10^8 K, and thus the emitted radiation is observed mainly in the X-ray band. Moreover, if the magnetic axis is not aligned with the spin axis, the rotation of the NS caused a light-house effect which modulates the X-ray emission at the spin period of the star and gives rise to pulsations in the X-ray flux as observed at the earth. On the other hand, if $R_{\rm M}$>$R_{\rm co}$, the centrifugal force onto the magnetospheric radius is too strong and inhibits accretion. In this case the NS is in the so called "propeller regime": the NS transfers angular momentum to the inflowing matter ("spin-down"), which, in turn is flung out by the fast rotating NS magnetosphere. In the propeller regime the X-ray luminosity is produced by dissipation of the NS rotational energy, and is typically much lower than the luminosity observed in the accretion regime. The rate at which the NS is expected to spin-up or spin-down and the total X-ray luminosity of the system in the accretion or the propeller regime must be calculated according to detailed models of disk and wind accretion. For a refined treatment of this subject, we refer the reader to Chapters 2 and 7.

1.3 X-ray bursts

In this section we briefly discuss observational and theoretical aspects of X-ray bursts. These phenomena were discovered in 1975 independently by Grindlay *et al.* (1975) and Belian *et al.* (1976). About one year later Maraschi & Cavaliere (1977) and Woosley & Taam (1976) independently suggested that these bursts were due to thermonuclear flashes on the surface of accreting NSs. Generally, X-ray bursts are divided into two different types, type I and type II bursts. Only the first type is believed to be generated by

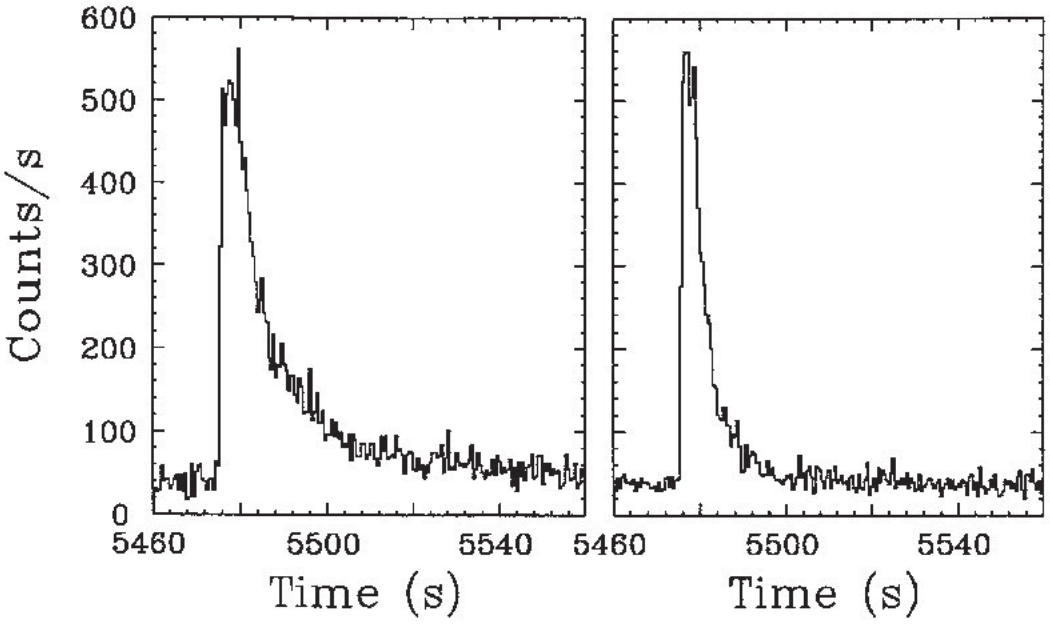

Figure 1.14: An X-ray burst from the source 1702-429 observed with EXOSAT (Lewin *et al.* 1995). The left panel shows the X-ray burst in the 1.2-5.3 keV energy band, whereas the right panel shows the same burst in the 5.3-19.0 keV band. A longer-lasting tail in the soft energy band is clearly visible.

thermonuclear flashes, whereas type II bursts are likely related to episodes of "spasmodic" accretion due to accretion instabilities. Here we will concentrate only on type I X-ray bursts (hereafter simply X-ray bursts).

Type I X-ray bursts are emitted by LMXBs, i.e. old ($>10^8$ yr) binary systems hosting a NS and a low mass companion (see Sec. 1.1). These bursts show a variety of recurrence times and profiles. In particular, the profiles might have rise times ranging from less than a second to ∼10 s, and decay times that are in the range of ∼10 s to minutes. In particular, the so called "normal bursts" have decay times of a few seconds, "intermediate long bursts" of few minutes, whereas "superbursts" might have decay times up to several hours (e.g., Kuulkers 2004; in't Zand *et al.* 2004; Molkov *et al.* 2005; in't Zand *et al.* 2005; Chenevez *et al.* 2006, 2007; Falanga *et al.* 2008). Generally, the decay profiles depend strongly on the photon energy (decays last longer at lower energies), and the recurrence time of these busts ranges from few hours to years, depending on the nuclear reactions involved (see, e.g., Lewin *et al.* 1993; Strohmayer & Bildsten 2006, for reviews). In a number of sources also double-peaked bursts have been observed. We show an example of X-ray burst in Fig. 1.14, and some double peaked bursts are shown in Fig. 1.15.

The X-ray spectra of these bursts are usually well fit by using a black body (BB) model. These fits provided useful information on the BB temperature, that can be used to estimate the bolometric flux from the source, and the apparent BB radius, which gives a measure of the burst emitting region. The relevant relation is

$$R_{\rm BB} = d(F_{\rm bol}/\sigma T_{\rm BB}^4)^{1/2}, \tag{1.25}$$

where d is the distance to the source. The typical result that derives from the spectral analysis of the burst is the variation with time of BB temperature, bolometric flux and

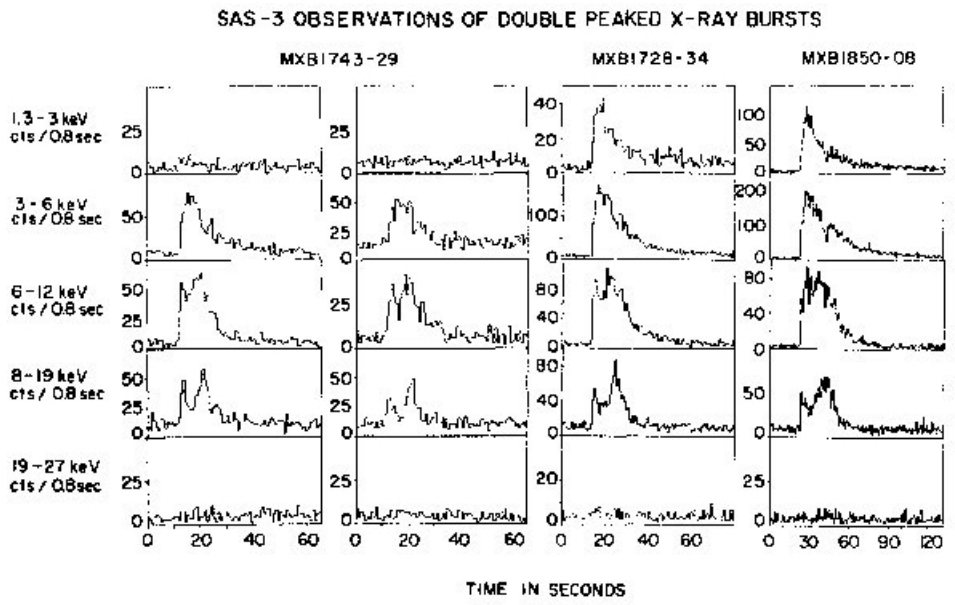

Figure 1.15: X-ray burst observed from three different sources. The energy dependence of the burst and the double-peaked profiles are clearly visible (Cominsky *et al.* 1980).

apparent radius. An example of a typical plot of these results is shown in Fig. 1.17. In this plot it can be seen that during the decay from the burst, $R_{\rm BB}$ is approximately constant. Only in some cases a photospheric radius expansion occurs due to the strong radiation force (see later on this section). In this case is the luminosity that remains approximately constant.

Type I X-ray burst with photospheric radius expansion are typically longer than other bursts, and last up to ∼1500 s. These bursts start with a "precursor", i.e. a small increase in the X-ray luminosity which rises rapidly (less than a second) and lasts for a few seconds. After few seconds (typically 5-10 s) a new burst follows, which is the main part of the event. A slow rise in the X-ray appears first at low energies ($\lesssim$5 keV), and then becomes visible also at higher energies. During the rise of the main event, the X-ray spectrum turns out to be harder and harder; the BB temperature reaches a maximum (kT∼2-3 keV) and then the decay phase begins, with a gradual decrease in the X-ray flux, accompanied by a softening of the spectrum. This corresponds to the cooling of the BB component, with an approximately constant size in time. The decay is thus similar to other classical type I X-ray bursts. An example of type I X-ray burst with photospheric radius expansion is shown in Fig. 1.16.

In bursts with photospheric radius expansion, the precursor and the main event are both part of the same very energetic burst. However, at odds with other type I X-ray bursts, in these cases the luminosity is higher than the Eddington limit (see Eq. 1.3), and the radiation transported through the atmosphere induces a stronger force than gravity and thus causes the expansion of the atmosphere itself. Possibly, an outflow of material from the NS surface is generated through a short-lived stellar-wind. Detailed calculations of super-Eddington type I X-ray bursts have shown that during the expansion of the photosphere, the luminosity always remains close to the Eddington value, whereas the excess luminosity is transformed in kinetic and potential energy of the expanded atmosphere.

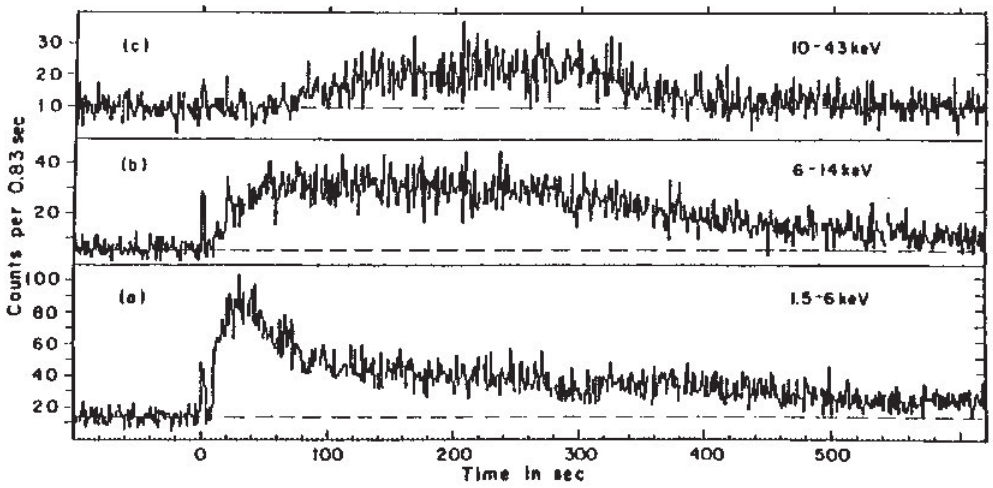

Figure 1.16: An example of a type I X-ray burst with photospheric radius expansion. The precursor and the main event are clearly distinguishable (Lewin *et al.* 1995).

Therefore, as the photospheric radius increases, at a nearly constant luminosity, the effective temperature decreases, according to Eq. 1.25. The end of the precursor corresponds to the point at which the temperature has decreased below the threshold for X-ray emission. Later, when the photospheric radius starts to decrease, the temperature increases and X-rays are emitted again. This corresponds to the raise of the main event. The decrease of the photospheric radius stops when the photosphere has shrunk to its original value, after which the NS surface cools, and we observe the decreasing part of the main event.

It is widely accepted that type I X-ray bursts can be interpreted in terms of accretion of matter onto a compact object. In particular, the energy for the burst is thought to be drawn from the nuclear energy stored in the accreted matter. The model for type I X-ray bursts that is most widely accepted involves thermonuclear shell flash instabilities in the NS surface layers. The basic picture of this model is that nuclear fuel in the form of hydrogen and helium is accreted onto the NS from its stellar companion. As the accreted material builds up onto the NS surface, the increasing pressure due to its weight lead to fusion of hydrogen and helium into iron. These thermonuclear reactions are explosive due to the high degree of electron degeneracy. In fact, for temperature sensitive nuclear reaction rates, the layers of accreted material are susceptible to thermal instabilities driven by exothermic reactions. The nuclear energy released in these explosions is then transported to the NS surface, and gives rise to the X-ray burst.

The models involving thermonuclear reactions have been successful in reproducing the basic properties of X-ray bursts. Moreover, they predict that magnetic fields higher than 10^{10}-10^{11} G would suppress the thermal instabilities giving rise to the burst. This is in agreement with observations, which have so far detected X-ray bursts only from old accreting NS in LMXBs (these typically have magnetic fields lower than the above threshold, see Sect. 1.1).

The details of the nuclear reactions that take place onto the NS surface, have been reviewed by Taam (1985). It was demonstrated that hydrogen burning alone cannot produce an X-ray burst. This is because the rate at which protons are burned is limited by the β decays associated with the weak interaction process of transforming a proton into

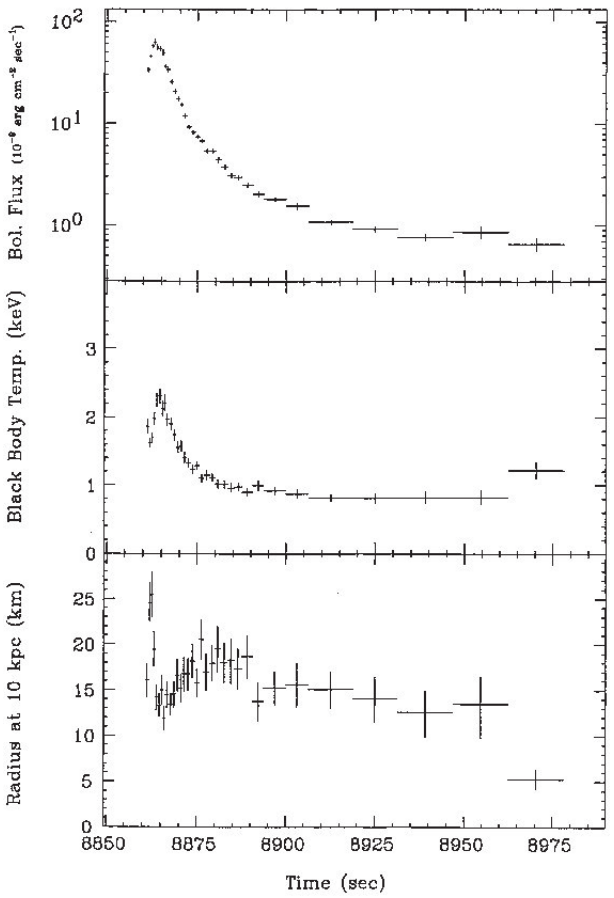

Figure 1.17: Variation of the bolometric flux, BB temperature and radius during a type I X-ray burst observed with EXOSAT (Lewin *et al.* 1995).

a neutron. However, hydrogen burning into helium has been identified as a fundamental process in X-ray bursts, as the energy liberated in this process can heat the NS envelope to such temperatures that helium and other elements can ignite and burn rapidly.

At odds with the pure hydrogen burning, the ignition of helium can give rise to a thermonuclear instability leading to an X-ray burst, since helium burns via the highly temperature-sensitive triple-alpha reaction.

Generally, the stability of a nuclear burning shell depends on the mass accretion rate and the temperature. Stable burning of hydrogen and helium can occurs: (i) for mass accretion rates larger than the Eddington limit (see Eq. 1.4) and high temperatures ($\gtrsim 5\times10^8$ K), at which the degree of electron degeneracy is low; (ii) for low mass accretion rates ($\lesssim 10^{-6}\dot{M}_{\rm edd}$) and low temperatures ($<5\times10^6$ K), at which the nuclear burning occurs in the pycnonuclear regime. On the contrary, unstable mass accretion rate can occur for a wide range of mass accretion rates, and three different regimes can be identified:

- High mass accretion rates ($\dot{M}_{\rm edd}<\dot{M}<\dot{M}_1$): a helium flash develops in the presence of a hydrogen rich environment.

- Low mass accretion rates ($10^{-6}\dot{M}_{\rm edd}<\dot{M}<\dot{M}_2$): the helium flash is triggered by the instability of the hydrogen rich layer.

- Intermediate mass accretion rates: an unstable layer of helium burning is generated by the raising above layer of hydrogen burning.

In the above cases $\dot{M}_1$ and $\dot{M}_2$ depend on the metal abundance of the accreted matter and are in the 5×10^{-11}-5×10^{-10} and 10^{-12}-5×10^{-11} range, respectively. For intermediate mass accretion rates all the helium at the base of the accreted layer is burned to heavy elements through a series of helium-capture reactions. This process leads to recurrence times of $\sim$10 h and fast rise times, due to the rapidity with which nuclear energy is released (typically $\lesssim$1 s). On the contrary, in case of low or high accretion rates, nuclear burning involves a series of complex reactions that end with the formation of iron nuclei. Because of the involved weak interactions, the nuclear burning process is slower with respect to the case of intermediate accretion rates, and the rise time of the burst is longer than that generated by a pure helium flash. It is generally believed that these aspects are responsible for the differences in bursts with slower and faster rise times.

The simple picture summarized above has been complicated substantially by recent numerical calculations, which included the effect of a number of different physical parameters (like the temperature of the burning layer). Some details of these developments will be discussed in Chapter 6, where we study a type I X-ray burst observed from the recently discovered LMXB XTE J1701-407.

1.4 Magnetars

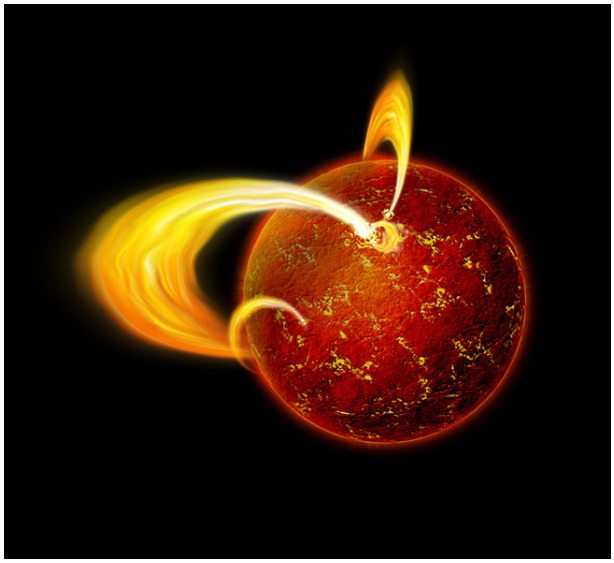

Figure 1.18: An artist impression of a Magnetar

On March 5, 1979, several gamma ray detectors on board different spacecrafts recorded an intense spike of radiation from a source in the direction of the Large Magellanic Cloud. Gamma ray detectors onboard Venera 11 and Venera 12, two Soviet interplanetary space probes, reached about 40.000 counts and then saturated in a fraction of a millisecond.

"A plane wavefront of gamma rays was evidently sweeping through the Solar system at the speed of light. It soon reached Venus, where the Pioneer Venus Orbiter's gamma ray detector also went over the top. Then only 7 seconds later it reached Earth. No-

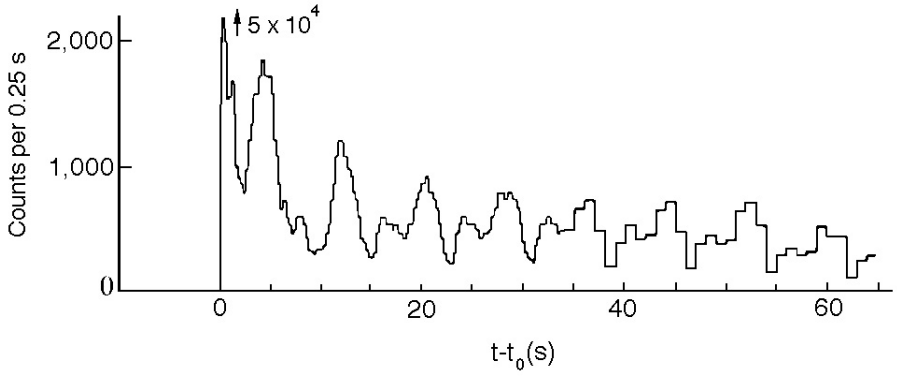

Figure 1.19: Light curve of the March 5th event recorded by Venera 12 (Mazets *et al.* 1979).

body noticed as it passed: life went on calmly beneath the protective atmosphere." (R. Duncan[7]).

This "Giant flare" began with a "hard pulse" of gamma rays lasting 0.2 seconds, and released an enormous energy ($\sim 10^{44}$ erg). The pulse was about 100 times more intense than any burst of cosmic gamma rays that had been detected up to that time.

A much fainter "soft tail" of hard X-rays followed the initial spike, and lasted over 3 minutes, steadily fading. The ∼8s pulsations that were present in this tail suggested that a NS gave rise to the event (see Fig. 1.19).

By using data recorded simultaneously by 7 different spacecrafts, the position of burst was accurately determined, and later an X-ray steady point source, SGR 0566-26, was identified at this position.

"Nobody understood why a NS would have this strange set of properties, or what would cause it to burst so spectacularly. Many theories were proposed in the 1980s, suggesting, for example, that the March 5th event was due to a small planet or a large asteroid slamming into a NS, or a "phase transition" in the core of a NS (i.e., the NS's core somehow abruptly changed its state as it cooled, like water does when it freezes, releasing energy in the process), or even more speculative suggestions involving hypothetical new objects, such as "a quark nugget falling onto a strange quark star." Most of these ideas accounted for only a limited subset of the known facts. Almost none of them attracted many believers, or were the subject of more than one research paper. It was particularly difficult for theorists to account for the enormous gamma-ray brightness of the hard initial pulse of the March 5th event. If you try to power this from some material falling onto a NS (e.g., from a planet or asteroid) then the pressure associated with the outflowing gamma rays itself halts the inflow, and cuts off the energy supply. But if you try to power it from a source deep inside the NS, like a phase transition, then it is hard to get all the energy out quickly and completely enough in the form of gamma rays." (R. Duncan).

The discovery of the Giant Flare (and of the emission of other, less powerful bursts, see Fig. 1.21) from SGR 0566-26 was followed in the years by the identification of other sources with similar properties, i.e. erratic bursting activity, periodicities in the 5-10 s range, and large spin-down rates (as compared with those of ordinary radio pulsars). At present about a dozen sources are known, falling into two main subgroups, the Anomalous

[7] http://solomon.as.utexas.edu/ duncan/magnetar.html

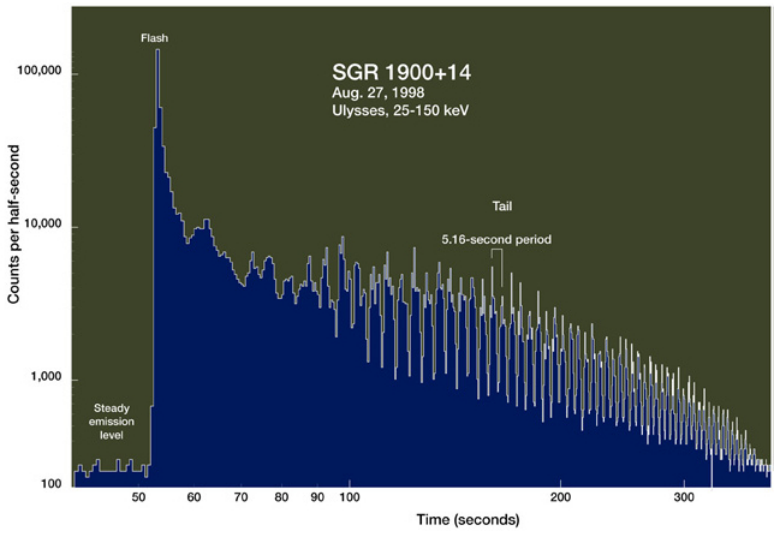

Figure 1.20: Light curve of the Giant Flare detected 27th August 1998 from SGR 1900+14. The initial spike of radiation, as well as the oscillating tail, are clearly visible.

X-ray Pulsars (AXPs) and the Soft Gamma-ray Repeaters (the only ones from which Giant Flares have been seen). Although little doubt is left that these are NS sources, the mechanism powering their activity has long been debated.

Over the last two decades, strong observational evidence was gathered in favour of the "magnetar" scenario, according to which SGRs/AXPs host a ultra-magnetized NS (i.e MAGNETAR, acronym of MAGNEtic sTAR), whose emission is powered by (impulsive and/or steady) dissipation of their exceptionally high magnetic field ($\gtrsim 10^{15}$ G).

Before the magnetar model, the origin of the high magnetic fields of NSs had been assumed to be due to the frozen flux of the progenitor star. The contraction from solar radius (10^{10} cm) to NS radius (10^{6} cm) takes the magnetic field to 10^{12} G, if the solar field was 1 G (but see also Bisnovatyi-Kogan & Fridman 1970). In the early 90s, Duncan & Thompson (1992) examined the possibility of creation of much higher magnetic fields at the time of the supernova explosion which produced the NS. They argued that the large neutrino flux created at the time of the explosion can cause vigorous convection inside the star. When this combines with rapid rotation it may result in a helical dynamo action which produces a very high magnetic field. These authors find that turbulent diffusion does not suppress the helical dynamo action if the so called Rossby number, i.e. $R_{\rm d}=P_{\rm spin}/t_{\rm convection}=1(P_{\rm spin}/1$ ms), is less than unity. They claim that magnetic fields as high as $\sim 10^{17}$ G can be generated. This field stress the NS outer crust and a magnetic force is generated when this field diffuses diffuses through it. The deformation of the crust causes the magnetic field penetrating it to shift and move, and, occasionally, the crust and the field above it become catastrophically unstable.

"As the instability grows, the changing, shearing, and twisting field drives strong dissipative currents above the star, energizing particles trapped in the exterior magnetic field. Simultaneously, the magnetic field rearranges itself to a state of lower energy. This produces a burst of hard X-rays (soft gamma rays) observed as ordinary, powerful SGR bursts. [...] Only occasionally, the magnetic field becomes unstable on much larger scales, and rapidly rearranges itself to a state of lower energy. Giant flares inevitably involve significant shifts in the crust structure as well. [...] In a magnetar, the energy available for

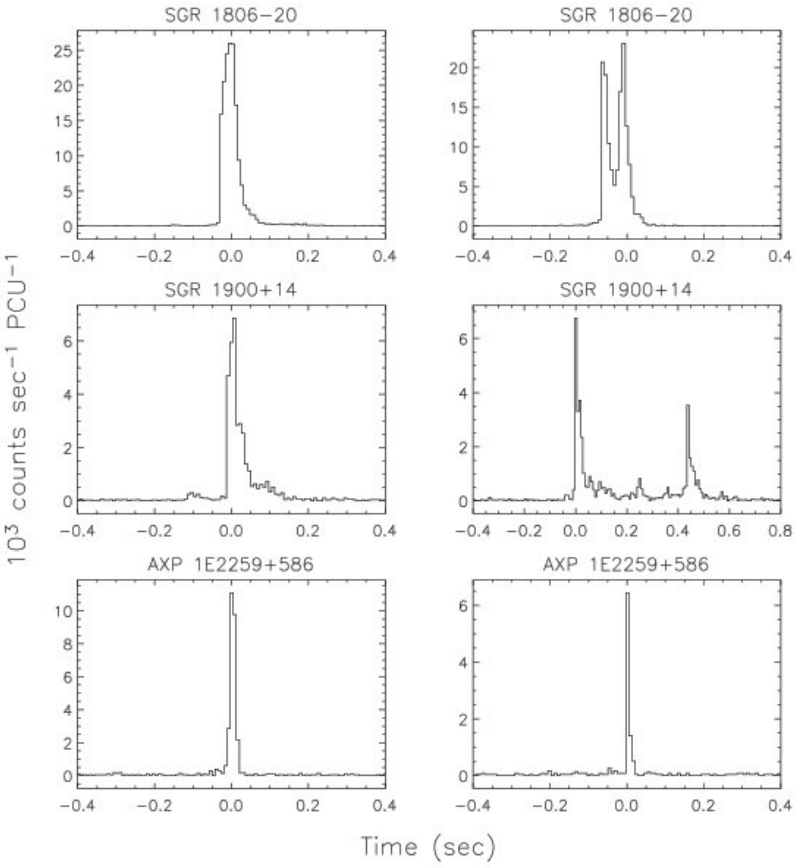

Figure 1.21: Some examples of typical magnetar bursts with durations of hundreds of ms. The light curves were observed with RXTE. The count rate is in the 2-20 keV band and the time resolution is 7.8 ms (Woods & Thompson 2006).

these magnetic flares is tremendous because the field is so strong. A magnetar's magnetic energy is easily sufficient to power the 1979 March 5th or 1998 August 27th giant flares (see Fig. 1.20); as well as all the common, short-duration bursts from SGRs." (R. Duncan).

All candidate magnetars that are currently observed, i.e. AXPs and SGRs, are isolated. However, the possibility that magnetars are hosted also in binary systems cannot be ruled out at present. In fact, the magnetar model does not predict that these highly magnetic NSs receive a larger kick-velocity than standard NSs at the moment of their formation, neither it is currently known the exact decay time-scale of a supercritical magnetic field. In order for binary systems to host magnetars their dipole magnetic field must retain values in the μ_{33}=0.1-1 range for a few 10^6 yr, i.e. the typical age of a NSHMXBs. Different models for the long-term decay of the NS magnetic field have been proposed which lead to different predictions. Among these, if the irrotational mode of ambipolar diffusion dominates the B-field decay, μ_{33}=0.1-0.3 can be expected for ages of a few 10^6 yr (Colpi *et al.* 2001). Therefore, many magnetars are expected to reside also in young binary systems, perhaps in some of the currently known high mass X-ray binaries (HMXB). Observationally, the modest number of known NSs in binaries which may have magnetic field of $>10^{14}$ G is puzzlingly, because it is substantially lower than that inferred from the magnetar birth

rate (which is estimated to be 10% of the total NS birth rate Li & van den Heuvel 1999). This suggests that a number of "missing" magnetars might have remained undetected so far.

On September 10th 2008, a typical 200 ms long magnetar burst was detected from a direction in the sky that includes the HMXB LSI+61303 (Dubus & Giebels 2008). Even though some uncertainties exist on the position of the burst, and the possibility of a short gamma-ray burst occurring very close to the binary cannot be completely ruled out, this discovery opened up new horizons on the possibility to detect and study magnetars in binary systems.

Without entering the full details of the theory of magnetars, we will discuss in Chapter 7 the possibility that magnetars are hosted in a recently discovered subclass of HMXBs, collectively termed supergiant fast X-ray transients (SFXT).

1.5 X-ray Satellites

This thesis makes an extensive use of X-ray observations achieved through the high energy telescopes on board *RXTE*, *XMM-Newton* and *Swift*. Therefore, in this chapter, we describe briefly these instruments.

1.5.1 *RXTE*

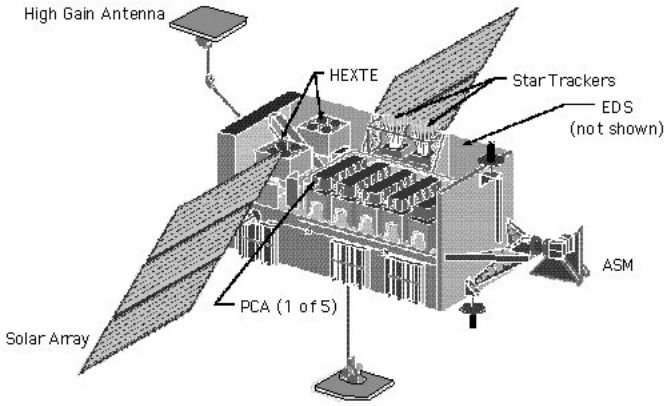

Figure 1.22: A sketch of the *RXTE* satellite.

The Rossi X-ray Timing Explorer (RXTE) was launched on December 30, 1995 from NASA's Kennedy Space Center. It was named for the X-ray astronomy pioneer Bruno Rossi (1905-1993), and designed to facilitate the study of time variability in the emission of X-ray sources with an unprecedented timing resolution of the order of microseconds in the energy range from 2 to 250 keV.

RXTE comprises 3 instruments: i) a Proportional Counter Array (PCA) of large area (6250 cm^2, sensitive to X-rays from 2 to 60 keV and capable of processing high rates up to about 500,000 counts/s), ii) the High Energy X-ray Timing Experiment (HEXTE, which consists of crystal scintillator detectors that extend the XTE energy sensitivity up to 200 keV), and iii) an All Sky Monitor (ASM) that scans most of the sky every 1.5 hours in order to monitor the intensities and spectra of the brightest sources in the sky.

Table 1.1: Characteristics of the instruments on board *RXTE*.

Instrument	Detector	Net Area (cm^2)	Band-width (keV)	Field of View (FWHM)	Time Resolution (mcrab)	Sensitivity
Proportional Counter Array (PCA)	5 Xe Proportional Counters	6250	2-60	1 deg.× 1 deg.	1 μs	0.1 (10min.)
High-Energy X-ray Timing Experiment (HEXTE)	NaI/CsI (2 clusters)	1600	20-200	1 deg.× 1 deg.	10μs	1 (105s)
All-Sky Monitor (ASM)	1-dim PSPC+Mask	90	2-10	0.2× 1 deg.[a]	1.5 h	30 (1.5h)

a: Effective beam of crossed fields; positions at 5σ are obtained within 3'×15'.
Gross FOV of each SSC is 6 deg.×90 deg. (FWHM).
b: 10 mCrab in 1 day.

The power and uniqueness of RXTE comes in large part from the natural synergism of the 3 instruments and the versatile spacecraft, which permits rapid pointing to almost any point on the sky. In particular, the PCA/HEXTE measures short-term variability to microsecond levels while the ASM measures long-term (hours to months) light curves of bright sources.

Below we describe each instruments onboard RXTE in detail, and a summary of their properties is provided in Table 1.1.

- The PCA instrument consists of 5 large proportional counters with anticoincidence features which provide a very low background. A mechanical hexagonal collimator provides 1 deg. (FWHM) collimation. Sources as faint as 1/1000 of the Crab nebula can be detected in a few seconds. The 5 proportional counters have a total net area of 6250 cm^2 and are filled with xenon gas. The PCA is effective over the range 2-60 keV with 18% energy resolution at 6 keV. The gain of the counter is monitored continuously with an americium radioactive source for which detection of the alpha particle identifies the calibration X-rays.

- The HEXTE features a large area and low background with a 1 deg. field of view coaligned with the PCA field of view. Eight "phoswich" NaI/CsI detectors are arranged in 2 clusters, each of which rocks on and off the source. This and automatic gain control for each of the 8 detectors together yield a well determined background which permits the spectral measurement of a faint source (1/1000 of the Crab nebula) at 100 keV in about 1 day. The HEXTE operates in the energy range 20-200 keV, and the total net area of the instrument is 1600 cm^2.

- The All-Sky Monitor is the watchdog that alerts RXTE to flares and changes of state in X-ray sources. It consists of three rotating Scanning Shadow Cameras (SSC) that can scan about 80% of the sky in 1.5 hours. The cameras provide measurements of intensities of about 75 known celestial sources in a day and can measure the position of a previously unknown source with a precision of about 3'. Each SSC detector is a sealed proportional counter filled to 1.2 atm with xenon-CO2, and is sensible to 2-10 keV X-rays with three energy channels.

The intensities and other basic results derived from the RXTE data are immediately

made available in the XTE Science Operations Center and to the community in general via computer links.

1.5.2 *XMM-Newton*

Figure 1.23: A sketch of the *XMM-Newton* satellite.

XMM-Newton, the X-ray Multi-Mirror Mission, is the second cornerstone of the Horizon 2000 program of the European Space Agency (ESA). This satellite was launched on December 10 1999 at 14:32 GMT (09:32 EST).

The observatory consists of three coaligned high throughput 7.5m focal length telescopes with 6 arc second FWHM angular resolution. The total field of view is of 30 arc minutes. Moderate spectral resolution can be achieved by using the European Photon Imaging Camera (EPIC), which consists of two MOS (Metal Oxide Semi-conductor) and one PN CCD arrays operating in the energy range from 0.15 to 15 keV. High-resolution spectral information ($E/\Delta E \sim 300$) is provided by the Reflection Grating Spectrometer (RGS) that deflects half of the beam on two of the X-ray telescopes. The observatory also has a coaligned 30 cm optical/UV telescope, the Optical Monitor (OM). A summary of the satellite capabilities is given in Table 1.2.

All EPIC CCDs operate in photon counting mode with a fixed, mode dependent frame read-out frequency. This mode produces event lists, i.e. tables with one entry line per received event, and lists attributes of the events such as the position at which they were registered, their arrival time and their energies. The two types of EPIC cameras, however, differ in some major aspects. Not only this does hold for the geometry of the CCD arrays and the instrument design but also for other properties, like e.g., their readout times. Below we describe the two cameras separately.

- *MOS*: Each of the MOS camera is composed of seven front-illuminated CCDs. The central CCD is at the focal point on the optical axis of the telescope while the outer six are stepped towards the mirror by 4.5 mm to follow approximately the focal plane curvature, and improve the focus for off-axis sources. The imaging area is $\sim 2.5 \times 2.5$ cm, so that a mosaic of seven covers about 28.4 arcmin. The imaging section has 600×600 40 micron square pixels, one pixel covers 1.1×1.1 arcsec on the FOV, and 15 pixels cover the mirror PSF half energy width of 15 arcsec.

- *PN*: The pn camera comprises twelve 3×1 cm CCDs on a single waver. The four individual quadrants each having three CCD subunits with a format 200 x 64 pixels

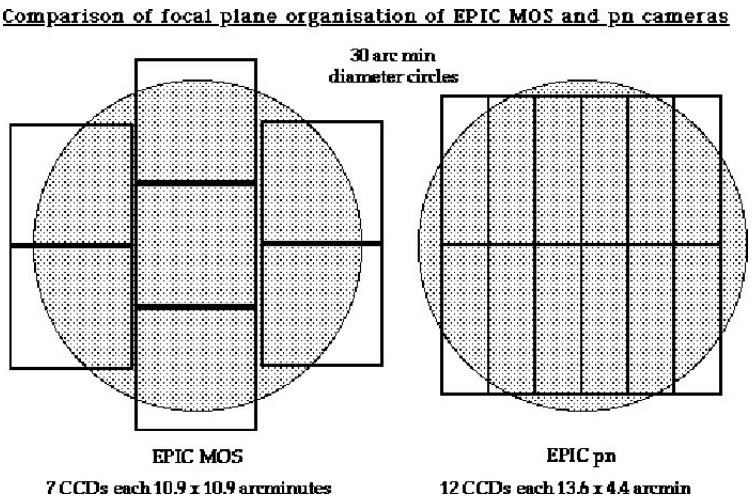

Figure 1.24: A sketch of the field of view of the two types of EPIC camera. The MOS cameras are represented on the left panel, whereas the pn camera is on the right. In both cases the circle drawn corresponds to a 30' diameter area (see also, http://xmm.vilspa.esa.es/external/xmm_user_support/documentation/uhb_2.5).

are operated in parallel. The pn camera has an imaging area of 6×6 cm, covering about 97% of the FOV, and a pixel size of 150×150 microns (4.1 arcsec) with a position resolution of 120 microns, resulting in an equivalent angular resolving capability for a single photon of 3.3 arcsec.

The EPIC cameras allow several modes of data acquisition. In the case of MOS the outer ring of 6 CCDs remain in standard full-frame imaging mode while the central MOS CCD can be operated separately. The pn camera CCDs can be operated in common modes in all quadrants for full frame, extended full frame and large window mode, or just with one single CCD for small window, timing and burst mode. Below we describe this operation modes in detail.

- *Full frame and extended full frame (pn only)*: In this mode, all pixels of all CCDs are read out and thus the full FoV is covered.
- *Partial window (pn and MOS)*:

Table 1.2: *XMM-Newton* Characteristics

Instrument	EPIC MOS	EPIC PN	RGS	OM
Bandpass	0.15-12 keV	0.15 15 keV	0.35-2.5 keV	180-600 nm
Orbital target visibility	5-135 ks	5-135 ks	5-135 ks	5-145 ks
Sensitivity (after 10 ks)	$\sim 10^{-14}$ (1)	$\sim 10^{-14}$ (1)	$\sim 8^{-5}$ (2)	20.7 mag (3)
FOV	30'	30'	$\sim$ 5'	17'
PSF (FWHM/HEM)	5"/14"	6"/15"	N/A	1.4"-2.0"
Pixel size	40μ m (1.1")	150 μ m (4.1")	81 μ m (9 x 10^{-3} A)	0.476513"
Timing resolution	1.5 ms	0.03 ms	0.6 s	0.5 s
Spectral resolution	$\sim$ 70 eV	$\sim$ 80 eV	0.04/0.025 A	350

(1): erg cm^{-2} s^{-1} .
(2): ph cm^{-2} s^{-1} in 10^4 s .
(3): 5σ detection of an AO star in 1000s .

MOS:
In a partial window mode the central CCD of both MOS cameras can be operated in a different mode of science data acquisition, reading out only part of the CCD chip: in small window mode an area of 100×100 pixels is read out, whereas in large window mode an area of 300×300 pixels is active.
pn:
In large window mode only half the area of all 12 CCDs is read out, whereas in small window mode only the part of CCD0 in quadrant 1 at the focal point is used to collect data.

- *Timing(pn and MOS)*:
  MOS + pn:
  In timing mode, imaging is made only in one dimension, along the column axis. Along the row direction, data from a predefined area on one CCD chip are collapsed into a one-dimensional row to be read out at high speed.
  pn only:
  A special flavour of the timing mode of the EPIC pn camera is the burst mode, which offers a very high time resolution of 7 μs (but has a low duty cycle of 3%).

Different operational modes require different analysis techniques; therefore, we describe these techniques in detail in the following Chapters, where data in different modes have been used separately.

1.5.3 *Swift*

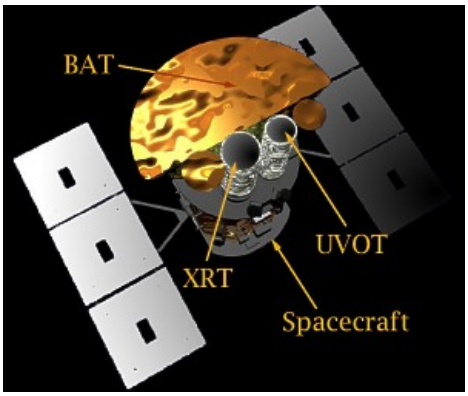

Figure 1.25: A sketch of the *Swift* satellite.

Swift is a multiwavelength observatory dedicated to the study of gamma-ray burst (GRB) science. Within seconds of detecting a burst, Swift is able to relay a burst's location to ground stations, allowing both ground-based and space-based telescopes around the world the opportunity to observe the burst's afterglow. Swift is part of NASA's medium explorer (MIDEX) program and was launched into a low-Earth orbit on a Delta 7320 rocket on November 20, 2004.

It has a complement of three co-aligned instruments: the Burst Alert Telescope (BAT), the X-ray Telescope (XRT) and the Ultraviolet/Optical Telescope (UVOT). Technical description of these three instruments are reported in Tables 1.3, 1.4, and 1.5. Below we describe the BAT and XRT telescope in detail, whereas we refer the reader to the *Swift*

Table 1.3: Burst Alert Telescope: BAT

Aperture	Coded Mask
Detecting Area	5200 cm^2
Detector	CdZnTe
Detector Operation	Photon Counting
FOV	2.0 sr (partially coded)
Detection Elements	256 modules of 128 elements
Detector Size	4mm x 4mm x 2mm
Telescope PSF	17 arcminutes
Location Accuracy	1-4 arcminutes
Energy Range	15-150 keV

Table 1.4: X-ray Telescope: XRT

Telescope	Wolter I
Detector	XMM EPIC CCD
Effective Area	135 cm^2 @ 1.5 keV
Detector Operation	Photon Counting & Windowed Timing
FOV	23.6 x 23.6 arcminutes
Detection Elements	600 x 600 elements
Pixel scale	2.36 arcsec/pixel
Telescope PSF	18 arcsec HPD @ 1.5 keV
Location Accuracy	3-5 arcseconds
Energy Range	0.2-10 keV
Sensitivity	2 x 10^{-4} erg cm^{-2} s^{-1} in 10^{-4} sec

website[8] for further information on UVOT, since we will not make use of UVOT data in this thesis.

- *B*AT: The Burst Alert Telescope (BAT) is a highly sensitive, large FOV instrument, and can provide the position of the burst within a 4-arcmin error circle. It is a coded aperture imaging instrument with a 1.4 steradian field-of-view (half coded). The energy range is 15-150 keV. The aim of this instrument is to calculate the initial position of a burst, and decide whether the burst merits a spacecraft slew. In the latter case, the position of the burst is sent to the spacecraft. BAT have a large dynamic range and trigger capabilities designed to study bursts with a variety of intensities and durations. The BAT comprises 32,768 pieces of 4×4×2 mm CdZnTe (CZT), which form a 1.2×0.6 m sensitive area in the detector plane, assembled in a hierarchical structure. With this structure the BAT can tolerate the loss of individual pixels, individual detector modules, and even whole blocks without losing the ability to detect bursts and determine locations. The BAT runs in two modes: burst mode, which produces burst positions, and survey mode, which produces hard X-ray survey data. In the survey mode the instrument collects count-rate data in 5-minute time bins for 80 energy intervals. When a burst occurs it switches into a photon-by-photon mode with a ring-buffer to save pre-burst information.

- *X*RT: The XRT is a sensitive, flexible, autonomous X-ray CCD imaging spectrometer designed to measure the position, spectrum, and brightness of gamma-ray bursts (GRBs) and afterglows over a wide dynamic range covering more than 7 orders of

[8] http://www.swift.psu.edu/uvot/.

Table 1.5: Ultraviolet/Optical Telescope: UVOT

Telescope	Modified Ritchey-Chrétien
Aperture	30 cm diameter
F-number	12.7
Detector	Intensified CCD
Detector Operation	Photon Counting
FOV	17 x 17 arcminutes
Detection Elements	2048 x 2048 pixels
Telescope PSF	0.9 arcsec @ 350 nm
Location Accuracy	0.3 arcseconds
Wavelength Range	170 nm - 650 nm
Colors	6
Spectral Resolution (Grisms)	$\lambda/\Delta\lambda \sim 200$ @ 400 nm
Sensitivity	B = 24 in white light in 1000 sec
Pixel Scale	0.48 arcseconds
Bright Limit	$m_v = 7$ mag

magnitude in flux. It is able to refine the BAT positions (∼1-4' uncertainty) to 2.5 arcseconds within 10 seconds of target acquisition for typical bursts, allowing ground-based optical telescopes to begin immediate spectroscopic observations of the afterglow. GRB positions and X-ray spectra are transmitted in near real time through TDRSS to the GCN network on the ground for broadcast to the world-wide gamma ray burst community.

Due to the unique capability of this satellite to trigger and observe X and γ-ray bursts, it is commonly used not only to study GRBs, but also transient and bursting sources in general. Type I X-ray bursts from LMXBs, as well as bursts from HMXBs, are among the possible target of *Swift* observations. We will discuss in detail the *Swift* data analysis of a type I X-ray burst in Chapter 6.

PART I: Theory of disk accretion and observations of LMXBs

Chapter 2

Accretion from Keplerian disks: disk-magnetosphere interaction models

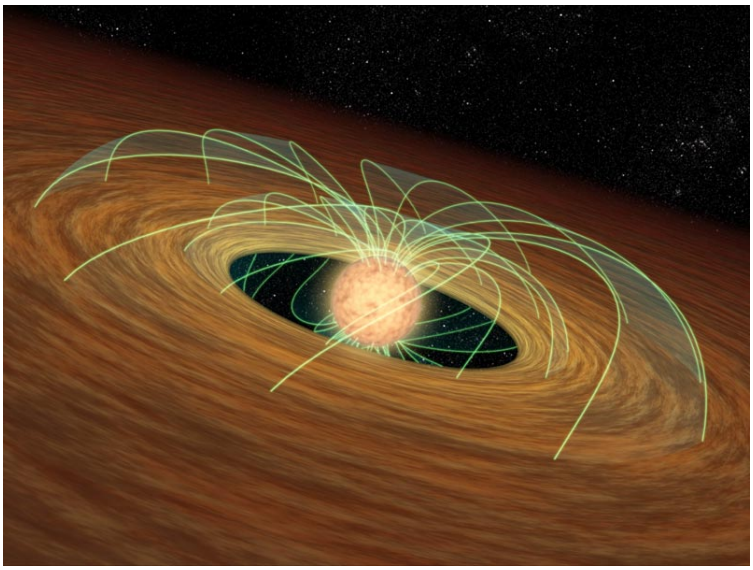

Figure 2.1: An artist impression of the neutron star magnetic field interacting with the sorrounding accretion disk.

In this Chapter we analyze in detail the accretion process onto magnetic NSs interacting with their sorrouding accretion disks (as we discussed in Sect. 1.1, this typically occurs in NSLMXBs and during incipient Roche Lobe overflow in NSHMXBs). From a theoretical point of view, the main open issue in this context is the understanding of how the NS magnetic field interacts with the disk plasma, and how this affects the accretion process. A number of studies have investigated this topic by adopting different approaches (Lamb & Pethick 1974; Scharlemann 1978; Ghosh & Lamb 1978; Ghosh *et al.* 1977; Ghosh & Lamb 1979a,b; Lovelace *et al.* 1995), and recently also several magnetohydrodynamic simulations have been carried out in order to gain further inside this problem (Romanova *et al.* 2002, 2003, 2004; Ustyugova *et al.* 2006). Despite some aspects of disk-magnetosphere interaction

are still poorly understood, the idea that the NS magnetic field must penetrate to some extend into the accretion disk (due to instabilities leading to finite conductivity of the plasma) is now widely accepted. This "magnetically threaded disk model", first developed in detail by Ghosh *et al.* (1977) and Ghosh & Lamb (1979a; 1979b) and later revised by Wang (1987; 1995), predicts that, as a result of the NS magnetic field threading the disk, a magnetic torque is generated that exchanges angular momentum between the NS and the disk. The strength of this magnetic torque increases in the disk regions closest to the NS and exceeds the viscous stresses at the magnetospheric radius $R_{\rm M}$, where the disk is terminated. The expression for the magnetospheric radius

$$R_{\rm M}^{\rm sp} = \mu^{4/7} \dot{M}^{-2/7} (2GM)^{-1/7}, \tag{2.1}$$

that we discussed in Sect. 1.2.3, holds strictly only for spherically symmetric accretion, and thus can be considered only a rough approximation when the accretion flow is mediated by a disk (Lamb & Pethick 1974).

In Sect. 2.1 we review theories of the threaded disk model, and explain how the disk accretion process onto magnetic NSs is schematized in these models. In particular, we concentrate on the different magnetic torque prescriptions of Ghosh & Lamb (1979a; 1979b) and Wang (1987; 1995), and on the calculation of the magnetospheric radius in the two cases (hereafter GLM and WM, respectively). We show that the differences between these magnetic torques led to relatively different predictions on the inner disk boundary, which in turns have a major impact on the spin-up/spin-down torques and the time variability properties of the accreting NSs (e.g. their QPO frequencies, see Sect. 1.1). Since the spin-up/spin-down behaviour, as well as the time variability of these sources can be studied by means of X-ray observations, in Sect. 2.3 we compare the results of the threaded disk models to a sample of observational data of X-ray pulsars. In particular, we selected those accreting X-ray pulsars that displayed both spin-up/spin-down torque reversals and QPOs in their X-ray flux (see Sect. 1.1). The X-ray luminosity at the onset of the spin-up/spin-down transition is used to fix poorly known parameters in the equations of the magnetospheric radius in both the GLM and WM, whereas the observed QPO frequencies are assumed to match the predictions of the beat frequency model (BFM, see Sect. 2.2) in order to derive an independent estimate of $R_{\rm M}$. By comparing the derived values of the magnetosheric radius, the threaded disk models can be tested against observations. In Sect. 2.4 we conclude, however, that neither the GLM nor the WM are able to reproduce observations for the whole sample of X-ray pulsars considered here. We thus argue that the problem of the threaded accretion disk might still lack a more general and comprehensive solution, and provide an outline of a revision of the GLM that will be presented in a forthcoming paper (Bozzo et al., 2009, in preparation).

2.1 A Review of the Magnetic Threaded Disk Model

The magnetic threaded disk model was developed by Ghosh & Lamb (1979a; 1979b) and partly revised by Wang (1987; 1995), under the assumption that the NS is rotating about its magnetic axis and that this axis is perpendicular to the plane of the disk (the so called "aligned rotator", see Fig. 2.2). The model is based on the idea that the stellar magnetic field must to some extend penetrate the accretion disk due to a variety of effects that prevent this field from being completely screened from the disk. Once this occurs, the differential motion between the disk, rotating at the Keplerian rate $\Omega_{\rm k}$, and the star,

rotating with angular frequency $\Omega_{\rm s}$ generates a toroidal magnetic field, B_ϕ, from the dipolar stellar field component

$$B_z(r) = -\eta\frac{\mu}{r^3} \tag{2.2}$$

(η is the screening coefficient, see below). The shear amplification of B_ϕ occurs on a time scale $\tau_{\rm d}\simeq|\gamma(\Omega_{\rm s}\text{-}\ \Omega_{\rm k})|^{-1}$. Here $\Omega_{\rm k}=(GM/r^3)^{1/2}$, $\Omega_{\rm s}=2\pi/P_{\rm s}$, $P_{\rm s}$ is the spin period of the NS (M is its mass), h is the disk height, r is the radial distance from the NS, and $\gamma\simeq1$ parametrizes the steepness of the vertical transition between Keplerian motion in the disk and rigid corotation with the NS. The finite disk plasma conductivity leads to slippage of field lines through the plasma, and thus to reconnection of these lines above and below the symmetry plane of the disk. This opposes to the shear amplification of the toroidal magnetic field on a time scale $\tau_\phi\sim h/(\xi v_{A\phi})$. Here the term $\xi v_{A\phi}$ defines the reconnection velocity in terms of the local Alfvén speed $v_{A\phi}$, and $\xi\sim$0.01-0.1, if the main dissipation effect is the annihilation of the poloidal field near the disk midplane, or $\xi\sim1$, if magnetic buoyancy is considered. Ghosh & Lamb (1979a) and Wang (1987; 1995) proposed different prescriptions for B_ϕ, and in the following we discuss their models separately.

2.1.1 The Ghosh & Lamb model

Ghosh & Lamb (1979a) estimated the toroidal magnetic field by equating the amplification and reconnection time-scales, *i.e.*

$$\frac{B_\phi}{B_z} \simeq \mp\frac{\gamma(\Omega_s-\Omega_k)h}{\xi v_{Az}}, \tag{2.3}$$

In their model, the coupling between the NS and the disk occurs in a broad transition zone located between the flow inside the NS magnetosphere and the unperturbed disk flow. The transition zone comprises two different regions:

- The boundary layer, that extends from the inner disk boundary $R_{\rm M}^{gl}$ inward to a distance $\Delta_{\rm r}\ll R_{\rm M}^{gl}$. In the boundary layer the poloidal field is twisted at a level $B_\phi/B_{\rm z}\sim1$, the angular velocity of the disk plasma significantly departs from the Keplerian value, and matter leaves the disk plane in the vertical direction and accretes onto the star. The currents generated on the disk surface by the magnetic field line twisting lead to an $\sim$80% screening of the NS magnetic field ($\eta\sim$0.2 outside the boundary layer).

- The outer transition zone, where the disk flow is only slightly perturbed and the coupling between the disk and the star is provided by the residual NS magnetic field that survives the screening of the boundary layer. Despite this is only a small fraction of the NS magnetic field ($\sim$20%), the broader extension of the outer transition zone makes this coupling appreciable.

In this model the magnetospheric radius coincides with the outer radius of the boundary layer, and is defined as the radius at which viscous torques in the disk are balanced by magnetic torques produced by field line twisting within the boundary layer. Ghosh & Lamb (1979a) found

$$R_{\rm M}^{\rm gl} \simeq 0.52 R_{\rm M}^{\rm sp}, \tag{2.4}$$

where $R_{\rm M}^{\rm sp}$ is given by Eq. 2.1.

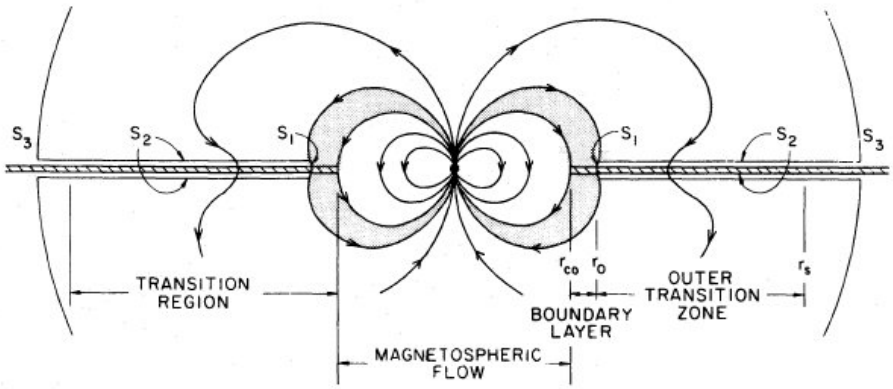

Figure 2.2: A schematic representation of the different interaction regions in the GLM (Ghosh & Lamb 1979b).

The total torque N on the star depends on the torque N_0, produced by matter leaving the disk at R_M^{gl} and accreting onto the NS, and the torque N_{mag} generated by twisted magnetic field lines threading the disk outside R_M^{gl}. Expressed in an adimensional form this torque is

$$n = (N_0 + N_{magn})/N_0 = 1 - \frac{\int_{R_M^{gl}}^{R_s} B_\phi B_z R^2 dR}{\dot{M}(GMR_M^{gl})^{1/2}}, \tag{2.5}$$

where $N_0 = \dot{M}(GMR_M^{gl})^{1/2}$ and $N_{mag} = -\int_{R_M^{gl}}^{R_s} B_\phi B_z R^2 dR$. Beyond R_s, the outer radius of the transition zone, the NS magnetic field is completely screened by the disk, and no torque is produced. Note that the poloidal magnetic field B_z in Eq. 2.5 differs from the simple dipolar approximation of Eq. 2.2. In fact, Ghosh & Lamb (1979a) calculated this component taking into account the effect of the screening currents flowing on the disk surface (see their Eq. 40). As a result, Ghosh & Lamb (1979b) found that n is primarily a function of the so called "fastness parameter"[1]

$$\omega_s^{gl} = \Omega_s/\Omega_k(R_M^{gl}) = (R_M^{gl}/R_{co})^{3/2}, \tag{2.6}$$

where R_{co} is the corotation radius (see Eq. 1.24). For a fixed mass accretion rate, the torque n of Eq. 2.5 can be either positive (the NS spins up) or negative (the NS spins down), depending on the NS spin period. In particular, for slow rotators ($\omega_s \ll 1$) $n \simeq 1.4$, and the star spins up, while increasing ω_s, $n(\omega_s)$ first decreases and then vanishes for the critical value $\omega_s = \omega_c^{gl}$. For $\omega_s > \omega_c^{gl}$, n becomes negative and the star rotation is slowed down by the interaction with the accretion disk, whereas for $\omega_s \gtrsim 0.95$ no stationary solution exists and steady state accretion is not permitted.

The critical fastness parameter ω_c^{gl} depends on the magnetic pitch angle at the inner disk radius, $\gamma_0 = B_\phi(R_M^{gl})/B_z(R_M^{gl})$; Ghosh & Lamb (1979b) suggested $\gamma_0 \simeq 1$, which corresponds to $\omega_c^{gl} \simeq 0.35$ (see their Fig. 4). A critical fastness parameter much smaller than unity implies the torque on the NS is zero only when the magnetospheric radius is well inside the corotation radius and close to the compact star (see also Sect. 2.3).

[1] The explicit functional form of $n(\omega_s)$ is given by Eq. 7 in Ghosh & Lamb (1979b).

The magnetospheric radius in the Ghosh & Lamb model

In the GLM, the magnetospheric radius is given by Eq. 2.4. We define the variable $x_{\rm gl}$=$R_M^{\rm gl}/R_{\rm co}$=$(\omega_s^{\rm gl})^{2/3}$, and rewrite Eq. 2.4 in an adimensional form

$$x_{\rm gl} = 2.17 \mu_{30}^{4/7} \dot{M}_{16}^{-2/7} m^{-10/21} P_s^{-2/3}. \tag{2.7}$$

Equation 2.7 gives the ratio x between the magnetospheric and corotation radii, for fixed values of μ_{30}, m, P_s, and $\dot{M}_{16}$. Using the definition of the critical fastness parameter and defining $x_c^{\rm gl}$=$(\omega_c^{\rm gl})^{2/3}$, Eq. 2.7 translates into

$$x_{\rm gl} = x_c^{\rm gl} (\dot{M}_{16}/\dot{M}_{\rm tr16})^{-2/7}, \tag{2.8}$$

such that the only free parameter is the mass accretion rate $\dot{M}_{\rm tr16}$ at which x=x_c.

In the GLM the magnetospheric radius can be easily estimated from Eq. 2.8, as a function of the mass accretion rate $\dot{M}_{16}$, provided the only free parameter $\dot{M}_{\rm tr16}$ is somehow constrained by observations. This is discussed in Sect. 2.3.

2.1.2 The Wang Model

Wang (1987) suggested that the toroidal field of Eq. 2.3 is overestimated, as the magnetic torque diverges in the limit $R_s \to \infty$. Instead of balancing the two time scales τ_ϕ and τ_d, he introduced a different prescription for the toroidal magnetic field based on Faraday's induction law. Assuming that the growth of the toroidal magnetic field is limited by reconnection in the disk (see also Sect. 2.1.1), he found that

$$\frac{B_\phi}{B_z} \simeq \pm \left| \frac{\gamma(\Omega_s - \Omega_k)h}{\xi v_{Az}} \right|^{1/2}, \tag{2.9}$$

and proved the amplification of the toroidal field to be smaller than previously thought (note that Eq. 2.9 is the square root of Eq. 2.3).

In a later study, Wang (1995) considered also that the growth of the toroidal field B_ϕ might be limited by other mechanisms than magnetic reconnection. In case the amplification of the toroidal field is damped by diffusive decay due to turbulent mixing within the disk, τ_ϕ=$(\alpha\Omega_k)^{-1}$ (α is the viscosity parameter of Shakura & Sunyaev 1973, hereafter SS73) and Eq. 2.9 is replaced by

$$\frac{B_\phi}{B_z} \simeq \frac{\gamma(\Omega_s - \Omega_k)}{\alpha\Omega_k}. \tag{2.10}$$

Another possibility is that, in the case of a force-free magnetosphere, the winding of the field lines threading the disk is limited by magnetic reconnection taking place within the magnetosphere itself. In this case

$$\frac{B_\phi}{B_z} = \begin{cases} \gamma_{max}(\Omega_s - \Omega_k)/\Omega_k, & \Omega_k \gtrsim \Omega_s; \\ \gamma_{max}(\Omega_s - \Omega_k)/\Omega_s, & \Omega_k \lesssim \Omega_s, \end{cases} \tag{2.11}$$

where $\gamma_{max} \lesssim 1$.

At odds with the GLM, the model developed by Wang (1987,1995) does not involve the presence of a boundary layer: the effect of the screening currents is not taken into account self-consistently, and B_z is described by Eq. 2.2, by assuming a constant screening $\eta \lesssim 1$

from the inner disk radius, $R_{\rm M}^{\rm w}$, up to the external boundary of the disk (taken to be at infinity). Accordingly, the total adimensional torque onto the NS is

$$n = 1 - \frac{\int_{R_{\rm M}^{\rm w}}^{\infty} B_\phi B_{\rm z} R^2 dR}{\dot{M}(GMR_{\rm M}^{\rm w})^{1/2}}, \tag{2.12}$$

where B_ϕ is given by Eqs. 2.9, or 2.10 or 2.11, and $R_{\rm M}^{\rm w}$ is derived from the equation

$$\frac{B_\phi(R_{\rm M}^{\rm w})B_{\rm z}(R_{\rm M}^{\rm w})}{\dot{M}(GMR_{\rm M}^{\rm w})^{1/2}} = -\frac{1}{2(R_{\rm M}^{\rm w})^3}. \tag{2.13}$$

Equation 2.13 expresses the balance between the rates at which the stellar magnetic field and viscous stresses remove angular momentum from the disk.

The torque given by Eq. 2.12 is positive for slow rotators ($\omega_{\rm s}\ll 1$) and negative in the opposite limit, in agreement with the results found in the GLM. However, the torque vanishes for critical values of the fastness parameter in the 0.88-0.95 range, *i.e.* well above the value $\omega_{\rm c}^{\rm gl}$=0.35 predicted by Ghosh & Lamb (1979b). In particular, $\omega_{\rm c}^{\rm w}$=0.949, 0.875, and 0.95 for B_ϕ given by Eqs. 2.9, 2.10, and 2.11, respectively. A similar value is found in appendix 2.6, where we calculate the value of $\omega_{\rm c}$ for region "C" of a SS73 disk, as opposed to region "B" used by Wang (1987).

At odds with the GLM, such large values of the critical fastness parameters in the WM imply that the magnetospheric radius must lie close to the corotation radius when $n\simeq 0$. Therefore, NS spin-down can take place over a tiny range of mass accretion rate. This conclusion turns out to be nearly independent of the prescription used in the WM for the toroidal field. Taking these results into account, Wang (1996) proposed that a constant magnetic pitch at the inner disk boundary, *i.e.* $\gamma_0 = B_{\phi 0}B_{z0}$, might be assumed in Eq. 2.13, and derived the simplified expression for the magnetospheric radius

$$R_{\rm M}^{\rm w} = \xi_{\rm p} R_{\rm M}^{\rm sp}. \tag{2.14}$$

Here $\xi_{\rm p}\simeq 1.35\gamma_0^{2/7}\eta^{4/7}$, η is the screening factor of Eq. 2.2, and $R_{\rm M}^{\rm sp}$ is given by Eq. 2.1.

In Sect. 2.1.2, we solve Eq. 2.13 numerically and compare the results with those obtained by using a constant pitch angle approximation.

The magnetospheric radius in the Wang model

Here we solve Eq. 2.13 for the three different prescriptions of the toroidal magnetic field discussed in the previous section. We consider first the prescription of Eq. 2.9. In this case a model for the region of the accretion disk that is just outside the magnetosphere is required to evaluate the disk height h and Alfvén velocity $v_{\rm Az}$. In accordance with Wang (1987) we use the thin disk model of SS73 (see e.g., Vietri 2008). Using the well known relation $h{=}c_{\rm s}^2/\Omega_{\rm k}$ connecting the disk vertical height h to the sound speed $c_{\rm s}{=}(P/\rho)^{1/2}$ (here ρ the matter density and p the thermal pressure inside the disk), Eq. 2.3 translates into (Wang 1987)

$$\frac{B_\phi}{B_z} \simeq \pm \left| \frac{\gamma(\Omega_s - \Omega_k)}{\xi\Omega_k} \frac{(4\pi p)^{1/2}}{B_z} \right|^{1/2}. \tag{2.15}$$

Table 2.1: Properties of accretion powered X-ray pulsars discussed in the text

Source	P_s	ν_s	ν_{QPO}	L_{QPO} (band)	L_{tr} (band)	x_{QPO}^{BFM}	x_{QPO}^{w}	x_{QPO}^{gl}	Class[a]
	s	mHz	mHz	erg s^{-1} (keV)	erg s^{-1} (keV)				
Her X-1[15,16,17]	1.24	806.5	8 43	2.1×10^{37} $(0.1-200)$	2.1×10^{37} $(0.1-200)$	0.95-0.98	0.91-0.97	0.5	F
4U 0115+63 [9,10,18]	3.62	276.2	62	8×10^{37} $(0.1-200)$	5×10^{36} $(0.1-200)$	0.56	0.61-0.71	0.23	F
Cen X-3 [13,14,19]	4.8	208.3	35	1.0×10^{38} $(0.12-100)$	3.3×10^{37} $(0.12-100)$	0.89	0.82-0.92	0.36	F
LMC X-4 [11,12]	13.5	74.1	0.65-1.35	10^{39} $(2-25)$	2×10^{38} $(2-25)$	0.97-0.98	0.76-0.88	0.31	F
4U 1626-67 [6,7,8]	7.66	130.6	40	1.36×10^{36} $(0.7-60)$	1.7×10^{36} $(0.7-60)$	0.83	0.98-0.99	0.88	F/S
EXO 2030+375 [1,2]	42	23.8	213	2×10^{38} $(1-20)$	10^{38} $(1-20)$	0.22	0.86-0.94	0.4	S
	42	23.8	213	2×10^{38} $(1-20)$	2.4×10^{36} $(1-20)$	0.22	0.43-0.56	0.14	S
A0535+262 [3]	103	9.7	72	4.3×10^{37} $(20-100)$	4.83×10^{36} $(20-100)$	0.24	0.69-0.82	0.26	S
4U 1907+09 [4,5]	440	2.3	55	6.3×10^{36} $(2-60)$	2×10^{36} $(1-15)$	0.12	0.81-0.92	0.36	S

a: F=Fast rotator, S=Slow rotator.
References: (1) (Parmar *et al.* 1989); (2) (Angelini *et al.* 1989); (3) (Finger *et al.* 1996); (4) (Fritz *et al.* 2006); (5) (in't Zand *et al.* 1998); (6) (Chakrabarty & Roche 1997); (7) (Chakrabarty 1998); (8) (Shinoda *et al.* 1990); (9) (Tamura *et al.* 1992); (10) (Campana *et al.* 2000); (11) (Woo *et al.* 1996); (12) (Moon & Eikenberry 2001); (13) (Howe *et al.* 1983); (14) (Takeshima *et al.* 1991); (15) (Dal Fiume *et al.* 1998); (16) (Parmar *et al.* 1999); (17) (Boroson *et al.* 2000); (18) (Soong & Swank 1989); (19) (Burderi *et al.* 2000)

Introducing the expressions for the thermal pressure in the "B" and "C" regions of the SS73 accretion disk, we obtain

$$x_w^{-211/80}\sqrt{1-x_w^{3/2}} = 2.72\times10^{-3}\sqrt{\xi\gamma^{-1}\eta^{-3}}\alpha^{9/40}\cdot \cdot\mu_{30}^{-3/2}\mu_p^{1/4}m^{7/6}P_s^{211/120}\dot{M}_{16}^{4/5}, \quad (2.16)$$

and

$$x_w^{-85/32}\sqrt{1-x_w^{3/2}} = 3.184\times10^{-3}\sqrt{\xi\gamma^{-1}\eta^{-3}}\alpha^{9/40}\cdot \cdot\mu_{30}^{-3/2}\mu_p^{1/4}m^{7/6}P_s^{85/48}\dot{M}_{16}^{63/80}, \quad (2.17)$$

respectively. In the following we refer to these models as WM1 and WM2, respectively. Here $\dot{M}_{16}$ is the mass accretion rate in units of 10^{16} g s^{-1}, μ_{30} is the magnetic moment of the neutron star in units of 10^{30} G cm^{-3}, μ_p is the mean molecular weight, and, in analogy to Sect. 2.1.1, we introduced the adimensional variable x_w=R$_M^w$/R$_{co}$. With similar calculations, we find

$$x_w^{-7/2}-x_w^{-2} = 2.38\times10^{-3}\alpha\gamma^{-1}\eta^{-2}\mu_{30}^{-2}\cdot \cdot m^{5/3}P_s^{7/3}\dot{M}_{16} \quad (2.18)$$

and

$$x_w^{-7/2}-x_w^{-2} = 2.38\times10^{-3}\gamma_{max}^{-1}\eta^{-2}\mu_{30}^{-2}\cdot \cdot m^{5/3}P_s^{7/3}\dot{M}_{16}, \quad (2.19)$$

by using the prescriptions for the toroidal magnetic field in Eqs. 2.10 and 2.11, respectively. In the following we refer to these models as WM3 and WM4, respectively.

Equations 2.16, 2.17, 2.18, and 2.19 give the ratio x between the magnetospheric and the corotation radius (we assume $x \lesssim 1$), for fixed values of ξ, γ, η, α, μ_{30}, m, $P_{\rm s}$, and $\dot{M}_{16}$. Some of these parameters are measured or constrained through observations ($\dot{M}$, $P_{\rm s}$, μ, m); other parameters are still poorly determined by current theory: the values of ξ and α (see Sect. 2.1.2) are uncertain by at least an order of magnitude (King *et al.* 2007), η is in the 0.2-1 range and γ, γ_{max} can be larger than 1 (Wang 1995).

In analogy to what we have done in Sect 2.1.1, we use here the definition of the critical fastness parameter and define $x_{\rm c}^{\rm w}=(\omega_{\rm c}^{\rm w})^{2/3}$. In this case, Eqs. 2.16, 2.17, 2.18, and 2.19 translate into

$$x_{\rm w}^{-211/80}(1-x_{\rm w}^{3/2})^{1/2} = x_{\rm c1}^{\rm w\ -211/80}(1-x_{\rm c1}^{\rm w\ 3/2})^{1/2}(\dot{M}_{16}/\dot{M}_{\rm tr16})^{4/5}, \tag{2.20}$$

$$x_{\rm w}^{-85/32}(1-x_{\rm w}^{3/2})^{1/2} = x_{\rm c2}^{\rm w\ -85/32}(1-x_{\rm c2}^{\rm w\ 3/2})^{1/2}(\dot{M}_{16}/\dot{M}_{\rm tr16})^{63/80}, \tag{2.21}$$

$$x_{\rm w}^{-7/2}-x_{\rm w}^{-2} = (x_{\rm c3}^{\rm w\ -7/2}-x_{\rm c3}^{\rm w\ -2})\dot{M}_{16}/\dot{M}_{\rm tr16}, \tag{2.22}$$

and

$$x_{\rm w}^{-7/2}-x_{\rm w}^{-2} = (x_{\rm c4}^{\rm w\ -7/2}-x_{\rm c4}^{\rm w\ -2})\dot{M}_{16}/\dot{M}_{\rm tr16}, \tag{2.23}$$

respectively. Here $x_{\rm c1}^{\rm w}$=0.966, $x_{\rm c2}^{\rm w}$=0.967, $x_{\rm c3}^{\rm w}$=0.915, $x_{\rm c4}^{\rm w}$=0.967, and we defined $\dot{M}_{\rm tr16}$ as the mass accretion rate (in unit of 10^{16} g s^{-1}) for which $x_{\rm w}=x_{\rm c}^{\rm w}$. In analogy to what we found for Eq. 2.8, Eqs. 2.20, 2.21, 2.22, and 2.23 show that all uncertain parameters cancel out and the magnetospheric radius can be easily estimated, as a function of the mass accretion rate $\dot{M}_{16}$, provided $\dot{M}_{\rm tr16}$ is somehow constrained by the observations. This is carried out in Sect. 2.3 for the sample of X-ray powered pulsars we selected in the present study.

A similar calculation can be applied to the case of the constant magnetic pitch approximation. We define $x_{\rm cmp}=R_{\rm M}^{\rm w}/{\rm R_{co}}$, and rewrite Eq. 2.14 as

$$x_{\rm cmp} = 4.175\xi_{\rm p}\mu_{30}^{4/7}\dot{M}_{16}^{-2/7}M_1^{-10/21}P_{\rm s}^{-2/3}. \tag{2.24}$$

Using the definition of the critical fastness parameter, Eq. 2.24 translates into

$$x_{\rm cmp} = x_{\rm c}^{\rm w}(\dot{M}_{16}/\dot{M}_{\rm tr16})^{-2/7}, \tag{2.25}$$

where $x_{\rm c}^{\rm w}=x_{\rm c1}^{\rm w}$, $x_{\rm c2}^{\rm w}$, $x_{\rm c3}^{\rm w}$, $x_{\rm c4}^{\rm w}$, depending on the prescription used for the toroidal magnetic field. Note that, in the constant magnetic pitch approximation, the magnetospheric radius does not depend on the prescription used for the toroidal field: using a different equation for B_ϕ only affects the value of the critical fastness parameter that must be used in Eq. 2.25. In Fig. 2.3 we arbitrarily fixed $\dot{M}_{\rm tr16}$=3 and compare the values of $x=R_{\rm M}/R_{\rm co}$, as a function of the mass accretion rate, obtained by solving numerically Eq. 2.13 and using the constant pitch approximation for all the toroidal magnetic field prescriptions discussed in Sect. 2.1.2. Despite all models approach the same asymptotic behaviour $x \propto \dot{M}^{-2/7}$ in the limit $x \ll 1$, the constant pitch approximation results in a systematic smaller magnetospheric radius, for any considered value of the mass accretion rate and prescription of the toroidal magnetic field. On the other hand, in the limit $x \sim 1$, the solution obtained with the constant magnetic pitch approximation significantly differs

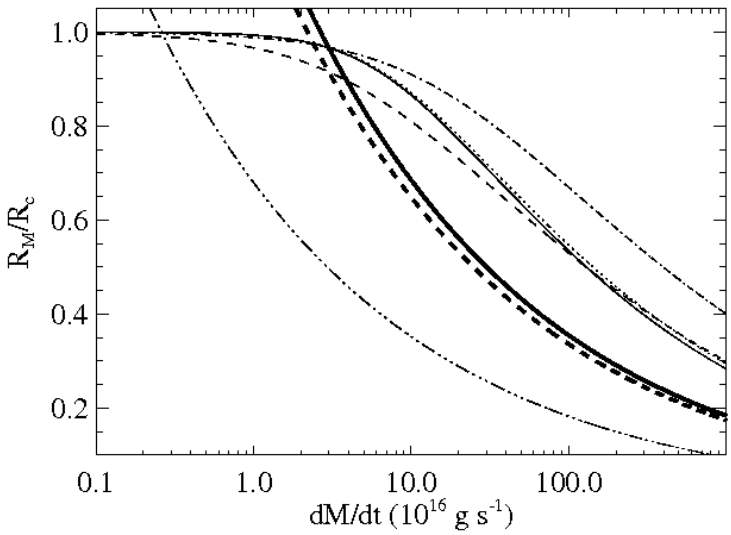

Figure 2.3: The ratio $x{=}R_{\rm M}/R_{\rm co}$, as a function of the mass accretion rate, for different prescriptions of the toroidal magnetic fields and $\dot{M}_{\rm tr16}{=}3$. The solid line is for Eq. 2.20 (WM1), dotted line for Eq. 2.21 (WM2), dashed line for Eq. 2.22 (WM3), and dot-dashed line for Eq. 2.23 (WM4). Thicker lines are the constant magnetic pitch approximations corresponding to each of the above prescriptions (note that the approximations corresponding to Eqs. 2.20, 2.21, and 2.23 almost overlap). The triple-dot-dashed line represents the GLM (Eq. 2.8).

from the numerical solutions obtained with Eq. 2.13. In particular, the latter results in a magnetospheric radius that approaches the corotation radius more gradually, while decreasing the mass accretion rate: the range of $\dot{M}$ for which $x{=}R_{\rm M}/R_{\rm co}{<}x_{\rm c}^{\rm w}$ (and thus the NS spins down), is much larger with respect to the range obtained by assuming a constant magnetic pitch angle (see also Sect. 2.1.2). The discrepancy between these results demonstrate that the constant magnetic pitch approximation does not provide a reliable estimate of the magnetospheric radius in the WM. Therefore, we do not use Eq. 2.25 in the application to X-ray accretion powered pulsars in Sect. 2.3. For comparison we plot in Fig. 2.3 also Eq. 2.8, which represents the magnetospheric radius in the GLM. The differences between this curve and those derived by using the constant magnetic pitch approximation and the WM are due to the different values of the critical fastness parameter in the GLM and WM (0.35 in the GLM and 0.875-0.95 in the WM; see Eqs. 2.8 and 2.25).

2.2 The beat frequency model

Besides the threaded disk model, another probe of the position of the inner disk radius is offered by observations of QPOs in accreting NSs. These timing features have been detected in the X-ray flux of a number of astrophysical sources, especially old accreting NSs and black hole candidates in LMXBs but also in young accreting X-ray pulsars in high mass X-ray binaries (see Sects. 1.1.1 and 1.1.2). LMXBs often display a complex variety of simultaneous QPO modes, with frequencies ranging from few Hz up to ∼1 kHz. On

the contrary, young X-ray pulsars mostly display a single QPO, with a considerably lower frequency $\nu_{\rm QPO}$~0.008-0.2 Hz (see Table 2.1 and references therein). Different models have been developed in order to interpret the nature of this X-ray variability. The fastest variability, manifested through kHz QPOs and timescales of ~ms, must be generated by phenomena occurring in the innermost regions of the accretion disk and reflect the fundamental frequencies of motions in the close vicinity of the compact object (see Sect. 1.1.1, 1.1.2 and e.g., van der Klis 1995). On the contrary, mHz QPOs observed in accretion powered X-ray pulsars result from variability phenomena occurring farther away from the NS (the relevant timescales are of hundreds of seconds). In these sources, a magnetic field of order $\gtrsim 10^{12}$ G disrupts the disk flow at the magnetospheric radius $R_{\rm M}$~10^8 cm, and thus the orbital motion at this radius provides an obvious source of variability. However, the involved time scales at $R_{\rm M}$ are a few tens of seconds at the most, and the beat between the orbital frequency at this radius and the spin frequency of the NS is generally invoked in order to interpret the observational properties of the slower (mHz) QPOs that are observed in these systems.

As we discussed in Sect. 1.1.2, QPOs in NSHMXBs are well explained by using the beat frequency model (BFM, Alpar & Shaam 1985; Lamb *et al.* 1985). According to this model, matter from inhomogeneities orbiting at the inner disk boundary ($R_{\rm M}$) is gradually removed through the interaction with the neutron star magnetosphere, thus giving rise to a modulation in the accretion rate and source luminosity. Therefore the QPO frequency $\nu_{\rm QPO}$ results from the beat between the orbital frequency $\nu_{\rm orb}$ of the blobs at $R_{\rm M}$ and the spin frequency of the NS $\nu_{\rm s}$=$2\pi\Omega_{\rm s}$, *i.e.* $\nu_{\rm QPO}$=$\nu_{\rm orb}(R_{\rm M})$-$\nu_{\rm s}$. In practice $\nu_{\rm orb}(R_{\rm M})$ is well approximated with $\nu_{\rm K}(R_{\rm M})$, *i.e.* the Keplerian frequency at $R_{\rm M}$ (see below) and the above equation can be solved for the magnetospheric radius. This gives:

$$R_{\rm M}^{\rm BFM} = 3.3 \times 10^8 \left(\frac{0.3Hz}{\nu_{\rm s}+\nu_{\rm QPO}}\right)^{2/3} \left(\frac{M}{M_\odot}\right)^{1/3} \ {\rm cm}, \tag{2.26}$$

or

$$x_{\rm BFM} = 2.2 \left(\frac{0.3Hz}{\nu_{\rm s}+\nu_{\rm QPO}}\right)^{2/3} P_{\rm s}^{-2/3}, \tag{2.27}$$

where $x_{\rm BFM}$=$R_{\rm M}^{\rm BFM}/R_{\rm co}$. By assuming that the BFM applies, QPOs in X-ray pulsars can be used to probe the physical condition of the disk flow at the inner disk radius; in particular, Eq. 2.27 allows for a straightforward estimate of $R_{\rm M}$. We note that the magnetospheric radius is, by definition, the innermost radius at which the disk plasma maintains a nearly Keplerian orbit. It might be expected that the beat between the disk inhomogeneities (blobs) and the magnetosphere takes place when the former have achieved a sub-Keplerian orbital frequency. However, in this case a blob would not be centrifugally supported any longer and would drift inwards, where the magnetic stresses would rapidly bring the blob into corotation with the NS; therefore modulated accretion at the beat frequency could not extend over several beat cycles, as required to explain the QPO Q-factors (which range from a few to tens in most cases; see e.g. van der Klis 2004). Therefore, it can be ruled out that disk inhomogeneities giving rise to modulated accretion at the beat frequency orbit at substantially slower frequencies than Keplerian. On the other hand, a larger orbital frequency at $R_{\rm M}$ than the corresponding Keplerian frequency, can be certainly ruled out by the effect of viscosity in the accretion disk.

2.3 Applications to accretion powered X-ray pulsars

Here we apply the calculations discussed in the previous sections to accretion powered X-ray sources. In particular, we selected the sources which displayed QPOs in their X-ray flux, as well as evidence for transitions between spin-up and spin-down states (see also Sect. 1.1). For each source, we use the luminosity measured when QPO were detected ($L_{\rm QPO}$) and the luminosity at which spin-up/spin-down transitions took place ($L_{\rm tr}$) in order to estimate the magnetospheric radius within the BFM (see Sect. 2.2) and magnetically threaded disk models (see Sect. 2.1.1 and 2.1.2), respectively. A comparison between these estimates of the magnetospheric radius is then carried out. In Table 2.1 we report the relevant values of $L_{\rm QPO}$ and $L_{\rm tr}$ we used, while in appendix 2.7 we give a brief summary of the properties of each source in our sample.

In order to calculate the magnetospheric radius in the threaded disk models, we first use the observations of spin-up/spin-down transitions. According to the threaded disk models, these transitions are the results of changes in the sign (from positive to negative) of the torque n acting onto the NS. Therefore, the luminosity $L_{\rm tr}$ can be used to constrain the value of $\dot{M}_{\rm tr}$, at which, according to the models, the torque n is expected to undergo a sign reversal (see Eqs. 2.5 and 2.12). In accretion powered X-ray pulsars, the conversion between $L_{\rm tr}$ and $\dot{M}_{\rm tr}$ can be obtained by using the relation

$$L_{\rm tr36} = 1.3\zeta \dot{M}_{tr16}(M/M_{\odot})(R_{\rm NS}/10^{6}), \tag{2.28}$$

where $L_{\rm tr36}$ is the X-ray luminosity in unit of 10^{36} erg s^{-1} and $\zeta{\sim}1$ is an efficiency factor that takes into account, e.g. geometrical and bolometric corrections (see Sect. 1.1 and later in this section).

Once $\dot{M}_{tr16}$ is determined, the magnetospheric radius in both the GLM and WM can be easily estimated as a function of the mass accretion rate, since all the uncertain parameters cancel out (see Sect. 2.1.1 and 2.1.2). This is shown in Fig. 2.4 for the X-ray pulsars in our sample (we assumed a NS mass of m=1.4 and a radius of $R_{\rm NS}$=10^6 cm). For each source we plot in the panels of this figure the derived values of the magnetospheric radius (units of the corotation radius), as a function of the mass accretion rate (units of 10^{16} g s^{-1}), for the threaded disk models described by Eq. 2.8 (GLM, triple-dot-dashed line), Eq. 2.20 (WM1, solid line), Eq. 2.21 (WM2, dotted line), Eq. 2.22 (WM3, dashed line), and Eq. 2.23 (WM4, dot-dashed line). At this point we use Eq. 2.28 and values of $L_{\rm QPO}$ in Table 2.1 to calculate the mass accretion rate at which QPOs are observed in each X-ray pulsar of our sample. The derived mass accretion rates are represented in panels of Fig. 2.4 with dotted vertical lines. For each source, the intersection between the dotted vertical line and the curves representing the magnetic threaded disk models gives the magnetospheric radius predicted by these models at the mass accretion rate corresponding to the $L_{\rm QPO}$ luminosity. In particular, the intersection with the curves that represent Eq. 2.20, 2.21, 2.22, and 2.23 give the range of allowed values of $x_{\rm w}$=$R_{\rm M}^{\rm w}/R_{\rm co}$, *i.e.* the magnetospheric radius in the WM (in unit of the corotation radius) calculated at the mass accretion rate that corresponds to $L_{\rm QPO}$. We indicate this parameter with $x_{\rm QPO}^{\rm w}$ in Table 2.1. Similarly, $x_{\rm QPO}^{\rm gl}$ is the value of $x_{\rm gl}$=$R_{\rm M}^{\rm gl}/R_{\rm co}$ for which the vertical dotted line intersects the curve from the GLM (Eq. 2.8). Finally, we derive for each source the value of the magnetospheric radius in the BFM at the mass accretion rate that corresponds to $L_{\rm QPO}$ by using Eq. 2.27. We call this parameter $x_{\rm QPO}^{\rm BFM}$ (a range of values for $x_{\rm QPO}^{\rm BFM}$ is indicated in Table 2.1 only for those sources which displayed more than one QPO frequency).

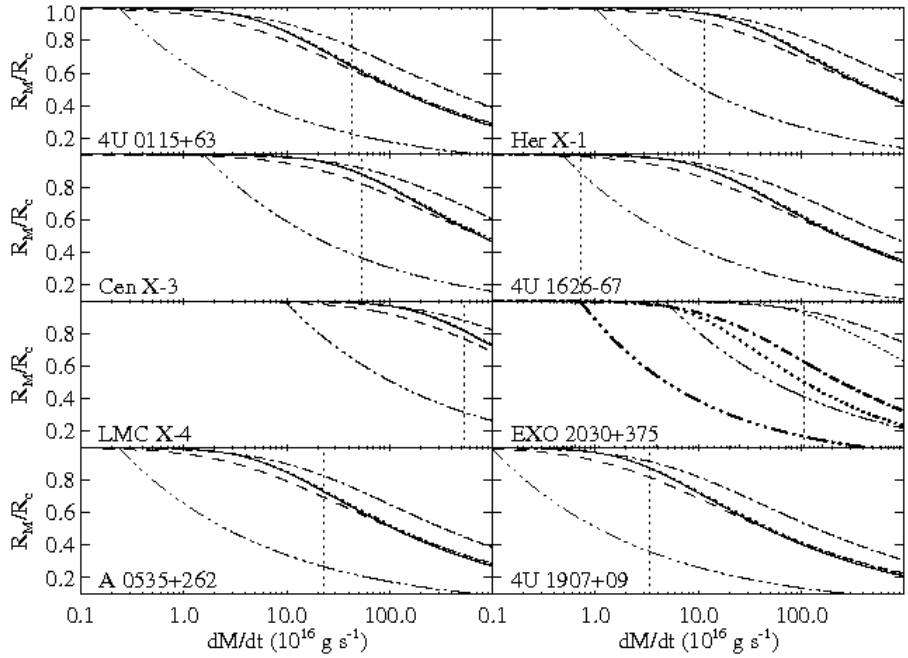

Figure 2.4: The ratio between the magnetospheric radius and the corotation radius, as a function of the mass accretion rate, for sources in Table 2.1. The solid line is for Eq. 2.20 (WM1), dotted line for Eq. 2.21 (WM2), dashed line for Eq. 2.22 (WM3), dot-dashed line for Eq. 2.23 (WM4), and triple-dot-dashed line for Eq. 2.8 (GLM). In the case of EXO 2030+375, spin-up/spin-down transitions were observed at luminosities in the range $\sim 10^{38}$-2.4×10^{36} erg s^{-1}, and we represented in the figure only those models that provide the higher and lower bound of $R_{\rm M}/R_{\rm co}$ as a function of the mass accretion rate. The thinner lines are for $L_{\rm tr}$=10^{38} erg s^{-1}, whereas the thicker lines are for $L_{\rm tr}$=2.4×10^{36} erg s^{-1}. In all panels the dotted vertical lines represent values of the mass accretion rate corresponding to the luminosity $L_{\rm QPO}$ at which QPOs are observed in each source of our sample.

With values of $x^{\rm w}_{\rm QPO}$, $x^{\rm gl}_{\rm QPO}$, and $x^{\rm BFM}_{\rm QPO}$ at hand, the GLM and WM can be tested against observations of accretion powered X-ray pulsars. Looking at values of these parameters in Table 2.1, we note that the selected sample of sources can be roughly divided into two groups. The first 4 sources (Her X-1, 4U 0115+63, Cen X-3, LMC X-4) displayed QPO frequencies that, if interpreted in terms of the BFM, agree with predictions of the WM. In fact, in these cases, $x^{\rm BFM}_{\rm QPO}$ and $x^{\rm w}_{\rm QPO}$ have similar values, whereas $x^{\rm gl}_{\rm QPO}$ is typically a factor of 2-3 smaller (for 4U 0115+63 and LMC X-4 the small discrepancy between $x^{\rm BFM}_{\rm QPO}$ and $x^{\rm w}_{\rm QPO}$ can be easily accounted for, e.g. by assuming small bolometric corrections in the X-ray luminosities $L_{\rm QPO}$ and $L_{\rm tr}$, see Sect. 2.3). Values of x close to $\sim$1, as measured for these four sources, imply a magnetospheric radius that is very close to the corotation radius for the luminosities at which QPOs are detected (for example, in the cases of Her X-1 and LMC X-4, the magnetospheric and corotation radii differ by less than few percent); therefore, in the following we refer to these sources as "fast rotators". Instead, results obtained for EXO 2030+375, A0535+262, and 4U 1907+09 suggest the GLM is better suited to account for observations of this second group of sources. In this

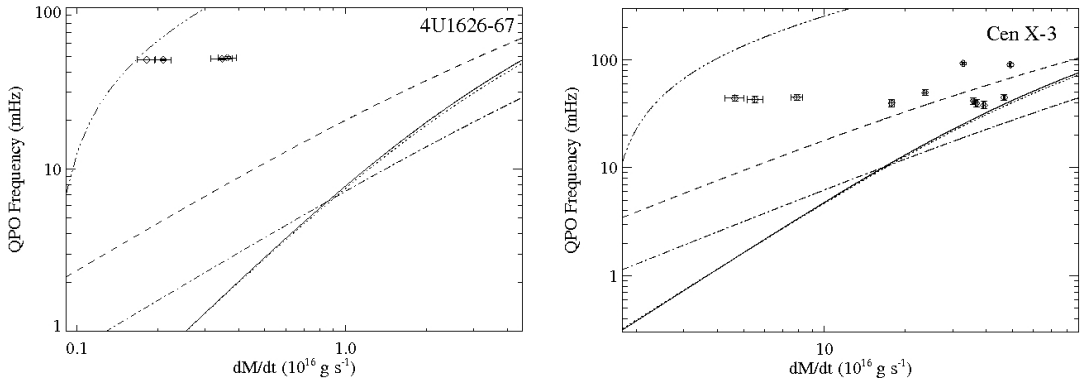

Figure 2.5: Predicted QPO frequencies in the BFM when the magnetospheric radius is calculated according to Eq. 2.20 (WM1, solid line), Eq. 2.21 (WM2, dashed line) Eq. 2.22 (WM3, dotted line), Eq. 2.23 (WM4, dash-dotted line), and Eq. 2.8 (GLM, triple-dot-dashed line). The left panel is for 4U 1626-67, whereas the right panel is for Cen X-3. In both cases QPO frequencies inferred from observations of these sources at different X-ray fluxes are shown together with measurement errors. These data taken from Kaur *et al.* (2007), Krauss *et al.* (2007), and Raichur & Paul (2008); we used Eq. 2.28 to convert between X-ray fluxes and mass accretion rates.

case values of $x_{\rm QPO}^{\rm BFM}$ are much closer to $x_{\rm QPO}^{\rm gl}$ than $x_{\rm QPO}^{\rm w}$. However, only for A0535+262 a good agreement between the BFM and the GLM is obtained. In the other two cases (EXO 2030+375 and 4U 1907+09) $x_{\rm QPO}^{\rm gl}$ is at least a factor of 2 larger than $x_{\rm QPO}^{\rm BFM}$ ($x_{\rm QPO}^{\rm w}$ is a factor of 2-3 larger than $x_{\rm QPO}^{\rm gl}$). In these sources the magnetospheric radius at the mass accretion rate corresponding to $L_{\rm QPO}$ is well inside the corotation radius ($x \ll 1$), and thus in the following we refer to them as "slow rotators". The QPO properties of 4U 1626-67 suggest a magnetospheric radius close to the corotation radius ($x_{\rm QPO}^{\rm BFM}$=0.83), like in the case of fast rotators, but they are well interpreted within the GLM. This source might thus be a sort of "transition object" between fast and slow rotators.

The conversion in Eq. 2.28 between observed X-ray luminosity and mass accretion rate is affected by several uncertainties. Besides the NS mass and radius, effects which can make ζ in Eq. 2.28 differ from unity, such as non-isotropic emission and bolometric corrections, should be kept in mind. Despite these uncertainties, we note that the results derived in this and the next section are virtually insensitive to variations by a factor of few in $L_{\rm tr}$ and $L_{\rm QPO}$. This is due to the weak dependence of the magnetospheric radius on the mass accretion rate. In all models discussed in Sect. 2.1, the steepest dependence of $R_{\rm M}$ on $\dot{M}$ is $\propto \dot{M}^{-2/7}$; therefore, an uncertainty by a factor 2-3 in the X-ray luminosity (and thus on $\dot{M}$, see Eq. 2.28) would cause a 20-30% change in the magnetospheric radius at the most.

2.3.1 Two case studies: 4U 1626-67 and Cen X-3

In this section we discuss further the cases of 4U 1626-67 and Cen X-3, for which detailed studies of the long term variations of the QPO frequency with the X-ray flux were recently published.

In particular, Kaur *et al.* (2008) studied QPOs in 4U 1626-67 at different X-ray fluxes

and compared the observed frequencies with those calculated by using the BFM and with the magnetospheric radius determined based on the GLM. These authors noted a discrepancy between the observations and the predictions, and argued that the BFM might not apply to this source. In Fig 2.5 (upper panel) we show the same calculation, but included also the QPO frequencies estimated by using the BFM with the magnetospheric radius as determined in the WM. In this plot the solid line corresponds to the QPO frequency predicted by the BFM when Eq. 2.20 (WM1) is assumed for the magnetospheric radius, the dashed line is for Eq. 2.21 (WM2), dotted line for Eq. 2.22 (WM3), and the dash-dotted line for Eq. 2.23 (WM4). The triple-dot-dashed line represents the QPO frequencies predicted by the BFM when the magnetospheric radius is calculated according to the GLM (Eq. 2.8). We selected those data from Kaur *et al.* (2008) and Krauss *et al.* (2007) for which QPO frequencies and X-ray fluxes were measured simultaneously, and used Eq. 2.28 to convert these fluxes into mass accretion rates. In the upper panel of Fig. 2.5 we show that, due to the different prescriptions available for the magnetospheric radius (*i.e.* the GLM and the WM), the region of predicted QPO frequencies in the BFM, as a function of the mass accretion rate, is very broad and all observational measurements lie within this region.

The lower panel of Fig. 2.5 show the case of Cen X-3. We used data from Raichur & Paul (2008). In this work, the authors showed that the QPO frequency of this source has almost no dependence on the X-ray flux. By using the GLM to calculate the magnetospheric radius, they argued that, if the BFM applies, then the long term X-ray intensity variations of Cen X-3 are likely due to obscuration by an aperiodically precessing warped disk, rather than being related to changes in the mass accretion rate (and thus location of the inner disk radius). In fact, in the latter case the QPO frequency would be expected to vary according to Eqs. 2.27 and 2.4. However, our calculations show that all measured QPO frequencies lie inside the region spanned by different magnetically threaded disk models. We conclude that the observations of 4U 1626-67 and Cen X-3 do not support simple applications of either the GLM or WM to the BFM. We further comment on this in Sect. 2.4.

2.4 Discussion

The results obtained in the previous section indicate neither the GLM nor the WM, when used in conjunction with the BFM, are able to reproduce the range of observations discussed here for the entire sample of X-ray pulsars. We also note that for all sources in Fig. 2.4, the magnetospheric radius in the GLM turns out to be somewhat smaller than that derived by using the WM. This point was discussed also by Wang (1996), who suggested that the reason for this disagreement resides in the different prescription of the toroidal field used in the two models: the assumed B_ϕ in the GLM implies a larger magnetic torque that spins down the NS more efficiently and reduces the value of the critical fastness parameter. As a consequence, the GLM magnetospheric radius is located closer to the NS (see Fig. 2.4). We showed here that the magnetospheric radius predicted by the GLM is still too large to account for observations of the QPOs over the entire sample of the slow rotators (see Table 2.1). This remains true even when the GLM is revised to include a more accurate prescription of the toroidal magnetic field, which leads to larger values of the critical fastness parameter (Wang 1987; Ghosh & Lamb 1992; Ghosh 1996).

At odds with the GLM, the magnetospheric radius in the WM approaches the corotation radius more gradually as the mass accretion rate decreases, a result that seems to

account for observations of fast rotating sources (see Table 2.1). However, in the cases of 4U 1626-67 and Cen X-3, for which detailed studies of the long term variations of the QPO frequency with the X-ray flux are available, the WM is not able to reproduce the observations. It was also noted that the treatment of the NS poloidal field screening by currents flowing onto the disk surface in this model might be oversimplified (Ghosh & Lamb 1992; Ghosh 1996).

Furthermore, in Sect. 2.1.2 we pointed out that an important caveat in the WM is that the interaction between the accretion disk and the NS magnetic field takes place in a similar fashion over the whole accretion disk. This is at odds with the GLM that predicts the strong coupling between the NS and the disk takes place mostly within a small boundary layer, such that this region alone determines the position where the disk terminates (*i.e.* $R_{\rm M}$). On the other hand, the theory of the boundary layer envisaged in the GLM might not be applicable to fast rotators, being the radial extent of the boundary layer of the same order of the separation between the magnetospheric and the corotation radii in these cases[2]. Some works have investigated the importance of the boundary layer in the threaded disk model (Li & Wang 1996, 1999; Li *et al.* 1996; Erkut & Alpar 2004)[3]. Li & Wang (1999) suggested that there exists an uncertainty by a factor of 4 in the Wang (1987) equation defining the magnetospheric radius; using this result, Li & Wang (1996) demonstrated that the boundary layer in NS accreting binaries can survive the destructing action of the NS magnetic field down to a radius $\simeq 0.8 R_{\rm M}$. The boundary layer might thus be significantly larger than previously thought (Ghosh & Lamb 1979a). However, the derived corrected value of the critical fastness parameter ($\sim$0.71-0.95) does not differ much from previous estimates (Wang 1995) and the problem of slow rotating sources remains open. Similar results were obtained by Erkut & Alpar (2004), which demonstrated that the width of the boundary layer might be a strong function of the fastness parameter: they found that broad "boundary layers" are expected for spinning-up sources, whereas much reduced boundary layers should be expected for sources in a spin-down state (these boundary layers are typically a factor $\sim$6-60 less wider than those found for spinning-up sources). However, a general analytical equation for the magnetospheric radius cannot be easily derived, due to the presence of few additional parameters in their model. Broad boundary layers were found also in the simulations by Romanova *et al.* (2003). These authors found a reasonable agreement with the predictions of the GLM, with the inner region of the disk behaving like a boundary layer, while the outer region is only partially coupled with the magnetic field of the star. These numerical simulations suggested a critical fastness parameter of $\sim$0.6. Despite this value is in between the values obtained within the GLM and the WM, it cannot account for observations of both fast and slow rotators. Our results in Table 2.1 imply that the critical fastness parameter cannot be constant for all these sources. A more general solution for the magnetic threaded disk model might be found in the future in which the WM and the GLM give the limiting cases of fast and slow rotation, respectively.

The present study suggests that all the discussed limitations of both the WM and GLM might be the reason why none of these models is able to reproduce the combination of QPO and torque behaviour observed at different X-ray luminosity levels in the X-ray pulsars

[2] Note that Ghosh & Lamb (1979b) showed steady state accretion might not be allowed in their model for $\omega_{\rm c} \gtrsim 0.95$.

[3] "Torqueless accretion" (Li *et al.* 1996; Li & Wickramasinghe 1997) was not considered here since that mechanism is unlikely to be applicable to accretion powered X-ray pulsars (Wang 1997b; Romanova *et al.* 2003).

considered. Alternatively, the BFM might not be applicable to (all) QPOs observed from X-ray pulsars.

2.5 Conclusions

We showed that, if the BFM applies to the QPOs of X-ray pulsars, then the GLM and WM cannot completely account for observations of the sources in our sample. Instead, taking into accounts results in Table 2.1, we noted that these sources can be divided into two classes:

- Fast rotators, for which the Keplerian velocity of matter at the inner disk radius, as inferred from the application of the BFM to the observed QPO frequency, is close to the rotational velocity of the star. In this case, the magnetospheric radius inferred from the WM and the BFM predict QPO frequencies which seem in good agreement with the observations. However, we showed in Sect 2.3.1 that at least in the cases of 4U 1626-67 and Cen X-3, the WM is not able to reproduce observations of QPO frequencies at different X-ray fluxes.

- Slow rotators, for which the Keplerian velocity of matter at the inner disk radius, as inferred from the application of the BFM to the observed QPO frequency, is well above the spin velocity of the NS. In this case, the magnetospheric radius derived from the BFM is less discordant with the predictions of the GLM. In fact, only for A0535+262 a good agreement between the GLM and the observations is obtained. For slow rotators the WM give a magnetospheric radius that is at least $\gtrsim$2-8 times larger than that derived from the BFM.

We conclude that either a more advanced theory of magnetically threaded disks is required, or that the BFM does not apply to (all) QPOs observed from X-ray pulsars.

Appendix

2.6 Calculation of the torque for region "C" of the SS73 accretion disk model

In order to evaluate ρ and h in Eqs. 2.9 and 2.12, Wang (1987) considered only the "B" region of the SS73 accretion disk, *i.e.* the gas-pressure dominated region where electron scattering gives the main contribution to the opacity. Here we carry out the same calculation by using the expressions of ρ and h that are appropriate to region "C" of the SS73 accretion disk model (where the main contribution to the opacity is provided by free-free absorption). According to Vietri (2008), the thermal pressure of disk matter has a radial dependence $p = p_{\rm M}(R_{\rm M}/R)^{21/8}$, where the subscript M denotes quantities evaluated at the inner disk radius. From Eq. 2.9 we get

$$|B_\phi(R)| = B_{\phi 0}\frac{\omega_{\rm s}^{23/16}}{|1-\omega_{\rm s}|^{1/2}}\left(\frac{R_{\rm co}}{R}\right)^{69/32}\cdot \cdot\left|1-\left(\frac{R}{R_{\rm co}}\right)^{3/2}\right|^{1/2}, \tag{2.29}$$

where the same notation as that of Sect. 2.1 is used. Setting $y = (R/R_{\rm co})^{3/2}$ and using Eq. 2.30 into Eq. 2.12 we obtain

$$n(\omega_{\rm s}) = 1+\frac{1}{3}\frac{\omega_{\rm s}^{23/16}}{|1-\omega_{\rm s}|^{1/2}}\cdot \cdot\left[\int_\omega^1\frac{(1-y)^{1/2}}{y^{39/16}}dy-\int_1^\infty\frac{(y-1)^{1/2}}{y^{39/16}}dy\right]. \tag{2.30}$$

By numerically evaluating integrals in the above equation we find $\omega_c = 0.95$.

2.7 Values of $L_{\rm tr}$, $L_{\rm QPO}$ for accretion powered X-ray sources

Here we briefly summarize the relevant observations of the accretion powered X-ray pulsars considered in Table 2.1, in order to explain values used for the luminosities $L_{\rm tr}$ and $L_{\rm QPO}$.

- *Her X-1*: Her X-1 is one of the best studied X-ray binary system. It consists of a ∼1.24 s spinning NS and a A/F companion (the orbital period is 1.7 day). The X-ray flux displays a regular modulation at a 35 day period, that has been associated to the precession of a highly warped accretion disk that periodically obscures the NS (Petterson 1975; Choi *et al.* 1994; Wilson *et al.* 1997; Dal Fiume *et al.* 1998; Parmar *et al.* 1999; Klochkov *et al.* 2007). This suggested that transitions between high ("main-on states") and low luminosity states (the "anomalous" low states) of this source are to be interpreted as due to local obscuration phenomena, rather than large changes in the mass accretion rate. Evidence in favor of this interpretation has been recently obtained through detailed phase-resolved spectroscopy (Zane *et al.* 2004) as well as observations of X-ray heating of the companion star (Boroson *et al.* 2000). Since QPOs and spin-up/spin-down transitions were observed during both

high and low luminosity states, for the purpose of the calculations presented here we assume $L_{\rm tr}$=$L_{\rm QPO}$=2.1×10^{37} erg s^{-1} (a distance of 5 kpc is considered), where the latter is the typical main-on state luminosity.

- *4U 0115+63*: 4U 0115+63 is a binary system hosting a 3.6 s spinning NS orbiting a Be companion (the orbital period is 24.3 day). The distance to the source is ∼8 kpc (Negueruela & Okazaki 2001). An HEAO observation caught this source in outburst (the typical outburst luminosity is ∼8×10^{37} erg s^{-1}, Campana *et al.* 2000), and a prominent peak in the power spectrum of the X-ray light curve was detected at 62 mHz (Soong & Swank 1989). Tamura *et al.* (1992) reported that the spin-up trend the source usually displayed while in outbursts reversed during lower luminosity states. These typically occurred at 5×10^{35} erg s^{-1} (Campana *et al.* 2000).

- *Cen X-3*: Cen X-3 is a high mass X-ray binary with a spin period of ∼4.8 s and an orbital period of ∼2.1 day. The companion star is an O-type supergiant and the distance is estimated to be ∼8 kpc (Burderi *et al.* 2000, and references therein). The presence of a ∼35 mHz QPO in the power spectrum of this source was first discovered by Takeshima *et al.* (1991), after the source egress from an X-ray eclipse. The typical X-ray luminosity was determined with BeppoSAX, and is of order ∼1.0×10^{38} erg s^{-1} (0.12-100 keV). Cen X-3 has a secular spin-down trend (Bildsten *et al.* 1997), but episodes of spin reversal were found to occur at a luminosity that is typically a factor of ∼3 below that of the post-eclipse high luminosity state (Howe *et al.* 1983). We thus considered in Table 2.1 that $L_{\rm QPO}$ is equal to the typical X-ray luminosity observed in the post-eclipse egress state, whereas $L_{\rm tr}$∼$1/3L_{\rm QPO}$.

- *LMC X-4*: LMC X-4 is an accretion powered X-ray pulsar with a spin period of ∼13.5 s and an orbital period of ∼1.4 day. The X-ray luminosity of the system varies with a periodicity of ∼30.3 day, alternating between high (∼2×10^{38} erg s^{-1}) and low (a factor of ∼60 below) luminosity states (for an estimated distance of ∼50 kpc, Woo *et al.* 1996). This periodicity have been attributed to the effect of an obscuring tilted accretion disk (Moon & Eikenberry 2001, and references therein). During the high states, spin torque reversals were repeatedly observed, whereas during episodes of very bright flares (∼10^{39} erg s^{-1}, 2-25 keV) QPOs were detected at frequencies in the ∼0.65-1.35 mHz range Moon & Eikenberry (2001).

- *4U 1626-67*: 4U 1626-67 is a low mass X-ray binary hosting a ∼7.7 s spinning neutron star in a ∼42 min orbit around a ∼0.004 $M_\odot$ companion star. QPOs were detected in the X-ray observations of this source more than once (for a review see, e.g. Kaur *et al.* 2008). A torque reversal was observed by Chakrabarty & Roche (1997), who also estimated a source distance of ∼3 kpc. For a review of the flux history of 4U 1626-67, we reefer the reader to Krauss *et al.* (2007).

- *EXO 2030+375*: EXO 2030+375 is a Be X-ray transient with an orbital period of ∼46 day, hosting a ∼42 s spinning neutron star, and located at a distance of 7.1 kpc (Wilson *et al.* 2002). In 1985 this source underwent a bright outburst (peak luminosity ∼2×10^{38} erg/s), and a QPO at ∼213 mHz was detected (Angelini *et al.* 1989). Spin-up/spin-down transitions were observed more than once, at luminosities in the ∼10^{38}-2.4×10^{36} erg/s (1-20 keV) range.

- *A0535+262*: A0535+262 is a ∼103 s X-ray pulsar, orbiting a O9.7 companion star (the orbital period is ∼111 day). QPOs and spin reversals were best observed during the giant outburst in 1994 (Finger *et al.* 1996). This outburst was detected with BATSE in the energy 20-100 keV range, and the flux at the peak of the outburst was ∼6 Crab. Observations of this outburst at lower energies (<20 keV) were not available, but, based on previous results, Finger *et al.* (1996) estimated the 2-10 keV flux might not be larger than 2 Crab. Due to the uncertainties in this estimate we have not corrected values reported in Table 2.1 for this factor. As discussed in Sect. 2.3 an uncertainty of ∼30% on the luminosity used to derive the position of the magnetospheric radius cannot affect much our results. Note that the distance used by Finger *et al.* (1996) to convert the observed flux into an X-ray luminosity is 2 kpc (Steele *et al.* 1998).

- *4U 1907+09*: 4U 1907+09 is a ∼440 s spinning NS in a ∼8 day orbit around a supergiant companion. QPOs were discovered during an hour long flare at $\sim 6.3\times10^{36}$ erg/s (2-60 keV, and an assumed distance of 5 kpc, in't Zand *et al.* 1998; Cox *et al.* 2005). After the discovery of the pulsations by Makishima *et al.* (1992), the NS in 4U 1907+09 exhibited a steady spin-down for about 20 yrs. This trend changed in 2006, when a torque reversal was observed at $\sim 2\times10^{36}$ erg/s (1-15 keV, Fritz *et al.* 2006).

Chapter 3

On the spin-up/spin-down transitions in accreting X-ray binaries

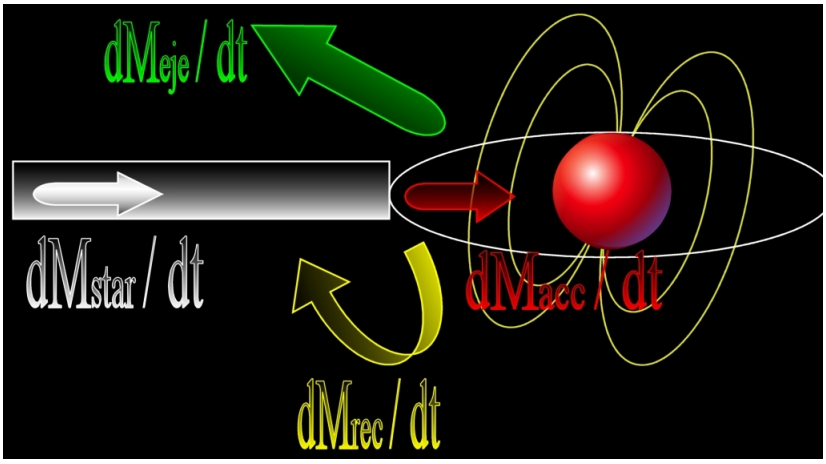

Figure 3.1: The recycling magnetosphere geometry.

In this Chapter, we develop a model to interpret the spin-up and spin-down behaviour of some disk-fed NSXBs that cannot be understood within the threaded disk models (see Chapter 2). As we discussed in Sects. 1.1.1 and 1.1.2 an accretion disk around a NS can be formed in HMXBs and in LMXBs when the donor star in these systems fills (at least temporarly) its Roche Lobe and a RLO phase is initiated. Furthermore, in Sect. 1.2.3 we showed that if the NS is magnetized, then the material from the disk is channelled toward the magnetic poles of the NS, where it releases its gravitational energy and gives rise to the X-ray luminosity we observe. Pulsations at the neutron star spin frequency are generated from a lighthouse-like effect (see Sect. 1.2.3).

While the X-ray luminosity yields an estimate of the mass accretion rate (see Chapter 2), pulse timing measurements allow one to measure the torque, and hence probe the nature of the accretion process mediated by the magnetosphere of the star. When accretion occurs through a prograde disk, the angular momentum transferred by the accreting material to the star (material torque) tends to spin the star up, until the centrifugal bar-

rier inside the corotation radius of the magnetosphere becomes large enough to inhibit further accretion (see Sect. 1.2.3). The star is then expected to settle in a state with an equilibrium spin period which depends mainly on the mass accretion rate provided by the companion and the neutron star magnetic field (e.g. Frank *et al.* 2002).

Observations of disk-accreting X-ray pulsars during the 1970s and 1980s were rather sparse, and appeared to be roughly compatible with the near-equilibrium picture (e.g. Nagase 1989), although there were already hints at times of some unexpected behaviours. These included torque reversals for some time while still accreting, or spin up rates much smaller than expected for the observed luminosity. In the 1990s, continuous monitoring of several disk-fed X-ray pulsars with the Burst and Transient Source Experiment (BATSE) on board the Compton Gamma-Ray observatory, shed light on the long-term behaviour of several objects (for a comprehensive review see Bildsten *et al.* 1997). Particularly striking were the findings for GX 1+4 and 4U 1626-67: after about 15 years (for GX 1+4) and 20 years (for 4U 1626-67) of spin up, both systems showed a torque reversal, which made them switch to a spin-down phase. Other systems, like Cen X-3, Vela X-1, Her X-1, often showed an alternation of spin up and down sometime overimposed on a longer term of either spin down or spin up. In most cases, the magnitude of the torques is comparable during the spin-up and the spin-down regimes. These unusual behaviours were a sign that the simple scenario outlined above might be incomplete, and hence they triggered a revival of research, mostly in the direction of finding other sources of torque in addition to the one provided by the accreting material alone.

As we discussed in Chapter 2, Ghosh & Lamb (1979a; 1979b; hereafter GL) and Wang (1987; 1995) suggested that, in addition to the material torque, there is also an extra source of torque provided by the magnetic field lines threading the disk. While in the spherical free-fall approximation the disk is truncated at the point at which the magnetic pressure of the magnetosphere balances the pressure of the accreting material (see Eq. 1.23), in the GL model there exists a broad transition zone in which the magnetic field lines still thread the disk even if the viscous stress in the disk material dominates over the magnetic stress. This is made possible through the combination of a number of effects, such as the Kelvin-Helmotz instability, turbulent diffusion and reconnection. Within this model torque reversals similar to the cases discussed above are very difficult to explain, since it is expected a gradual reversal from spin-up to spin-down while changing the mass accretion rate onto the NS.

In the models of Arons *et al.* (1984) and Lovelace *et al.* (1995) the extra torque is provided by the expulsion of a magnetically-driven wind. Transitions between spin up and spin down states are possible, but they must be induced by external perturbations, such as variations in the viscosity parameter α of the disk or, most plausibly, the accretion rate from the companion star. These variations would have to be finely tuned just so that the two torque states have comparable magnitude but opposite sign. This seems unlikely in general, but even more so in a system like 4U 1626-67, in which the average mass accretion rate is likely determined by the loss of orbital angular momentum via gravitational radiation (Chakrabarty *et al.* 1997a). Alternatively, in the case of GX 1+4, Makishima *et al.* (1992) and Dotani *et al.* (1989) suggested that the spin down could be due to accretion from a retrograde disk formed from the stellar wind of the red giant companion. White (1988) however showed that this was unlikely to be the case. A retrograde disk around the NS spin axis could also be produced by magnetic torques generated in the interaction between surface currents on the disk and the component of the NS magnetic field parallel to the disk (Lai 1999).

In this Chapter we discuss a new scenario for the spin up/spin down transitions observed in binary systems accreting from a disk. The torque exchange between the magnetosphere and the disk material is supposed to be dominated by the material component as in the early models (Pringle & Rees 1972). In this respect, our toy model is very simple and idealized: possible torques non parallel to the rotation axis are neglected, as well as magnetic torques (e.g. Ghosh & Lamb 1979b; Lai 1999). What is new in our model is a computation of the fate of the ejected material during the propeller phase of the neutron star. Our calculation accounts for the following facts: *i)* not all the "propelled" material receives sufficient energy to unbind from the system; *ii)* if the magnetic moment of the neutron star is inclined with respect to its rotation axis, there can be, at the same time, regions of the magnetospheric boundary which are allowed to accrete while others are propelling material away. This is a fundamental assumption of our model. While in this Chapter we provide arguments in its support, a final validation will have to wait for detailed numerical simulations. This work should therefore be considered as an investigation (the first of its kind to the best of our knowledge) of the characteristic timing behaviour of a pulsar whose magnetosphere can simultaneously eject and accrete matter in different regions of its boundary. As it will be shown in the following, accounting for this possibility leads to fundamentally different conclusions for the long-term, equilibrium state of the system. Rather than settling at the equilibrium period at which the Keplerian frequency of the disk matches the star rotation frequency at the point of interaction (e.g. Frank *et al.* 2002), the system settles, for a wide range of conditions, in alternating cycles of spin-up/spin-down for a constant accretion rate from the companion star. A qualitative summary of our model is described below, and is formalized mathematically in the following sections.

A magnetic neutron star surrounded by an accretion disk is able to accrete only under the condition that the velocity of the magnetosphere at the point of interaction (magnetospheric radius, R_M) is smaller than the local Keplerian velocity of the disk material (see Sect. 1.2.3). If this condition is not satisfied, accretion is inhibited (Illarionov & Sunyaev 1975), and angular momentum is transferred from the star to the gas. Whether this propelled gas can be completely unbound from the system will depend on the location of the magnetospheric radius within the gravitational field of the neutron star. There exists a minimum distance, $R_{\rm inf}$, beyond which ejection of matter to infinity is possible. If $R_M < R_{\rm inf}$, the propelled material cannot be unbound, and therefore it will fall back on the disk and accrete again. This matter is, in this sense, "recycled". An accreting system with recycled material can, under certain conditions, have multiple states available. This is due to the fact that, for the system to be in a steady-state condition, the total mass inflow rate at the magnetospheric boundary (which determines the position of the magnetospheric boundary itself), $\dot{M}_{\rm tot} = \dot{M}_{\rm acc} + \dot{M}_{\rm rec} + \dot{M}_{\rm eje}$ must be such that $\dot{M}_{\rm acc} + \dot{M}_{\rm eje} = \dot{M}_*$, where $\dot{M}_*$ is the mass inflow rate provided by the companion star, and $\dot{M}_{\rm acc}$, $\dot{M}_{\rm rec}$ and $\dot{M}_{\rm eje}$ are, respectively, the rate at which mass is accreted, recycled and ejected. Whenever the term $\dot{M}_{\rm rec}$ is non-negligible, there could be in principle different solutions to the above condition corresponding to the same value $\dot{M}_*$ of the mass inflow rate. As the system spins up or down on a certain branch of the solution, this solution can be lost, and the system is consequently forced to jump to a different state, often characterized by opposite torque. This qualitative argument is formalized mathematically in detail in Sect. 3.1, while Sect. 3.2 presents specific applications to the cases of the accreting sources GX 1+4 and 4U 1626-67. Our results are summarized and discussed in Sect. 3.3.

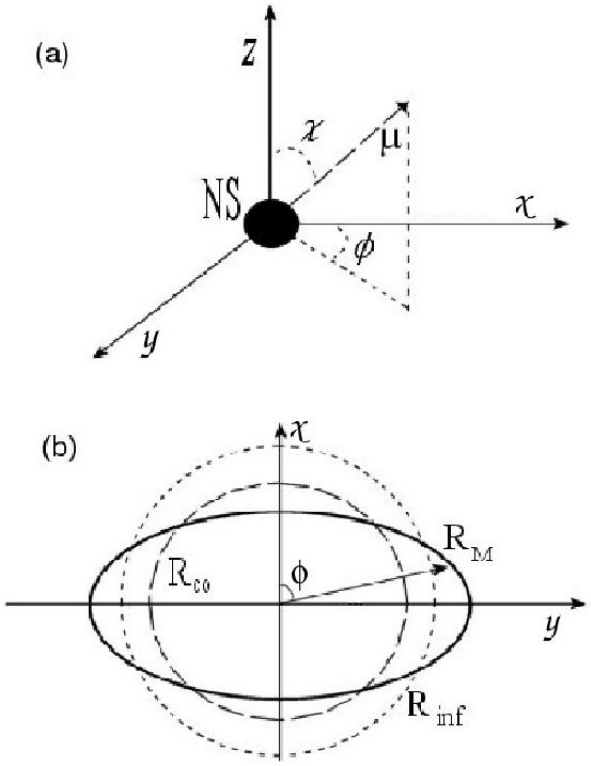

Figure 3.2: Schematic illustration of the NS-disk system for an oblique rotator. Figure (a) shows the relative positions of the magnetic dipole moment axis, the phase angle ϕ, and the inclination angle χ. The NS is assumed to rotate around the z-axis. Figure (b) is a two dimensional rapresentation of the position of the magnetosphere (continuous line) with respect to the corotation radius (long dashed line) and the infinity radius (short dashed line), for arbitrarily fixed values of the NS parameters.

3.1 Model description

3.1.1 Magnetosphere-disk interaction in an oblique rotator

In this section we discuss the main concepts and assumptions upon which our disk-magnetosphere model is based. The basic geometry is depicted in Fig. 3.2. The axis of the magnetic moment μ of the neutron star (NS) is inclined with respect to the rotation axis by the magnetic colatitude χ. In cylindrical coordinates (r, ϕ, z), where the z-axis coincides with the rotation axis, the component of the magnetic field in the disk plane is (Jetzer *et al.* 1998)

$$B^2 = \frac{\mu^2}{r^6}\left[1 + 3(\sin\chi \sin\phi)^2\right] , \tag{3.1}$$

under the assumption that the disk is planar and its axis is parallel to the spin axis of the NS. When the rotation axis of the NS is inclined (i.e. $\chi \neq 0$), the strength of the magnetic field in the plane of the disk depends on the longitude ϕ. As shown below, this angular dependence results in an asymmetric magnetospheric boundary.

The fate of the matter funnelled from the accretion disk to the rotating, magnetized neutron star depends on a number of factors, the most important of which are the relative strength of the magnetic pressure and the pressure of the accreting material, and the

relative velocity of the magnetosphere of the star at the inner radius of the disk with respect to the Keplerian velocity at that same radius. Following Lamb & Pethick (1974), the former condition can be formalized by equating the magnetic energy with the kinetic energy of the infalling matter:

$$\frac{1}{2}\rho v^2 = \frac{B^2}{8\pi} \ . \tag{3.2}$$

In the free-fall approssimation the density is given by $\rho = \rho_{ff} = \dot{M}/(4\pi v_{ff} r^2)$, where $v_{ff} = (2GM/r)^{1/2}$ is the free-fall velocity. Using these expressions, together with Eq.(3.1) and (3.2), the magnetospheric radius for an oblique rotator can be obtained (Jetzer *et al.* 1998; Campana *et al.* 2000):

$$R_M(\phi) = 3.2 \times 10^8 \mu_{30}^{4/7} M_1^{-1/7} \dot{M}_{17}^{-2/7} \left[1 + 3(\sin\chi \sin\phi)^2\right]^{2/7} \ , \tag{3.3}$$

where μ_{30} is the magnetic moment in units of 10^{30} G cm^3, M_1 is the NS mass in units of 1 $M_\odot$ and $\dot{M}_{17}$ is the accretion rate in units of 10^{17} g s^{-1}. The minimum radius $R_{\rm M}(0)$ also corresponds to $\chi = 0$, the approximation usually adopted in models of the disk-magnetosphere interaction. The maximum radius $R_{\rm M}(\pi/2)$ is only a factor of $(1 + 3\sin^2\chi)^{2/7} \leq 1.49$ larger. Note that the elongated shape of the magnetospheric boundary plays a fundamental role in our model.

An important assumption of our model is that, during the rotation of the magnetosphere (whose shape depends upon the instantaneous position of the magnetospheric radius as a function of ϕ), matter in the Keplerian disk is able to fill the region that separates the disk and the magnetospheric flow on a timescale shorter than the spin period of the star. This ensures that the inner boundary of the disk remains in constant contact with the magnetosphere. We show in the appendix that the Kelvin-Helmholtz instability operates on a sufficiently short timescale and wide range of radii that this assumption can be justified.

Accretion to the star is possible only under the condition that, at the magnetospheric radius, the Keplerian velocity of the accreting gas, $\Omega_{\rm K}(R_M)$, is larger than the velocity Ω_0 of the rotating magnetosphere of the star (equal to the velocity of the star), otherwise centrifugal forces will inhibit accretion (Illarionov & Sunyaev 1975). The above condition is equivalent to saying that the magnetospheric radius must be smaller than the corotation radius (see Sect. 1.2.3). In an oblique rotator, the onset of the propeller stage will occur when $R_M(\phi) = R_{\rm co}$ at least in one point of the magnetospheric boundary. Note that, while a parallel rotator can be *either* in the propeller *or* in the accreting regime, an oblique rotator can be in both states *simultaneously* for different longitudes of the magnetospheric boundary. Indeed, this special feature of the oblique rotator was used by Campana *et al.* (2000) in building up a model that explained the dramatic luminosity variations seen in the *BeppoSAX* observation of the transient X-ray pulsar 4U 0115+63[1].

The interaction between the magnetosphere of the NS and the matter in the disk is likely to be at least partially anelastic because of dissipative effects in the mixing process between the magnetospheric plasma and the disk matter during the propeller phase. For clarity of presentation, here we consider first the two limiting cases of a completely anelastic and a completely elastic interaction, and then we will generalize our results to the partially anelastic case.

[1] This simultaneous presence of different regimes, which is crucial to our model, has not yet been seen in numerical simulations. However, to the best of our knowledge, current numerical simulations of the propeller regime (Romanova *et al.* 2004) are axisymmetric; because of this geometry, they cannot verify the simultaneous presence of different regimes of the kind discussed here.

In the anelastic case, the magnetic field of the NS is able to force matter to corotate at the same velocity of the star, and it is endowed at the magnetospheric boundary with specific kinetic energy $\epsilon = 1/2\Omega_0^2 R_M^2$ and angular momentum $l = \Omega_0 R_M^2$. In order for matter to be ejected from the system via the propeller mechanism, the magnetic field must provide it with enough energy to reach a velocity in excess of the local escape velocity at R_M. Because in the anelastic case the ejection velocity is $v_{ej} = \Omega_0 R_M$, the requirement above converts to an "ejection radius"

$$R_{\rm inf,ane} = (2GM/\Omega_0^2)^{1/3} \simeq 1.26 R_{\rm co} \ . \tag{3.4}$$

Only matter which is located beyond this radius during the interaction with the magnetosphere of the NS can be unbound from the system through the propeller mechanism. Therefore there exists a region ($R_{\rm co} < R_M < R_{\rm inf}$) in which the propeller is active but matter cannot be unbound from the sytem by merging with the disk matter (Spruit & Taam 1993). We assume that matter in this zone is swung out and circularizes at the radius where its angular momentum equals the Keplerian value, i.e. when $l = \Omega_0 R_M^2 = l_{\rm K} = \Omega_{\rm K}(R_{\rm K}) R_{\rm K}^2$ (here $R_{\rm K}$ is the circularization radius). This condition defines the Keplerian circularization radius:

$$R_{\rm K,ane} = \frac{\Omega_0^2 R_M^4}{GM} \ . \tag{3.5}$$

Matter that is not ejected from the system will fall back into the disk and restart its motion toward the NS from the radius defined in Eq. 3.5.

In the case of the elastic propeller, we assume that material in the disk at R_M moves toward the magnetosphere with a tangential relative velocity of $-v_{\rm rel} = R_M(\Omega_0 - \Omega_{\rm K})$, where $\Omega_{\rm K}$ is the Keplerian angular velocity at R_M. In a completely elastic interaction this matter bounces off at the magnetospheric boundary with an opposite velocity of $+v_{\rm rel}$ that in the non-rotating frame sums with $v_{\rm rot} = \Omega_0 R_M$. Thus the ejection velocity is $v_{ej} = R_M[2\Omega_0 - \Omega_{\rm K}(R_M)]$. In this case the requirement that this velocity be larger than $v_{esc}(R_M)$ can be written as:

$$\frac{R_M^2}{2}\left[4\frac{GM}{R_{\rm co}^3} + \frac{GM}{R_M^3} - 4\frac{GM}{R_{\rm co}^{3/2} R_M^{3/2}}\right] \geq \frac{GM}{R_M}$$

where we have used the definition of the corotation radius. This equation can be solved as a function of the magnetospheric radius to define the limit beyond which ejection of matter to infinity is possible in the purely elastic case:

$$R_{\rm inf,el} = \left[\frac{1+\sqrt{2}}{2}\right]^{2/3} R_{\rm co} \simeq 1.13 R_{\rm co} \ . \tag{3.6}$$

The matter leaving the magnetospheric boundary is endowed with specific angular momentum $l_{el} = R_M^2(2\Omega_0 - \Omega_{\rm K})$; equating this to $l_{\rm K}$ gives a new circularization radius for matter that is not ejected to infinity. Using the same notation as above we find:

$$R_{\rm k,el} = \frac{R_M^4(2\Omega_0 - \Omega_{\rm K})^2}{GM} \ . \tag{3.7}$$

Let us now consider the most general case of a partially elastic interaction. Following the formalism developed by Eksi *et al.* (2005), we define the "elasticity parameter" β, which is a measure of how efficiently the kinetic energy of the neutron star is converted into kinetic energy of ejected matter through the magnetosphere-disk interaction. Taking into

account the definitions given above, we now consider the generalized rotational velocity of matter at the magnetospheric boundary:

$$v_{\rm gen} = \Omega_{\rm K}(R_M) R_M (1-\gamma) \tag{3.8}$$

where $\gamma = (1+\beta)(1-\Omega_0/\Omega_{\rm K})$. The elastic case is obtained in the limit $\beta = 1$, and the totally anelastic one when $\beta = 0$. Using Eq. 3.8 we can then generalize also the expression for the infinity radius

$$R_{\rm inf} = \left(\frac{\beta+\sqrt{2}}{1+\beta}\right)^{2/3} R_{\rm co} \tag{3.9}$$

and for the circularization radius

$$R_{\rm K} = R_M (1-\gamma)^2 \ . \tag{3.10}$$

In our model we will consider the general case of a partially elastic interaction, and use β as one of the model parameters.

Figure 3.2 (b) shows the various characteristic radii defined above on the disk plane $z = 0$. Depending on the phase (ϕ) and the inclination angle (χ), it is possible to have regions of the magnetospheric boundary in which accretion is possible ($R_M(\phi,\chi) < R_{\rm co}$) together with other portions in which the propeller is already active, resulting in ejection of matter to larger radii ($R_{\rm co} < R_M(\phi,\chi) < R_{\rm inf}$), or to infinity ($R_M > R_{\rm inf}$). In those cases in which the inclination angle is sufficiently large, it is possible to have all the three regimes described above simultaneously.

It should be noted that, in our model, we consider ejection of matter from regions of the disk that are away from the corotation radius, where the Keplerian velocity of matter becomes rapidly supersonic (Frank *et al.* 2002). This could in principle lead to the formation of supersonic shocks which can heat the plasma and eventually stop the ejection mechanism. However in this situation, due to the high relative rotation rate between the plasma inside the magnetosphere and that inside the disk, the Kelvin-Helmholtz instability can be very efficient. As previously discussed, this instability can lead to a large mixing of the two fluids, providing a mechanism to mantain the interaction between the magnetic field of the NS and the matter in the disk. Under these circumstances, it has been shown that outflowing bubbles of matter are likely to be accelerated magnetically by the NS towards the outer region of the disk (Wang & Robertson 1985), in turn supporting the idea that ejection far away from the corotation radius can be sustained.

3.1.2 Conditions for the existence of a limit cycle

Let $\dot{M}_*$ be the rate of inflowing matter, regulated through the Roche Lobe overflow or capture of part of the wind of the companion star. We assume that this matter possesses in all cases enough angular momentum that a prograde accretion disk forms. We further assume that the mass inflow at the inner disk boundary is azimuthally symmetric (i.e. independent of ϕ). As illustrated in Fig. 3.3 and discussed in Sect. 3.1, for a general, oblique, orientation of the magnetic field of the NS with respect to the normal to the disk and the spin axis of the NS (which we assume are parallel), there will be regions where $R_M(\phi) < R_{\rm co}$, and therefore some matter is able to accrete, regions for which $R_M(\phi) > R_{\rm inf}$ that result in matter being ejected, and intermediate zones with $R_{\rm co} < R_M(\phi) < R_{\rm inf}$ from which matter gets "recycled". The fraction of material in each of these regions is expected to be proportional to the angle ϕ subtended by the relevant region in the

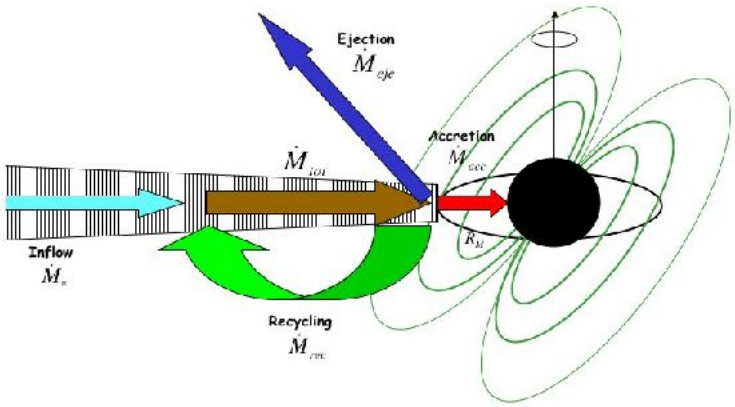

Figure 3.3: The fate of the matter provided by the companion at a rate $\dot{M}_*$ depends on the relative position of the magnetospheric radius with respect to the corotation radius and the ejection radius. Matter can be accreted, ejected or recycled into the disk.

magnetosphere as shown in Fig. 3.3. As in Sect. 3.1, let us define $\dot{M}_{\rm acc}$, $\dot{M}_{\rm eje}$ and $\dot{M}_{\rm rec}$ to be respectively the rates of accreting, ejected and recycled material at any given time. These various components are illustrated in Fig. 3.3. If $d\dot{M}_{\rm tot}/d\phi$ is the total rate of matter exchanged at the magnetosphere-disk boundary per unit angle, these components are given by $\dot{M}_{\rm comp} = 1/2\pi \int_{\phi_1}^{\phi_2} d\phi \left(d\dot{M}_{\rm tot}/d\phi\right)$, where the integration interval $[\phi_1, \phi_2]$ of ϕ is such that $R_M(\phi) < R_{\rm co}$ when comp="acc" , $R_{\rm co} < R_M(\phi) < R_{\rm inf}$ when comp="rec" and $R_M(\phi) > R_{\rm inf}$ when comp="eje". Figure 3.4 shows an example of these components as a function of the total mass inflow across the entire magnetospheric boundary, $\dot{M}_{\rm tot}$. At low values of $\dot{M}_{\rm tot}$, $R_{\rm inf} > R_M$ for all values of ϕ, and therefore all matter is ejected (i.e. $\dot{M}_{\rm eje} = \dot{M}_{\rm tot}$). On the other hand, at high values of $\dot{M}_{\rm tot}$, $R_{\rm co} > R_M$ for any ϕ, and therefore all matter is accreted ($\dot{M}_{\rm acc} = \dot{M}_{\rm tot}$). For values of $\dot{M}_{\rm tot}$ such that $R_M(\phi)$ crosses $R_{\rm co}$ at some values of ϕ, $\dot{M}_{\rm rec} \neq 0$.

While the total mass inflow rate available to the system is determined by the mass transfer rate from the companion, $\dot{M}_*$, the value of the magnetospheric radius R_M, on the other hand, is determined by the total pressure of the accreting matter, i.e. $\dot{M}_{\rm tot} = \dot{M}_{\rm acc} + \dot{M}_{\rm eje} + \dot{M}_{\rm rec}$. Since, in general, $\dot{M}_{\rm tot} \geq \dot{M}_*$, the magnetospheric radius can be smaller than it would be if the "recycled" mass component were not accounted for (as commonly assumed in the literature). Therefore, including $\dot{M}_{\rm rec}$ in the computation of R_M, allows accretion at the same rate to occur for smaller values of $\dot{M}_*$ than it would otherwise.

In order to demonstrate the existence of a limit cycle, testified by a hysteresis-like loop in the $\dot{M}_* - \dot{M}_{\rm tot}$ plane, we start by noting that the rate at which matter is "recycled", $\dot{M}_{\rm rec}$, does not contribute to the mass budget; therefore a steady-state solution is possible only if

$$\dot{M}_* = \dot{M}_{\rm acc} + \dot{M}_{\rm eje} \ . \tag{3.11}$$

Let us therefore examine the behaviour of the curve $\dot{M}_{\rm tot}$ as a function of the accretion

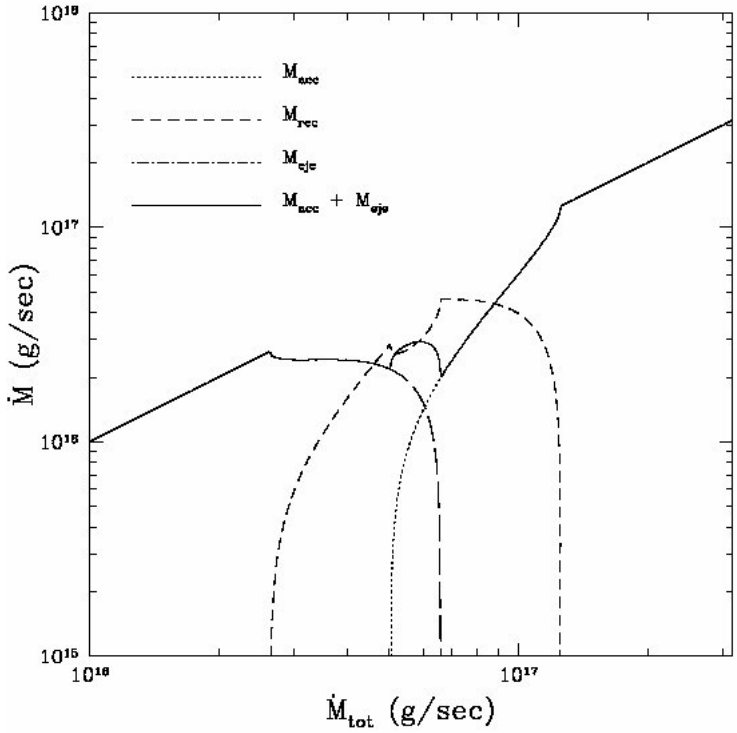

Figure 3.4: The various contributions to the total accretion rate $\dot{M}_{\rm tot} = \dot{M}_{\rm acc} + \dot{M}_{\rm rec} + \dot{M}_{\rm eje}$ at the magnetospheric-disk boundary. The system parameters are $B = 6 \times 10^{13}$ G, $\nu = 9$ mHz, $\chi = 45°$, $\beta = 0.3$.

rate $\dot{M}_{\rm acc} + \dot{M}_{\rm eje} = \dot{M}_*$. An example of such a curve for a rotator inclined by an angle of $\chi = 50°$ is shown in Fig. 3.5. All the characteristic parameters of the NS (B, Ω_0, R_{NS}, M_{NS}) and the angle χ are kept fixed while the mass supply from the companion is varied. For a given value of the external rate of mass supply $\dot{M}_*$, the corresponding points on the curve yield the value (or values) of $\dot{M}_{\rm tot}$ for which there exists a solution. Again, we stress that the "state" of the system, and the characteristics of the solution, are determined by $\dot{M}_{\rm tot}$ since it is this quantity (and not $\dot{M}_*$) which determines the position of R_M. There can be multiple solutions for a given $\dot{M}_*$, and the one that is realized at a certain time depends on the previous history of the system. This situation is reminiscent of a system with hysteresis, and in fact, as Fig. 3.5 shows, the shape of the curve $\dot{M}_{\rm tot}(\dot{M}_*)$ resembles a hysteresis curve, where the role of the external magnetic field is played by the rate of mass supply by the companion, $\dot{M}_*$ (the independent variable in the present context). If at a certain point the system is in, say, the state indicated by the point "C" in the figure, and $\dot{M}_*$ increases, the solution (i.e. only available state for the system) will be forced to jump to the state indicated by point "D". As $\dot{M}_*$ decreases, the solution will move from "D" to "A" but from that point on, any further decrease in $\dot{M}_*$ will cause the solution to jump to point "B". Therefore, like in the traditional hysteresis cycle, continuous variations in $\dot{M}_*$ result in discontinuous states for the system.

In the following section, after discussing the computation of the torque, it will be shown that the points where the solution jumps from one place to another in the $\dot{M}_{\rm tot}(\dot{M}_*)$ curve often straddle the point of torque reversal. Therefore, transitions between different states

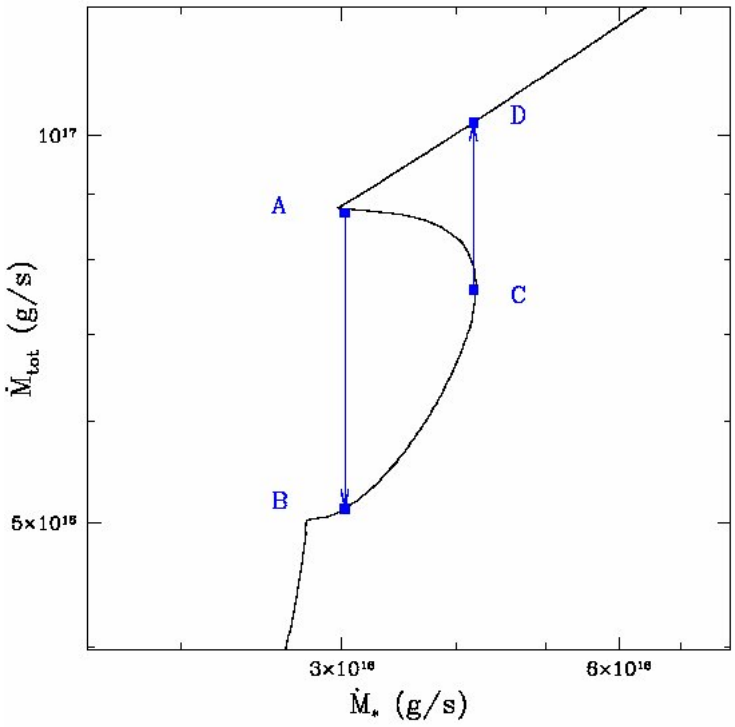

Figure 3.5: Schematic representation of the hysteresis-type limit cycle. The arrows indicate the points where the system "jumps" between different states as a result of variations in the external mass supply rate $\dot{M}_*$. The system parameters in this example are $\nu = 9$ mHz, $B = 6 \times 10^{13}$ G, $\chi = 80°$, $\beta = 0$.

are often characterized by a torque reversal.

The case we have illustrated in Fig. 3.5 is only an example of a cyclic behaviour. The shape of the curve $\dot{M}_{\rm tot}(\dot{M}_*)$ changes with the parameters χ and β (while ν and B only cause a translation in the $\dot{M}_{\rm tot} - \dot{M}_*$ plane). This can result in several types of cycles with a different number of jumps. More examples are shown in Fig. 3.6.

3.1.3 Torque and luminosity in the different states of an oblique rotator

We calculate here the net specific angular momentum trasferred between the disk and the NS. In the region of the magnetospheric boundary where accretion is allowed, the net specific angular moment transferred from the disk to the NS is given by

$$l_{\rm acc} = \frac{1}{2\pi} \int_{R_M < R_{\rm co}} (GMR_M)^{1/2} d\phi \, . \tag{3.12}$$

In the ejection region, the NS accelerates the material to the ejection velocity, which, as discussed in Sect. 3.1, is different in the two limiting cases of a completely elastic or anelastic propeller. For the general case of a partially elastic interaction, using Eq. 3.8,

the angular momentum given by the NS to the ejected matter is:

$$l_{eje} = \frac{1}{2\pi}\int_{R_M>R_{\rm co}} (v_{gen}R_M - \Omega_{\rm K}R_M^2)d\phi = \frac{1}{2\pi}\int_{R_M>R_{\rm co}} \Omega_{\rm K}R_M^2(1+\beta)(\Omega_0/\Omega_{\rm K}-1)d\phi\ . \tag{3.13}$$

By relating this transfer of angular momentum between the NS and the disk to the variation of the NS angular momentum, we have

$$\frac{d\Omega_0}{dt} = \frac{\dot{M}_{\rm tot}l_{\rm tot}}{I} \tag{3.14}$$

where $l_{\rm tot}$ is the sum of the angular momentum computed from Eqs. 3.12 and 3.13, and we have assumed that the variation of the NS moment of inertia (I) is negligible. Using Eqs. 3.12 and 3.13 in 3.14, we obtain:

$$\frac{d\Omega_0}{dt} = \frac{\dot{M}_{\rm tot}}{2\pi}\int_0^{2\pi}(GMR_M)^{1/2}\left\{1-\theta(R_M-R_{\rm co})\left[(1+\beta)(\Omega_0/\Omega_{\rm K}-1)\right]\right\}d\phi \tag{3.15}$$

where $\theta(R_M - R_{\rm co})$ is 1 for $R_M > R_{\rm co}$ and 0 for $R_M < R_{\rm co}$.

Next we compute the different contributions to the luminosity. A schematic representation of these contributions is shown in Fig. 3.8. Let us consider first the region of the magnetosphere in which there is accretion ($R_M(\phi) < R_{\rm co}$). The accretion luminosity is given by the potential and kinetic energy released by matter falling from the magnetospheric radius to the surface of the neutron star; this is

$$L_{\rm acc} = \int_{R_M<R_{\rm co}}\left[GM\left(\frac{1}{R_{NS}}-\frac{1}{R_M}\right)+\frac{1}{2}\Omega^2\left(R_M^2-R_{NS}^2\right)\right]d\dot{M}_{\rm acc}\ , \tag{3.16}$$

where $\dot{M}_{\rm acc}$ is the fraction of $\dot{M}_{\rm tot}$ which accretes. Next we consider the contribution to the luminosity coming from the "recycled matter". This can be calculated by summing the luminosity derived from the release of energy of matter impacting the disk at $R_{\rm K}$, and the luminosity released from the same matter spiralling in the disk from $R_{\rm K}$ back to R_M. This gives

$$L_{\rm rec} = \int_{R_{\rm co}<R_M<R_{\rm inf}}\left(\frac{v_{gen}^2}{2}-\frac{GM}{2R_M}\right)d\dot{M}_{\rm rec} \tag{3.17}$$

where $\dot{M}_{\rm rec}$ is the rate corresponding to the "recycling" part of the magnetospheric boundary ($R_{\rm co} < R_M(\phi) < R_{\rm inf}$).

Another contribution to the total luminosity is provided by the release of energy in the boundary layer which separates the magnetosphere from the Keplerian disk. This term applies to matter at any longitude ϕ if we consider a completely anelastic propeller ($\beta = 0$), because in this case the magnetosphere forces matter to corotate with it during both the accretion and the propeller regime. On the other hand, in the limit of a completely elastic propeller ($\beta = 1$), this term is present only for those angles ϕ for which $R_M < R_{\rm co}$ and matter is thus slowed down in the boundary layer before it can begin falling toward the NS. If we consider a generic value for the elasticity parameter, the luminosity of the boundary layer can be written as:

$$L_{\rm BL} = \begin{cases} \dfrac{\dot{M}_{\rm tot}}{4\pi}\displaystyle\int_0^{2\pi}\left[R_M^2(\Omega_{\rm K}^2-\Omega_0^2)\right]d\phi & \text{for } R_M < R_{\rm co} \\ \dfrac{\dot{M}_{\rm tot}}{4\pi}(1-\beta)\displaystyle\int_0^{2\pi}\left[R_M^2(\Omega_0^2-\Omega_{\rm K}^2)\right]d\phi & \text{for } R_M \geq R_{\rm co}\ . \end{cases} \tag{3.18}$$

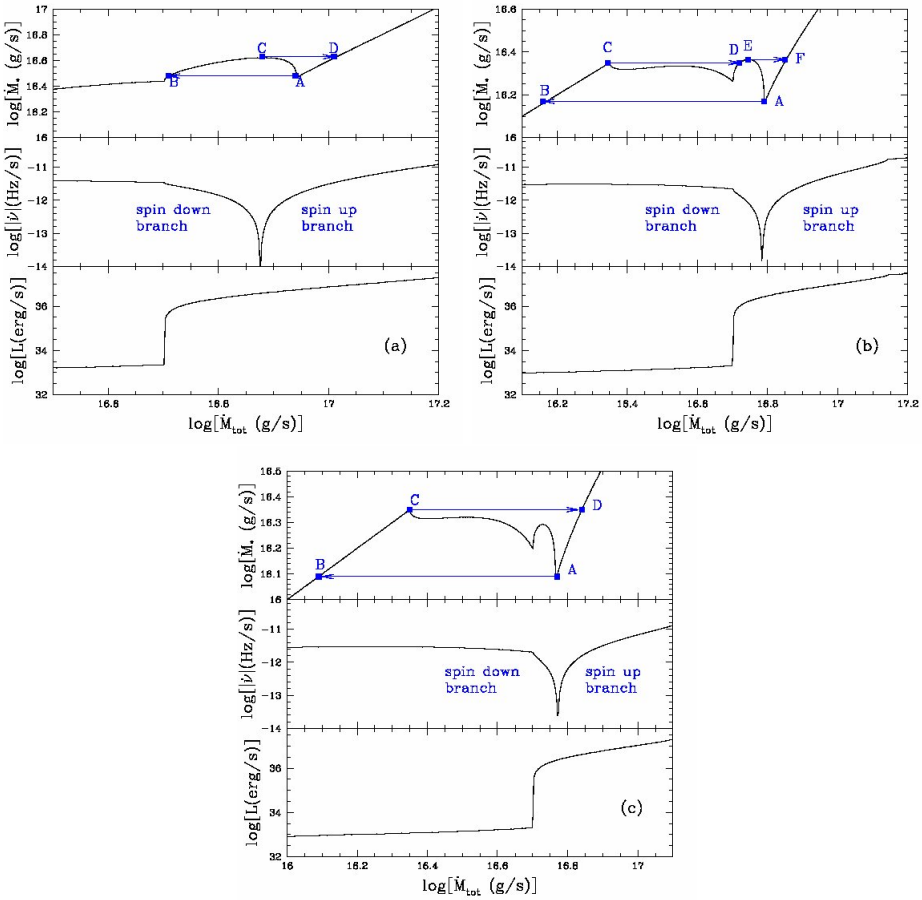

Figure 3.6: Various types of hysteresis limit cycles. The system parameters are $\nu = 9$ mHz, $B = 6 \times 10^{13}$ G and $\beta = 0$ in all cases, while $\chi = 80°$ in panel (a), $\chi = 50°$ in panel (b) and $\chi = 47°$ in panel (c). In the top panels of each case, the arrows indicate the points where the system "jumps" between different states as a result of variations in the external mass supply rate $\dot{M}_*$. The middle panels show that, under most circumstances, a jump is accompanied by a torque reversal and, in some cases, by an abrupt change in luminosity (displayed in the bottom panels).

Finally, we have to account for the luminosity produced by the matter inflowing from the companion as it spirals in towards the magnetospheric radius in the Keplerian disk. This contribution, which is obviously present in all different regimes, is given by

$$L_{\rm disk} = \frac{GM\dot{M}_*}{2R_M} \, . \tag{3.19}$$

It is important to emphasize that in our model both the torque and the luminosity depend on the total mass inflow rate $\dot{M}_{\rm tot}$ at the magnetospheric boundary, and this can take different values for the same mass accretion rate $\dot{M}_*$. The three panels of Fig. 3.6 show the behaviour of the torque and luminosity as a function of $\dot{M}_{\rm tot}$ for three combinations of NS parameters. These are chosen to represent different types of limit cycles (also shown in the figure for each case – note the axes here are swapped with respect to Fig. 3.5 for consistency with the other panels). In Fig. 3.6(a), a transition between the points A and

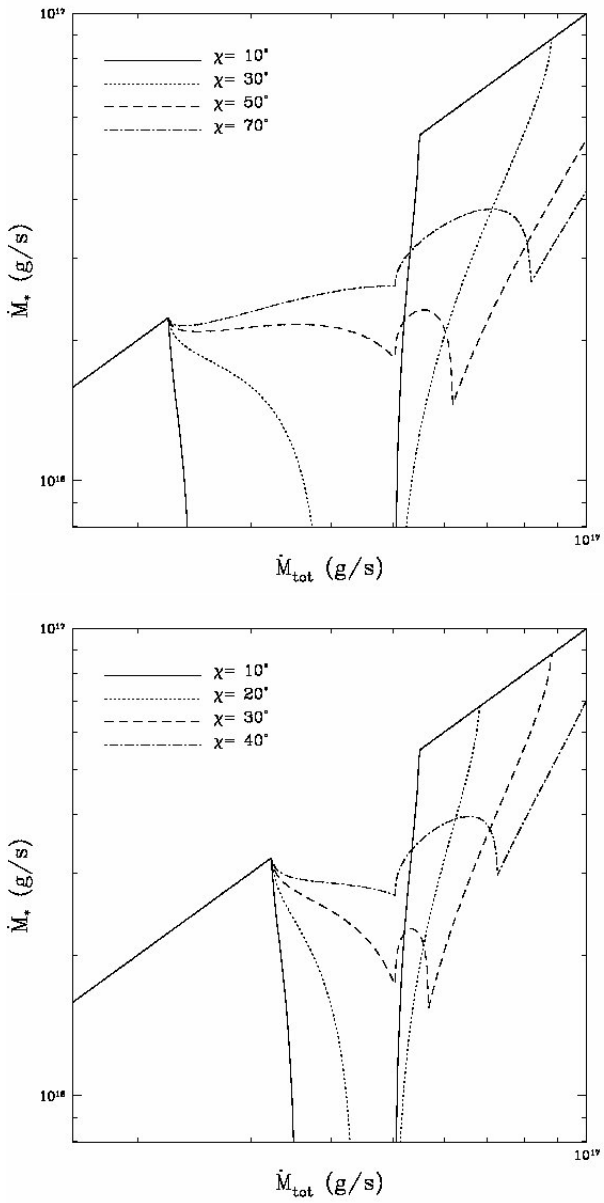

Figure 3.7: The break of the cyclic solution in the $\dot{M}_* - \dot{M}_{\rm tot}$ plane is shown for a system with $\nu = 9$ mHz s, $B = 6 \times 10^{13}$ G, $\beta = 0$ (left panel) and $\beta = 1$ (right panel). When the inclination angle is small, it is no longer possible to find a steady state, cyclic solution. The value of χ around which the solution breaks depends on the anelasticity parameter β but is independent of the values of ν and B.

B is accompanied by a reversal from spin up to spin down, while the jump from point C to D will cause a transition from spin down to spin up. The luminosity is at its lowest at point B and at its highest at point D, but the overall variation during the cycle is well within an order of magnitude. A more complicated cycle is depicted in Fig. 3.6(b); here a transition from point A to B causes a spin-up to spin-down reversal, while the opposite happens during the jump from point E to F. This cycle comprises also another jump, from

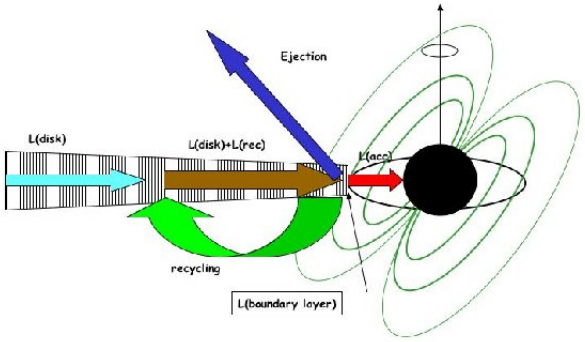

Figure 3.8: The various contributions to the total luminosity budget for an accreting neutron star.

point C to D, with both points on the spin-down branch. The luminosity varies by more than three orders of magnitude during the cycle, being at its lowest during most of the spin down phase. The third example of limit cycle, the one shown in Fig. 3.6(c), has only two allowed jumps, both of them straddling the point of torque reversal, as in case a), but the luminosity is substantially larger when the system is on the spin-up branch (A – D), than when it is on the spin-down branch (B – C).

Whether there exists a limit cycle depends crucially on the angle χ: this has to be large enough to ensure that some regions of the magnetosphere are in the accretion regime while, at the same time, others are in the propeller phase. There exists a critical value of the magnetic colatitude, $\chi_{\rm crit}$, below which the steady state solution breaks into two disjoint curves and it is no longer possible to find a cyclic behaviour through a sequence of steady-state solutions. This is illustrated in Fig. 3.7 for the cases $\beta = 0$ and $\beta = 1$. If the accretion rate $\dot{M}_*$ from the companion is above a certain value (which depends on ν, B, χ and β), only one solution is available to the system, and it corresponds to the spin up branch (see Fig. 3.6). On the other hand, if $\dot{M}_* \leq \dot{M}_{\rm crit}$ (for the example under consideration, $\dot{M}_{\rm crit} = 2.4 \times 10^{16}$ g/s for $\beta = 0$ and $\dot{M}_{\rm crit} = 3.5 \times 10^{16}$ g/s for $\beta = 0$, but it varies with ν and B), then multiple solutions are available for any value of χ displayed, and the one that is realized at any given time depends on the history of the system. However, a cyclic jump of the solutions between the spin-up and the spin-down branches can only be realized for angles above $\chi_{\rm crit}$.

The critical angle ranges from about $25° - 30°$ for $\beta = 1$ to about $40° - 45°$ for $\beta = 0$, and, for a given β, it is independent of ν and B. Therefore, for the curves shown in the figure, a limit cycle can only be achieved in the cases with $\chi = 30°$ and $\chi = 40°$ for $\beta = 1$, and in the cases with $\chi = 50°$ and $\chi = 70°$ for $\beta = 0$. In the other cases displayed, the $\dot{M}_*(\dot{M}_{\rm tot})$ curve is discontinuous. The shape of the curve is such that, if the system is spinning up, a solution on the spin-up branch can be found for any value of $\dot{M}_*$, and therefore the system will continue spinning up. On the other hand, if the system is originally on the spin-down branch (which is possible only for $\dot{M}_* \leq \dot{M}_{\rm crit}$), then any decrease in $\dot{M}_*$ will keep the system on the spin-down branch, while an increase in $\dot{M}_*$ above $\dot{M}_{\rm crit}$ will cause a jump on the spin-up branch, and from that point on the system will be spinning up independent of the value of $\dot{M}_*$. Note that, depending on the angle

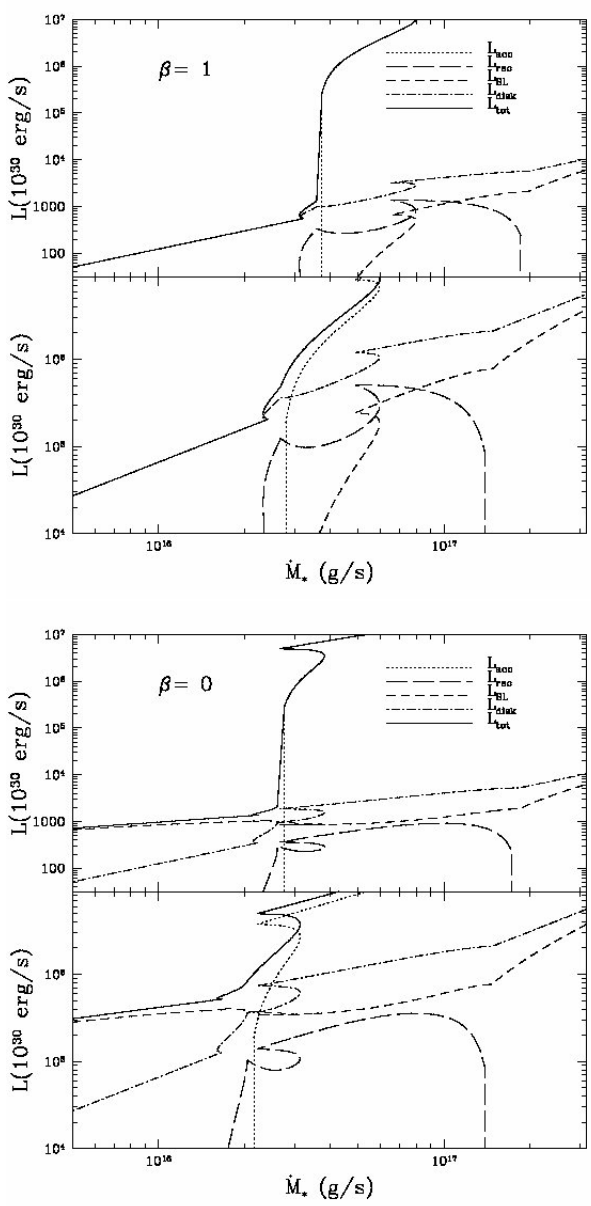

Figure 3.9: The various contributions to the total luminosity budget $L_{\rm tot} = L_{\rm acc} + L_{\rm rec} + L_{\rm disk} + L_{\rm BL}$ for an accreting neutron star as function of the mass accretion rate from the companion, $\dot{M}_*$. The system parameters are $\nu = 9$ mHz, $B = 6 \times 10^{13}$ G, $\chi = 80°$ in the top panels and $\nu = 9$ mHz, $B = 10^9$ G, $\chi = 80°$, in the bottom ones. The two limiting cases of a completely elastic interaction (left panels) and of a completely anelastic interaction (right panels) are shown.

χ, there can be spin-up solutions even at very low mass inflow rates $\dot{M}_*$. This result is a novelty of our model, deriving from the fact that the recycled mass component $\dot{M}_{\rm rec}$ can keep the magnetospheric radius in "pressure" even if $\dot{M}_*$ is very small.

Among all the components that make up the total luminosity, the accretion term is the only that is certainly pulsed, since the accretion material is funnelled by the magnetic

field of the star onto the NS magnetic poles, where its energy is released. The accretion luminosity therefore varies with the phase of the star, resulting in a pulsating flux. Also the boundary layer luminosity might be pulsed at the NS spin. Therefore, the maximum pulsed fraction in our model is constrained to be between $f_{\rm pul} = L_{\rm acc}/L_{\rm tot}$ and $f_{\rm puls} = (L_{\rm acc} + L_{\rm BL})/L_{\rm tot}$.

Note that the sum of the various contributions in Eqs. (3.16), 3.17, 3.18, and 3.19 can result in a complex, non-monotonic dependence of $L_{\rm tot}$ as function of the accretion rate from the companion, $\dot{M}_*$. In the classical model of accretion onto magnetized neutron stars, the transition between the standard accretion regime onto the NS surface to the regime of accretion onto the magnetospheric boundary in the propeller regime is marked by the change between the $\propto \dot{M}_*$ and the $\propto \dot{M}_*^{9/7}$ scaling of the luminosity (Stella *et al.* 1994; Campana & Stella 2000). In the propeller phase, the underlying assumption of these works is that the main contribution to the luminosity derives from the disk luminosity (Eq. 3.19). In the present model, this might not be the case if there is a non-negligible contribution to the luminosity from recycled matter. Moreover, at low accretion rates, we find that the contribution to the luminosity from the boundary layer generally dominates over that from the disk for an anelastic propeller (see Fig. 3.9). For sufficiently low values of $\dot{M}_*$ (so that $\Omega_{\rm K}^2(R_M)/\Omega_0^2 \ll 1$), the boundary layer luminosity scales as $\propto \dot{M}_*^{3/7}$, while $L_{\rm BL} \propto \dot{M}_*^{9/7}$ at high values of $\dot{M}_*$ (for which $\Omega_{\rm K}^2(R_M)/\Omega_0^2 \gg 1$). When the corotation radius is of the order of the magnetospheric radius, however, these dependences are changed. Since the Keplerian frequency at the magnetospheric radius is an increasing function of $\dot{M}_*$, in the propeller regime the term $\left|\Omega_0^2 - \Omega_{\rm K}^2(R_M)\right|$ decreases with the increase of $\dot{M}_*$, while in the accretion regime the same term increases with increasing $\dot{M}_*$. As a result, when R_M is of the order of $R_{\rm co}$, the luminosity of the boundary layer has a flatter dependence on $\dot{M}_*$ for $R_M > R_{\rm co}$ and a steeper dependence for $R_M < R_{\rm co}$. This can be seen in Fig. 3.9. Both the case of a completely anelastic propeller ($\beta = 0$), and a totally elastic one ($\beta = 1$) are considered, showing respectively the maximum and the minimum boundary layer luminosity that the system can have. In the former case we find that, for sufficiently low accretion rates (so that the whole magnetospheric boundary is in the propeller regime), the boundary layer luminosity is substantially larger than the disk luminosity. The relative contribution $L_{\rm BL}/L_{\rm disk}$ clearly increases as the degree of anelasticity increases, since $L_{\rm BL} \propto (1-\beta)$. As the mass accretion rate $\dot{M}_*$ increases, so that at least some regions of the magnetospheric boundary are in the accretion regime, the disk luminosity begins to dominate over that of the boundary layer (this is now independent of β). However, $L_{\rm BL}$ has a stronger dependence on $\dot{M}_*$, and, for sufficiently large $\dot{M}_*$ that $R_M \ll R_{\rm co}$, $L_{\rm BL}$ becomes $\sim L_{\rm disk}$.

The two panels in Fig. 3.9 show the cases of a slow pulsar ($\nu = 9$ mHz) and a fast one ($\nu = 100$ mHz). The discussion above regarding the relative contribution of $L_{\rm BL}$ and $L_{\rm disk}$ to the total luminosity budget holds in both cases. Furthermore, once accretion sets in, the accretion luminosity dominates over both $L_{\rm disk}$ and $L_{\rm BL}$. The slower the pulsar, the larger is this term compared to the others. Therefore, in the accretion regime and for $R_M \ll R_{\rm co}$, $L_{\rm tot} \propto \dot{M}_*$ as in the classical models. However, for $R_M \sim R_{\rm co}$, the presence of the "recycled" term of luminosity in our model causes a non-monotonic dependence of the total luminosity on $\dot{M}_*$, with multiple solutions allowed. The actual solution that is realized at any given time will depend on the history, i.e. whether the system is on the spin-up or spin-down branch of the limit cycle (see Fig. 3.5). This is an important difference of our model with respect to the classical solution where, once the system is in

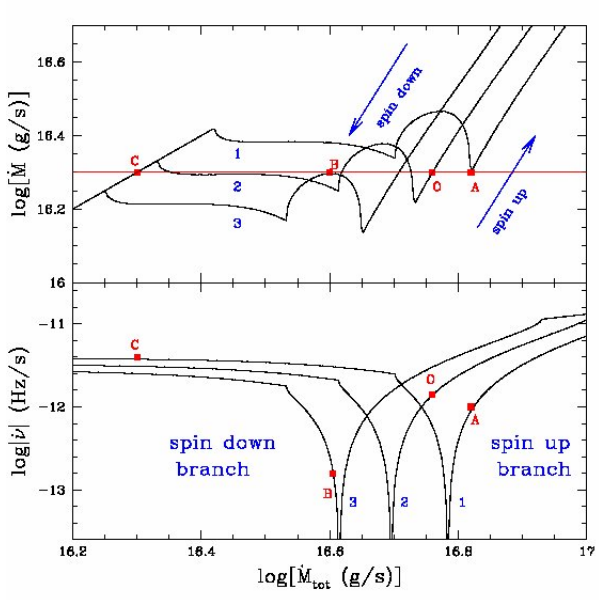

Figure 3.10: Variation of the function $\dot{M}(\dot{M}_{\rm tot}) \equiv \dot{M}_{\rm acc} + \dot{M}_{\rm eje}$ (top panel) and of the corresponding spin rate variation (bottom panel) at three different times during a spin up/spin-down cycle. The system parameters are $B = 6 \times 10^{13}$ G, $\chi = 45°$ and $\beta = 0.3$. The three curves correspond to frequencies $\nu = 9.1$ mHz (curve 1), $\nu = 8.3$ mHz (curve 2) and $\nu = 7.7$ mHz (curve 3). Allowed states for the system are only those satisfying the condition $\dot{M}_* = \dot{M}(\dot{M}_{\rm tot})$; in this case, $\log(\dot{M}_*) = 16.3$. When multiple solutions are allowed, the state in which the system will be found depends on its previous history.

the accreting phase, the luminosity scales monotonically with $\dot{M}_*$. On the other hand, Fig. 3.9 shows that there are regions for which a small variation in $\dot{M}_*$ can cause a large jump in luminosity.

Similar to the luminosity, the behaviour of the torque in the surroundings of the region with $R_M \sim R_{\rm co}$ is complex and non-monotonic. Small variations in $\dot{M}$ can cause the system to jump between states with opposite sign of the torque. Within this region, because of the complex dependence of both L and $\dot{\Omega}$ on $\dot{M}_*$, our model does not make any specific prediction regarding correlations between torque and luminosity. In most situations, these are expected to be uncorrelated, and different types of limit cycles (see Fig. 3.6) will generally lead to different behaviours in the various spin-up and spin-down phases.

3.1.4 Cyclic spin-up/spin-down evolution at a constant $\dot{M}_*$

In systems in which mass transfer takes place through Roche Lobe overflow, the rate at which material is fed to the disk is expected to be roughly constant, or characterized by relatively low-amplitude, long-term variations. We are not concerned in this section with the accretion disk instabilities that likely give rise to the very large amplitude variations of the mass inflow rate in binary X-ray transient systems. Rather, in the following we describe how recurrent episodes of spin up and spin down can be achieved in our model in response to a strictly constant accretion rate $\dot{M}_*$ from the companion star.

Figure 3.10 shows the behaviour of the curve $\dot{M} = \dot{M}_{\rm eje} + \dot{M}_{\rm acc}$ (top panel) and

the corresponding frequency derivative, $\dot{\nu}$, (bottom panel) as a function of $\dot{M}_{\rm tot}$ and for different values of the period (corresponding to different times). The parameters B, χ and β are the same in all cases. They yield a limit cycle of the type described in Fig. 3.6(b). While the specific points of torque reversal will vary depending on the type of cycle (as shown in the various examples of Fig. 3.6), the underlying structure determining the transitions is the same in all cases and therefore we analyze in detail only one of the possible scenarios.

In order to illustrate how the spin up/spin down states are achieved at a constant $\dot{M}_*$, let's start, say, with the system at a frequency ν so that the corresponding $\dot{M}(\dot{M}_{\rm tot})$ curve is the one labeled "2" in Fig. 3.10, and let's assume that the system is in a spin-up state. The intersection between the curves $\dot{M}$ and $\dot{M}_*$ on the spin-up branch of the cuspid determines the value of $\dot{M}_{\rm tot}$, $\dot{M}_{\rm tot,sol}$, corresponding to the allowed spin-up state for that value of the frequency. This value of $\dot{M}_{\rm tot,sol}$ in turn determines the value of the frequency derivative at that point in time (point "O" in both panels of the figure). The frequency at time $t + dt$ is simply determined as $\nu(t + dt) = \nu(t) + d\nu(\dot{M}_{\rm tot,sol})/dt$. As the pulsar spins up, the curve "2" moves towards curve "1" until the point at which the spin-up branch of the solution rises higher than the system $\dot{M}_*$ (point A). From that point on, the only possible state for the system that satisfies the condition $\dot{M} = \dot{M}_*$ is the one corresponding to point C in the figure, on the spin-down branch (negative torque). Once again, the new (current) value of $\dot{M}_{\rm tot,sol}$ determines the actual value of $\dot{\nu}$ (corresponding point C in bottom panel) which is used for the next time step to determine the new ν. While on the spin down branch of the solution, the curve $\dot{M}$ now moves from the curve "1" towards the curve "2" and then "3". Spin down continues until this branch of the solution does not intersect any longer the $\dot{M}_*$ line (point B), at which point the only allowed state for the system to be is on the spin-up branch, and the system reverses from spin down to spin up. This is the beginning of a new cycle.

In this model, the points of spin reversals are determined by the maximum and minimum of the $\dot{M}(\nu)$ curve. The shape of this curve depends on the anelastic parameter β and on the angle χ. For a given β and χ, a change in the strength of the magnetic field simply results in a shift of the curve without a change in shape: a higher B field would move the curve to higher values of $\dot{M}_{\rm tot}$, therefore resulting in stronger spin-up and spin-down torques, and hence in a shorter timescale for torque reversals. For the model to work as described, it is clear that the points where the solution jumps must straddle the point of torque reversal. We find this to be the case for a wide range of combinations of χ and β. However, for each value of β, there is a narrow range of angles χ for which the torque inversion point falls outside the allowed region for the transitions. For these particular and rare cases, the system would tend towards the point $\dot{\Omega}_0 = 0$ and remain there, for a strictly constant $\dot{M}_*$. However, small fluctuations in $\dot{M}_*$ can still cause the system to jump from one solution to another. For the rest of this discussion we will focus on the greatest majority of cases for which torque reversals naturally occur at $\dot{M}_* = {\rm const}$, unless we explicitly state otherwise.

If the magnetic colatitude angle χ is larger than $\chi_{\rm crit}$, the system is bound to end up in a cyclic sequence of spin-up/spin-down transitions. In fact, as it can be seen from Fig. 3.10, if the system starts with a much larger frequency than the maximum frequency in the cycle, $\nu_{\rm max}$, it will spin down since only one solution (on the spin down branch) is allowed as long as $\nu > \nu_{\rm max}$. Similarly, if the system starts with a frequency much smaller than the mimimum frequency in the cycle, $\nu_{\rm min}$, it will spin up as only one solution (on the spin up branch) is allowed as long as $\nu < \nu_{\rm min}$. Therefore, our model predicts that the

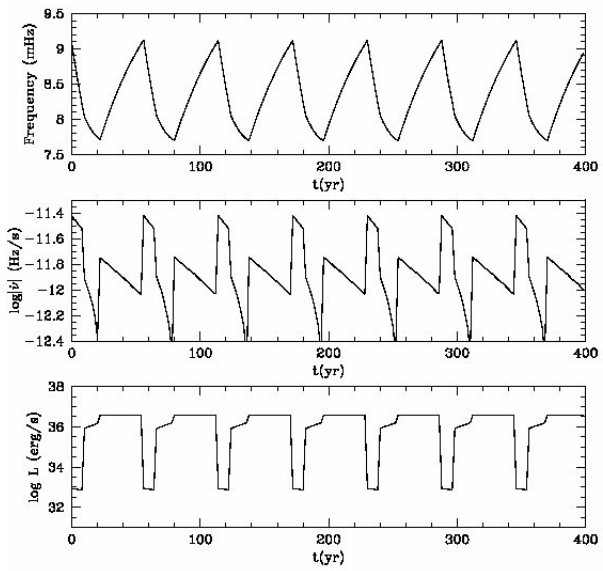

Figure 3.11: An oblique NS rotator with magnetic field $B = 6 \times 10^{13}$ G, inclination angle $\chi = 45$ deg, and elasticity parameter $\beta = 0.3$ is able to reproduce the main spin-up/spin down characteristics of GX 1+4. The luminosity is comparable during the spin-up and spin-down phases, except for a few years at the beginning of the spin-down phase, when it drops abruptly.

system, independent of the initial conditions, eventually settles in a region where there are cyclic transitions between spin-up and spin-down states. This limit cycle is not induced by external perturbations, but is the natural equilibium state torwards which the system tends.

3.2 Application of our model to persistent X-ray pulsars

In the following, we will apply our model to two objects for which long term-monitoring showed a marked transition between a spin-up and spin-down phase. We will then discuss the way our model can be generalized to other cases where short-term episodes of spin-up/spin-down are superimposed onto longer term spin-up or spin-down trends. The most comphrensive monitoring of the spin behaviour of accreting X-ray pulsars in binaries is given in Bildsten *et al.* (1997), and here we briefly summarize the observations for the two cases that we model.

3.2.1 GX 1+4

GX 1+4, discovered in 1970 through an X-ray balloon experiment (Lewin *et al.* 1971) is an accreting X-ray pulsar binary hosting an M red giant (Davidsen *et al.* 1977); the orbital period is likely to be of a few years (Chakrabarty & Roche 1997). Early observations through the 1970s showed that this source was spinning up at a very high pace with a spin-up timescale $|\nu/\dot{\nu}| \sim 40$ yr. The frequency changed from ~ 7.5 mHz to ~ 9 mHz during the first 15 years of observations. In the early 1980s, however, the flux dropped abruptly and the source could not be detected by *Ginga*. Given the sensitivity of the

instrument, the flux must have decresead by more than two orders of magnitudes for a few years. Once its flux raised, the source could be monitored again, and it was found to spin down on a timescale comparable to the previous spin-up timescale (Makishima *et al.* 1988).

A solution that closely reproduces the observed source behaviour was found by running the time-dependent code described in Sect. 2.4 for a range of parameters B, χ, β. The corresponding value of M_* is determined so that the point of torque reversal of the system between spin up and spin down matches the observed value. The larger the magnetic field, the larger $\dot{M}_*$ and hence the torque, and therefore the more rapid the timescales of the torque transitions are; the parameters χ and β, by determining the shape of the $\dot{M}$ curve, especially influence the total frequency range $\nu_{\max} - \nu_{\min}$ that the system spans in a cycle.

For the case of GX 1+4, we found that a good choice of parameters is the combination $B = 6 \times 10^{13}$ G, $\chi = 45°$, and $\beta = 0.3$. These yield a cycle of the type displayed in panel (b) of Fig. 3.6 and in Fig. 3.10. In particular, the parameters B, χ and β used in Fig. 3.10 are the same as those used for GX 1+4. The accretion rate provided by the donor companion must be $\dot{M}_* \sim 2 \times 10^{16}$ g/s in order to produce a turnover in frequency around 9 mHz. With this choice of parameters, Fig. 3.11 shows the behaviour of the system that our model predicts. Cycles of spin-up/spin-down alternate in response to torque reversals. The luminosity of the source is comparable during the spin-up and spin-down phases, except for a few years around the time of spin reversal from spin up to spin down, when it drops abruptly. This is due to the fact that, after the system has "jumped" to point "C" in Fig. 3.10 (at the beginning of the spin down phase), there are no regions in the magnetosphere-disk boundary where accretion onto the NS can take place, the NS is in the propeller regime, and therefore $\dot{M}_{\rm acc} = 0$ (see Fig. 3.4). During that time, the only contribution to the luminosity comes from the disk and the boundary layer, which are however much smaller than the accretion luminosity (since this is a slow pulsar). A prediction of our model is that, while large drops in luminosity can be expected when the system reverses from spin up to spin down, they should not occur in correspondence of the spin-down/spin-up transition, because when this transition occurs (refer to the jump from point "B" to point "A" in Fig. 3.10), most regions at the magnetospheric boundary are allowed to accrete. While these overall features are generally robust predictions of our model, the detailed variation of $\dot{M}$ (and hence the luminosity) with torque shown in our examples should not be taken too rigorously. These variations depend on the shape of the $\dot{M}(\dot{M}_{\rm tot})$ curve, and this is in turn determined by the shape of the magnetospheric boundary as a function of time. As discussed in Sect. 3.3, a number of effects neglected here can influence this shape, and hence affect the detailed behaviour of the solution. In particular, note that observations of GX 1+4 show that luminosity and torque strength are correlated during part of the spin down phase (Chakrabarty *et al.* 1997b). This feature is not reproduced by the current version of our model.

3.2.2 4U 1626-67

4U 1626-67, discovered by SAS-3 in 1977 (Rappaport *et al.* 1977) is an ultracompact binary with an extremely low-mass companion (Chakrabarty *et al.* 1997a) and a 42 minute orbital period (Middleditch *et al.* 1981). During the first $\sim$ 20 years of observations, the source was found to spin up with a timescale $\nu/\dot{\nu}$ of about 5000 yr. The frequency increased from 130.2 mHz to about 130.5 mHz, at which point the source started to spin down. Unlike the case of GX 1+4, there was no evidence for a large change in the bolometric luminosity

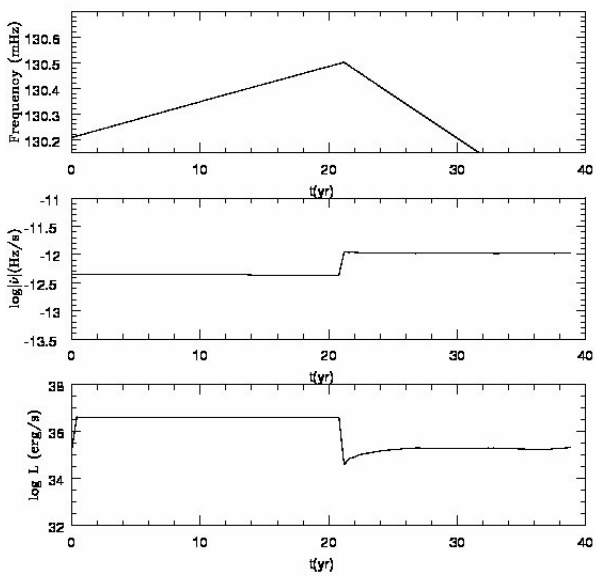

Figure 3.12: An oblique NS rotator with magnetic field $B = 2.5 \times 10^{12}$ G, inclination angle $\chi = 68°$, and elasticity parameter $\beta = 0$ is able to reproduce the main spin-up/spin down characteristics of 4U 1626.

of the source during the transition.

The very long timescale for spin reversal of this source (due to a smaller torque compared to the case of GX 1+4) requires a smaller magnetic field. We found that our model yields a reasonable match to the observations with the choice of parameters $B = 2.5 \times 10^{12}$ G, $\chi = 68°$, $\beta = 0$. The corresponding solution found with our model is displayed in Fig. 3.12. The upper panel shows only one spin-up/spin-down torque reversal, since the complete spin-up/spin-down cycle, of the order of several thousand years, lasts much longer than the observed time. Although the luminosity somewhat drops around the time of spin reversal, it does so to a lesser extent and for a much shorter time than for the case of GX 1+4. The reason for these differences lies in the variation of the shape of the function $\dot{M}(\dot{M}_{\rm tot})$ for different choices of the parameters χ and β. The parameters that best match the solution for 4U 1626-67 yield a cycle of the type in panel (a) of Fig. 3.6. The transition from spin up to spin down (point A to B in the figure) is accompanied by a less dramatic variation in luminosity than it is for the cycles of the type shown in panels (b) and (c). Note how, for this source, since the observation window is much smaller than the timescale for torque reversal, other torque inversions are not expected in the near future, unless induced by external perturbations.

3.2.3 Generalizations and limitations of our model

The two examples given above, for two sources spinning up and down at very different rates, show that our model can reproduce different types of cyclic behaviours. In the two cases discussed, we assumed that the mass accretion rate from the companion, $\dot{M}_*$, does not vary with time. Under this assumption, our model predicts that the points of torque reversals will always occur at the same value of the frequency. On the other hand, if the donor accretion rate varies with time, this will no longer be the case. If $\dot{M}_*$ increases

with time, then the points of torque reversals will occur at larger frequencies as time goes on. Viceversa if $\dot{M}_*$ decreases with time, then the points of torque reversals will occur at smaller and smaller frequencies with time. A combination of discrete states in an oblique rotator (producing cyclic torque reversals), with longer-term variation in the external $\dot{M}_*$ can produce a long-term spin evolution with superimposed shorter cyclic episodes of spin up and spin down.

Also note that, depending on the system parameters (namely the inclination angle χ and the elasticity parameter β, which determine the shape of the $\dot{M}(\dot{M}_{\rm tot})$ curve, and hence the points of torque reversals), the transition from a state of spin up to a state of spin down can result in a period of time during which accretion is completely inhibited (i.e. $\dot{M}_{\rm acc} = 0$) and the luminosity is orders of magnitude lower (unless the pulsar has a very fast spin in the ms range and the luminosity of the disk and the boundary layer are conspicuous even when $\dot{M}_{\rm acc} = 0$). The system can then behave as a "transient" even when the accretion rate from the companion is constant.

In the present (simplest) version of our model, the frequency range $(\nu_{\rm max} - \nu_{\rm min})$ spanned in a spin-up/down cycle cannot however be made arbitrarily small. In order for the torque reversals to occur at constant $\dot{M}_*$ and without any other external perturbation, the curves $\dot{M}(\nu_{\rm max})$ and $\dot{M}(\nu_{\rm min})$ (curves 1 and 3 respectively in Fig. 3.10) must be such that the two points of torque reversals (A and B in Fig. 3.10) satisfy the conditions $\dot{M}_{\rm A}(\nu_{\rm max}) = \dot{M}_*$ and $\dot{M}_{\rm B}(\nu_{\rm min}) = \dot{M}_*$ respectively. Arbitrarily small cycles require arbitrarily small loops in the $\dot{M}(\dot{M}_{\rm tot})$ curve, so that the inversion points can be extremely close. This cannot be achieved with the current version of our model, in which the shape of the $\dot{M}(\dot{M}_{\rm tot})$ curve (and hence the "size" of the loop around the points of torque reversals) depends only on the inclination angle χ and the elasticity parameter β. However, there are a number of effects that we have neglected here, and which could be potentially important for small-scale torque reversals. In particular, if the disk plane is not orthogonal to the NS rotation axis, a precession of the disk around the spin axis can be induced (Lai 1999), producing a time-dependent modulation of the various regimes on a time scale on the order of the spin period of the star. We reserve to future work a more comprehensive exploration of the physical effects that influence the magnitude and frequency of the torque reversals.

3.3 Summary and Discussion

A magnetic rotating neutron star surrounded by an accretion disk is an intuitive example of an accreting system in which the conditions can be realized such that a fraction of the matter is accreted, another fraction is ejected and completely unbound from the system, and another part is propelled out but does not possess enough energy to unbind, and therefore falls back onto the disk, getting "recycled". We have shown that, for a given mass rate supply from the companion, accretion with the mass feedback term included leads to multiple available states for the system, characterized by different (and discrete) values of the total mass inflow at the magnetospheric boundary. The luminosity in each of these states is generally different, as it depends on the relative amounts of the various components of the total mass inflow rate. The available states often straddle the point of torque reversal, and therefore correspond to states with opposite sign of the torque.

The character of the solutions is essentially determined by the inclination angle χ of the NS axis with respect to the disk. At angles $\chi \leq \chi_{\rm crit}$, the limit cycle breaks down. In this case, for an external mass supply larger than a critical value (which depends on the system

parameters), the system can only be on the spin up branch. For accretion rates smaller than this critical value, both the spin up and the spin down branches of the solution are possible, and the one that is realized will depend on the history of the system. After a sufficiently long time, however, if the system is spinning down, the available solutions will be drifting and the source will jump out of the spin-down branch, and continue evolving on the spin-up branch. For $\chi \geq \chi_{\rm crit}$, cyclic transitions between states of opposite torque can be realized even at a constant value of the accretion rate from the companion. This is a particularly nice feature of our model: *periodic variations between spin up and spin down states take place without requiring the presence of any external, periodic, and fine-tuned perturbation.* Most importantly, we have shown that periodic, cyclic episodes of spin up/spin down behaviour *must* be realized in a number of situations. While in the classical theory of accreting X-ray binaries (where the effect of mass feedback is not accounted for) the system is expected to eventually settle at the equilibrium frequency which matches the Keplerian frequency at the magnetospheric boundary, in our model, where recycling is accounted for, the system will eventually settle around a limit-cycle behaviour in which different spin derivative and luminosity states alternate, recurrently. The points of spin reversal and the timescales of the torque reversals depend on a combination of factors, namely the accretion rate from the companion, the magnetic field of the NS, the inclination angle of the NS axis, and the degree of anelasticity at the disk-magnetospheric boundary.

In the case of the two X-ray binaries GX 1+4 and 4U 1626-67, we have determined a set of parameters B, χ, β which is able to reproduce the main features of their timing behaviours, such as the timescales and frequency span of the transitions, as well as the large luminosity drop observed around the transition spin up-down in the case of GX 1+4 but not of 4U 1626-67. The correlation between torque strength and luminosity in the spin down phase observed in GX 1+4 (Chakrabarty *et al.* 1997b) is however not reproduced by the present scenario. On the other hand, we still need to emphasize that ours is a very simplified model and therefore the detailed behaviour of our solution should not be considered too rigorously: while our model appropriately accounts for the material torque at the disk-magnetospheric boundary when a fraction of mass is recycled, it neglects other possible sources of torque, such as magnetic stresses (e.g. GL) or magnetically driven outflows in an extended boundary layer (Arons *et al.* 1984; Lovelace *et al.* 1995). The presence of other torque terms could modify the character of the solutions if non-material torques dominate over the material one. A general treatment that includes all possible sources of torques is beyond the scope of the present calculations, especially since the relative strength of the various terms would be hard to estimate from first principles.

Finally, while the details of the solutions that we have discussed specifically apply to the case of a rotating neutron star accreting from a disk fueled by a companion star, the general feature of a multeplicity of states available for a given mass inflow rate of matter can probably be generalized to other accreting systems in which "recycling" occurs. An example is that of an accretion disk around a rotating black hole. Numerical simulations (e.g. Krolik *et al.* 2005) show that, while a fraction of the accreting mass is ejected through a jet, another fraction, of slower velocity and at larger angles from the jet axis, falls back into the disk, getting recycled. It would be interesting to include this mass feedback process into numerical simulations of accretion disks around black holes, and investigate whether the discountinuos states and cyclic behaviour might ensue in those cases as well.

Appendix

3.4 The KHI

Here we justify our assumption that, during the rotation of the magnetosphere, matter in the disk is able to fill the region that separates the disk and the magnetospheric flow on a timescale shorter than (or comparable to) the spin period of the star.

Let $\tau_\nu = R^2/\nu = R/v_R$ be the viscous timescale in the disk, where R is the radial distance from the star, ν the kinematic viscosity coefficient and v_R the radial velocity in the disk. In the reference frame of the disk (in which τ_ν is measured), the stellar rotation time is $\tau_{\rm rot} = 2\pi/|\Omega_0 - \Omega_{\rm K}|$. Using the thin disk approximation, the disk height H can be written as $H = fR$, where $f << 1$ is a numerical factor that can be assumed approssimatively costant for small variations of the radial distance from the NS (typically $f \sim 1/10$). Furthermore, using the α prescription for the viscosity (Shakura & Sunyaev 1973), we can write $v_R = \alpha v_s^2/v_{\rm K} = \alpha f^2 v_{\rm K}$ where v_s is the sound speed in the disk and we have assumed $v_s/v_{\rm K} \simeq H/R$.

Let us consider first the propeller regime ($R_M > R_{\rm co}$). For $R = R_M$, we obtain that $\tau_\nu < \tau_{\rm rot}$ only if

$$R_{\rm co} < R_M < (1 + 2\pi\alpha f^2)^{2/3} R_{\rm co} \tag{3.20}$$

which corresponds to a very narrow region around the corotation radius. Beyond this region, the viscous timescale becomes too long to permit a replenishment of the inner regions of the disk as the star rotates. Here another mechanism is needed to justify our assumption. Indeed, in the propeller regime, the surface of separation between the magnetospheric and disk flow is Kelvin-Helmholtz (KHI) unstable due to the large shear velocity (Wang & Robertson 1985; Spruit & Taam 1993). In the frame corotating with the NS this velocity is $v_{\rm rel} = R_M[\Omega_* - \Omega_{\rm K}(R_M)]$. Because of the KHI, matter in the disk is mixed with the NS magnetic field lines, thus mantaining a strong interaction between the disk and the magnetosphere.

The characteristic timescale for the development of the KHI (in the direction of the shear motion) can be estimated as (e.g. Stella & Rosner 1984) $\tau_{KH} \approx 4\pi(k|v_{\rm rel}|)^{-1}$, where $k = 2\pi/\lambda$ is the wave vector of the perturbation which inizializes the instability. The condition that the KHI develops within a time shorter than the local timescale $\tau_{\rm rot}/2$ is hence satisfied for wave vectors $k > 2/R$. Furthermore, in order for the interaction between the disk and the magnetospheric flow to be maintained throughout the rotation of the star, the KHI must be able to mix disk matter and magnetic field lines at least on a distance $d \sim [R_M(0) - R_M(\pi/2)] \leq 0.5 R_M(0)$ (see Eq. 3.3 and Fig. 3.3). The simulations of Wang & Robertson (1985) show that perturbations of lengthscale λ become rapidly unstable and evolve into elongated vortices of magnitude comparable to λ. This means that a perturbation of length λ is able to produce mixing between matter and field lines on a distance scale of the same order. Wang & Robertson also argue that the dominant mode of the instability will likely be the one just sufficient to offset the effect of viscous damping through the turbulent motions in the shear layer. In our case this condition traslates into $\lambda/2\pi v_t \sim (\Omega_* - \Omega_{\rm K})^{-1}$ where v_t is the turbulent velocity. If we choose $v_t \sim v_s$ and use $f \sim H/R$, we can roughly estimate

$$\lambda \sim \frac{2\pi f}{(\frac{R_M}{R_{\rm co}})^{3/2} - 1} R_M \ , \tag{3.21}$$

that is of the order required to cover the radial extension d discussed above (here we have used the fact that in our model the propeller regime typically occurs for R_M within the range $R_{\rm co} < R_M < (1.6 - 1.7)R_{\rm co}$). Since the wavelength in Eq(3.21) satisfies the condition $k > 2/R_M$, the dominant mode of instability develops in a shorter time than the local dynamical timescale, and therefore the KHI is able to maintain a close interaction between the disk and the magnetosphere on this timescale.

Let us now consider the accretion regime ($R_M < R_{\rm co}$). Using the same derivation as above, the analogous of Eq.(3.20) is

$$(1 - 2\pi\alpha f^2)^{2/3} R_{\rm co} < R_M < R_{\rm co} \tag{3.22}$$

which is again a narrow region in the vicinity of the corotation radius. In the accretion regime however, considering the argument used in the propeller case (where now $v_{\rm rel} = R_M(\Omega_{\rm K} - \Omega_0)$), we obtain the same conclusion about the efficiency of the KHI, and the analogous of equation 3.21 is now

$$\lambda \sim \frac{2\pi f}{(1 - \frac{R_M}{R_{\rm co}})^{3/2}} R_M \ , \tag{3.23}$$

which clearly satisfies the requirement $\lambda \gtrsim 0.5 R_M$ for any value of R_M in the region of interest. Furthermore, after the KHI has brought matter just inside the magnetospheric radius, the enhanced contribution of the gravitational with respect to the centrifugal force, forces matter to fall toward the NS also under the effect of the Rayleigh-Taylor instability (Arons & Lea 1980; Wang & Robertson 1984). This enhances the transport of matter toward the NS and therefore strengthens the reliability of our assumption.

Chapter 4

The propeller effect: a calculation of the maximum efficiency of the mass-ejection mechanism

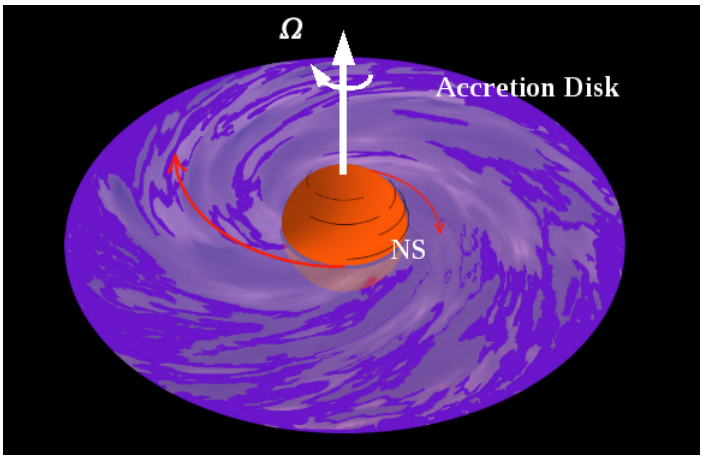

Figure 4.1: The propeller effect: matter in the accretion disk is trown away from the system, instead of being accreted, due to the rapid rotating neutron star magnetosphere.

In this Chapter we concentrate on the study of the propeller effect, that has been introduced in Sect. 1.2.3 and briefly discussed in Chapter 3. Here we use simple arguments to derive an upper limit on the efficiency with which the propeller mechanism is able to eject matter inflowing toward an accreting NS. This calculation is particularly relevant for the formation of millisecond pulsars (MSP), i.e. the typical endpoint of the evolution of NSs in LMXBs (see Sect. 1.1).

MSPs are indeed rapidly spinning NSs with weak surface magnetic field ($\sim 10^8 - 10^9$ G), which are believed to be spun-up to millisecond periods by the accretion of mass and angular momentum from matter in a disk formed through RLO of a low-mass companion star (see Sect. 1.1). After the accretion phase has ended, the NS may turn on as a radio MSP. In recent years, the prediction that LMXB host NSs with spin periods in the ms range has been confirmed through the discovery of 300 – 600 Hz nearly-coherent oscillations during type I X-ray bursts from some 10 LMXBs of the Atoll class (e.g., Strohmayer *et al.*

1997). This was followed by the detection of coherent X-ray pulsations in the persistent emission of seven low luminosity transients of the same class. The spin frequencies lie between 180 and 600 Hz and the orbital periods between 40 min and 5 hr (Wijnands 2005). For the first time, the predicted decrease of the NS spin period during accretion was measured in the accreting MSP IGR J00291+5934 (Falanga *et al.* 2005; Burderi *et al.* 2007). This provided a strong confirmation of the theory of 'recycled' pulsars in which the old NS in LMXBs become millisecond radio pulsars through spin-up by transfer of angular momentum by the accreting material.

All accreting MSPs are X-ray transient systems (see Sect. 1.1). They spend most of the time in a quiescent phase, with X-ray luminosities of the order of $10^{31} - 10^{32}$ erg s^{-1}, and occasionally show weeks to months long outbursts, reaching X-ray luminosities of $10^{36} - 10^{37}$ erg s^{-1}, during which coherent X-ray pulsations are observed. The magnetic fields inferred for these NS are of order $10^8 - 10^9$ G (e.g., Campana *et al.* 1998; Psaltis & Chakrabarty 1999; Di Salvo & Burderi 2003). These findings added a great deal of confidence in the likely connection between accreting NS and millisecond radio pulsars.

Models for the evolution of LMXBs as progenitors of radio MSPs still involve significant assumptions about the transfer of mass from one star to the other and the role of dynamically influential NS magnetic fields (Podsiadlowski *et al.* 2002). The MSP formation depends on the amount of matter accreted from the companion which, in turn, is likely limited by mass ejection from the binary. Cook *et al.* (1994), following a full GR treatment, show that a NS of 1.4 $M_\odot$ has to accrete $\sim 0.2 - 0.5$ $M_\odot$ to reach periods in the range 0.6–1.5 ms (see also e.g., Burderi *et al.* 1999). Most donor stars in systems hosting recycled radio pulsars must have lost most of their mass during their evolution. They now appear as white or brown dwarfs of mass $\sim 0.15 - 0.30$ $M_\odot$ (Taam *et al.* 2000), the progenitors of which were likely stars of $\sim 1.0 - 2.0$ $M_\odot$ (e.g., Burderi *et al.* 1996; Tauris & Savonije 1999). Hence, a crucial issue for evolutionary models for MSPs is which fraction of mass lost by the companion ($M_{\rm lost} \sim 0.7 - 1.8$ $M_\odot$) effectively accretes onto the NS. Mass ejection must be efficient, at least in some cases, to avoid that accretion of a large amount of mass onto the NS could induce collapse to a black hole. For most equations of state of ultra-dense matter, this is expected to occur for NS masses above ~ 2 $M_\odot$ (Cook *et al.* 1994). Different models have been proposed to explain how mass can be ejected from binary system, thus limiting the amount of matter that is accreted by the NS to about 0.2–0.4 $M_\odot$ (Illarionov & Sunyaev 1975; Wang & Robertson 1985; Romanova *et al.* 2005; Ustyugova *et al.* 2006).

4.1 Ejector-Propeller efficiency

Matter transferred from the companion star via Roche-Lobe overflow possesses enough specific angular momentum that an accretion disk forms around the accreting NS. The disk is truncated at the magnetospheric radius, $R_{\rm M}$. Different calculations, carried out by adopting different models and/or assumptions, produce only slightly different estimates of the value of $R_{\rm M}$ (a factor of 2–3 at the most, see Chapter 2).

The value of $R_{\rm M}$ as a function of the system parameters is only of marginal relevance to the present calculations. Therefore we consider here the value inferred from simple theory (see e.g., Eq. (4) of Lamb & Pethick 1974); that is

$$R_{\rm M} = 3.2 \times 10^8 M_1^{-1/7} \mu_{30}^{4/7} \dot{M}_{17}^{-2/7} \ {\rm cm}, \tag{4.1}$$

where M_1 is the NS mass in units of 1 $M_\odot$, μ_{30} is the NS magnetic dipole moment in units of 10^{30} G cm^3, and $\dot{M}_{17}$ is the mass accretion rate in units of 10^{17} g s^{-1}.

Disk accretion onto a spinning, magnetic NS is expected to be centrifugally inhibited, once the magnetospheric radius is larger than the corotation radius (see Eq. 1.24) and inside the light cylinder radius, $R_{\rm lc}$ (Illarionov & Sunyaev 1975). The latter is the radius at which the corotating magnetic field lines reach the speed of light c, $R_{\rm lc} = c/\Omega_0$. Outside $R_{\rm lc}$ the magnetic field lines cannot corotate any longer and a radiative electromagnetic field must be generated. If an element of matter $dM_{\rm in}$ is accreted onto a NS from a Keplerian disk, part of its energy is stored as rotational energy of the NS; this can later be used to eject a mass $dM_{\rm out}$. We define the propeller efficiency as the ratio of the ejected to accreted matter $\eta_{\rm pro} \equiv dM_{\rm out}/dM_{\rm in}$. Moreover we assume that only the rotational energy gained by the star during the previous accretion phase can be used to eject matter in the propeller phase.

In order to determine the rotational energy gained by the NS we first consider the accretion phase. During accretion the rate of rotational energy transferred to the NS can be written in terms of the transfer of angular momentum, L, at the inner boundary of the disk:

$$\dot{E}_{rot} = \Omega_0 \dot{L} - \frac{1}{2}\Omega_0^2 \dot{I}, \tag{4.2}$$

where $\dot{L} = I\dot{\Omega}_0 + \Omega_0 \dot{I} = \dot{M} l$. Here $I = \beta^{-1} M R_{\rm NS}^2$ is the moment of inertia of the NS, and l is the specific angular momentum of the accreted mass. For NS models with mass above an initial value of M ~ 1.4 $M_\odot$ (Weaver *et al.* 1978) and well below the maximum mass, values of β are expected in the 2.3–3.1 range for a variety of equations of state. In our calculations we use $\beta = 2.5$, the value for a uniform Newtonian star. For a disk truncated at the magnetospheric radius, $R_{\rm M}$, we approximate the specific angular momentum transferred to the NS with the Keplerian value at $R_{\rm M}$, i.e. $l \simeq l_{\rm M} = (GMR_{\rm M})^{1/2}$. According to detailed models of the disk-magnetosphere interaction this approximation is accurate in the limit in which $R_{\rm M} \ll R_{\rm co}$, whereas it provides an upper limit in the case in which $R_{\rm M} \simeq R_{\rm co}$ and non-material (spin-down) torques due to the interaction of the NS magnetic field with disk regions outside $R_{\rm co}$, become important (see Chapter 2). Since our aim here is to derive an upper limit on the propeller efficiency, we can safely adopt the Keplerian value of the specific angular momentum. Equation (4.2) thus writes

$$dE_{\rm rot} = \Omega_0 (GMR_{\rm M})^{1/2} dM_{\rm in} - \frac{1}{2}\beta^{-1} R_{\rm NS}^2 \Omega_0^2 dM_{\rm in}, \tag{4.3}$$

which describes the amount of energy accreted from a disk ending at the magnetospheric radius. For a given angular velocity of the NS, the rotational energy, $dE_{\rm rot}$, is highest when the magnetospheric radius, $R_{\rm M}$, takes the largest value, compatible with accretion onto the NS surface: that is at $R_{\rm M} = R_{\rm co}$. Setting $R_{\rm M} = R_{\rm co}$ Eq. (4.3) gives

$$dE_{\rm rot} = \frac{GM}{R_{\rm co}} dM_{\rm in} - \frac{1}{2}\beta^{-1} R_{\rm NS}^2 \Omega_0^2 dM_{\rm in}. \tag{4.4}$$

This is the maximum increase in $E_{\rm rot}$ that an element of disk-accreting mass $dM_{\rm in}$ can cause.

We now consider the propeller phase. According to the virial theorem, the energy required to eject a disk mass element, $dM_{\rm out}$, from a radius R to infinity, is $dE_{\rm eje} = GMdM_{\rm out}/2R$. In order to estimate the maximum possible propeller efficiency we suppose that ejection takes place from the largest possible radius at which the propeller can work, such that the energy required to eject is minimized. That is $R = R_{\rm lc}$.

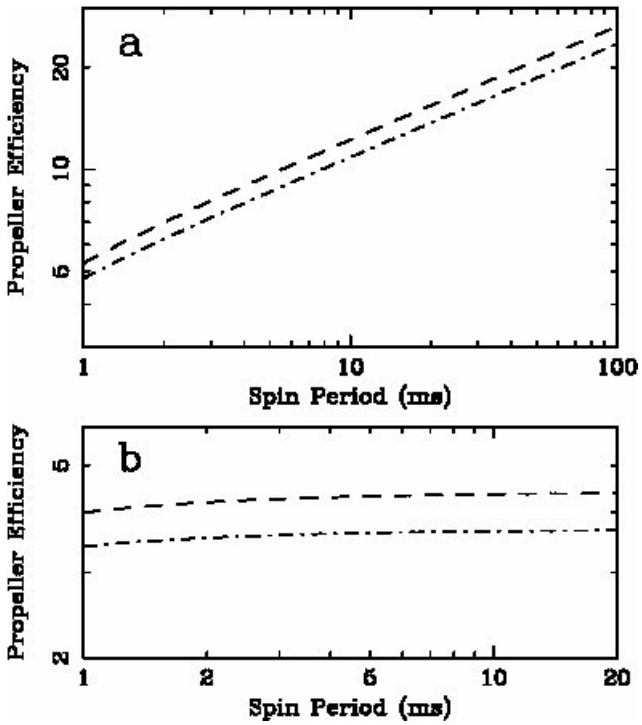

Figure 4.2: The highest possible propeller efficiency, $\eta_{\rm pro}$, the ratio of the ejected mass to the accreted mass, versus spin period. The dashed and dot-dashed lines correspond to Eq. (4.5) (panel a) and Eq. (4.7) (panel b), for a NS of 1.4 $M_\odot$ and 2.0 $M_\odot$, respectively.

.

Setting $dE_{\rm rot} = dE_{\rm eje}$ and assuming that ejection takes place at $R_{\rm lc}$, we have for the maximum efficiency of the propeller:

$$\eta_{\rm pro} \leq 6.37\Big(\frac{M}{\rm M_\odot}\Big)^{-1/3}(P_{-3})^{1/3} - 0.57\Big(\frac{M}{\rm M_\odot}\Big)^{-1}(P_{-3})^{-1} \tag{4.5}$$

where we used $R_{\rm NS} = 10$ km.

An alternative possibility is that there is no magnetosphere in the accretion phase, and the disk extends all the way to the NS surface (such that we set formally $R_{\rm M} \simeq R_{\rm NS}$, where $R_{\rm NS}$ is the NS radius). This might be the case in LMXBs which do not display coherent pulsations in their persistent X-ray flux. In this case

$$\eta_{\rm pro} = \frac{\Omega_0 (GMR_{\rm NS})^{1/2}}{GM/2R_{\rm lc}} - \frac{\beta^{-1}R_{\rm NS}^2\Omega_0^2}{GM/R_{\rm lc}} = 2\Big(\frac{R_{\rm NS}}{R_{\rm g}}\Big)^{1/2} - \frac{c\beta^{-1}}{GM}R_{\rm NS}^2\Omega_0 \ , \tag{4.6}$$

with $R_{\rm g} = GM/c^2 = 1.48 \times 10^5 (M/{\rm M_\odot})$ cm the gravitational radius.

For a typical NS, $R_{\rm NS} \simeq 6R_{\rm g}$, one has

$$\eta_{\rm pro} \leq 5.20\Big(\frac{\rm M}{M_\odot}\Big)^{-1/2} - 0.57\Big(\frac{\rm M}{M_\odot}\Big)^{-1}(P_{-3})^{-1} \tag{4.7}$$

a result that is similar to that in Eq. (4.5).

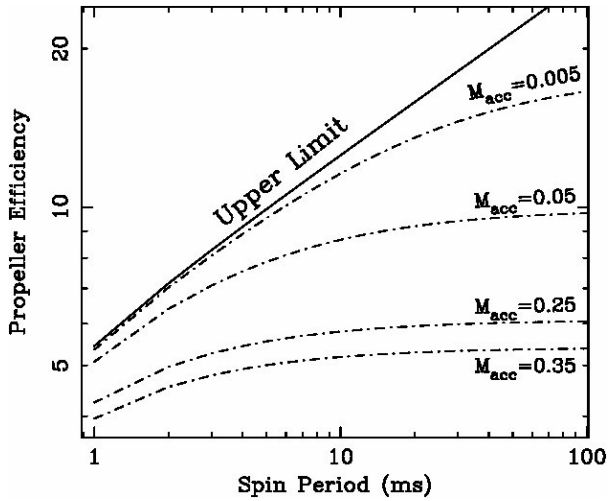

Figure 4.3: The highest possible propeller efficiency, $\eta_{\rm pro}$, versus spin period for different amounts of mass accreted onto a 1.3 $M_\odot$ NS are shown by dot-dashed lines. The solid line is the propeller efficiency upper limit (Eq. 4.5).

The above derived limits on $\eta_{\rm pro} = dM_{\rm out}/dM_{\rm in}$ involve a great deal of fine tuning with respect to the ejection of matter from close to the light cylinder. Indeed, despite the fact that the NS magnetic field lines approach c at $R_{\rm lc}$, it assumed that ejection takes place at much lower speeds, precisely the lowest required for matter to reach infinity.

Eqs. (4.5) and (4.7) are plotted in Fig. 4.2 as a function of the spin period and for different values of the NS mass. In the following we discuss the impact of the limits in Eqs. (4.5) and (4.7) on evolutionary models of accreting NS's binaries and MSP's.

4.2 Discussion

The limits that we have derived on the mass ejection efficiency of the propeller mechanism are based on the assumption that, when accretion takes place, the highest angular momentum is transferred to the NS, whereas ejection occurs at the expense of the NS rotational energy from the largest radius compatible with the propeller mechanism. This minimizes the loss of rotational energy.

Somewhat different limits are obtained depending on whether during the accretion phase, the disk ends at the magnetospheric boundary or extends all the way to the NS surface. The latter case might be relevant to the case of systems with weakly magnetized NSs (for these systems $R_{\rm M} \simeq R_{\rm NS}$; these are typically high luminosity systems and do not display periodic pulsations). The corresponding limit on $\eta_{\rm pro}$ (see Eq. 4.7) applies only over a limited range of fast NS spin periods. Indeed, if the magnetosphere is "squeezed" inside the star surface during the accretion phase (formally $R_m \simeq R_{\rm NS}$), then, as the mass inflow rate decreases by up to ∼4–5 orders of magnitude (as inferred from the luminosity NS X-ray transient systems, e.g., Campana & Stella 2000), the magnetosphere can expand up to ∼20 $R_{\rm NS}$ at the maximum. This is due to the stiffness of the NS magnetosphere, reflected in the weak dependence of $R_{\rm M}$ on $\dot{M}$ in Eq. (4.1). For the NS to be in propeller phase the corotation radius, $R_{\rm co}$, must be smaller than the magnetospheric radius $R_{\rm M}$ ($\sim 20 R_{NS}$), in turn implying that the NS spin cannot be longer than $\sim$ 30 ms (for NS with spin period longer than this, the propeller efficiency limit in Eq. (4.7) would thus be

inapplicable). In this case, from Fig. 4.2 (panel b), we note that the maximum propeller efficiency cannot be larger than $\simeq 4$ for NS with a spin period of $\simeq 1$ ms. The limit on η_{pro} derived in the case in which there exists a magnetosphere also during the accretion phase (see Eq. 4.5) applies instead over a large range of spin periods and its value is ~ 5, for a spin period of $\simeq$1 ms and increases for longer periods.

Strictly speaking, our reasoning applies only to the accretion/ejection of (infinitesimally) small amounts of matter. The limits we derived are thus immediately relevant to NSs that often cycle between the accretion and ejection regimes. These include transient X-ray systems which alternate active periods, lasting up to years, to quiescent intervals of up to ~ 100 yr. During each outburst cycle the NS paramaters (e.g., mass, spin period, magnetic dipole moment) change only by very small amounts. These systems likely evolve through a very long sequence of accretion/ejection cycles, while within each cycle the efficiency of the propeller ejection remains limited by the values we have derived. It is easy to see that in this case the overall efficiency must be limited by the maximum possible value of $\eta_{\rm pro}$, given by Eq. (4.5) independent of whether accretion occurs through the magnetosphere or not.

Therefore, flunging away matter with higher efficiency than permitted by the above limit would require a different ejection mechanism such as the radio pulsar ejection mechanism (Illarionov & Sunyaev 1975). This mechanism can operate at much larger radii (comparable to the NS Roche-lobe radius) where the gravitational potential is much shallower and thus the energy required to expel matter to infinity is much smaller (e.g., Burderi *et al.* 2001).

In the case of accretion and ejection of finite amounts of matter, an analytical expression of $\eta_{\rm pro}$ cannot be found. In fact, in this case, one has to consider the variation of the stellar parameters during the evolution of the system. The equations relating the rotational energy acquired during accretion to the ejection energy lost during the propeller phase depend on the instantaneous value of the stellar mass and angular velocity, and their evolution can be followed numerically. To obtain an estimate of the maximum propeller efficiency we again assumed that the accretion phase takes place from the corotation radius, the ejection phase from $R_{\rm lc}$ and that all the rotational energy acquired during accretion is used to eject matter from the system. In our numerical integrations we neglected the decrease in the NS radius which results from increasing its mass through accretion. In any case, using the simple relation $R_{NS} \propto M_{NS}^{-1/3}$ we checked that this is a small effect and the induced variations on $\eta_{\rm pro}$ are less that $\sim 2\%$. The parameters that we used in our calculations are those in the evolutionary models of Ergma & Sarna (2003) and Tauris & Savonije (1999). In the first paper the authors assume that propeller ejection takes place from an increasing radius, as the mass inflow rate toward the NS decreases. Using their parameters, i.e. NS mass of ~ 1.4 M$_\odot$, initial spin period ~ 0.03 s, ~ 0.25 M$_\odot$ accreted onto the NS, and a final spin period of ~ 3.6 ms, our calculations show that the efficiency is bound by the maximum value of $\lesssim 5$. This is a reasonable result since accretion causes Ω_0 to increase and consequently, ejection takes place (mainly) at smaller values of $R_{\rm lc}$. In this case the energy required to eject matter is higher and the propeller less efficient. An additional effect comes from the fact that the corotation radius slightly increases during accretion due to the building up of the NS mass. However, our calculations show that this effect is small (due to the limited range in NS mass). In fact in all cases we obtained a lower efficiency than the maximum value of $\eta_{\rm pro}$ of Eq. (4.5), which holds for short accretion/ejection cycles. Fig. 4.3 shows that the upper limit of Eq. (4.5) is approached only when the accreted mass on the NS is very small. We note that the propeller effi-

ciency required in the work of Ergma & Sarna (2003) is ~ 2.6, consistent with the limit we have derived. It is more difficult to carry out a comparison with the work of Tauris & Savonije (1999). We refer to their models for relatively close binary systems with light donors ($P_{\rm orb} < 10$ d, $M_{\rm donor} < 1.3$ M$_\odot$). This is because, in those cases, the mass-transfer rate remains sub-Eddington during the entire binary system evolution, preventing the formation of super-Eddington strong outflows and causing the binary system to eject matter mainly via the propeller effect. We use a NS mass of $\sim$1.3 M$_\odot$, $\sim$0.1–0.4 M$_\odot$ accreted onto the NS and an initial NS spin period in the range $\sim$ 0.001–0.006 s. Again we find the required propeller efficiency in Tauris & Savonije (in some cases $\eta_{\rm pro} \lesssim 1$) is smaller than our numerically estimated upper limit ($\eta_{\rm pro} \lesssim 7$).

A refined treatment of the propeller effect for a magnetic accreting ms pulsar was carried out by Ustyugova *et al.* (2006). Using a magnetohydrodynamic approach, and considering a detailed model for the interaction between the NS magnetosphere and the accretion disk, they showed that propeller outflows can be expected from a fast rotating ($P_{\rm spin} \sim$ 1.2–1.6 ms) weakly magnetic NS ($B \sim 5 \times 10^8$–2×10^9 G). A comparison between their results and ours $\eta_{\rm pro}$ is straightforward if one consider that all the NS rotational energy used in the propeller phase derives from accretion of matter at the corotation radius. Dividing their total ejected matter ($\dot{M}_j + \dot{M}_w$) by the above estimated accreted matter, we obtain $\eta_{\rm pro} \sim 0.4$, for a 1.26 ms pulsar with $B \sim 10^9$ G.

In summary the evolutionary calculation of Ergma & Sarna (2003) and Tauris & Savonije (1999) correspond to a propeller efficiency of $\sim$1–3, which as such would be adequate to explain how the ejection of a large fraction of the mass transferred by the companion can take place in these systems. The upper limit that we have derived here for the propeller efficiency is only a factor of $\sim$2 higher. However achieving such a limit would require a high degree of fine tuning. This indicates that a propeller efficiency of order $\sim$2–3 might be difficult to achieve in real systems.

As suggested by the detailed propeller simulations by Ustyugova *et al.* (2006) a propeller efficiency < 1 might be more realistic. If this was the case, then a different mechanism to eject from the binary most of the mass transferred by the companion is required. The onset of the radio pulsar ejection mechanism is thus probably to be favored.

Chapter 5

A quiescent NSLMXB accretion disk corona source: 4U 2129+47

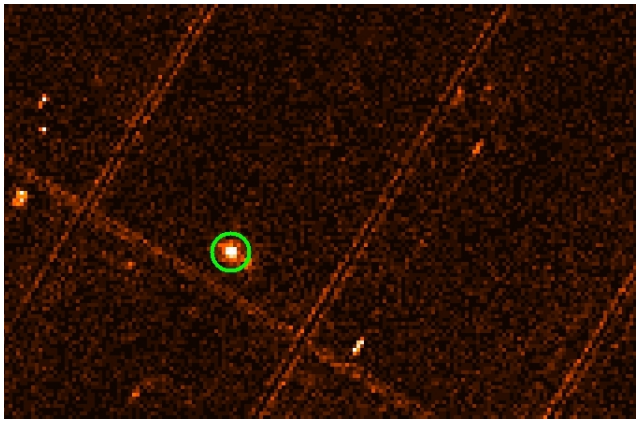

Figure 5.1: An image of the Epic-PN field of view around 4U 2129+47. The position of the source is highlighted by using a green circle. The Epic-PN was operating in Full Frame mode (see Sect. 1.5).

In this Chapter we study the NSLMXB 4U 2129+47 in depth. Since this source showed in the past several interesting observational aspects, we describe its history in fairly good details; in particular we concentrate on its ADC nature (see Sect. 1.1.1) and on the possibility that it belongs to a hierarchical triple system.

4U 2129+47 was discovered by Forman *et al.* (1978) at a flux level variable between 2.4 and 4.8×10^{-10} erg cm^{-2} s^{-1} (2–10 keV band). Observations of 4U 2129+47 in the early 80's showed that both its X-ray and optical light curves were modulated over a 5.24 hr period, with a partial V-shaped minimum maintaining approximately the same shape and phase (see Fig. 5.2; Thorstensen *et al.* 1979; Ulmer *et al.* 1980; McClintock *et al.* 1982, hereafter MC82). A late K or M spectral type companion of $\sim$0.6 M$_\odot$ was suggested, assuming it filled its Roche lobe, and the discovery of a type I X-ray burst (Garcia & Grindlay 1987) led to the classification of 4U 2129+47 as a NSLMXB (Thorstensen *et al.* 1979; McClintock *et al.* 1981). The source distance was estimated to be $\sim$1–2 kpc, corresponding to an X-ray luminosity of $\sim 5 \times 10^{34}$ erg s^{-1} (Horne *et al.* 1986). The optical light curve could be understood in terms of the varying viewing geometry of the X-ray heated face of the companion, while the V-shaped minimum in the X-ray light curve was

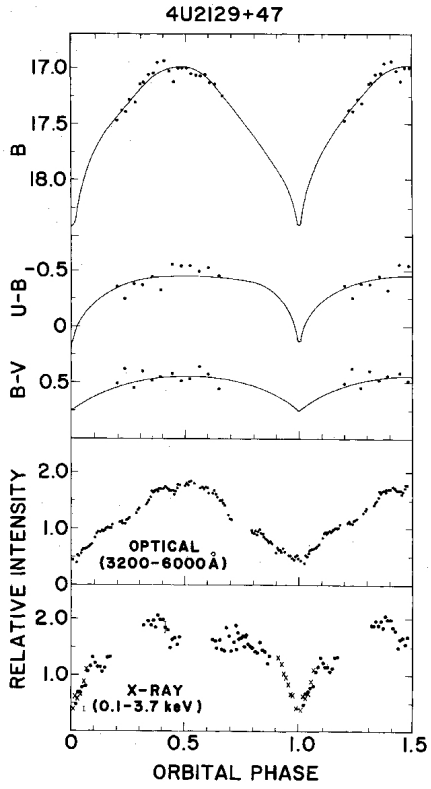

Figure 5.2: UBV, broad-band optical and X-ray observations of 4U 2129+47 obtained in 1980 June 13 UT through the Louisiana State University and McGraw-Hill telescopes, and EINSTEIN satellite (McClintock *et al.* 1982). Optical and X-ray data were obtained in continuous, simultaneous observations, except for the X-ray data plotted as crossed (these were taken about 40 min later than the first observation). The partial V-shaped eclipse, aligned in phase with the optical eclipse, is assumed as an evidence for the presence of an ADC (see text).

interpreted as being due to the gradual eclipse of an extended ADC. The shape of the partial X-ray eclipse and the rapidity of its ingress and egress have been used to place upper limits on the size of this X-ray scattering region ($\sim 5\times10^{10}$ cm for the 4U 2129+47 high luminosity state, MC82). The origin of ADCs is not well understood yet, but it is most likely related to systems in which the mass accretion rate is sufficiently high that a tenuous scattering corona is formed as a consequence of matter evaporation from the accretion disk (see Sect. 1.1.1).

4U 2129+47 was first revealed in a low state ($F_{0.3-6\ \mathrm{keV}} \lesssim 10^{-12}$ erg cm^{-2} s^{-1}) in September 1983 (Pietsch *et al.* 1986; Wenzel 1983). Optical observations carried out between 1983 and 1987 showed a flat light curve without any evidence for orbital modulation, while the spectrum displayed features fully compatible with a late type F8 IV star (Kaluzny 1988; Chevalier *et al.* 1989). The hypothesis of a foreground or a background star seemed unlikely, due to the low probability ($\lesssim 10^{-3}$) of chance superposition. This led to the suggestion that 4U 2129+47 is part of a triple system (Thorstensen et al. *et al.* 1988). The revised estimate of the source distance was ∼6.3 kpc (Cowley & Schmidtke 1990; Deutsch *et al.* 1996).

Hints of a possible detection of a dynamical interaction between the F star and 4U 2129+47

Table 5.1: Mid-eclipse epoch measurements.

Observatory	Mid-eclipse Epoch[a] (JD)	Orbital Period[a] (s)	References
HEAO 1 and *Lick Observatory telescope*	2443760.755(3)	18857(3)	Thorstensen *et al.* (1979) (Th79)
McGraw Hill telescope and *KPNO telescope*	2444107.785(3)	18857.5(1)	McClintock *et al.* (1981) (MC81)
Einstein *Louisiana State Telescope*, *McGraw Hill telescope*	2444403.743(2)	18857.48(7)	McClintock *et al.* (1982) (MC82)
Chandra	2451879.5713(2)	18857.631(5)[b]	Nowak *et al.* (2002) (N02)
XMM-Newton	2453506.4825(3)	18857.594(7)	this work (tw)
XMM-Newton	2453528.3061(4)	-	this work (tw)

[a] Numbers in parentheses are the uncertainties on the last significant digit (errors at 1σ level).
[b] Average orbital period calculated by using the two *Chandra* eclipses.

were discussed by Garcia *et al.* (1989) and Cowley & Schmidtke (1990), after the discovery of a ∼40 km s^{-1} shift in the mean radial velocity measurement derived from the F star spectrum. Shifts of this amplitude are indeed expected if the F star is in a month-long orbit around the binary (Garcia *et al.* 1989).
ROSAT and *Chandra* observations, carried out between 1991 and 2000, led to a characterization of the low luminosity state of 4U 2129+47 (Garcia *et al.* 1992; Garcia 1994; Garcia & Callanan 1999). The refined *Chandra* position turned out to be coincident with the F star to within $0''.1$ (Nowak *et al.* 2002, hereafter N02) providing support in favor of the triple nature of 4U 2129+47. However, a firm conclusion could not be reached.

Here we report on *XMM-Newton* observations of 4U 2129+47, and discuss the likely detection of a mid-eclipse epoch variation between two ∼22 day distant observations. We show that this delay is naturally explained as being due to the orbital motion of the binary 4U 2129+47 with respect to the center of mass of a triple system. This delay is thus probably the first "Doppler" (or, more accurately, "Roemer") X-ray signature of the triple nature of 4U 2129+47. We outline our data reduction procedure in Sect. 5.1, and present the results of timing and spectral analysis in Sect. 5.2. Our conclusions are summarized in Sect. 5.3.

5.1 Observations and data

XMM-Newton (Jansen *et al.* 2001) observed 4U 2129+47 on May 15 and on June 6, 2005 for a total time span of ∼80 ks (about four orbital periods). The total effective exposure time for each observation was ∼13 ks for the EPIC-PN, EPIC-MOS1, and EPIC-MOS2 cameras. The remaining observing time was discarded due to ground station anomalies and high radiation from solar activity filling up of the EPIC-PN scientific buffer. Heavy contamination due to solar activity resulted in poor orbital phase coverage, especially during the first observation. Furthermore, the EPIC-PN and EPIC-MOS cameras were found to be unequally affected by this contamination, thus forcing a different selection of good time intervals for the spectral and timing analyses (see Sect. 5.2). The observation data files (ODFs) were processed to produce calibrated event lists using the standard *XMM-Newton* Science Analysis System (SAS 7.0). We used the EPCHAIN and EMCHAIN tasks for the EPIC-PN and the two MOS cameras, respectively. Source light curves and spectra were extracted in the 0.2–10 keV band, using circles of ∼$14.6''$ radius centered on the source. This corresponds to ∼70% encircled energy [1] for both the EPIC-PN and EPIC-MOS cameras. Larger circles could not be used due to the proximity of the S3–

[1] As described in chapter 3.2.1.1 (Issue 2.5) of the *XMM-Newton* users' handbook.

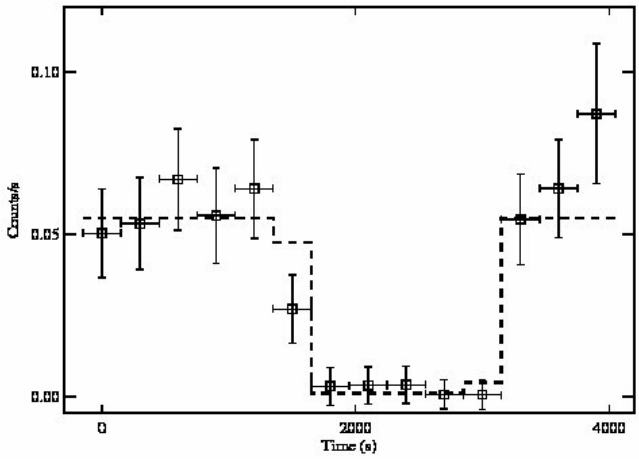

Figure 5.3: Fit of the mid-eclipse epoch during the first observation. The 0.2–10 keV light curve (bin time 300 s) is shown together with the best fit model (dashed line).

β Digital Sky Survey stellar object (N02). We extracted the background light curves and spectra from circles of radii $\sim$116″ in the nearest source-free region to 4U 2129+47. Background and source circles were all chosen to lie within the same CCD. The difference in extraction areas between source and background was accounted for by using the SAS BACKSCALE task for the spectra and the LCMATH task from HEASOFT (version 6.1.1) for the light curves. The average source count rate was found to be 0.041±0.001 count s^{-1} in the EPIC-PN and 0.010±0.001 count s^{-1} in the two EPIC-MOS cameras (errors are 1σ). Given the short effective exposure time, the low count rate of the EPIC-MOS1 and EPIC-MOS2 cameras did not contribute significantly to the spectral analysis; therefore in Sect. 5.2.2 we discuss only the spectrum from the EPIC-PN camera.

5.2 Results

5.2.1 Orbital ephemerides and eclipse parameters

In the *XMM-Newton* EPIC-PN light curves, two eclipses were clearly detected, one in each pointing. These eclipses were also unambiguously found in the EPIC-MOS1 and EPIC-MOS2 data. In order to avoid any non-synchronicity problems between the three EPIC cameras, we followed method III of Barnard *et al.* (2006). In accordance with this method, all the source and background time series of the same observation were extracted within the time interval around the eclipse that was found not to be interrupted by the presence of a previously removed solar flare (Sect. 5.1). In all cases, the time interval selection was carried out by filtering each light curve with the EVSELECT (version 3.59) keywords "timemin" and "timemax". This additional reduction of the effective exposure time (in addition to the one described in Sect. 5.1) was especially restrictive for the first observation, for which a total exposure time of only $\sim$4 ks around the eclipse could be used. The times of all light curves were corrected to the barycentre of the Solar System with the SAS BARYCEN task (version 1.17.3), and summed up in each observation with the LCMATH task, in order to maximize statistics and thus improve the accuracy with which the eclipse parameters could be determined. To estimate the mid-eclipse times, the light

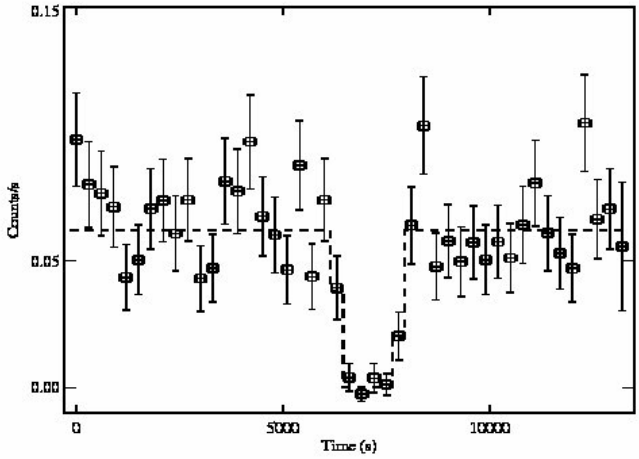

Figure 5.4: Fit of the mid-eclipse epoch during the second observation. The 0.2–10 keV light curve (bin time 300 s) is shown together with the best fit model (dashed line).

curves were rebinned in 300 s bins[2].

These light curves were then fit with a rectangular eclipse model, in which the mean count-rate outside ($F_{\rm max}$) and inside ($F_{\rm min}$) eclipse, and the mid-eclipse epoch (T_0), were treated as free parameters. In these fits we fixed the duration of the eclipse at the value 1523 s, as measured by N02. Being dictated by the secondary star, the duration of the eclipse limb is unlikely to have changed since the time of the *Chandra* observation (see Sect. 5.2.2 for details). χ^2 minimization was performed with an IDL routine written by the authors. The model rectangular eclipse was integrated over each time bin before the χ^2 was computed, in order to take data binning into account[3]. With this method we obtained an accurate determination of the eclipse mid-epoch, even though the ingress and egress eclipse times could not be determined with the same accuracy. The χ^2 hypersurface was directly sampled in a fine grid of values in order to distinguish local minima. The variance between model and data was then calculated in each point and for each set of parameters, in order to investigate the local χ^2 minima in the 4D parameter space. The best fits to the eclipse epochs were found to be T_0(a)=2453506.4825±0.0003 JD and T_0(b)=2453528.3061±0.0004 JD with χ^2/dof(a)=9/11, χ^2/dof(b)=44/42 (errors are at 68% confidence level unless otherwise specified; our epochs are given in UT[4]). The values of the reduced χ^2 in the above fits are close to 1 and therefore the addition of any other free parameter in the fit would not be justified from a statistical point of view. We also checked that by allowing the eclipse duration to vary within the N02's 1σ confidence level, i.e., 1473–1553 s, the other parameters of the best fit remain unchanged to within the

[2]A check was carried out *a posteriori* to verify that our results are virtually independent of the light binning time.

[3]Standard fitting routines that compute the fitting function punctually in the center of the bin are not adequate when a function with a large first derivative or features with a scale smaller than the bin time is considered. In our case the derivative diverges at the ingress and egress times.

[4]Note that HJD(UT)=HJD(TT)-64.68 s at our epochs. We did not consider the correction for the difference between heliocentric Julian date in the geocentric (terrestrial) dynamical time system, HJD(TT), and barycentric dynamical time system, BJD(TB). The latter is the one used by the SAS BARYCEN task, but the difference between BJD(TB) and HJD(TT) is less than ∼3 s at any given time, which is much smaller than the accuracy of our measurement here.

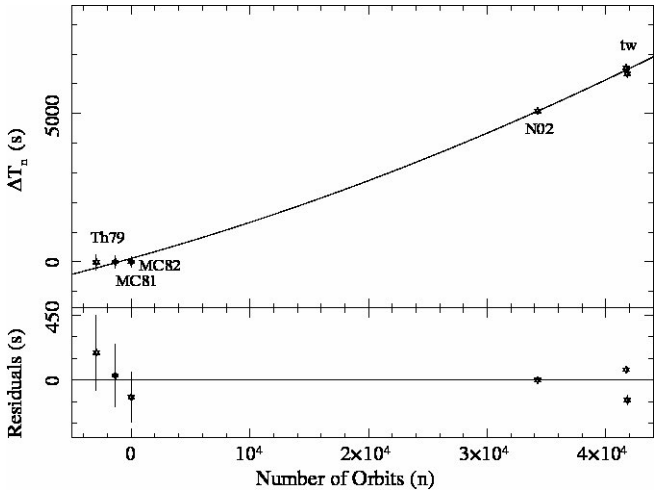

Figure 5.5: Delays of the mid-eclipse epochs with respect to a constant $P_{\rm orb}$=$P_{\rm ref}$ model. The solid line in the upper panel represents the quadratic best fit to the epochs (see Sect. 5.2.1). The lower panel shows the residuals from this fit.

errors (mid-eclipse epochs differed by less than 10 s and the 1σ errors remained below 26 s). We note however that if the eclipse duration is included as a free parameter without any constrains, a less significant eclipse delay of $\delta T_{\rm m}$=151±55 s would be obtained.

In the following we adopt values of the two mid-eclipse epochs as derived from the first fit. We show in Figs. 5.3 and 5.4 the two eclipses, together with the best fit models discussed above. We also carried out the fits by using a modified version of the eclipse model by Mangano *et al.* (2004) in order to estimate the eclipse ingress and egress time. We allowed these times to take independent values during the fit (N02). Only upper limits of $\lesssim$310 s could be derived, which are significantly larger than those obtained from the *Chandra* observation (in 130–260 s range, N02).

In order to determine a refined orbital solution, we considered the above mid-eclipse epochs together with the epochs, $T_{\rm n}$, derived from earlier observations (see Table 5.1). As discussed above, the observed phase alignment between the X-ray and optical light curve minima, allows the comparison of optical and X-ray measurements of the system's ephemerides. The long time span covered by the eclipse measurements (1979–2005 or $n_{\rm max}\sim$44800) can be used to improve the accuracy of the orbital solution and, possibly, measure the orbital period derivative. To this aim we used a standard O–C technique[5]. We considered the ephemeris from MC82 as reference ($T_{\rm ref}$=2444403.743±0.002 JD, $P_{\rm ref}$=18857.48±0.07 s), and plotted in Fig. 5.5 the delays $\Delta T_{\rm n}$=$T_{\rm n}$-$T_{\rm n_{pred}}$. Here $T_{\rm n_{pred}}$=$T_{\rm ref}$+n$P_{\rm ref}$, with n the closest integer to ($T_{\rm n}$-$T_{\rm ref}$)/$P_{\rm ref}$ (our two observations correspond to n=41706, 41806). In the same figure we have also plotted the best quadratic fit to the O–C residuals, corresponding to an orbital period evolution with constant time derivative. A linear fit (i.e., a constant orbital period) to the same data gave an unacceptable fit (χ^2/dof=91/4). Table 5.2 gives our corrected reference time, $T_{\rm ref}$, orbital period, $P_{\rm ref}$, and the derived orbital period evolution $P_{\rm orb}\dot{P}_{\rm orb}^{-1}$=(5.8±0.7)×$10^6$ yr. This value is a factor of ∼4 larger than that in N02, but we note that N02's estimate was deduced by adopting the MC82 value of $P_{\rm orb}$ and accounting for the entire measured delay as being

[5]Observed minus calculated residuals, which are the delay in eclipse time over that expected for a constant period system (see, e.g., Parmar *et al.* 1991; Papitto *et al.* 2005, and references therein.)

Table 5.2: Orbital solution obtained with the best quadratic fit to the O–C delays $\Delta T_{\rm n}$ (see Fig. 5.5).

$T_{\rm ref}$ (JD)	2444403.7443±0.0013
$P_{\rm orb}$ (s)	18857.594±0.007
$\dot{P}_{\rm orb}$ (s s^{-1})	(1.03±0.13)×10^{-10}
$P_{\rm orb}\dot{P}_{\rm orb}^{-1}$ (yr)	(5.8±0.7)×10^{6}
χ^2/dof	25.6/3

due to an orbital period derivative. The observed delay of ∼6500 s between the ephemeris of MC82 and the one found in the present work (see Fig. 5.5), implies an orbital phase shift of ∼0.35. Small deviations in the eclipse centroid between the active and quiescent state of 4U 2129+47 may be introduced by changes in the shape of the ADC around the compact object. However a ∼6500 s delay is far too large to be explained as a result of such geometrical variations. The poor χ^2 in Table 5.2 is due to the large shift of the first *XMM-Newton* point with respect to the second one ($\delta T_{\rm m}$=192±43 s), which could not be accounted for by any quadratic fit to the eclipse phase evolution. While this delay is much smaller than that discussed above, we argue that it is also very unlikely to result from geometrical variations within the 4U 2129+47 binary system. This is because the eclipse profile is consistent with the central source being eclipsed by the companion star. Moreover, the source X-ray flux and spectrum remained virtually the same across the two *XMM-Newton* observations and the *Chandra* observation discussed by N02 (see Sect. 5.2.2). In Sect. 5.3 we discuss the possibility that this delay is due to light propagation in a triple system.

We also extracted the EPIC-PN light curves of the observations, since these have a better orbital phase coverage than those obtained by summing all three instruments. This however resulted in a lower count rate and S/N. These light curves and those obtained by using data summed over the three EPIC cameras were folded at the best orbital solution using 10 phase bins. We fitted these two light curves with the function F(ϕ)=A+Bsin[2π(ϕ-ϕ_0)], and looked for a sinusoidal modulation similar to that observed by N02. No significant modulation was observed (fitting with a constant value gave a χ^2/dof of 12/13 and 10/17 respectively). We derived a 90% confidence upper limit on the amplitude modulation of ∼17%, i.e., a factor of ∼2 smaller than the value reported by N02. This result was also checked by using light curves extracted only in the 0.5–2.0 keV band, where the amplitude modulation might be higher (N02). No significant differences were found. We discuss these results in Sect. 5.3, together with the results from the spectral analysis (Sect. 5.2.2).

5.2.2 Spectral analysis

Spectral analysis was carried out by using XSPEC version 11.3.2t (Arnaud 1996); the data were rebinned in order to have at least 20 photons in each energy bin. Owing to poor statistics, phase-resolved spectroscopy could not be carried out. Instead, the spectra of the two observations were accumulated during the same time intervals selected for the extraction of the EPIC-PN light curves, except for the eclipses (see Sect. 5.2.1).

The spectrum of the first observation was modeled with only an absorbed blackbody (poor statistics did not allow for more complex models).
The second observation was first modeled with an absorbed power law plus a blackbody

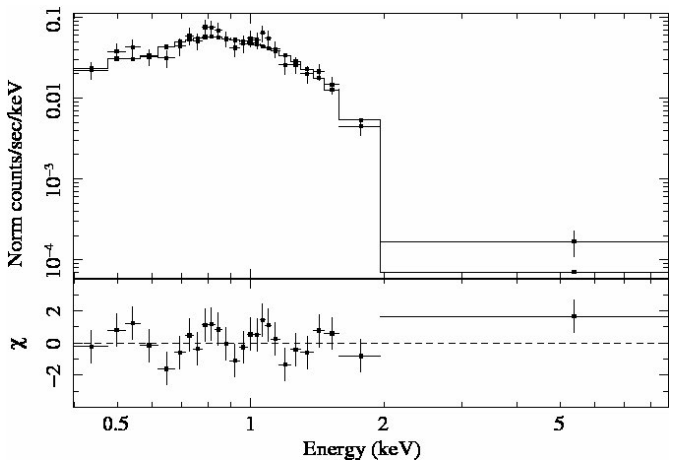

Figure 5.6: Measured 0.2–10 keV spectrum of 4U 2129+47 during the second pointing. The best fit model and the contribution of the fit residuals to the χ^2 are also shown.

component, but the F-statistics probability with respect to a simple absorbed blackbody model was found to be ∼0.2. The best fit was then obtained, also in this case, by adopting an absorbed blackbody model.
A power law component with fixed photon index Γ=1.1 (N02) was added to the fit of the second observation in order to estimate an upper limit. For such a power law component, the 90% confidence upper limit was about 10% of the 0.2–10 keV unabsorbed flux (in agreement with N02, see their model A). C-statistics model fitting (Cash 1979) was also performed on the unbinned spectra: the results were fully compatible with those obtained by using χ^2 minimization. Figure 5.6 shows the spectrum and model of the second pointing as an example, while the best fit parameters are reported in Table 5.3. No significant difference was found between the two *XMM-Newton* observations, and all parameters were compatible, to within the errors, with those determined by N02 for the quiescent state of 4U 2129+47. We also tested our results with the XSPEC NSA model (Arnaud 1996; Zavlin *et al.* 1996). Fits were carried out, first by using a fixed distance of 6.3 kpc, and then by fixing a neutron star radius of 5 and 10 km (N02). Results of these fits were found to agree with those of N02 (our errors on all parameters are a factor of ∼1.5 larger).

5.3 Discussion

We reported on *XMM-Newton* observations of 4U 2129+47 in its quiescent state, which has lasted, apparently uninterrupted, since 1983 (Wenzel 1983). The discovery of a late F-type star coincident with the position of 4U 2129+47 (Thorstensen et al. *et al.* 1988; Chevalier *et al.* 1989) led to the hypothesis that this binary system might be part of a hierarchical triple. Our detection of a delay $\delta T_{\rm m}$=192±43 s across two eclipses separated by ∼22 days, can be naturally explained as being due to the orbital motion of the binary with respect to the center of mass of a triple, and thus lends support in favor of the triple system hypothesis.

Using a third star of mass M_1, an inner binary with M_2∼2 $M_\odot$, and a non-eccentric orbit, the expected delay between two mid-eclipse epochs separated by a time interval τ can be expressed as

$$\delta T = a_2 \sin i/c \left[\sin\left(\phi_0 + \delta\phi\right) - \sin\phi_0\right]. \qquad (5.1)$$

Table 5.3: Best-fit spectral parameters with $N_{\rm H}$ and BB model (90% confidence level error bars).

	1 Obs. (May-15-2005)		2 Obs. (June-6-2005)	
	χ^2-Stat	C-Stat	χ^2-Stat	C-Stat
$N_{\rm H}$ (10^{22} cm^{-2})	$0.14^{+0.11}_{-0.09}$	$0.24^{+0.03}_{-0.09}$	$0.21^{+0.1}_{-0.06}$	$0.28^{+0.03}_{-0.08}$
$kT_{\rm bb}$ (keV)	$0.25^{+0.03}_{-0.03}$	$0.22^{+0.03}_{-0.02}$	$0.20^{+0.02}_{-0.02}$	$0.18^{+0.02}_{-0.01}$
$R^{\rm a}_{\rm bb}$ (km)	$1.3^{+1.1}_{-0.4}$	$1.9^{+0.74}_{-0.53}$	$2.42^{+1.8}_{-0.7}$	$2.87^{+1.7}_{-0.6}$
χ^2/dof	14.30/14	-	20.6/23	-
C-Stat	-	496.8	-	592.24
$F^{\rm a}_{0.2-10{\rm keV}}$ (10^{-14} erg cm^{-2} s^{-1})	9.3	9.3	8.9	9.0
$F^{\rm b}_{0.2-10{\rm keV}}$ (10^{-13} erg cm^{-2} s^{-1})	1.6	2.3	2.2	3.3
$L^{\rm c}_{0.2-10{\rm keV}}$ (10^{32} erg s^{-1})	7.7	10.9	10.5	15.8

[a] Absorbed Flux
[b] Unabsorbed Flux
[c] From the unabsorbed flux and assuming a distance of 6.3 kpc.

Here a_2=(G/4π^2)$^{1/3}$ P$_{\rm tr}^{2/3}$ $M_1/(M_1+M_2)^{2/3}$ is the radius of the inner binary orbit around the triple system center of mass (with a period $P_{\rm tr}$), ϕ_0 is the phase at T_0(a) of the binary system along such an orbit, c is the speed of light, i is the inclination angle of the triple system orbit, $\delta\phi$=2$\pi\tau$ P$_{\rm tr}^{-1}$ and, in our case, τ=T_0(b)-T_0(a)$\simeq$22 d.

Figure 5.7 shows a plot of the range of allowed values of the triple orbital period as a function of the third star mass[6], which give delays compatible with the measured value $\delta T_{\rm m}$ (to within the uncertainties at a given confidence level). The dashed, dot-dashed and dot-dot-dot-dashed lines represent the ranges for 1σ=43 s, 2σ=85 s and 3σ=165 s confidence intervals in $\delta T_{\rm m}$, respectively. The solid lines give the constraints on $P_{\rm tr}$ imposed by the measured $\sim$40 km s^{-1} shift in the mean radial velocity of the F star (Garcia *et al.* 1989), under the assumption that this represents the maximum observable radial velocity shift of its orbit. The two panels of Fig. 5.7 show the cases of i=90°, and i=60° respectively. From the upper panel of this figure (i=90°) it can be seen that, at 1σ confidence level, we can set a lower limit on the F star mass of $\sim$1.2 M$_\odot$. Considering a 2σ uncertainty on $\delta T_{\rm m}$ removes the upper limit on M_1 and only the orbital period can be constrained (39 d<$P_{\rm tr}$<200 d, for $M_1\simeq$1 M$_\odot$). We note that a decrease of the inclination angle results in a smaller range of allowed orbital periods, while the effect of a non-zero eccentricity (hypothesis not considered in our calculation) would have the opposite effect. The possibility that 4U 2129+47 is in a triple system might also have noticeable consequences for our measured orbital period derivative, $P_{\rm orb}\dot{P}_{\rm orb}^{-1}$=(5.8$\pm$0.7)$\times$10^6 yr (see Sect. 5.2.1). At first sight, this value seems to imply that, as in other known LMXBs (e.g., X 1822-371, Parmar *et al.* 2000; Heinz & Nowak 2001; White *et al.* 1995) the orbital period of 4U 2129+47 is increasing. This would be contrary to evolutionary expectations. In fact, angular momentum losses (such as gravitational wave emission and magnetic breaking) in a binary system with an orbital period of $\sim$5 hr and a non-degenerate companion would imply a decreasing orbital period (Verbunt 1993). However, if a modulation in the eclipse arrival time of amplitude $T_{\rm a}$=$a_2 \sin i$/c (as discussed above) contributes to the measured epochs of the eclipses, caution should be used with any estimate of $P_{\rm orb}\dot{P}_{\rm orb}^{-1}$ (such as that in Sect. 5.2.1) that does not take this modulation into account. Given our poor knowledge of the parameters of the triple system, a detailed correction for the orbital motion of the inner binary around the center of mass of the triple cannot be carried out yet. A conservative estimate of $P_{\rm orb}\dot{P}_{\rm orb}^{-1}$ can be derived by increasing the uncertainties on the observed $\Delta T_{\rm n}$ up to a value $T_{\rm a}$,

[6] For an F-type star it is expected $M_1\sim$1–1.6 M$_\odot$ (see e.g., Bohm-Vitense 1992).

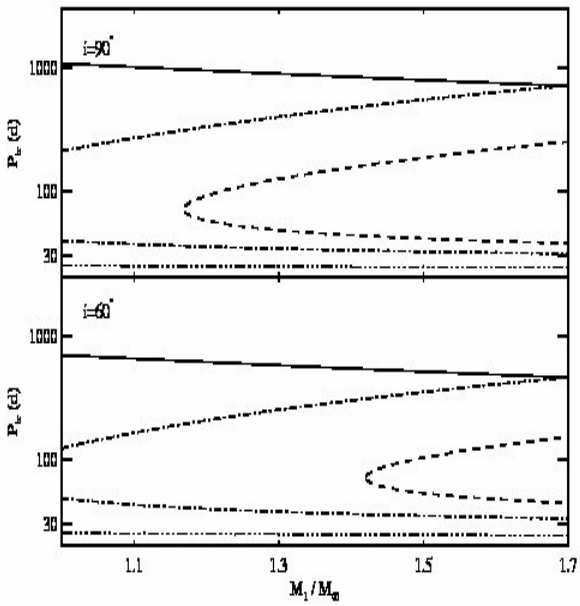

Figure 5.7: Allowed regions of the triple orbital period, $P_{\rm tr}$, as a function of the third star mass, M_1, in the cases in which the measured delay $\delta T_{\rm m}$=192 s is varied within 1σ (dashed line), 2σ (dot-dashed line) and 3σ (dot-dot-dot-dashed line) confidence level. For the 3σ range only the lower limit is drawn. Solid lines represent the limits imposed by the measured radial velocity shifts of the F-star (see text for more details). The two panels show the cases i=90° and 60°.

which represents the unknown amplitude of the modulation in the eclipse arrival times. The range of values that $T_{\rm a}$ may attain depends mainly on the range of orbital periods for which a solution of Eq.5.1, compatible with the values of τ and $\delta T_{\rm m}$ we measured, exists. Unfortunately, the range on $P_{\rm tr}$ that can be inferred from Fig. 5.7 is fairly loose. Based on our 1σ range of $\delta T_{\rm m}$, we derive a minimum upper limit of $P_{\rm tr}^{\rm upp}\simeq$75 d for the third star orbital period (for $M_1\simeq$1.2 $M_\odot$ and i=90°), which corresponds to $T_{\rm a}\simeq$100 s. We checked that increasing the uncertainty on the measured values of the eclipse epochs by this value would remove entirely the need to introduce an orbital period derivative. By analogy we speculate that the presence of a third body in a wide orbit around the inner binary might explain the positive orbital period derivatives observed in some LMXBs, which is at odds with the expectations of the standard evolutionary scenario.

Due to the low count-rate, and short effective exposure time, our *XMM-Newton* observations did not detect any spectral component above 2 keV. An absorbed ($N_{\rm H}\sim0.2\times10^{22}$ cm^{-2}) blackbody component with kT$_{\rm bb}\sim$0.2 keV and $R_{\rm bb}\sim$2 km provided an adequate modeling of the spectrum.

For quiescent NSs in LMXBs, like 4U 2129+47, this soft X-ray emission can be produced in several alternative ways. One possibility is that this emission is powered by thermal energy released as the NS cools in between accretion phases (Brown *et al.* 1998; Colpi *et al.* 2001). Alternative models invoke a NS in the propeller regime, shock emission due to the interaction between the pulsar wind and matter in the vicinity of the companion star, and residual accretion onto the compact star (see, e.g., Stella *et al.* 1994;

Campana *et al.* 1998). While the properties of the propeller regime are still rather uncertain, a power law emission of photon index 1–2 should be expected at least in the last two interpretations (Campana *et al.* 1998, N02). Discriminating between these models is not possible based on our results, given the lack of information at energies above 2 keV.

A soft spectral component with similar properties, plus a power law component with photon index ∼1.1, was observed in the quiescent state of 4U 2129+47 in December 2000 (N02). However, also this observation was hampered by a low number of counts above 2 keV, thus preventing an accurate characterization of the power law emission. Some indication was found that the power law component was consistent with being of constant amplitude and slope, while the blackbody component was sinusoidally modulated over the orbital period, in a manner consistent with neutral column density variation (a factor of ∼2). This modulation was ascribed to the presence of a vertically extended disk atmosphere, thicker at the outer rim, close to the region where the accretion stream from the secondary star impacts.

As discussed in Sect. 5.2.2, our folded light curve showed no clear indication of a sinusoidal modulation. The upper limit we derived on the amplitude of this modulation is significantly lower than that discussed by N02 (a factor of ∼2). This suggests that there has been some change in the geometry of the outer disk region (in particular the region where the stream from the secondary impacts) across the *Chandra* and *XMM-Newton* observations.

A series of monthly spaced *XMM-Newton* or *Chandra* observations would afford a much more accurate characterization of the quiescent emission of 4U 2129+47 and measure with good accuracy the modulation in the X-ray eclipse times due to the third body. This will yield much needed information on the triple system parameters and single out unambiguously any orbital period evolution.

Chapter 6

A type I X-ray burst from XTE J1701-407

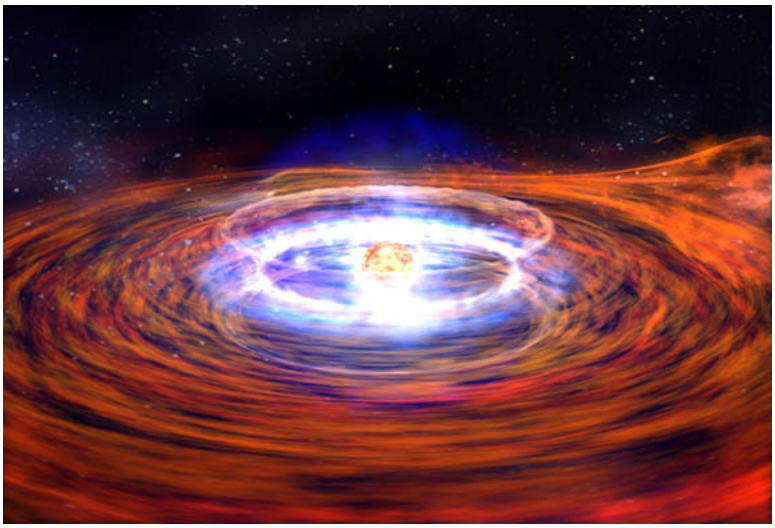

Figure 6.1: An artist impression of a type I X-ray burst from a NS.

In this Chapter we discuss an observation of an intermediate long type I X-ray burst (see Sect. 1.3) from the NSLMXB XTE J1701-407. This source was discovered by the *Rossi X-ray Timing Explorer* (*RXTE*) during a routine Galactic bulge scan on June 8, 2008 (Markwardt *et al.* 2008a). At the time of the discovery, the source spectrum was best fit with an absorbed power-law with photon index ≈ 2.1 and a neutral absorption column of $\approx 3.5 \times 10^{22}$ cm^{-2} (in the following we refer to this as the "persistent" emission). The measured flux was $\approx 1.4 \times 10^{-10}$ erg cm^{-2} s^{-1} (2–10 keV, Markwardt *et al.* 2008a; Degenaar & Wijnands 2008). On July 17, 2008, the discovery of an intermediate long type I X-ray burst, with the BAT and XRT instruments onboard the *Swift* observatory, led to the classification of XTE J1701-407 as a NS low-mass X-ray binary (Barthelmy *et al.* 2008; Markwardt *et al.* 2008b; Linares *et al.* 2008). Ten days later, i.e., on July 27, BAT observed in the 15–150 keV band a short bursts lasting ≈ 10 s (Sakamoto *et al.* 2008). Kilohertz quasi-periodic oscillations were observed at ≈ 1150 Hz (see Strohmayer *et al.* 2008, for details). The most accurate position of the source was provided by *Swift* at $\alpha_{\rm J2000}$=17$^{\rm h}$01$^{\rm m}$44$^{\rm s}$3 and $\delta_{\rm J2000}$=-40°51'29"9 with an estimated accuracy of 1.7" (Starling

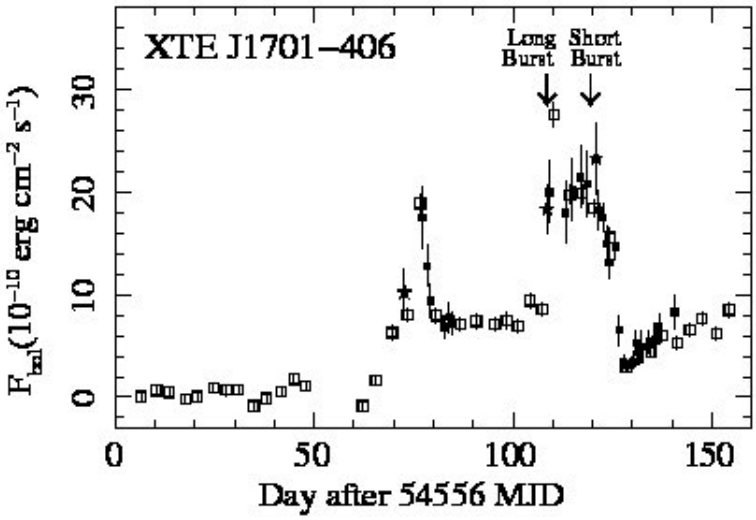

Figure 6.2: Flux history of the X-ray transient XTE J1701-407. Open squares represent fluxes derived from *RXTE* bulge observations in the period from March 31, to Septembre 2, 2008. Fluxes derived from *RXTE*/PCA and *Swift*/XRT target of opportunity and follow-up observations are marked with filled squares and stars, respectively. The arrow indicates the time of the type I X-ray burst.

& Evans 2008). No infrared counterpart candidate was found at this position (Kaplan & Chakrabarty 2008).

6.1 Data Analysis and results

For the present study we used public available data from *Swift* and *RXTE* observatories. The dataset include *RXTE* target of opportunity observations, performed after the discovery of the source (observation ID. 93444), as well as *Swift* follow-up observations (ID. 31221001, 31221002, and 317205001). The *Swift* data set includes also the intermediate long burst discovered on July 17, (ID. 317205000) and the short burst from July 27, 2008 (ID. 318166000). The total effective exposure time is 75.4 ks (30 pointings) and 1.1 ks for *RXTE*/PCA and *Swift* respectively. Data reduction of the *RXTE* Proportional Counter Array (PCA; 2–60 keV, Jahoda *et al.* 1996) and the High Energy X-ray Timing Experiment (HEXTE; 15–250 keV, Rothschild 1998) was performed according to the default selection criteria for background subtraction, light curve, and spectrum extraction. We used only PCU2 data. Data from *Swift*/XRT were analyzed in both Windowed Timing (WT) and Photon Counting (PC) mode. We reduced all the XRT data with standard procedures (Burrows *et al.* 2005), using the Heasoft package version 6.4 and the latest calibration files available. For the WT data, source events were extracted from rectangular regions with widths of 40 pixels and heights large enough to include most of the source photons. For the PC data, different extraction regions were defined, depending on the source strength, in order to increase the source signal vs. the background. Specifically, annular regions with inner (outer) radius of 10 (20) pixels were used when the source was very bright, whereas 20 pixel circular regions were preferred when the count rate from the source was <0.6 cts/s. According to the present known capability of the XRT telescope, no pile-up is expected for a count rate that is below $\approx$ 0.6 cts/s. We excluded from the

following analysis PC data that were affected by a strong pile-up; where available, we used only quasi-simultaneous observations carried out in WT mode. Ancillary response files were generated with `xrtmkarf` and accounted for different extraction regions, vignetting, and point-spread function.

6.1.1 Persistent emission

Spectra obtained from *RXTE*/PCA and *Swift*/XRT observations were fit separately by using a photoelectrically-absorbed power-law model. The best fit parameters for the absorption column, $N_{\rm H}$, are between 1.7 ± 1 and $4.4\pm1.2\times10^{22}$ cm^{-2} and a power-law index $\Gamma = 2.0\pm0.1-2.7\pm0.3$ the corresponding unabsorbed fluxes are between $1.1\pm0.07\times10^{-10}$ and $8.3\pm0.6\times10^{-10}$ in the 2–20 keV energy band. All uncertainties are at a 90% confidence level. PCA spectra were extracted in the 2–20 keV energy band; the source was only detected at low significance in the HEXTE (15–50 keV band). A fit to the joined broad-band PCA/HEXTE (2–50 keV) spectrum did not lead to a significant improvement in the determination of the model parameters; therefore, we report in the following only on the PCA data. *Swift*/XRT spectra were extracted in the 2–10 keV band. All the measured unabsorbed fluxes were extrapolated to the 0.3–100 keV band by generating dummy responses (XSPEC version 11.3.2ag), and are shown in Fig. 6.2. We included in this figure also fluxes derived from *RXTE* bulge observations[1] (Swank & Markwardt 2001). In these cases, the conversion between *RXTE* count rate and flux was obtained using the spectra results and the values reported by Markwardt *et al.* (2008a).

The light curve and spectral analysis shows that XTE J1701-407 underwent flaring activity lasting a few days, during which the X-ray flux has varied by over a factor of 2–3. This variability can be ascribed to changes in the mass accretion rate or in the position of the source along its colour-colour diagram (CCD, see e.g., Hasinger & van der Klis 1989). The latter possibility is investigated in Fig. 6.3. The CCD was realized by using background subtracted *RXTE*/PCA light curves with a 516 s time resolution. The soft colour is defined as the logarithm of the ratio between count rates in the energy bands 2.1–3.7 keV and 3.7–5.7 keV, whereas for the hard colour the energy bands 5.7–9.8 keV and 9.8–18.9 keV are used. No obvious transition between a hard to a soft state is observed from Fig. 6.3. Future observations are thus required in order to investigate further the origin of flux variations in XTE J1701-407.

6.1.2 Intermediate long burst light curves and spectra

In Fig. 6.4, we show the *Swift*/BAT 15–150 keV (upper panel) and XRT 0.3–10 keV (lower panel) light curve of the intermediate long burst. The burst start time, is the time at which the BAT X-ray intensity of the source rose to 10% of the peak above the persistent intensity level. The XRT light curve starts with a delay of 133 s after the beginning of the burst as seen by BAT. The BAT light curve shows a slow rise time[2] of ≈ 45 s. The XRT decay time from the burst is best fit by using two exponential functions, with e-folding times of $\tau_1 = 44\pm8$ s and $\tau_2 = 271\pm21$ s, respectively (see also Linares *et al.* 2008). The total duration of the burst, i.e. the time spent to go from and back to the persistent state,

[1] http://lheawww.gsfc.nasa.gov/users/craigm/galscan/main.html

[2] The rise time is defined as the time spent between the start of the burst and the point at which the 90% of the peak burst intensity is reached.

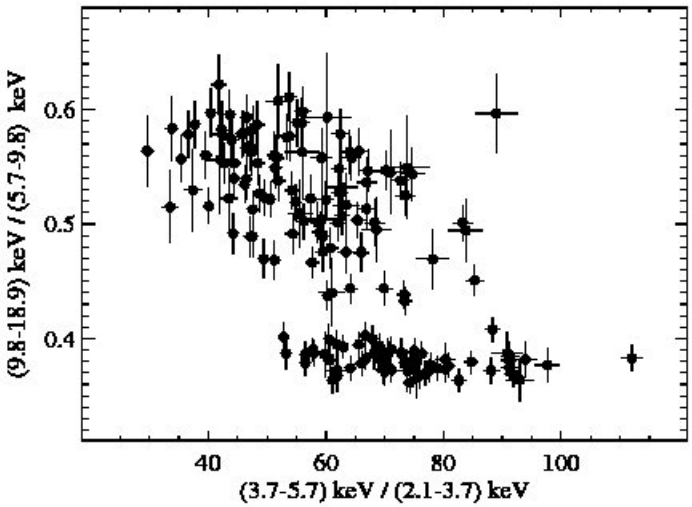

Figure 6.3: CCD of XTE J1701-407. Each point corresponds to 516 s of integration time.

was of ≈ 86 s and ≈ 18 minutes in the BAT (15–150 keV) and the XRT (0.3–10 keV) light curves, respectively.

The time-resolved spectral analysis of the burst was carried out by using BAT and XRT data in the 15–35 keV and 0.3–10 keV bands, respectively. Burst spectra were well fit by a simple black-body, BB, model. The inferred BB temperature, $kT_{\rm bb}$, apparent BB radius at 6.2 kpc (see Sec. 6.2.1), $R_{\rm bb}$, and bolometric luminosity are shown in Fig. 6.5. The burst fluence is calculated from bolometric fluxes, $F_{\rm bol}$; these correspond to the observed 2–10 keV *Swift*/XTR fluxes extrapolated to the 0.1–100 keV energy range. The peak flux, $F_{\rm peak}$, is derived from the BAT 15–35 keV light curve spectra and extrapolated to the 0.1–100 keV energy range. In Table 6.1 we report all the measured bust parameters.

From the time-resolved spectral results we converted the light curve count rates to flux and found also in this case, that a double exponential function are required to fit the intermediate long burst decay. The derived e-folding time are $\tau_1 \approx 40 \pm 3$ s and $\tau_2 \approx 221 \pm 9$ s, respectively with a $\chi^2_{\rm red} = 1.1$ (for 163 d.o.f.). In this fit we included also the first two BAT data points. Note, using only the XRT data points we found the same results within the error bars. A single exponential function is found to be inadequate with $\chi^2_{\rm red} = 5.2$ (166 d.o.f.). In order to compare the decay tail with the intermediate long X-ray burst from 2S 0918-549 and SLX 1737-282 (in't Zand *et al.* 2005; Falanga *et al.* 2008), and with the decay cooling model from Cumming & Macbeth (2004) we fitted the data with a power-law, and found an index of $\Gamma = -2.14 \pm 0.02$ with a $\chi^2_{\rm red} = 1.7$ (167 d.o.f.). In Fig. 6.6 we show the double exponential best fit (upper panel) and in a log-log scale the power-law best fit (lower panel) to the data. The double exponential fit is statistically preferred over an power-law fit by the F-test probability of 1.2×10^{-14}. Similar values of $\tau_1 = 44 \pm 7$ s and $\tau_2 = 218 \pm 55$ s or power-law index $\Gamma = -1.97 \pm 0.09$ can be obtained from the fit to the bolometric luminosity reported in Fig. 6.5. Also in this case the double exponential fit is statistically preferred over an power-law fit by the F-test probability of 6.6×10^{-3}.

The decay time determined with the light curve in unit of count rates, is restricted to the XRT 0.3–10 keV energy band. This decay time does not take into account the different

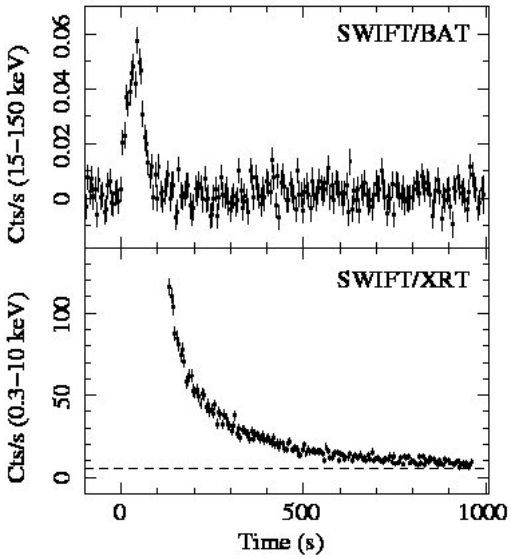

Figure 6.4: The intermediate long type I X-ray bursts detected from XTE J1701-407 on July 17, 2008. The time T_0 expressed in UTC corresponds to $17^h31^m55^s$. The *Swift*/BAT (15–150 keV) and XRT (0.3–10 keV) light curve are shown with a time bin of 5 s. The data gap of ≈ 133 s in the XRT light curve is due to the time elapsed between the BAT trigger and the follow-up observation. The dashed line indicates the background level measured ≈ 3000 s after the burst end.

rise and cooling effect for different energy bands during the outburst, where converting the rates to the bolometric flux or luminosity using the time-resolved spectral results a more realistic decay time can be obtained. Therefore, in the following we consider only the $\tau_1 \approx 40$ s and $\tau_2 \approx 221$ s or the power-law index -2.14.

In Table 6.1 we report the $\tau \equiv f_b/F_{peak} = 92 \pm 22$ s which is only valid if one exponential function describe the decay tail. In our case this value is consistent within the error bars if we consider the double exponential decay as; $f_b/F_{peak} = \epsilon(\tau_1 - \tau_2) + \tau_2 = 71 \pm 12$, where $\epsilon = F_x/F_{peak} = 0.83$ and F_x is the peak flux for τ_1.

6.1.3 Short burst light curves and spectra

In Fig. 6.7 we show the *Swift*/BAT 15–150 keV short burst light curve. The time T_0 expressed in UTC corresponds to $22^h31^m19^s$. The rise time is 1 ± 0.5 s where the total duration is ≈ 8 s. To determine the rise time and burst duration we rebined the light curve to 1 s. For this short burst the XRT light curve starts with a delay of 180 s after the beginning of the burst as seen by BAT. In the XRT data (0.3–10 keV) the burst has not been detected, so the total duration of this burst has to be considered < 180 s. In Fig. 6.7 we show the short burst, and for comparison we plot also the intermediate long burst seen by BAT.

Given the short duration and statistic of the burst light curve we were not able to study a time-resolved spectral analysis. Here we report the burst spectrum analysis integrated over 6 s in order to measure as accurate as possible the peak flux. Burst spectra were well fit by a simple black-body model. The inferred BB temperature, $kT_{bb} = 3.9 \pm 0.5$ keV with an unabsorbed bolometric peak fluxes, $F_{bol} = 3.8 \pm 1.1 \times 10^{-8}$ (0.1–100 keV). The burst occurred at a flux persistent level of $2.3 \pm 0.4 \times 10^{-9}$ erg cm^{-2} s^{-1}. This short burst

occurred at a comparable persistent emission level as the intermediate long burst.

6.2 Discussion

6.2.1 Source distance, persistent flux, and accretion rate

As we discussed in Sect. 1.3, when a burst undergoes a photospheric radius expansion (PRE), the source distance can be determined based on the assumption that the bolometric peak luminosity is saturated at the Eddington limit, $L_{\rm Edd}$, (see Eq. 1.25, Lewin *et al.* 1993; Kuulkers *et al.* 2003). During the PRE episode, while the bolometric luminosity remains constant at the Eddington value, the high energy flux may display a double peak profile and/or a delay in the rise time (e.g., Kuulkers *et al.* 2002; Galloway *et al.* 2006; Falanga et al. 2007). The BAT light curve shows a slow rise time of ≈ 45 s, which is typically observed at high energy in intermediate long helium bursts with PRE (e.g., Kuulkers *et al.* 2002; Molkov *et al.* 2005; Falanga *et al.* 2008).

Since *Swift*/XRT missed the first 133 second of the burst from XTE J1701-407 we cannot exclude that this burst underwent a PRE. This issue cannot be resolved with BAT time-resolved spectral analysis due to limited statistics (see Fig. 6.5). However, the comparison with other PRE bursts showing this slow rise time at high energy leads us to take the observed profile in the BAT light curve as an evidence for a PRE during the first ≈ 50 s of the intermediate long burst, in which case this should correspond to the timescale for the photosphere to fall back to the neutron star surface. For the short burst no conclusion can be drawn as to whether a PRE event occurred (see Fig. 6.7).

Another possibility is that the burst has an intrinsically long rise time. For example, the mixed H/He bursts observed from GS 1826-24 (Galloway *et al.* 2004) do not show PRE, but have a rise lasting for 10 seconds set by hydrogen burning (Heger *et al.* 2007). The duration of the bursts from GS 1826-24 is much less than the long burst from XTE J1701-407. It is not clear whether a long duration mixed H/He burst could have a 50 second rise (see discussion of light curves in section 6.2.4). The fact that helium burning can be extremely rapid, whereas hydrogen burning involves slow weak interactions means that the rise time is longer when hydrogen is present, and PRE much less likely. For example, Fujimoto *et al.* (1987) derived a critical helium fraction necessary to achieve PRE.

Assuming a bolometric peak luminosity equal to the Eddington value for a He type I X-ray burst ($L_{\rm Edd} \approx 3.8 \times 10^{38}$ ergs^{-1}, as empirically derived by Kuulkers *et al.* 2003), we obtain the source distance of $d = 6.2^{+1.6}_{-0.9}$ kpc. For comparison, the theoretical value of this distance (e.g., Lewin *et al.* 1993) found by assuming a He atmosphere and canonical NS parameters (1.4 solar mass and radius of 10 km), is $5.5^{+1.3}_{-0.8}$ kpc. Note also that assuming

Table 6.1: Parameters of the Intermediate long burst.

$F^a_{\rm peak}$ (erg cm^{-2} s^{-1})	$8.2 \pm 2 \times 10^{-8}$
$f^b_{\rm b}$ (erg cm^{-2})	$7.6 \pm 0.3 \times 10^{-6}$
$\tau \equiv f_{\rm b}/F_{\rm peak}$ (sec)	92 ± 22
$\gamma \equiv F^c_{\rm pers}/F_{\rm peak}$	$2.2 \pm 0.5 \times 10^{-2}$

[a]Unabsorbed flux (0.1–100 keV). [b]Fluence (0.1–100 keV). [c]Unabsorbed persistent flux $F_{\rm pers} = (1.8 \pm 0.2) \times 10^{-9}$ erg cm^{-2} s^{-1} (0.1–100 keV).

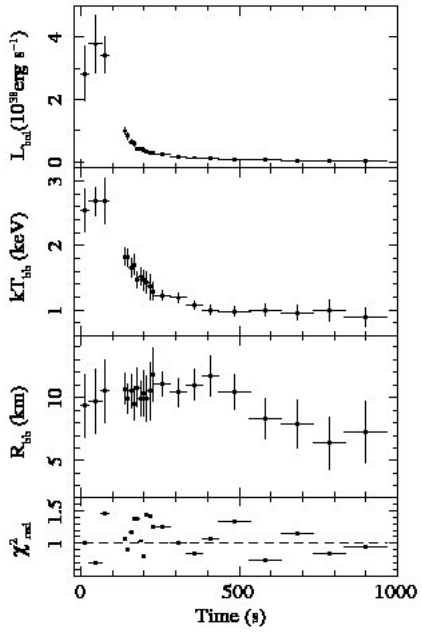

Figure 6.5: Evolution of the spectral parameters, as inferred from *Swift*/BAT (first 86 s) and *Swift*/XRT (833 s) observations. The bolometric luminosity is calculated by assuming a distance of 6.2 kpc, see Sec. 6.2.1. The bottom panel shows the $\chi^2_{\rm red}$ values for these fits.

a peak luminosity of a typical H burst ($X_0 = 0.7$) would give a closer source distance of ≈ 4 kpc. In the following we consider $d \approx 6.2$ kpc.

The best fit to the 2–20 keV persistent emission spectrum of XTE J1701-407 required an absorbed simple power-law model with $\Gamma \approx 2.1$. Assuming a distance of 6.2 kpc, the estimated intermediate long burst pre-burst persistent unabsorbed flux between 0.1–100 keV, $F_{\rm pers} \approx 1.8 \times 10^{-9}$ erg cm^{-2} s^{-1}, translates into a bolometric luminosity of $L_{\rm pers} \approx 8.3 \times 10^{36}$ erg s^{-1}, or $\approx 2.2\% L_{\rm Edd}$.

The local accretion rate per unit area is then given by $L_{\rm pers} = 4\pi R^2 \dot{m}(GM/R)/(1+z)$, or

$$\dot{m} = 4.0 \times 10^3 \text{ g cm}^{-2} \text{ s}^{-1} \left(\frac{R}{11.2 \text{ km}}\right)^{-1} \left(\frac{M}{1.4\ M_\odot}\right)^{-1} \left(\frac{d}{6.2 \text{ kpc}}\right)^2 \left(\frac{1+z}{1.26}\right). \quad (6.1)$$

A convenient unit for accretion rate is the Eddington accretion rate. Here, we define the local Eddington accretion rate as $\dot{m}_{\rm Edd} \equiv 1.8 \times 10^5$ g cm^{-2} s^{-1}, the local accretion rate onto a $M = 1.4\ M_\odot$, and $R = 11.2$ km neutron star that gives an accretion luminosity equal to the empirically derived Eddington luminosity 3.8×10^{38} erg s^{-1} from Kuulkers *et al.* (2003). This gives $\dot{m}/\dot{m}_{\rm Edd} = 2.2\%$.

6.2.2 The energy, ignition depth, and recurrence time of the long burst

The observed energy of the long burst allows us to estimate the ignition depth. The measured fluence of the burst is $f_b = 7.6 \times 10^{-6}$ erg cm^{-2}, giving a burst energy release $E_{\rm burst} = 4\pi d^2 f_b = 3.5 \times 10^{40}$ ergs $(d/6.2 \text{ kpc})^2$. The ignition depth is given by $E_{\rm burst} =$

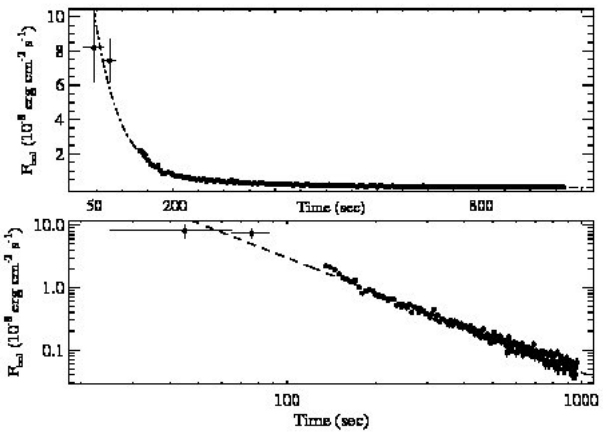

Figure 6.6: Top panel: We show the BAT and XRT intermediate long burst light curve with the double exponential best fit curve. Bottom panel: The same data presented in a log-log scale with the power-law best fit model.

$4\pi R^2 y_{\rm ign} Q_{\rm nuc}/(1+z)$, or

$$y_{\rm ign} = 1.8\times10^9 \text{ g cm}^{-2} \left(\frac{Q_{\rm nuc}}{1.6 \text{ MeV/nucleon}}\right)^{-1} \left(\frac{R}{11.2 \text{ km}}\right)^{-2} \left(\frac{1+z}{1.26}\right). \quad (6.2)$$

The value of $Q_{\rm nuc} \approx 1.6$ MeV corresponds to the nuclear energy release per nucleon for complete burning of helium to iron group elements. Including hydrogen with mass-weighted mean mass fraction $\langle X\rangle$ gives $Q_{\rm nuc} \approx 1.6 + 4\langle X\rangle$ MeV/nucleon (Galloway *et al.* 2004), where we include losses due to neutrino emission following Fujimoto *et al.* (1987). For $\langle X\rangle = 0.7$, the solar composition value, $Q_{\rm nuc} = 4.4$ MeV/nucleon, and $y_{\rm ign} = 6.5\times10^8$ g cm^{-2}.

At an accretion rate of 4×10^3 g cm^{-2} s^{-1}, the recurrence time corresponding to a column depth of $y_{\rm ign} = 1.8\times10^9$ g cm^{-2} (pure helium composition) is $\Delta t = (y_{\rm ign}/\dot{m})(1+z) = 6.6$ days, or for $y_{\rm ign} = 6.5\times10^8$ g cm^{-2} (solar composition) is $\Delta t = 2.4$ days. The intermediate long burst, as the first observed burst, occured 40 days after the detection of XTE J1701-407. The effective exposure time on the source from the beginning of the outburst to the intermediate long burst was 0.34 days, and 0.14 days between both bursts. The elapsed time on the source is thus too short compared to the theoretically derived recurrence time to allow us to get an observational measurement of the recurrence time.

6.2.3 Theoretical comparison with ignition models

To try to understand the nuclear burning processes responsible for the long burst, we compare the observed properties with type I X-ray burst ignition models. The ignition conditions are calculated as described in Cumming & Bildsten (2000), but we take $R = 11.2$ km, $M = 1.4\ M_\odot$, and the energy release in hot CNO burning[3] $E_H = 6.0\times10^{18}$ erg g^{-1}. The results are shown in Table 6.2 for several different choices of accreted hydrogen fraction

[3]Here we adopt the value of E_H from Wallace & Woosley (1981), which includes neutrino losses. These were not included by Cumming & Bildsten (2000).

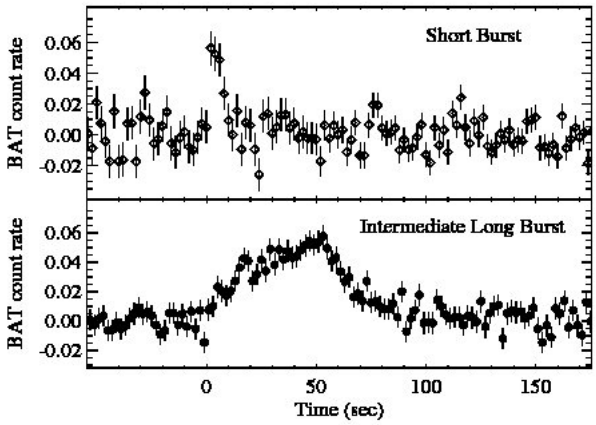

Figure 6.7: Top panel: The short type I X-ray burst detected from XTE J1701-407 on July 27, 2008. For comparison of the rise time and duration we show also the intermediate long burst (see also Fig. 6.4). The *Swift*/BAT (15–150 keV) light curves are shown with a time bin of 2 s.

X_0, accretion rate $\dot{m}$ and flux from the crust Q_b. The ignition conditions are calculated by modeling the temperature profile of the accumulating fuel layer, and adjusting the thickness of the layer until a condition for thermal runaway is met at the base. These models do not include the effects of previous bursts on the ignition conditions (e.g. Woosley *et al.* 2004), and we have not included gravitational sedimentation which is important at low accretion rates (Peng *et al.* 2007). In the following, we consider three posibilities: 1) accretion of pure helium, 2) hydrogen-rich matter at solar, and 3) low metallicity.

Pure helium accretion

For pure helium accretion, the accumulating fuel layer is heated from below by a flux $\dot{m}Q_b$ from the crust, where Q_b is the energy per accreted nucleon flowing outwards from the crust. We set the accretion rate at the observed value $\dot{m}/\dot{m}_{\rm Edd} = 2.2\%$, and adjust the value of Q_b until we find ignition at the inferred column for pure helium burning $y_{\rm ign} = 1.8 \times 10^9$ g cm^{-2} (and therefore obtain the observed burst energy). A flux from below $Q_b = 0.5$ MeV/nucleon matches the observed burst energy at 2.2% Eddington. We also include models with $Q_b = 0.3$ and 0.7 MeV/nucleon in Table 6.2 to show the sensitivity of the ignition depth to the amount of heat from below. Note that since the combination $\dot{m}Q_b$ sets the total flux heating the layer, an increase or decrease in Q_b keeping $\dot{m}$ fixed is equivalent to increasing or decreasing $\dot{m}$ with Q_b fixed. Therefore, if the inferred accretion rate is smaller by some factor, the value of Q_b needed to match the observed energy will be larger by the same factor.

The outwards flux expected from the crust depends on accretion rate and the core neutrino emissivity (Brown 2000), ranging from $\dot{m}Q_b \approx 0.1$ MeV per nucleon at high accretion rates up to $\dot{m}Q_b \approx 1.5$ MeV per nucleon at low accretion rates. The value depends on how much of the total ≈ 1.5 MeV per nucleon heat released in the crust by pycnonuclear and electron capture reactions (Haensel & Zdunik 1990, 2008) is conducted into the core and released as neutrinos compared to being conducted outwards. The number of 0.5 MeV/nucleon that we infer here is quite reasonable for an accretion rate

Table 6.2: Type I X-ray burst ignition conditions[a]

Model	$\dot{m}^b$ ($\%\,\dot{m}_{\rm Edd}$)	$Z_{\rm CNO}$	X_0^c	Q_b	$y_{\rm ign,9}$	$T_{\rm ign,8}$	$\langle X\rangle$	X_b	$Q_{\rm nuc}$	E_{40}	Δt (days)
Pure helium accretion[d]											
1	2.2	0.02	0	0.5	1.8	1.4	0	0	1.6	3.4	6.5
2	2.2	0.02	0	0.3	7.4	1.2	0	0	1.6	14	27
3	2.2	0.02	0	0.7	0.84	1.5	0	0	1.6	1.6	3.1
Accretion hydrogen rich material											
4	2.2	0.02	0.7	0.5	0.13	2.0	0.38	0.07	3.1	0.49	0.48
5	0.69	0.02	0.7	0.5	1.6	1.4	0.01	0	1.64	3.2	19
6	2.2	0.001	0.7	0.1	0.67	1.7	0.62	0.54	4.1	3.3	2.5
7	2.2	0.001	0.7	0.5	0.53	1.8	0.63	0.43	4.1	2.7	2.0

[a] Models 1, 5, and 6 provide a good match to the observed burst energy of 3.5×10^{40} ergs. In addition, models 1 and 6 have an accretion rate that matches the value inferred from the persistent luminosity.
[b]We define $\dot{m}_{\rm Edd} = 1.8\times10^5$ g cm^{-2} s^{-1}, the local accretion rate onto a 1.4 $M_\odot$, $R =$ 11.2 km neutron star that gives an accretion luminosity equal to the empirically derived Eddington luminosity 3.8×10^{38} erg s^{-1} from Kuulkers *et al.* (2003).
[c]The hydrogen mass fractions are: in the accreted material X_0, at the base of the layer at ignition X_b, and the mass-weighted mean value in the layer at ignition $\langle X\rangle$.
[d]Note that the ignition conditions for pure helium accretion do not depend on the choice of $Z_{\rm CNO}$.

of 2.2% Eddington; for example, the models calculated by Cumming *et al.* (2006) for persistently accreting sources have $Q_b = 0.3$ to 0.9 MeV/nucleon at this accretion rate. Galloway & Cumming (2006b) modelled the X-ray bursts observed from SAX J1808.4-3658 and found $Q_b \approx 0.3$ MeV/nucleon for $\dot{m} \approx 3\%\ \dot{m}_{\rm Edd}$.

Accretion of hydrogen rich matter with solar metallicity

Next, we consider that the source is accreting hydrogen rich matter with the solar hydrogen fraction $X_0 = 0.7$ and a metallicity similar to solar, with mass fraction of CNO elements $Z_{\rm CNO} = 0.02$. In that case, the hydrogen burns at a fixed rate during accumulation of the fuel layer, by the beta-limited hot CNO cycle of Hoyle & Fowler (1965). The hydrogen depletes at a column depth

$$y_{\rm d} = 1.5\times10^8\ {\rm g\ cm^{-2}} \left(\frac{\dot{m}}{0.022\dot{m}_{\rm Edd}}\right)\left(\frac{Z_{\rm CNO}}{0.02}\right)^{-1}\left(\frac{X_0}{0.7}\right) \quad (6.3)$$

smaller than the inferred ignition depth, so that a thick layer of pure helium accumulates and ignites beneath a steady hydrogen burning shell. Therefore, even though solar composition material is accreted, the mean hydrogen fraction at ignition in the fuel layer is very small, giving $Q_{\rm nuc}$ close to the value 1.6 MeV/nucleon for pure helium.

For a CNO mass fraction $Z_{\rm CNO} = 0.02$, the observed burst energy is obtained for an accretion rate three times lower than inferred from the observed X-ray luminosity $\dot{m}/\dot{m}_{\rm Edd} = 0.69\%$ (model 5 in Table 6.2). At an accretion rate of 2.2% Eddington, the burst energy is a factor of seven too small (model 4).

Accretion of hydrogen rich matter with low metallicity

In the third scenario, we consider that the material is hydrogen rich, but with a low metallicity. Model 6 has a burst energy close to the observed energy at the inferred accretion rate of 2.2% Eddington, with a CNO mass fraction $Z = 10^{-3}$, roughly 10% of the solar metallicity. In this case, the amount of hot CNO burning is reduced substantially, so that hydrogen permeates the entire fuel layer at ignition. Hot CNO burning still operates at a low level and causes some preheating of the fuel layer. The hydrogen increases the amount of nuclear release during the burst, giving $Q_{\rm nuc} \approx 4$ MeV/nucleon, and an ignition depth three times smaller than for the pure helium case. The low metallicity ignition is less sensitive to Q_b than the pure helium ignition. Model 7, which has the same conditions as model 6, but with $Q_b = 0.5$ rather than $Q_b = 0.1$, has a burst energy within almost 20% of the observed value.

One caveat regarding the low metallicity ignition models is that there can be substantial heating of the accumulating fuel layer because of nuclear reactions associated with the ashes of previous bursts. Woosley *et al.* (2004) found that the burst behavior at accretion rates ≈ 0.1 Eddington was insensitive to the metallicity of the accreted material due to this effect. However, they found that at lower accretion rates there was good agreement with the ignition models presented here (see Woosley *et al.* 2004, Table 9).

Summary of ignition models

We present three ignition models in Table 6.2 that fit the observations. Models 1 and 6 have the correct burst energy and accretion rate. They correspond to accretion of pure helium (model 1), for which the layer is heated by the outwards flux from the neutron star crust, and for accretion of hydrogen rich material with low metallicity (model 6), for which a low level of hydrogen burning preheats the layer during accumulation, but the hydrogen fraction at ignition is substantial and makes a significant contribution to the burst energetics. Third, model 5 has the correct burst energy, but at an accretion rate three times lower than observed. Given the uncertainties in translating the observed X-ray luminosity to accretion rate, it seems worthwhile considering this model further. In this model, the accreted composition is hydrogen-rich with a solar metallicity. This leads to depletion of the hydrogen by the hot CNO cycle and the build-up of a thick layer of pure helium beneath the hydrogen shell.

There is a fourth possibility, which is that the source is accreting hydrogen-rich material, but the hydrogen burns unstably in a series of short flashes. The helium produced in the short flashes builds up and make a pure helium layer that ignites to give the long burst. This is similar to model 5, but with unstable rather than stable hydrogen burning.

One way to distinguish the various possible explanations for the burst energetics would be a recurrence time measurement: as shown in Table 6.2, the different scenarios predict differences in recurrence time. In fact, this is equivalent to a measurement of the α parameter[4] for the bursts, which would indicate the fuel type (e.g. $\alpha \approx 40$ for solar

[4]The quantity α is defined as the ratio of the total energy emitted in the persistent flux to that emitted

hydrogen abundance as found for example in GS 1826-24, Galloway *et al.* 2004).

While this work was in preparation, a similar analysis of the intermediate burst from XTE J1701-407 was carried out and reported in the preprint by Linares *et al.* (2008b). The bolometric peak flux for the long burst and therefore the limits on the source distance are consistent with the values we obtain here. However, the persistent luminosity and burst energy given in Linares *et al.* (2008b) are a factor of two smaller than our values, being restricted to the energy range 1–50 keV, whereas we have included a bolometric correction. These values are used in the interpretation of the long burst, resulting in an accretion rate of $\dot{m} = 1.9 \times 10^3$ g cm^{-2} s^{-1} = 1.1% $\dot{m}_{\rm Edd}$ and a burst energy of $E_b = 1.6 \times 10^{40}$ ergs, both a factor of two smaller than the values we find in here. Repeating the ignition calculations presented earlier for this lower accretion rate, we find that accretion of solar composition material ($X_0 = 0.7$) gives a burst energy of $E_b = 1.5 \times 10^{40}$ ergs for $Q_b = 0.1$ MeV/nucleon, and $E_b = 1.0 \times 10^{40}$ ergs for $Q_b = 0.5$ MeV/nucleon. Therefore, accretion of solar composition naturally explains the burst energetics for these values of E_b and $\dot{m}$. For pure helium accretion at this rate, we find that $Q_b = 1.5$ MeV/nucleon is required to achieve a burst energy of 1.5×10^{40} ergs (lower values of Q_b result in a deeper ignition and more energetic burst). Whereas this is a larger value than expected at this accretion rate, it is within the range of the total energy released in the crust (Haensel & Zdunik 2008). In addition, since the flux heating the layer is $\propto \dot{m} Q_b$, the requirements on Q_b can be relaxed if the true accretion rate is larger than assumed here. Therefore, we find that the energetics argument given in Linares *et al.* (2008b) against explaining this burst as pure helium is overstated.

6.2.4 Constraints from the light curve

The shape and duration of the light curve offer another way to determine the composition of the fuel that burns during the burst. While we do not have models available with exactly the same burst energy, the low accretion rate models from Woosley *et al.* (2004) are within a factor of two to four in energy and accretion rate, and so we compare these models with the observed light curve. These models have $\dot{M} = 3.5 \times 10^{-10}$ $M_\odot$ yr^{-1}, corresponding to a local accretion rate $\dot{m} = 1\%$ $\dot{m}_{\rm Edd}$.

First, we compare the observed light curve with burst 2 from model zm of Woosley *et al.* (2004) (solid curve in Fig. 6.8). This model is for accretion of hydrogen rich ($X_0 \approx 0.7$) matter with a low metallicity, $Z = 10^{-3}$, and so is similar to model 6 in Table 6.2. The burst has a total energy release of 2.0×10^{40} ergs, just less than a factor of two smaller than the observed burst. The recurrence time is 3.0 days, and ignition column $y_{\rm ign} = 3.6 \times 10^8$ g cm^{-2}. The ignition column is just less than a factor of two smaller than the observed burst. The peak luminosity of this burst is close to the Eddington luminosity for solar composition, suggesting that the distance may be closer than the 6.2 kpc assumed here. A closer distance would bring these light curves into better agreement. The model light curve has a steep decline at late times, somewhat steeper than the observed decline. An extra factor of two in ignition column would give the correct burst energy and lengthen the model burst light curve, bringing it into better agreement with the observed burst. Another point to note is that this burst has a slow rise time, lasting for several seconds, as expected for a low helium mass fraction (Fujimoto *et al.* 1987).

The dashed curve in Fig. 6.8 shows burst 3 from model Zm of Woosley *et al.* (2004). This model has hydrogen-rich matter with solar metallicity, $Z = 0.02$, and so is similar

in a burst, $\alpha = F_{\rm pers} \Delta t / f_{\rm b}$, where Δt is the time interval between two bursts.

to model 5 of Table 6.2. The hydrogen burns away in a thin shell, leaving a pure helium layer that ignites. This burst has a total energy release of 8.0×10^{39} ergs, a factor of 4 smaller than observed. The recurrence time is 4.5 days, and ignition column depth 5.6×10^8 g cm^{-2}. The burst reaches close to the pure helium Eddington luminosity. The duration of the burst is shorter than the observed burst by a factor of $\approx$ 5–10. The slope of the decay is shallower than the observed slope. The rise time of this burst is very fast, a fraction of a second, in contrast to the much slower rise of the hydrogen-rich burst (model zm; solid line in Fig. 6.8).

We also include some cooling models calculated following Cumming & Macbeth (2004). For a given ignition column, an energy release per gram of 1.6 MeV per nucleon is deposited in the layer, as would be appropriate if the helium burned to iron group elements at each depth at the start of the burst. We have also computed models for a lighter ash and correspondingly smaller energy deposition (Woosley *et al.* 2004 find that the burning does not go all the way to iron group in their model zM), but the differences are small, and this does not change our conclusions. The cooling of the layer is then followed, with the flux from the surface limited to the Eddington luminosity for pure helium[5]. We show two examples in Fig. 6.8. The first has $y_{\rm ign} = 6 \times 10^8$ g cm^{-2} to match the Woosley *et al.* (2004) model Zm burst. The second has $y_{\rm ign} = 2 \times 10^9$ g cm^{-2} as needed to get the observed burst energy (models 1 and 5 in Table 6.2). The shape of the cooling models agrees well with the model Zm light curve, and agrees within a factor of two in the cooling timescale. Even allowing for this factor of two in the $y_{\rm ign} = 2 \times 10^9$ g cm^{-2} model, the cooling is faster than the observed light curve.

In summary, although the models from Woosley *et al.* (2004) are not at exactly the same ignition conditions as implied by the observations of XTE J1701-407, our comparison suggests that pure helium ignition at the inferred ignition column depth (with or without a small overlying hydrogen burning shell) have cooling times that are shorter than the observed light curve. On the other hand, a hydrogen-rich composition throughout the layer, as expected for low metallicity, produces a longer lasting light curve more consistent with the observed cooling time. Both helium and hydrogen-rich burst models reach the Eddington luminosity (either the pure helium or solar composition Eddington luminosity respectively), and therefore could explain the PRE suggested by the similarity between the observed BAT light curve and other intermediate long bursts (see section 3.1). If the slow rise time is intrinsic to the burst and not due to PRE, the hydrogen rich model is preferred as the presence of hydrogen leads to a much slower rise time than for pure helium (Fig. 6.8). The double exponential nature of the decay may also argue for hydrogen burning during the burst. The burst profiles from GS 1826-24 (Galloway *et al.* 2004) are well-fit by a double exponential decay. Further modeling is required to study the expected burst profiles of hydrogen-rich bursts produced as a result of low metallicity accretion.

6.2.5 Origin of the short burst

We have focused on the long duration burst, which has a well-measured fluence and therefore energy. For the short burst, we can only place an upper limit on its fluence. At low accretion rates, unstable ignition of hydrogen can give rise to short duration bursts (e.g.,

[5] As noted by Woosley *et al.* (2004), the shape of the light curve as the luminosity begins to drop below the Eddington luminosity is likely not accurately reproduced by these models, which do not follow the outer layers in detail. We will improve our treatment of this in future work. However, we expect that the late time cooling is not sensitive to this.

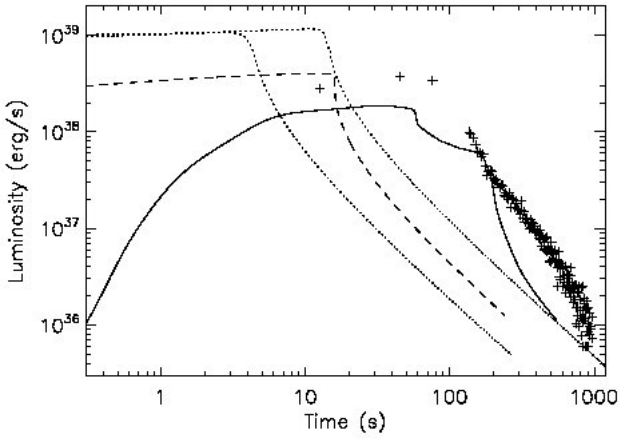

Figure 6.8: Model light curves compared with the observed light curve. The solid curve shows burst 2 from model zm of Woosley *et al.* (2004). This burst has an ignition column and energy a factor of 2 smaller than the observed burst. The dashed curve shows burst 3 from model Zm of Woosley *et al.* (2004). This burst has an ignition column a factor of three to four times smaller than the observed burst. The observed bolometric flux has been converted to luminosity using a distance of 6.2 kpc. Redshift corrections have been applied to the theoretical light curves, with $1 + z = 1.26$. The dotted curves show two cooling models calculated following Cumming & Macbeth (2004), for (left to right) $y_{\rm ign} = 6 \times 10^8$ g cm^{-2} corresponding to Woosley et al. (2004) model Zm (dashed curve), and $y_{\rm ign} = 2 \times 10^9$ g cm^{-2} as needed to explain the observed burst energy (models 1 and 5 in Table 6.2).

Strohmayer & Bildsten 2006; Chenevez *et al.* 2007). Linares *et al.* (2008b) suggest that this is the origin of the short burst from XTE J1701-407, and that either (i) hydrogen-ignited short bursts are producing the helium fuel for the long burst, or that (ii) the source is accreting close to the boundary between unstable and stable hydrogen burning, and stable hydrogen burning produces the helium for the long burst. The comparison to ignition models and model light curves that we have made earlier suggest that hydrogen survives to the ignition depth, implying a low metallicity in the accreted layer. Unfortunately, this would presumably make a thermal instability driven by CNO burning less likely.

For the low metallicity model or for pure helium accretion, another explanation is that the local accretion rate was higher at the time of the short burst. The ignition depth is very sensitive to the base flux or equivalently to the product $\dot{m}Q_b$ (see for example Fig. 8 of in't Zand *et al.* 2005). The persistent flux at the time of the short burst from XTE J1701-407 was slightly larger than at the time of the long burst, even at 30%, not enough to cause a significant reduction in the ignition column depth. We note that short bursts were observed from the intermediate long X-ray burster 2S 0918-549, a suspected ultracompact binary and therefore accreting hydrogen-deficient matter. Therefore, it is not clear to us that the observation of the short burst rules out pure helium accretion in XTE J1701-407, as argued by Linares *et al.* (2008b).

6.3 Conclusions

We have compared the observed properties of the long duration burst from XTE J1701-407 with models of type I X-ray burst ignition conditions and light curves. We showed that the observed burst energy could be understood as (i) pure helium ignition, either as a result of pure helium accretion or of depletion of hydrogen by steady burning during accumulation, or (ii) as ignition of a thick layer of hydrogen-rich material with low metallicity. Comparing with model light curves, we find that the pure helium ignitions cool faster than observed. On the other hand, a hydrogen rich layer gives a longer duration light curve with a steep decline in the tail of the burst, better matching the observed light curve. Therefore we suggest that the intermediate long burst from XTE J1701-407 was powered by unstable burning of a thick layer of hydrogen rich matter with low metallicity. Long X-ray bursts caused by pure helium ignitions beneath a hydrogen shell have been identified, as for example by Galloway & Cumming (2006b) who argued that this was happening in SAX J1808.4-3658. But to our knowledge XTE J1701-407 would be the first example of a source that shows long bursts driven by a thick layer of hydrogen-rich material. The bursts from GS 1826-24 are believed to be powered by rp-process hydrogen burning, giving long ≈ 100 second tails, but the ignition depth in those bursts is an order of magnitude smaller than inferred for the long burst from XTE J1701-407, so that hydrogen can survive until helium ignition, even for solar metallicity. At the low accretion rate in XTE J1701-407, this is not the case: low metallicity is required to reduce the rate of hot CNO burning and allow hydrogen to survive until helium ignites. This implies either that this source is a burster accreting low metallicity H-rich material at a low rate, or another possibility is that heavy elements are able to sediment out from the accumulating layer at this low accretion rate (Peng *et al.* 2007), reducing its effective metallicity. If so, future studies of this source could be used to test the physics of sedimentation at low accretion rates.

PART II: Theory of wind accretion and observations of HMXBs

Chapter 7

Are there magnetars in binary systems? The case of supergiant fast X-ray transients.

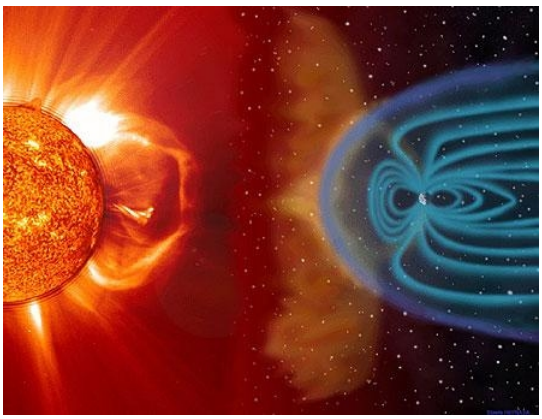

Figure 7.1: A very famous case of interaction between a stellar wind and a magnetosphere. In this case the star is our Sun and the magnetosphere is that of the Earth. Some similarities between this case and that of a magnetic neutron star in a HMXB are discussed in the text.

In the first part of this Chapter, we survey the theory of wind accretion onto a magnetic NS and investigate in-depth all the the different types of interaction between the inflowing wind matter and the neutron star magnetosphere (see also Sect. 1.2.2). We identify different interaction regimes and, expanding on earlier works, we calculate the expected luminosity for each regime and derive the conditions under which transition from one regime to another can take place. In the second part of this Chapter, we introduce a newly discovered subclass of NSHMXBs, collectively termed supergiant fast X-ray transients (SFXT), and apply the above scenario in order to interpret their X-ray activity. We argue that SFXT might host super-strong magnetized NSs, and might thus provide the very first opportunity to detect and study magnetars in binary systems (see Sect. 1.4).

7.1 The wind accretion theory

In Sect. 1.2.2 we described the general picture of a NS immersed in the dense wind of its companion and some of the properties of the binary systems for which this picture is relevant. Here we investigate in detail the conditions under which a magnetic NSs can accrete matter from the wind of its companion and those under which accretion of matter onto the neutron star surface is instead largely inhibited through a centrifugal and/or a magnetic barrier. We start with some definitions.

In the theory of wind accretion in HMXBs, the following radii are defined (Illarionov & Sunyaev 1975; Stella *et al.* 1986):

- The accretion radius, R_a is the distance at which the inflowing matter is gravitationally focused toward the NS (Bondi 1952). It is usually expressed as

$$R_a = 2GM_{NS}/v_w^2 = 3.7 \times 10^{10} v_8^{-2} \text{ cm}, \tag{7.1}$$

  where v_8 is the wind velocity in units of 1000 km s^{-1} and we assumed that the orbital velocity of the star is negligible (Frank *et al.* 2002, see also Sect. 1.2.2). Throughout this Chapter we fix the NS radius and mass at $R_{NS}=10^6$ cm and $M_{NS}=1.4$ $M_\odot$, respectively. The fraction $\dot{M}_{capt}/\dot{M}_w$ of the stellar wind mass loss rate ($\dot{M}_w$) captured by the NS depends on R_a through (see Eq. 1.19)

$$\dot{M}_{capt}/\dot{M}_w \simeq R_a^2/(4a^2) = 2 \times 10^{-5} v_8^{-4} a_{10d}^{-2}. \tag{7.2}$$

  Here $a=4.2\times10^{12} a_{10d}$ cm is the orbital separation, $a_{10d}=P_{10d}^{2/3} M_{30}^{1/3}$, P_{10d} is the binary orbital period in units of 10 days, and M_{30} is the total mass in units of 30 $M_\odot$. In the above equations, and throughout this Chapter we assumed circular orbits and scaled the different parameters with values typical for a binary system hosting a NS and a supergiant companion (see also Sect. 1.2.2).

- The magnetospheric radius, R_M, at which the pressure of the NS magnetic field ($\mu^2/(8\pi R_{NS}^6)$, with μ the NS magnetic moment) balances the ram pressure of the inflowing matter ($\rho_w v_w^2$). In the case in which $R_M>R_a$, the magnetospheric radius is given by (Davies & Pringle 1981)

$$R_M = 3.3 \times 10^{10} \dot{M}_{-6}^{-1/6} v_8^{-1/6} a_{10d}^{1/3} \mu_{33}^{1/3} \text{ cm}. \tag{7.3}$$

  Here we assumed a non magnetized spherically symmetric wind (Elsner & Lamb 1977, see also Sect. 1.2.3), with density[1] $\rho_w(R_M) \sim \dot{M}_w/(4\pi a^2 v_w)$, a dipolar NS magnetic field with $\mu_{33}=\mu/10^{33}$ G cm^3, and $\dot{M}_{-6}=\dot{M}_w/10^{-6}$ $M_\odot$ yr^{-1}. In the following sections we discuss the range of applicability of Eq. 7.3, and the regimes in which a different prescription for R_M should be used.

- The corotation radius, R_{co}, at which the NS angular velocity equals the Keplerian angular velocity, i.e.

$$R_{co} = 1.7 \times 10^{10} P_{s3}^{2/3} \text{ cm}. \tag{7.4}$$

  Here P_{s3} is the NS spin period in units of 10^3 s.

[1] We approximated $a\text{-}R_M \simeq a$, which is satisfied for a very wide range of parameters.

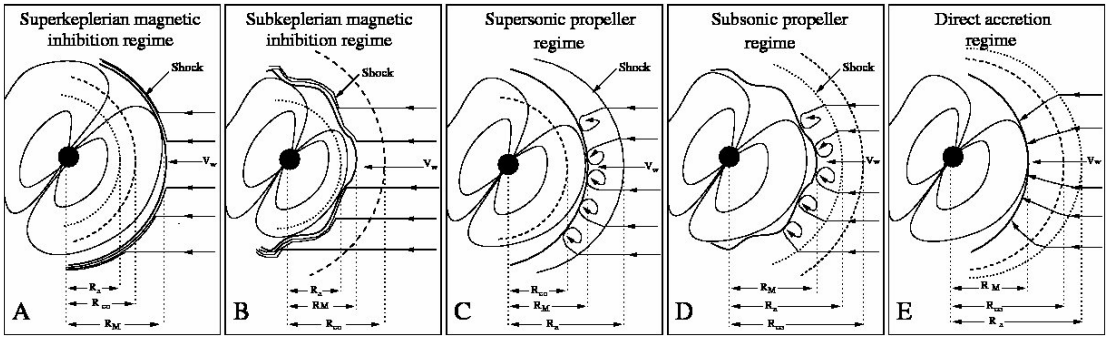

Figure 7.2: Schematic view of a magnetized NS interacting with the inflowing matter from its supergiant companion. All the regimes of Sect. 7.1 are shown, together with the relative position of the magnetospheric radius (solid line), the corotation radius (dashed line), and the accretion radius (dotted line). A wavy solid line is used when the magnetospheric boundary at R_M is Kelvin-Helmholtz unstable. In the supersonic and subsonic propeller regime convective motions at the base of the atmosphere are represented with small eddies.

It is well known that changes in the relative position of these radii result into transitions across different regimes for the NS (Illarionov & Sunyaev 1975; Stella *et al.* 1986). Below we discuss these regimes singularly, and provide a schematic representation of each regime in Fig. 7.2. Being determined primarily by the spin of the neutron star, the corotation radius can change only over evolutionary timescales. Illarionov & Sunyaev (1975) summarises the different regimes experienced by a spinning down NS since its birth, from the initial radio pulsar (i.e. rotation powered) stage, to the regime in which mass accretion onto the neutron star surface can take place. On the other hand the accretion radius and magnetospheric radius depend on the wind parameters (see Eqs. 7.1 and 7.3), which can vary on a wide range of timescales (from hours to months). Therefore, variations in the wind parameters can cause the neutron star to undergo transitions across different regimes on comparably short timescales. In particular, the transition from the accretion regime to the propeller regime (and vice versa), across the so-called "centrifugal barrier", was identified as a likely mechanism responsible for the pronounced activity of Be X-ray pulsar transient systems (Stella *et al.* 1986). Below we summarise the different regimes of a magnetic rotating neutron star, subject to a varying stellar wind, with special attention to the condition under which a "magnetic" (as opposed to "centrifugal") barrier inhibits accretion onto the neutron star (Harding & Leventhal 1992; Rutledge 2001; Mori & Ruderman 2003; Toropina *et al.* 2006, 2001). As it will be clear in the following, new motivation for investigating magnetic inhibition of accretion comes from the discovery of magnetars, neutrons stars with extremely high magnetic fields ($\sim 10^{14}$-10^{15} G, see Sect. 1.4).

7.1.1 Outside the accretion radius: the magnetic inhibition of accretion: $R_M > R_a$

We consider here the case in which the magnetospheric radius is larger than the accretion radius[2]. In systems with $R_M > R_a$ the mass flow from the companion star interacts directly with the NS magnetosphere without significant gravitational focusing, forming a bow shock

[2] A similar case was considered also by Lipunov (1992), "the georotator regime", and by Toropina *et al.* (2001), "the magnetic plow regime".

at R_M (Harding & Leventhal 1992; Toropina *et al.* 2001). A region of shocked gas surrounds the NS magnetosphere with density $\rho_{ps} \simeq 4\rho_w$ and velocity $v_{ps} \simeq v_w/4$ (the subscript "ps" stands for post-shock). These are only rough estimates because the shock is very close to the magnetopause and it does not satisfy the standard Rankine-Hugoniot conditions (Toropina *et al.* 2001). At least in the front part of the shock, i.e. in the region around the stagnation point, the whole kinetic energy of the inflowing matter is converted into thermal energy, and the expected temperature of the heated gas is $T \simeq m_p v_w^2/(3k) \simeq 4\times10^7 v_8^2$ K. Thus, the power released in this region is of order

$$L_{\rm shock} \simeq \frac{\pi}{2} R_M^2 \rho_w v_w^3 = 4.7 \times 10^{29} R_{M10}^2 v_8^2 a_{10d}^{-2} \dot{M}_{-6} \text{ erg s}^{-1} \tag{7.5}$$

(R_{M10} is the magnetospheric radius in units of 10^{10} cm), and is mainly radiated in the X-ray band (Toropina *et al.* 2006). Below we distinguish two different regimes of magnetic inhibition of accretion.

The superKeplerian magnetic inhibition regime: $R_M > R_a, R_{co}$

In this "superKeplerian" magnetic inhibition regime the magnetospheric radius is larger than both the accretion and corotation radii ($R_M > R_a, R_{co}$). Matter that is shocked and halted close to R_M cannot proceed further inward, due to the rotational drag of the NS magnetosphere which is locally superKeplerian. Since magnetospheric rotation is also supersonic[3], the interaction between the NS magnetic field and matter at R_M results in rotational energy dissipation and thus, NS spin down. In order to derive an upper limit on the contribution of this dissipation to the overall luminosity, we assume that the above interaction is anelastic (e.g., Perna *et al.* 2006), i.e. that matter at R_M is forced to corotate. This process releases energy at a rate

$$L_{\rm sd} \simeq \pi R_M^2 \rho_w v_w (R_M \Omega)^2 \simeq 3.7 \times 10^{29} R_{M10}^4 \dot{M}_{-6} a_{10d}^{-2} P_{s3}^{-2} \text{ erg s}^{-1}, \tag{7.6}$$

which adds to the shock luminosity (Eq. 7.5).

The subKeplerian magnetic inhibition regime: $R_a < R_M < R_{co}$

If $R_a < R_M < R_{co}$ the magnetospheric drag is subKeplerian and matter can penetrate the NS magnetosphere. In this "subKeplerian" magnetic inhibition regime, the boundary between the inflowing matter and the magnetosphere is subject to the Kelvin-Helmholtz instability (KHI, Harding & Leventhal 1992). The mass inflow rate across R_M resulting from the KHI is approximately (Burnard *et al.* 1983)

$$\dot{M}_{\rm KH} \simeq 2\pi R_M^2 \rho_{ps} v_{conv} = 2\pi R_M^2 \rho_{ps} v_{sh} \eta_{KH} (\rho_i/\rho_e)^{1/2} (1 + \rho_i/\rho_e)^{-1}, \tag{7.7}$$

where $\eta_{KH} \sim 0.1$ is an efficiency factor, v_{sh} is the shear velocity, ρ_i and ρ_e the density inside and outside the magnetospheric boundary at R_M, respectively. Close to the stagnation point, virtually all the kinetic energy of the wind matter is converted into thermal energy (see also Sect. 7.1.1), and the shear velocity is thus dominated by the magnetosphere's rotation, such that $v_{sh} = v_{rot} = 2\pi P_s^{-1} R_M$. Away from this region, the tangential component of the wind velocity with respect to the NS magnetic field lines increases up to v_{ps} and,

[3] This can be easily seen by comparing v_w with ΩR_M, for the value of the parameters used in this section.

in general, the shear velocity and rate at which plasma enters the magnetosphere due to the KHI, depends on both v_{ps} and v_{rot}. For the aims of the present calculations, we adopt v_{sh}=max(v_{ps}, v_{rot}), and use mass conservation across the KHI unstable layer to estimate the density ratio at R_M (Burnard *et al.* 1983). If matter crossing the unstable layer of height h_t is rapidly brought into corotation with the NS magnetosphere and free-falls onto the NS, mass conservation implies

$$R_M^2 \rho_e v_{conv} \simeq R_M h_t \rho_i v_{ff}(R_M). \tag{7.8}$$

The height h_t of the unstable layer, where matter and magnetic field coexist, is mostly determined by the largest wavelength of the KHI unstable mode (Burnard *et al.* 1983). A detailed analysis of this instability is beyond the scope of the present calculation. In Eq. 7.8 we use conservatively $h_t \simeq R_M$, and discuss in Appendix 7.5 the effect of smaller values of h_t. Therefore accretion of matter at a rate $\dot{M}_{KH}$ onto the NS is expected to release a luminosity of

$$L_{KH} = 3.5 \times 10^{34} \eta_{KH} R_{M10}^2 a_{10d}^{-2} \dot{M}_{-6} (\rho_i/\rho_e)^{1/2} (1+\rho_i/\rho_e)^{-1} \text{ erg s}^{-1}, \tag{7.9}$$

if v_{sh}=v_{ps}, or

$$L_{KH} = 8.8 \times 10^{34} \eta_{KH} P_{s3}^{-1} R_{M10}^3 a_{10d}^{-2} v_8^{-1} \dot{M}_{-6} (\rho_i/\rho_e)^{1/2} (1+\rho_i/\rho_e)^{-1} \text{ erg s}^{-1}, \tag{7.10}$$

if v_{sh}=v_{rot}. The values of ρ_i/ρ_e that we use in Eqs. 7.9 and 7.10 are derived numerically from Eq. 7.8.

In the subKeplerian magnetic inhibition regime, plasma penetration inside the NS magnetosphere is sustained also by Bohm diffusion (Ikhsanov & Pustil'nik 1996). This diffusion, being dependent on the temperature of the plasma (rather than velocity), is highest in the region close to the stagnation point, where the shock slows down the inflowing plasma most efficiently (see also Sect. 7.1.1). In accordance with Ikhsanov *et al.* (2001b), the maximum inflow rate allowed by Bohm diffusion is

$$\dot{M}_{diff} \simeq 2\pi R_M^2 \rho_{ps} V_m = 4.5 \times 10^9 \zeta^{1/2} \dot{M}_{-6} \mu_{33}^{-1/2} R_{M10}^{11/4} a_{10d}^{-2} \text{ g s}^{-1}, \tag{7.11}$$

where V_m=$\sqrt{D_{eff}/t_{ff}}$ is the diffusion velocity, D_{eff}=$(\zeta c k T_i(R_M))/(16 e B(R_M))$ the diffusion coefficient, $T_i(R_M) \simeq m_p v_w^2/(3k)$ the post-shock ion temperature, t_{ff}=$\sqrt{R_M^3/(2GM)}$ the free-fall time, $\zeta \simeq 0.1$ an efficiency factor and m_p the proton mass. In the above equation we also approximated the density outside R_M, around the stagnation point, with ρ_{ps} (though this might be underestimate by a factor of a few, see Toropina *et al.* 2001). Over the whole range of parameters relevant to this work, the diffusion-induced mass accretion rate is orders of magnitude smaller than that due to the KHI. Similarly, the contribution to the total luminosity resulting from the shock and anelastic drag at the magnetospheric boundary can be neglected in this regime.

7.1.2 Inside the accretion radius: $R_M < R_a$

The supersonic propeller regime: $R_{co} < R_M < R_a$

Once R_M is inside the accretion radius, matter flowing from the companion star is shocked adiabatically at R_a and halted at the NS magnetosphere. In the region between R_a and R_M this matter redistributes itself into an approximately spherical configuration (resembling an "atmosphere"), whose shape and properties are determined by the interaction

between matter and NS magnetic field at R_M. This scenario was considered previously by Davies *et al.* (1979) and Davies & Pringle (1981), and we follow here their treatment. These authors demonstrated that hydrostatic equilibrium ensues when radiative losses inside R_a are negligible (we discuss this approximation in Appendix 7.6 and 7.7) and the atmosphere is stationary on dynamical time-scales. Assuming a polytropic law of the form $p \propto \rho^{1+1/n}$, the pressure and density of this atmosphere are:

$$p(R) = \rho_{ps} v_{ps}^2 \left[1 + (1/(1+n)) 8 R_a/R\right]^{n+1} \tag{7.12}$$

$$\rho(R) = \rho_{ps} \left[1 + (1/(1+n)) 8 R_a/R\right]^{n} . \tag{7.13}$$

The value of the polytropic index n depends on the conditions at the inner boundary of the atmosphere, and in particular on the rate at which energy is deposited there.

When the rotational velocity of the NS magnetosphere at R_M is supersonic (see also Sect. 7.1.1), the interaction with matter in the atmosphere leads to dissipation of some of the star's rotational energy and thus spin-down. In the supersonic propeller regime, Davies & Pringle (1981) showed that turbulent motions are generated at R_M which convect this energy up through the atmosphere, until it is lost at its outer boundary. In this case n=1/2. Accordingly, taking into account the structure of the surrounding atmosphere, the magnetospheric radius is given by

$$R_M^{-6} (1 + 16 R_a/(3R_M))^{-3/2} = \frac{1}{2} \dot{M}_w a^{-2} \mu^{-2} v_w . \tag{7.14}$$

This can be approximated by

$$R_M \simeq 2.3 \times 10^{10} a_{10d}^{4/9} \dot{M}_{-6}^{-2/9} v_8^{4/9} \mu_{33}^{4/9} \text{ cm}. \tag{7.15}$$

Matter that is shocked at $\sim R_a$, reaches the magnetospheric boundary at R_M where the interaction with the NS magnetic field draws energy from NS rotation (see also Sect. 7.1.1). According to Davies & Pringle (1981), this contributes

$$\begin{aligned} L_{sd} &= 2\pi R_M^2 \rho(R_M) c_s^3(R_M) \simeq \\ &\quad 5.4 \times 10^{31} \dot{M}_{-6} a_{10d}^{-2} v_8^{-1} R_{M10}^{1/2} (1 + 16 R_{a10}/(3R_{M10}))^{1/2} \text{ erg s}^{-1} \end{aligned} \tag{7.16}$$

to the total luminosity. In the above equation R_{a10}=$10^{-10} R_a$ and $c_s(R_M) = v_{ff}(R_M) = (2GM_{NS}/R_M)^{1/2}$ (Davies & Pringle 1981). In the supersonic propeller regime the energy released through the shock at R_a,

$$L_{shock} = \frac{9}{32} \pi R_a^2 \rho_w v_w^3 \simeq 2.6 \times 10^{29} R_{a10}^2 v_8^2 a_{10d}^{-2} \dot{M}_{-6} \text{ erg s}^{-1}, \tag{7.17}$$

is negligible.

The subsonic propeller regime: $R_M < R_a, R_{co}, \dot{M}_w < \dot{M}_{lim}$

The break down of the supersonic propeller regime occurs when $R_M < R_{co}$, i.e., when the magnetosphere rotation is no longer supersonic with respect to the surrounding material. The structure of the atmosphere changes and the transition to the subsonic propeller regime takes place. Since the rotation of the magnetosphere is subsonic, the atmosphere is roughly adiabatic (n=3/2), and the magnetospheric radius is given by (Davies & Pringle 1981):

$$R_M^{-6} (1 + 16 R_a/(5R_M))^{-5/2} = \frac{1}{2} \dot{M}_w a^{-2} \mu^{-2} v_w . \tag{7.18}$$

This can be approximated by

$$R_{\rm M} \simeq 2\times10^{10} a_{\rm 10d}^{4/7} \dot{M}_{-6}^{-2/7} v_8^{8/7} \mu_{33}^{4/7} \text{ cm}. \quad (7.19)$$

In the subsonic propeller regime, the centrifugal barrier does not operate because $R_M<R_{co}$, but the energy input at the base of the atmosphere (due to NS rotational energy dissipation) is still too high for matter to penetrate the magnetosphere at a rate $\dot{M}_{\rm capt}$ (Davies & Pringle 1981). Nevertheless a fraction of the matter inflow at R_a is expected to accrete onto the NS, due to the KHI and Bohm diffusion[4].

Based on the discussion in Sect. 7.1.1, we estimate the accretion luminosity of this matter by using Eqs. 7.7 and 7.11 (we approximate here the surface of interaction between matter and magnetic field with $4\pi R_M^2$). This gives

$$\begin{aligned} L_{\rm diff} &\simeq GM_{\rm NS}\dot{M}_{\rm diff}/R_{\rm NS} = 4.5\times10^{30}\dot{M}_{-6}\cdot \\ &\cdot a_{\rm 10d}^{-2} R_{\rm M10}^{9/4}\mu_{33}^{-1/2}\zeta^{1/2} v_8^{-1}(1+16R_{\rm a10}/(5R_{\rm M10}))^{3/2} \text{ erg s}^{-1}, \end{aligned} \quad (7.20)$$

and

$$\begin{aligned} L_{\rm KH} &\simeq GM_{\rm NS}\dot{M}_{\rm KH}/R_{\rm NS} = 1.8\times10^{35}\eta_{\rm KH} P_{\rm s3}^{-1} R_{\rm M10}^3 \dot{M}_{-6} a_{\rm 10d}^{-2} v_8^{-1}\cdot \\ &\cdot(1+16R_{\rm a10}/(5R_{\rm M10}))^{3/2}(\rho_{\rm i}/\rho_{\rm e})^{1/2}(1+\rho_{\rm i}/\rho_{\rm e})^{-1} \text{ erg s}^{-1}, \end{aligned} \quad (7.21)$$

for the accretion luminosity arising from matter entering the magnetosphere through Bohm diffusion and KHI, respectively. For the range of parameters of interest here, Eqs. 7.5, 7.20, and 7.21 show that $L_{\rm KH}$ dominates. The rotational energy dissipation at R_M (see Sect. 7.1.2) gives a small contribution with respect to Eq. 7.21 (Davies & Pringle 1981):

$$\begin{aligned} L_{\rm sd} &= 2\pi R_{\rm M}^5 \rho(R_{\rm M})\Omega^3 = \\ &2.2\times10^{30} P_{\rm s3}^{-3} R_{\rm M10}^5 \dot{M}_{-6} v_8^{-1} a_{\rm 10d}^{-2}(1+16R_{\rm a10}/(5R_{\rm M10}))^{3/2} \text{ erg s}^{-1}. \end{aligned} \quad (7.22)$$

The subsonic propeller regime applies until the critical accretion rate

$$\dot{M}_{\rm lim_{-6}} = 2.8\times10^2 P_{\rm s3}^{-3} a_{\rm 10d}^2 v_8 R_{\rm M10}^{5/2}(1+16R_{\rm a10}/(5R_{\rm M10}))^{-3/2} \quad (7.23)$$

is reached, at which the gas radiative cooling (bremsstralhung) completely damps convective motions inside the atmosphere (see Appendix 7.7). If this cooling takes place, direct accretion at a rate $\dot{M}_{\rm capt}$ onto the NS surface is permitted.

The direct accretion regime: $R_M<R_a$, R_{co}, $\dot{M}_w>\dot{M}_{\rm lim}$

If $R_M<R_{co}$ and matter outside the magnetosphere cools efficiently, accretion onto the NS takes place at the same rate $\dot{M}_{\rm capt}$ (see Eq. 7.2) at which it flows towards the magnetosphere. The corresponding luminosity is

$$L_{\rm acc} = GM_{\rm NS}\dot{M}_{\rm capt}/R_{\rm NS} = 2\times10^{35}\dot{M}_{-6}a_{\rm 10d}^{-2}v_8^{-4} \text{ erg s}^{-1} \simeq 2\times10^{35}\dot{M}_{15} \text{ erg s}^{-1}, \quad (7.24)$$

where $\dot{M}_{15}=\dot{M}_{\rm capt}/10^{15}$ g s^{-1}. This is the standard accretion regime; the system achieves the highest mass to luminosity conversion efficiency.

[4]To our knowledge this is the first application of the KHI to the subsonic propeller regime.

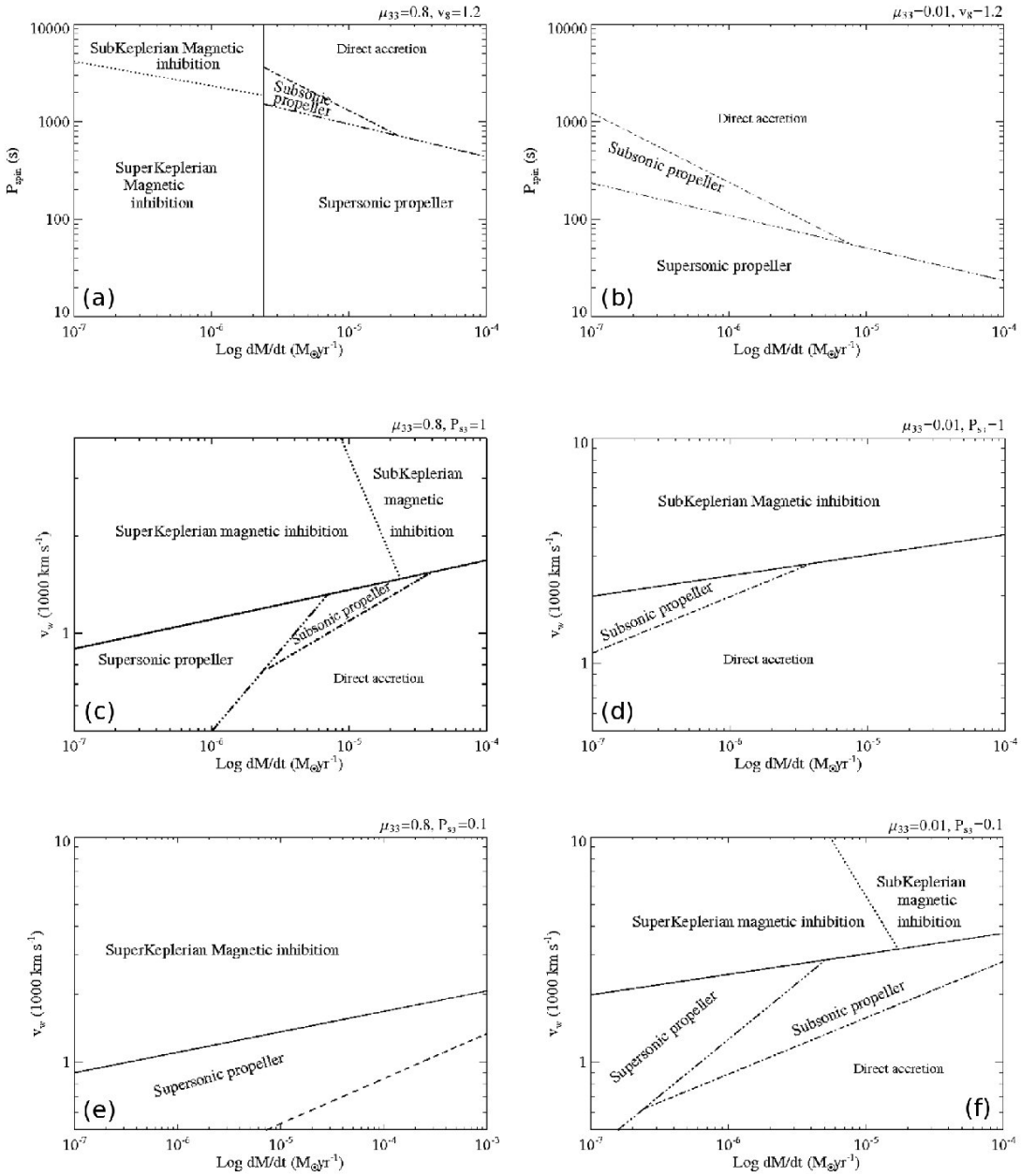

Figure 7.3: Transitions between regimes described in Sect. 7.1 for selected values of the parameters μ_{33}, P_{s3}, and v_8 (in each panel these parameters are indicated in the top right corner). In all cases we fixed a_{10d}=1 (see Sect. 7.2). In panels (a) and (b) we fixed μ_{33} and v_8 and investigated the different regimes in the P_{s3}-$\dot{M}_{-6}$ plane. In panels (c), (d), (e), and (f), instead, fixed parameters are P_{s3} and μ_{33}, and the relevant regimes are shown in the v_8-$\dot{M}_{-6}$ plane. In all cases Eqs. 7.25, 7.26, 7.27, 7.28, and 7.36 (see Appendix 7.6) are represented with a solid line, a dotted line, a dot-dot-dot dashed line, a dot-dashed line, and a dashed line, respectively. Note that the line from Eq. 7.36 is present only in panel (e), i.e our treatment of the the supersonic propeller is self-consistent everywhere except for a small region away from the range of interest for SFXT sources (see also Sect. 7.3).

7.2 Transitions and paths across different regimes

We explore here the conditions under which transitions across different regimes take place. As emphasised in Sect. 7.1, these transitions occur when the relative positions of R_M, R_a, and R_{co} change; we concentrate here on transitions that occur in response to variations in the stellar wind parameters. In the following, since R_M depends only weakly on the orbital period and the total mass of the system, we fix a_{10d}=1 (we explain this choice in Sect. 7.3), and investigate variations in the other four parameters: μ_{33}, P_{s3}, v_8, and $\dot{M}_{-6}$.

The equations that define the conditions for transitions between different regimes are[5]

$$R_M > R_a \Rightarrow \dot{M}_{-6} \lesssim 0.45 \mu_{33}^2 v_8^{11} a_{10d}^2 \tag{7.25}$$

(or equivalently $\dot{M}_{15} \lesssim 0.6 \mu_{33}^2 v_8^7$, see Eqs. 7.1, 7.3 and 7.2), for the magnetic barrier;

$$R_M > R_{co} \Rightarrow P_{s3} \lesssim 2.6 \dot{M}_{-6}^{-1/4} v_8^{-1/4} a_{10d}^{1/2} \mu_{33}^{1/2} \simeq 2.8 \dot{M}_{15}^{-1/4} v_8^{-5/4} \mu_{33}^{1/2} \tag{7.26}$$

(see Eq. 7.3) if $R_M > R_a$, or

$$R_M > R_{co} \Rightarrow P_{s3} \lesssim 1.8 a_{10d}^{2/3} \dot{M}_{-6}^{-1/3} v_8^{2/3} \mu_{33}^{2/3} \simeq 2 \dot{M}_{15}^{-1/3} v_8^{-2/3} \mu_{33}^{2/3} \tag{7.27}$$

(see Eq. 7.15) if $R_M < R_a$, for the centrifugal barrier.

The equation that defines the transition from the subsonic propeller to the direct accretion regime is

$$P_{s3} \gtrsim 4.5 \dot{M}_{-6}^{-15/21} a_{10d}^{30/21} v_8^{60/21} \mu_{33}^{16/21} \simeq 5.5 \dot{M}_{15}^{-15/21} \mu_{33}^{16/21}. \tag{7.28}$$

In Fig. 7.3 the above equations are represented as lines separating different regimes. In panels (a) and (b) we fixed μ_{33} and v_8 and investigated the different regimes in the P_{s3}-$\dot{M}_{-6}$ plane. In panels (c), (d), (e) and (f), instead, P_{s3} and μ_{33} were fixed and the relevant regimes shown in the v_8-$\dot{M}_{-6}$ plane. Below we summarise the different regimes that a system attains in response to variations of $\dot{M}_w$, in the different panels.

Panel (a) shows that, for a wind velocity of v_8=1.2, a strongly magnetized NS (μ_{33}=0.8) can undergo a transition between the superKeplerian and subKeplerian magnetic inhibition regimes in response to changes in the mass loss rate only for typical spin periods $\gtrsim$2000 s. When the mass loss rate reaches $\dot{M}_{-6} \sim 2.4$, the direct accretion or subsonic propeller regime sets in, depending on whether the spin period is longer or shorter than ∼3700 s. For spin periods $\lesssim$420 s the direct accretion regime is not attained for the interval of mass loss rates considered in Fig. 7.3 and only transitions between the superKeplerian magnetic inhibition and supersonic propeller regime are expected.

For lower magnetic fields (μ_{33}=0.01), panel (b) shows that only the supersonic propeller, subsonic propeller, and direct accretion regime can be attained. For spin periods in the range ∼60-230 s transitions can occur between all these three regimes, whereas systems with spin periods longer than ∼1300 s and shorter than ∼20 s are expected to be in the direct accretion and the supersonic propeller regime, respectively. For μ_{33}=0.01 transitions to the superKeplerian and subKeplerian magnetic inhibition regimes cannot take place because the magnetospheric radius is too small to exceed the accretion radius.

In panel (c) (μ_{33}=0.8 and P_{s3}=1), transitions can occur virtually between all the regimes described in Sect. 7.1. In particular, for v_8 in the range 0.9-1.5 transitions are expected to take place between the superKeplerian magnetic inhibition, the supersonic and

[5] Here we used Eqs. 7.15 and 7.19 for the magnetospheric radius in the supersonic and subsonic propeller regime, respectively.

subsonic propeller, and the direct accretion regime, as the mass loss rate increases from $\dot{M}_{-6}\sim0.1$ to $\dot{M}_{-6}\sim100$. For velocities $v_8<0.9$ transitions can occur only between the supersonic propeller, the subsonic propeller and the direct accretion regime, whereas transitions to the superKeplerian and subKeplerian magnetic inhibition regimes are impeded by the fact that the accretion radius cannot be overtaken by R_M. On the contrary, for $v_8>1.5$, the magnetospheric radius is located beyond the accretion radius for any considered value of the mass loss rate, and thus transitions can take place only between the superKeplerian and subKeplerian magnetic inhibition regimes. Similar considerations apply to panels (d), (e), and (f).

For a system with $\mu_{33}=0.01$ and $P_{s3}=1$ (panel (d)), the superKeplerian magnetic inhibition regime never occurs, because the magnetic field is too low and $R_M<R_{co}$ for any $0.1<\dot{M}_{-6}<100$. Instead, the subKeplerian magnetic inhibition regime can be attained for high wind velocities ($v_8=2$), because $R_a\propto v_w^{-2}$.

In panel (e), for $\mu_{33}=0.8$ and $P_{s3}=0.1$, the magnetospheric radius is larger than the corotation radius for the entire range spanned by $\dot{M}_{-6}$. Thus accretion onto the NS does not take place (note that in the region below the dashed line accretion can occur even if $R_M\gtrsim R_{co}$, Davies & Pringle 1981)[6].

Finally, in panel (f) we show the transitions for a system with $\mu_{33}=0.01$ and $P_{s3}=0.1$ s. In this case all the regimes described in Sect. 7.1 are present in the figure, similar to the case of panel (c). However, the region corresponding to the subsonic propeller regime is larger, such that there is only a modest range of (fixed) velocities for which mass loss rate variations in our chosen range ($0.1<\dot{M}_{-6}<100$) can cause transitions through all regimes, from the superKeplerian magnetic inhibition to the direct accretion regime. As we discuss below, this has important consequences for the expected luminosity variations.

We now compute the luminosity swings for some of the examples discussed above in a fashion similar to what was done in the context of centrifugally inhibited accretion in NS X-ray transients (Corbet 1996; Campana *et al.* 1998). Fig. 7.4A applies to a system with $\mu_{33}=0.8$, $P_{s3}=1$, and $v_8=1.2$ (this corresponds to the case $P_{s3}=1$ of Fig. 7.3 panel (a)). The lower panel of this figure shows that, for $0.1<\dot{M}_{-6}<100$, the magnetospheric radius crosses both the centrifugal (R_{co}) and magnetic (R_a) barriers. Correspondingly, the system moves from the superKeplerian magnetic inhibition regime, to the supersonic and subsonic propeller regime, and, finally, to the direct accretion regime, giving rise to a six-decade luminosity swing from $\sim10^{31}$ to $\sim10^{37}$ erg s^{-1}. We note that a large part of this swing (about five decades) is attained across the transitions from the superKeplerian magnetic inhibition to the direct accretion regimes, which take a mere factor of ~5 variation of $\dot{M}_w$.

In the presence of a standard NS magnetic field (10^{12} G), Fig. 7.4B shows that such abrupt luminosity jumps are not expected for a very slowly rotating (1000 s) NS (the other system parameters are the same as those of Fig. 7.4A), since the magnetospheric radius is smaller than both R_a and R_{co}, for any reasonable value of $\dot{M}_w$. Therefore, the direct accretion regime applies, with the the luminosity proportional to $\dot{M}_w$.

In Fig. 7.5 we show the transitions for a system with $\mu_{33}=0.01$ and $P_{s3}=0.1$. The wind velocity is $v_8=1.2$ in Fig. 7.5A, and $v_8=2.2$ in Fig. 7.5B (see also panel (f) of Fig. 7.3). These two figures show that, for sub-magnetar fields, a 100 s spinning NS can undergo a transition across the magnetic barrier (besides the centrifugal barrier), for suitable parameters (a high wind velocity in the case at hand). Such transitions take place over a

[6]This is because, in this region, the mass flow rate is so high that Eq. 7.36 is violated (the supersonic propeller is no longer self-consistent), and convective motions are damped by radiative cooling.

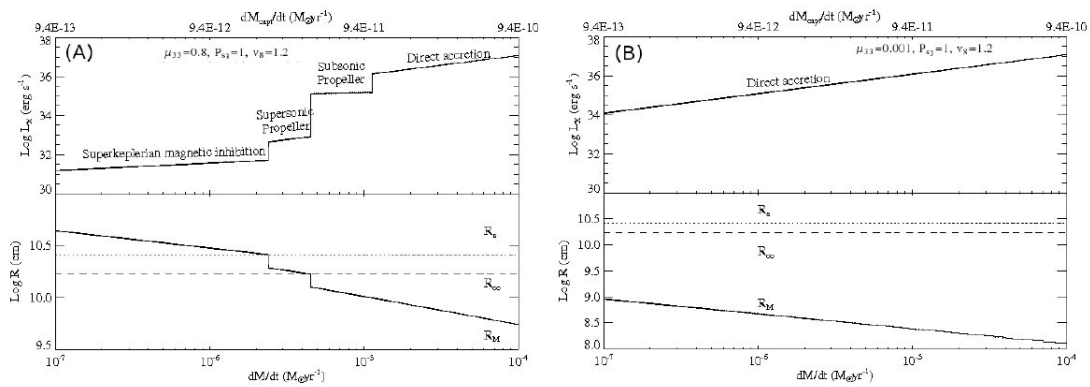

Figure 7.4: (A) *Upper panel*: Variation of the luminosity through different regimes, as a function of the mass loss rate from the companion star. In this case the parameters of the model are fixed at μ_{33}=0.8, P_{s3}=1, and v_8=1.2. *Lower panel*: Relative position of the magnetospheric radius, R_M (solid line), with respect to the accretion radius R_a (dotted line), and the corotation radius R_{co} (dashed line), as a function of the mass loss rate from the companion star.
(B) *Upper panel*: Variation of the luminosity through different regimes, as a function of the mass loss rate from the companion star. In this case the parameters of the model are fixed at μ_{33}=0.001, P_{s3}=1, and v_8=1.2. *Lower panel*: Relative position of the magnetospheric radius, R_M (solid line), with respect to the accretion radius R_a (dotted line), and corotation radius R_{co} (dashed line), as a function of the mass loss rate from the companion star.

more extended interval of mass loss rates. For instance Fig. 7.5B shows that an increase by a factor ∼100 in the mass loss rate is required, in this case, to achieve a factor $\sim 10^5$ luminosity swing comparable with the magnetar case of Fig. 7.4A.

In order to illustrate further the role of the magnetic field, spin period and wind velocity, we show in Fig. 7.6 the way in which the transitions across regimes take place, by holding two of the above variables fixed and stepping the third variable. Figure 7.6A shows the effect of increasing the value of v_8 from 1 to 1.8 (in turn resulting in a decrease of the accretion radius), in a system with μ_{33}=0.8 and P_{s3}=1.

The behaviour of the luminosity changes mainly because a different set of regimes is involved in each case. For v_8=1 (solid line) the system passes through the superKeplerian magnetic inhibition regime, the supersonic, and subsonic propeller regime, finally reaching the direct accretion regime at $\dot{M}_{-6} \simeq 6$. In the case v_8=1.2 (dotted line), the transition to the supersonic propeller shifts towards higher mass loss rates, such that superKeplerian magnetic inhibition applies up to $\dot{M}_{-6} < 2$. Further increasing the wind velocity to v_8=1.4 (dashed line), the system first undergoes a transition to the subsonic propeller at $\dot{M}_{-6} \simeq 10$, bypassing the supersonic propeller (this is because for $\dot{M}_{-6} \simeq 10$ the magnetospheric radius defined by Eq. 7.14 is smaller than the corotation radius). As the mass loss rate increases further, the direct accretion regime sets in for $\dot{M}_{-6} \simeq 20$. In the case v_8=1.8 (dot-dashed line), the corotation radius exceeds the accretion radius. The system is thus in the superKeplerian magnetic inhibition regime for $\dot{M}_{-6} < 20$, while for higher mass loss rates the subKeplerian magnetic inhibition regime applies and the luminosity is dominated by accretion through the KHI. A transition to the direct accretion regime is

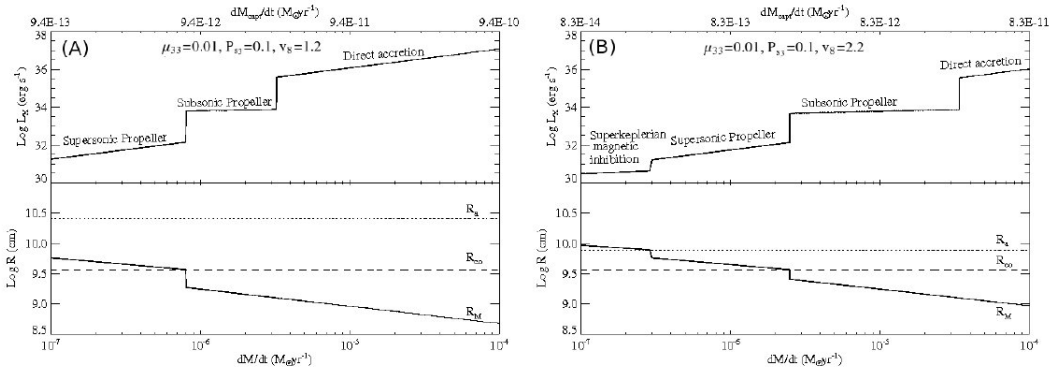

Figure 7.5: (A) *Upper panel*: Variation of the luminosity through different regimes, as a function of the mass loss rate. In this case the parameters of the model are fixed at μ_{33}=0.01, P_{s3}=0.1, and v_8=1.2. *Lower panel*: Relative position of the magnetospheric radius, R_M (solid line), with respect to the accretion radius R_a (dotted line), and corotation radius R_{co} (dashed line), as a function of the mass loss rate from the companion star. (B) Same as (A) but for μ_{33}=0.01, P_{s3}=0.1, and v_8=2.2.

expected for mass loss rates $\dot{M}_{-6}$>100.

Figure 7.6B shows the transitions across different regimes for selected values of the magnetic field, in a system with P_{s3}=1 and v_8=1.2. For the lowest magnetic field in this figure (μ_{33}=0.01, solid line), the magnetospheric radius is smaller than both the accretion and corotation radius for the whole range of mass loss rates spanned in the figure, and the system is always in the direct accretion regime. In the case μ_{33}=0.1 (dotted line), the system is in the subsonic propeller for $\dot{M}_{-6}$<1, while for higher mass inflow rates the direct accretion regime applies. For μ_{33}=0.5 (dashed line) the luminosity behaviour becomes more complex, as the system goes through the superKeplerian magnetic inhibition regime, the supersonic and subsonic propeller regime, and eventually reaches the direct accretion regime at $\dot{M}_{-6}\simeq$8. For μ_{33}=0.8 the same sequence of transitions applies, with the entire luminosity swing taking place over a smaller interval of mass loss rates.

Finally, in Fig. 7.6C we show the effects of increasing the spin period in a system with μ_{33}=0.1 and v_8=1.2. For the lowest spin period considered here (P_{s3}=0.01, solid line), the system remains in the supersonic propeller regime for the whole range spanned by $\dot{M}_{-6}$. In the case P_{s3}=0.5 (dotted line) transitions occur from the supersonic propeller regime ($\dot{M}_{-6}$<0.7), to the subsonic propeller (0.7<$\dot{M}_{-6}$<4) and then to the direct accretion regime ($\dot{M}_{-6}$>4). By further increasing P_{s3} to a value of 1 (dashed line), the system goes through the subsonic propeller and the direct accretion regime, while the supersonic propeller regime does not occur due to the longer spin period as compared to the previous case. For P_{s3}=6 (dot-dashed line) the spin period is so high that the direct accretion regime applies for any reasonable value of $\dot{M}_{-6}$.

The above results show that over a range of values of the key parameters μ_{33}, P_{s3}, and v_8, large luminosity swings can be achieved with comparatively modest changes in the mass loss rate, as the neutron star undergoes transitions from one regime to another. More generally, these transitions result from changes in the relative position of the accretion, magnetospheric, and corotation radii, reflecting short term variations of the wind velocity and mass loss rate, the only parameters that can vary on shorter timescales than secular. Therefore, transitions between different regimes take place once the source parameters are

such that the NS straddles the centrifugal barrier (i.e. $R_M \simeq R_{co}$, when $R_a > R_{co}$) or the magnetic barrier (i.e. $R_M \simeq R_a$, when $R_a < R_{co}$) or both (i.e. $R_M \simeq R_{co} \simeq R_a$). The centrifugal barrier applies to relatively short spin periods. It is well known that the longer the spin period of a transient neutron star, the higher its magnetic field must be for the centrifugal barrier to operate (see Eqs. 7.26 and 7.27). In particular, for periods of hundreds seconds, or longer, magnetic field strengths of $\gtrsim 10^{13}$-10^{14} G are required[7]. On the other hand, we have shown that neutron stars with even longer spin periods and magnetar-like fields are expected to undergo transitions across the magnetic barrier and thus are expected to have an inherently different "switch off" mechanism than short spin period systems. A necessary condition for this is that $R_{co} > R_a$, which translates into $P_{s3} \gtrsim 3 v_8^{-3}$. The magnetic and centrifugal barriers set in (nearly) simultaneously (i.e. $R_a \simeq R_{co} \simeq R_M$) for $\mu_{33} \simeq 0.3 P_{s3}^{7/6} \dot{M}_{15}^{1/2}$.

Taking into account of all the examples discussed in this section, we conclude that:

1. Long spin period systems ($P_{s3} \gtrsim 1$) require magnetar-like B-fields ($\mu_{33} \gtrsim 0.1$) in order for a large luminosity swing ($\sim 10^5$) to arise from modest variations in the wind parameters (e.g. a factor ~ 5 in $\dot{M}_{-6}$). These luminosity swings might result from transition across different regimes through both the centrifugal and magnetic barriers.

2. Shorter spin period systems ($P_{s3} \ll 1$) must posses lower magnetic fields ($\mu_{33} \ll 0.1$) for similar transitions to take place. Somewhat larger variations in the wind parameters are required in order to achieve similar luminosity swings to those of the long period case, and transitions between different regimes occur in most cases through the centrifugal barrier.

3. Few or no transitions are expected for systems with either high magnetic fields and short spin periods, or systems with lower magnetic fields and long spin periods. In the first case the centrifugal barrier halts the inflowing matter at R_M and accretion does not take place; such systems might thus be observable only at very low (X-ray) luminosity levels ($\simeq 10^{32}$-10^{33} erg s^{-1}). In the second case $R_M < R_{co}$ for a wide range of wind parameters, accretion can take place, and a high persistent luminosity is released ($\simeq 10^{35}$-10^{37} erg s^{-1}).

7.3 Application to supergiant fast X-ray transients

In this section we propose that transitions across different regimes caused by relatively mild variations of the wind parameters are responsible for the outbursts of a newly discovered class of HMXBs, i.e. the so called supergiant fast X-ray transients (SFXT).

7.3.1 Supergiant Fast X-ray Transients: a newly discovered subclass of HMXBs

As we discussed in Sect. 1.1.2, HMXBs consist of a collapsed object, usually a magnetic NS, that accretes matter from an OB companion star. Mass transfer takes place because of the intense stellar wind from the OB star, part of which is captured by the collapsed object. Only in some short orbital period systems, the early type star, often a supergiant,

[7] This point was already noted in Stella *et al.* (1986).

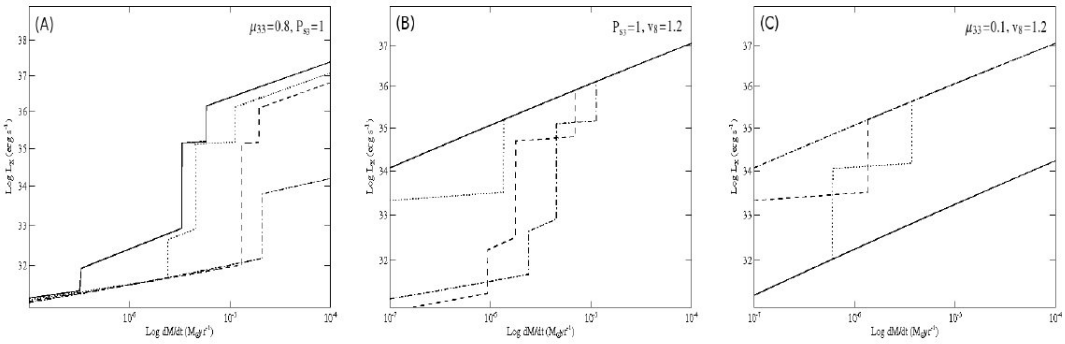

Figure 7.6: Variations of the luminosity through different regimes, as a function of the mass loss rate, for different sets of parameters.
(A): In this case we fixed μ_{33}=0.8 and P_{s3}=1. The solid line shows luminosity variations for v_8=1, the dotted line is for v_8=1.2, and the cases v_8=1.4 and v_8=1.8 are represented with a dashed and dot-dashed line, respectively.
(B): Here the fixed parameters are P_{s3}=1 and v_8=1.2. The different curves correspond to μ_{33}=0.01 (solid line), 0.1 (dotted line), 0.5 (dashed line), and 0.8 (dot-dashed line).
(C): In this case we fixed μ_{33}=0.1 and v_8=1.2. Luminosity variations across different regimes are shown for P_{s3}=0.01 (solid line), 0.5 (dotted line), 1 (dashed line), and 6 (dot-dashed line).

fills its Roche lobe and leads to mass transfer through Roche lobe overflow (Tauris & van den Heuvel 2006). Persistent HMXBs accrete all the time and in most cases display X-ray luminosities in the 10^{35}-10^{38} erg s^{-1} range. Many HMXBs are transient systems that remain at low X-ray luminosity levels (10^{32}-10^{33} erg s^{-1}) most of the time and undergo outbursts lasting from weeks to months. During these outbursts they display nearly identical properties to those of persistent HMXBs. Transient systems usually comprise a Be star donor and relatively long, moderately eccentric orbits, such that the star sits deep in its Roche lobe and stellar wind capture is the only mechanism through which mass transfer takes place. The occurrence of the outbursts is likely associated to variations in the stellar wind of the Be star, such as shell ejection episodes, or build up of matter around the resonant orbits in the slow equatorial wind component (van den Heuvel & Rappaport 1987). However, there are characteristics of the outbursts that are difficult to interpret if accretion onto the neutron star surface takes place unimpeded also in quiescence; these are (a) the large outburst to quiescence X-ray luminosity swing (factor of $\sim 10^3$ or larger) and (b) the presence in a given source of low-luminosity (Type I) outbursts recurring close to periastron and, at different times, of high-luminosity (Type II) outbursts that last for several orbital cycles and display little (if any) X-ray flux variations associated to the orbital phase. These characteristics of Be transients can be explained if the accretion rate (and thus X-ray luminosity) variations that are produced by the stellar wind alone, could be amplified by some "gating" mechanism. Since most Be star HMXB transients contain relatively fast spinning X-ray pulsars, such mechanism has been identified with the centrifugal barrier that results from the rotation of the neutron star magnetosphere (Stella *et al.* 1986).

About 11 transient systems have been recently discovered, which display sporadic outbursts lasting from minutes to hours (i.e. much shorter than Be star transients')

and reach peak luminosities of $\sim 10^{36}$-10^{37} erg s^{-1} (see e.g., González-Riestra *et al.* 2004; Sidoli *et al.* 2005; Grebenev & Sunyaev 2005; Lutovinov *et al.* 2005; Sguera *et al.* 2005; Masetti *et al.* 2006; Sguera *et al.* 2006; Götz *et al.* 2007; Sguera *et al.* 2007).

Between outbursts, SFXTs remain in quiescence with luminosities in the range $\sim 10^{31}$-10^{33} erg s^{-1} (González-Riestra *et al.* 2004; in't Zand 2005; Smith *et al.* 2006; Kennea & Campana 2006). In some cases, very high peak-to-quiescence X-ray luminosity swings (factor of $\sim 10^4$-10^5) were seen on timescales comparable to the outburst duration. Some SFXTs showed also flare-like activity at intermediate luminosity levels (e.g., González-Riestra *et al.* 2004). In the case of IGR J17544-2619, two states of intermediate luminosity were observed: one before the onset of the outburst and the other immediately after, with X-ray luminosities $\sim$3 and $\sim$1 decades below the value reached at the peak of the outburst, respectively (in't Zand 2005).

No firm orbital period measurement has been obtained yet[8]. A recent list of confirmed ($\sim$5) and candidate ($\sim$6) SFXTs is given by Walter & Zurita Heras (2007).

The sporadic character of SFXT outbursts, as observed with *INTEGRAL*, suggested that the duty cycle of these sources (the fraction of time spent in a high luminosity state) is small ($\sim$0.02-0.002, Walter & Zurita Heras 2007). However, recent observations carried out with the very sensitive X-ray telescopes on board *XMM-Newton* and *Chandra* revealed that some SFXTs display flares around a luminosity of $\gtrsim 10^{34}$-10^{35} erg s^{-1} (i.e. well below the *INTEGRAL* limiting sensitivity) for a large fraction of the time (González-Riestra *et al.* 2004; in't Zand 2005; Tomsick *et al.* 2006). Therefore, the indication is that the active phase of SFXT sources (as opposed to true quiescence) lasts longer than previously thought, and the duty cycles are of order $\sim$0.1 or higher.

Optical identifications of SFXTs show that these sources are associated to OB supergiant companion stars (see e.g., Walter & Zurita Heras 2007, and reference therein). The SFXT OB companions have typically mass of $M_*\sim 30 M_\odot$, luminosity of $\log (L_*/L_\odot)\sim$5-6, mass loss rate of $\dot{M}_{\rm w}=10^{-7}$-10^{-5} $M_\odot$ yr^{-1}, and wind velocity of 1000-2000 km s^{-1}. Note, that isolated OB stars with $\log(L_*/L_\odot)\sim$5-6 are persistent soft X-ray sources with luminosity around $\sim 10^{32}$ erg s^{-1} (Cassinelli *et al.* 1981; Berghoefer *et al.* 2001).

It is widely believed that SFXTs contain sporadically accreting neutron stars. Only little is known about their spin period. A coherent periodicity was detected at 4.7 s and 228 s in AX J1841.0-0536 and IGR J16465-4507, respectively (Bamba *et al.* 2001; Lutovinov *et al.* 2005). However, IGR J16465-4507 showed only a factor of $\sim$100 luminosity swing between quiescence and outburst, so it is unclear whether the source should be considered a transient (in fact it is classified as an "intermediate system", Walter & Zurita Heras 2007). The nature of the companion star in AX J1841.0-0536 is still debated (Halpern *et al.* 2004; Nespoli *et al.* 2007). Therefore, these two sources might not belong to the SFXT class. On the contrary, in the prototypical SFXTs XTE J1739-302 (Sguera *et al.* 2006) and IGR J16479-4514 (Walter *et al.* 2006) some evidence has been reported for periodicities in the $\sim$1000-2000 s range.

According to the standard wind accretion theory, the mass capture rate onto the NS scales like $\dot{M}_{\rm w} v_{\rm w}^{-4}$, with $\dot{M}_{\rm w}$, the mass loss rate and $v_{\rm w}^{-4}$, the wind velocity of the supergiant star (see Sect. 1.2.3). Therefore, if accretion onto the collapsed object of SFXTs takes place both in quiescence and outburst, then the corresponding X-ray luminosity swing,

[8] Only IGR J11215-5952 and AX J1749.1-2733 showed recurrent flaring activity, with periodicity of $\sim$165 d and $\sim$185 d, respectively. These are interpreted as outbursts from two systems with unusually long orbital periods ($\gtrsim$100 d, Grebenev & Sunyaev 2005; Sidoli *et al.* 2007; Zurita Heras *et al.* 2007). Thus Walter & Zurita Heras (2007) excluded these sources from their SFXT list.

typically a factor of $\sim 10^4$-10^5, would require wind inhomogeneities with a very large density and/or velocity contrast. Several authors (in't Zand 2005; Leyder *et al.* 2007; Walter & Zurita Heras 2007) suggested the presence of dense clumps in the wind of the OB companions in order to attain the luminosity variations of SFXTs. While some observations provide evidence for a clumpy wind, the characteristics of such inhomogeneities are still poorly known. Numerical simulations suggest that clumps may originate from small scale perturbations in the radiation-driven wind (Dessart & Owocki 2003; Prinja *et al.* 2005). Models involving accretion of clumps are still being actively pursued (Negueruela *et al.* 2008; Walter & Zurita Heras 2007). The requirement on the density and/or velocity contrasts in the wind can be eased if there is a barrier that remains closed during quiescence, halting most of the accretion flow, and opens up in outbursts, leading to direct accretion (this is similar to the case of Be star transients).

In this section we propose that transitions across different regimes caused by relatively mild variations of the wind parameters are responsible for the outbursts of SFXTs. In consideration of the wide range of spin periods inferred for SFTXs, the outbursts of these sources are expected to result from the opening of the magnetic barrier in very long spin period systems and the centrifugal barrier in all other systems (see also Grebenev & Sunyaev 2007; Sidoli *et al.* 2007). More crucially, we conclude that slowly spinning SFXTs should host magnetars, independent of which of the two mechanisms is responsible for their outbursts.

As a case study we consider IGR J17544-2619 (Sunyaev *et al.* 2003), a SFXT observed by *Chandra* during a complex transition to and from a $\sim$1 hour-long outburst, yielding the first detailed characterization of a SFXT light curve. The spin period of IGR J17544-2619 is presently unknown. in't Zand (2005) showed that four different stages, with very different luminosity levels, could be singled out during the *Chandra* observation: (a) a quiescent state with $L_X \simeq 2\times10^{32}$ erg s^{-1}, (b) a rise stage with $L_X \simeq 1.5\times10^{34}$ erg s^{-1}, (c) the outburst peak with $L_X \simeq 4\times10^{37}$ erg s^{-1}, and (d) a post-outburst stage (or "tail") with $L_X \simeq 2\times10^{36}$ erg s^{-1} (see panel (a) of Fig. 7.7; these luminosities are for a source distance of $\sim$3.6 kpc, Rahoui *et al.* 2008). The maximum luminosity swing observed across these stages was a factor of $\gtrsim 6.5\times10^4$.

Motivated by the evidence for >1000 s periodicities in XTE J1739-302 and IGR J16479-4514 (see above), we discuss first the possibility that IGR J17544-2619 contains a very slowly spinning neutron star. We use μ_{33}=1, P_{s3}=1.3, v_8=1.4, and show in Fig. 7.7(b) the different regimes experienced by such a neutron star as a function of the mass loss rate. For $\dot{M}_{-6}$<20 the above values values give $R_M > R_a$ and $R_M > R_{co}$, such that superKeplerian magnetic inhibition of accretion applies. The expected luminosity in this regime, $\sim 10^{31}$ erg s^{-1}, is likely outshined by the X-ray luminosity of the supergiant star (the companion star's luminosity is not shown in Fig. 7.7, but it is typically of order $\sim 10^{32}$ erg s^{-1}, Cassinelli *et al.* 1981; Berghoefer *et al.* 2001). We conclude that the lowest emission state (quiescence) of IGR J17544-2619 can be explained in this way, with the companion star dominating the high energy luminosity (in't Zand 2005). The rise stage is in good agreement with the subKeplerian magnetic inhibition regime, where the luminosity ($\sim 10^{34}$ erg s^{-1}) is dominated by accretion of matter onto the NS due to the KHI. The uncertainty in the value of h translates into an upper limit on the luminosity in this regime which is a factor of $\sim$10 higher than that given above (see Sect. 3 and Appendix 7.5).

During the outburst peak the direct accretion regime must apply at a mass loss rate of $\dot{M}_{-6}$=500. In this interpretation direct accretion must also be at work in the outburst tail at $\dot{M}_{-6} \sim 3$, where a slight decrease in $\dot{M}_w$ would cause the magnetic barrier to close and

the source to return to quiescence. According to this interpretation, if IGR J17544-2619 has a spin period of >1000 s, then it must host a magnetar.

Panel (c) of Fig. 7.7 shows an alternative interpretation of the IGR J17544-2619 light curve, where we fixed μ_{33}=0.08, P_{s3}=0.4, and v_8=1. For this somewhat faster spin (and lower magnetic field), the luminosity variation is mainly driven by a transition across the centrifugal barrier (as opposed to the magnetic barrier). In this case, the quiescent state corresponds to the supersonic propeller regime ($\dot{M}_{-6}$ <0.6), the rise stage to the subsonic propeller (0.6<$\dot{M}_{-6}$<2), while both the peak of the outburst and the tail take place in the direct accretion regime at $\dot{M}_{-6}$=200 and $\dot{M}_{-6}$=10, respectively.

Assuming an even faster NS spin period for IGR J17544-2619, a weaker magnetic field would be required. In panel (d) of Fig. 7.7, we show the results obtained by adopting μ_{33}=0.001, P_{s3}=0.01, and v_8=2. The $\sim 10^{34}$ erg s^{-1} luminosity in the subsonic propeller regime compares well with the luminosity in the rise stage. However, the luminosity of the supersonic propeller regime is now significantly higher than the quiescence luminosity of $\sim 10^{32}$ erg s^{-1} (this is consequence of the higher value of $\dot{M}_{\rm w}$ for which the supersonic propeller regime is attained in this interpretation). We note that, the whole luminosity swing takes place for a wider range of mass loss rates, and the outburst peak luminosity requires $\dot{M}_{-6} \simeq 3000$, an extremely high values even for an OB supergiant.

Interpreting the properties of IGR J17544-2619 in terms of a NS with a spin periods $\ll$100 s is more difficult. For instance, for the subsonic propeller regime to set in, the mass loss rate corresponding to the transition across R_M=R_{co} must be lower than the limit fixed by Eq. 7.23. If instead the transition takes place at higher mass loss rate, the system goes directly from the supersonic propeller to the direct accretion regime (or vice versa), bypassing the subsonic propeller: therefore, the rise stage would remain unexplained. Since fast rotating NSs require lower magnetic fields for direct accretion to take place while in outburst, Eq. 7.23 is satisfied only for very high wind velocities (v_8>2-3). On the other hand, an increase by a factor of $\sim$2 in the wind velocity (with respect to the longer spin period solutions) would give a substantially lower $\dot{M}_{\rm capt}$, such that the subsonic and the direct accretion regime luminosities fall shortwards of the observed values (unless unrealistically high mass loss rate are considered).

Based on the above discussion, we conclude that IGR J17544-2619 likely hosts a slowly rotating NS, with spin period >100 s. Whether the magnetic barrier or the centrifugal barrier sets in, causing inhibition of accretion away from the outbursts, will depend on whether the spin period is longer or shorter then $\sim$1000 s. We note that IGR J16418-4532, a $\sim$1240 s pulsating source with a 3.7d orbital period, displayed short duration flares similar to those of SFXTs and thus might be considered a candidate for hosting an accreting neutron star with a magnetar-like field. However there is no clear evidence yet that IGR J16418-4532 is a transient source, since the very low state revealed with *Swift* might well be due to an eclipse (Tomsick *et al.* 2004; Walter *et al.* 2006; Corbet *et al.* 2006).

As another example we discuss the case of IGR J16465-4507, a SFXTs with a spin period of 228 s. The luminosity behaviour of this source is still poorly known. An outburst at 5×10^{36} erg s^{-1} was observed with *INTEGRAL* (assuming a distance of 12.5 kpc, Lutovinov *et al.* 2005; Smith 2004), which did not detect the source before the outburst down to a level of 5×10^{35} erg s^{-1}. About a week later, *XMM-Newton* revealed the source at 5×10^{34} erg s^{-1} and discovered the 228 s pulsations (Lutovinov *et al.* 2005; Zurita Heras & Walter 2004). If the direct accretion regime applied all the way to the lowest luminosity level observed so far, then an upper limit of μ_{33}=0.004 would be obtained by imposing

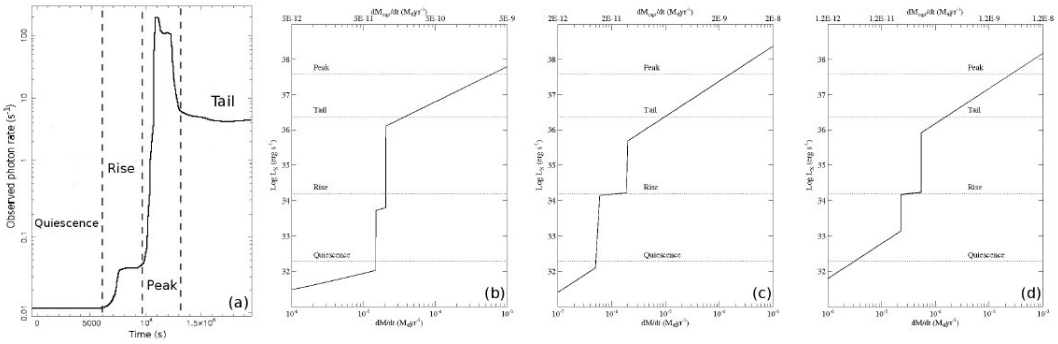

Figure 7.7: Application of the model described in Sect. 7.1 to the IGR J17544-2619 transition from quiescence to outburst.
Panel (a): A schematic representation of the *Chandra* light curve of IGR J17544-2619 obtained by using the segments that were not affected by pile-up (see both panels of figure 2 in in't Zand 2005). The different luminosity stages are clearly visible. According to in't Zand (2005), the count rates on the y-axis correspond to 2×10^{32} erg s^{-1}, 1.5×10^{34} erg s^{-1}, 2×10^{36} erg s^{-1}, and 4×10^{37} erg s^{-1}, in the quiescence state, the rise state, the tail, and the peak of the outburst, respectively.
Panel (b): Interpretation of the quiescence to outburst transition of IGR J17544-2619 in terms of the magnetic barrier model. The dotted horizontal lines mark the luminosity that divide the different regimes. The parameters of the model are fixed at P_{s3}=1.3, v_8=1.4, and μ_{33}=1.
Panel (c): Interpretation of the quiescence to outburst transition of IGR J17544-2619 based on the centrifugal barrier model. The parameters of the model are fixed at μ_{33}=0.08, P_{s3}=0.4, and v_8=1.
Panel (d): Same as panel (c) but here the parameters of the model are fixed at μ_{33}=0.001, P_{s3}=0.01, and v_8=2.

that the neutron star did not enter the subsonic propeller regime (see Eq. 7.28). On the other hand, if the luminosity measured by *XMM-Newton* signalled that the source entered the subsonic propeller regime, while direct accretion occurred only during the outburst detected by *INTEGRAL*, then a considerably higher magnetic field of μ_{33}=0.07 would be required.

The above discussion emphasizes the importance of determining, through extended high sensitivity observations, the luminosity at which transitions between different source states occur, in particular the lowest luminosity level for which direct accretion is still at work. In combination with the neutron star spin, this can be used to infer the neutron star magnetic field. Alternatively accretion might take place unimpeded at all luminosity levels of SFXTs, a possibility which requires a very clumpy wind as envisaged in other scenarios (Negueruela *et al.* 2008; Zurita Heras *et al.* 2007). In this case the neutron star magnetic field can be considerably lower than discussed here. More extensive studies of these sources (and, by analogy, other SFXTs) are clearly required.

7.3.2 Discussion

If the centrifugal barrier operates in IGR J17544-2619, then the activity of this source (and by extension that of SFXTs with similar properties) should parallel that of long spin

period X-ray pulsar transients with Be star companions (Stella *et al.* 1986). One crucial difference between the two classes, namely the duration of the outbursts, might well result from the presence in Be systems of an accretion disk mediating the flow of matter outside the NS magnetosphere. In fact, while in Be systems the star's slow equatorial wind has enough angular momentum to form such a disk, the supergiant's wind in SFXTs is fast and possesses only little angular momentum relative to the NS. In the absence of a disk, variations in the wind parameters take effect on dynamical timescales, whereas in the presence of a disk they are smoothed out over viscous timescales.

If the spin period is sufficiently long in IGR J17544-2619 and other SFXTs, the onset of the magnetic barrier will inhibit accretion. While steady magnetic inhibition of accretion is familiar, e.g. from the earth magnetosphere - solar wind interaction, transitions in and out of this regime have not yet been observed, to the best of our knowledge. Therefore, very long spin period SFXTs might provide the first opportunity to study transitions across such a magnetic barrier. Irrespective of whether the centrifugal or magnetic barrier operates in IGR J17544-2619, a long spin period would imply a high magnetic field, comparable to those inferred for magnetar candidates.

Scenarios involving magnetars with spin periods well above 1000 s have been considered in several studies (Rutledge 2001; Mori & Ruderman 2003; Toropina *et al.* 2001; Liu & Yan 2006; Zhang *et al.* 2004). Moreover a few known accreting X-ray pulsars with unusually long spin periods have already been proposed as magnetar candidates (see e.g., Ikhsanov 2007, and references therein). However these sources display different properties from SFXTs: some are persistent sources; others display week to month-long outbursts; the high spin up measured in IGR J16358-4726 testifies that the accretion flow is likely mediated by a disk (Patel *et al.* 2007). Therefore some of the features of the model discussed here would not be applicable to these sources.

In the context of wind-fed HMXBs, Zhang *et al.* (2004) pointed out that magnetars might be hosted in binary systems with relatively short orbits (∼1-100 d) and long pulse period ($\gtrsim 10^3$-10^5 s). By using evolutionary calculations, these authors showed that magnetars would be easily spun-down to such long spin periods by the interaction with the wind of the companion star, in less than 10^6 yr. The systems we considered here would likely result from a similar evolutionary path.

Once a system approaches the spin period that is required for direct accretion to occur, the short timescale (∼ hours) erratic variations that characterize a supergiant's wind will cause transitions across different NS regimes. Insofar as the average wind properties evolve only secularly, the NS spin will then remain locked around such period, alternating spin-up intervals during accretion and spin-down intervals during quiescence, when accretion is inhibited.

The relevant spin-up timescale during accretion intervals is approximately (see e.g. Frank *et al.* 2002)

$$\tau_{\rm su} = -P_{\rm spin}/\dot{P}_{\rm spin} = \Omega I/(\dot{M}_{\rm capt} l) \simeq 8\times 10^2 I_{45} v_8^4 P_{10\rm d} P_{\rm s3}^{-1} \dot{M}_{17}^{-1} \ {\rm yr}, \qquad (7.29)$$

where $l=2\pi R_{\rm a}^2/(4P_{\rm orb})$ the specific angular momentum of wind matter at the accretion radius, $I=10^{45} I_{45}$ g cm^2 the NS moment of inertia, and $\dot{M}_{17}=\dot{M}_{\rm capt}/10^{17}$ g s^{-1} (this corresponds to an outburst luminosity of $\sim 10^{37}$erg s^{-1}).

A rough estimate of the spin-down timescale is obtained by assuming that most of the quiescence luminosity draws from the rotational energy of the NS (Davies & Pringle 1981); this gives

$$\tau_{\rm sd} = P_{\rm spin}/\dot{P}_{\rm spin} = I\Omega^2/L_{\rm X} = 1.3\times 10^2 I_{45} L_{31}^{-1} P_{\rm s3}^{-2} \ {\rm yr}, \qquad (7.30)$$

where L_{31} is the luminosity produced by the interaction between the magnetosphere and the wind in units of 10^{31} erg s^{-1}. It is apparent that, for magnetar-like fields and long spin periods the above timescales are much shorter than the lifetime of the supergiant's strong wind phase. Therefore secular changes in the wind parameters and/or the NS magnetic field will be easily tracked by the NS spin. Moreover since spin-up and spin-down take place on comparable timescales, it is to be expected that spin-up intervals during outbursts are compensated for by spin-down during quiescent intervals of comparable duration. In other words accretion state of long spin period SFXTs would be expected to have a duty cycle of order $\sim$0.5 or higher. As we discussed before, evidence for high values of the duty cycle is gradually emerging from high sensitivity observations of SFXTs.

On the other hand spin-down may also occur during the accretion intervals as a results of velocity and density gradients in the supergiant's wind that lead to temporary reversals of the angular momentum of the captured wind relative to the neutron star (note that persistent wind accreting X-ray pulsars in HMXBs have long been known to alternate spin-up and spin-down intervals, see e.g. Henrichs 1983). This would tend to favor spin-down, such that the NS spin might gradually evolve longwards of the spin period that is required to inhibit direct accretion and a transient source becomes a persistent one. Interestingly, this might apply to 2S 0114+65, a persistent X-ray pulsar with a luminosity of $\sim 10^{36}$ erg s^{-1}, which displayed variations by a factor of $\lesssim$10. Since its spin period is extremely long ($\sim 10^4$) $R_{\rm M}$ is smaller than the corotation radius and the NS accretes continuously from the relatively weak supergiant companion's wind (see also Li & van den Heuvel 1999).

The SFXTs population might thus represent those supergiant HMXBs systems that have not (yet) evolved away from the spin period at which transitions across different NS state can take place.

We note that for SFXTs to host magnetars their dipole magnetic field must retain values in the μ_{33}=0.1-1 range for a few 10^6 yr, i.e. the typical timescale from the formation of the NS to the onset of the supergiant's strong wind. Presently known magnetar candidates (soft gamma repeaters, SGR, and anomalous X-ray pulsars, AXP) have estimated ages in the 10^4-10^5 yr range (for a review see e.g. Woods & Thompson 2006). Little is known on the long term evolution of the magnetic field of magnetars and different models have been proposed which lead to different predictions. We note that if the irrotational mode of ambipolar diffusion dominates the B-field decay, μ_{33}=0.1-0.3 can be expected for ages of a few 10^6 yr (Heyl & Kulkarni 1998).

According to our proposed scenario the combination of a long spin period and a very large luminosity swing is indicative of the presence of a magnetar. This can be further corroborated through other magnetars signatures, such as e.g. proton cyclotron features in the X-ray spectrum (Zane *et al.* 2001) or sporadic subsecond bursting activity such as that observed in AXPs and SGRs (Gavriil *et al.* 2002).

Finally we remark on the orbital period of SFXTs: in all regimes described in Sect. 7.1, the luminosity scales with $L_X \propto P_{\rm orb}^{-4/3} v_w^{-4}$. For our fiducial wind parameters, orbital periods of tens of days are required for the transition between low and high luminosity states to occur at $\simeq 10^{36}$ erg s^{-1}, a typical luminosity for the onset of SFXT outbursts (Walter & Zurita Heras 2007). This is why throughout the present calculations we scaled our equations by $P_{\rm orb}$=10 d and used the same value in the examples of Figs. 7.3-7.7. Negueruela *et al.* (2008) showed that orbital periods around $\sim$10 d are compatible with the NSs being embedded in the clumpy wind from the supergiant companions, rather than in a quasi-continuous wind. In this case SFXT outburst durations might be associated

with the transit time of a clump

$$\tau_{\rm out} \simeq a/v_{\rm w} = 4.2 \times 10^4 a_{\rm 10d} v_8^{-1} \ {\rm s}, \tag{7.31}$$

in reasonable agreement with the observed durations of individual flares (see Sect. 7.3).

We conclude that clumpiness of the stellar wind, an often-used concept for interpreting SFXT activity, applies to the gating scenarios described here as well. The main advantage of introducing a gating mechanism rests with the possibility to model the very large luminosity swings of SFXTs with much milder density (or velocity) contrasts in the wind.

7.4 Conclusions

In this Chapter we reviewed the theory of wind accretion in HMXBs hosting a magnetic neutron star with a supergiant companion, and considered in some detail the interaction processes between the inflowing plasma and the magnetosphere that are expected to take place when direct accretion onto the neutron star surface is inhibited. We then applied this theory to SFXTs and showed that their large luminosity swings between quiescence and outburst (up to a factor of $\sim 10^5$) can be attained in response to relatively modest variations of the wind parameters, provided the system undergoes transitions across different regimes. Expanding on earlier work, we found that such transitions can be driven mainly by either: (a) a centrifugal barrier mechanism, which halts direct accretion when the neutron star rotation becomes superKeplerian at the magnetospheric radius, a mechanism that has been discussed extensively in Be star X-ray transient pulsars, or (b) a magnetic barrier mechanism, when the magnetosphere extends beyond the accretion radius. Which mechanism and wind interaction regime apply will depend sensitively on the NS spin period and magnetic field, besides the velocity and mass loss rate in the supergiant's wind. In particular, the magnetic barrier mechanism requires long spin periods ($\gtrsim$1000 s) coupled with magnetar-like fields ($\gtrsim 10^{14}$ G). On the other hand, magnetar-like fields would also be required if the centrifugal barrier set in at relatively high luminosities ($\gtrsim 10^{36}$ erg s^{-1}) in neutron stars with spin periods of hundreds seconds.

Evidence has been found that the spin periods of a few SFXTs might be as long as 1000-2000 s. Motivated by this, we presented an interpretation of the activity of IGR J17544-2619 (whose spin period is unknown) in terms of the magnetic barrier by a 1300 s spinning neutron star and showed that the luminosity stages singled out in a *Chandra* observation of this source are well matched by the different regimes of wind-magnetosphere interaction expected in this case. We discussed also an interpretation of this source based on the centrifugal barrier and a slightly shorter spin period (400 s), which reproduced the luminosity stages comparably well. We emphasise that in both solutions the required magnetic field strength ($\gtrsim 10^{15}$ G and $\gtrsim 8\times 10^{13}$ G, respectively) are in the magnetar range.

While the possibility that magnetars are hosted in binary system with supergiant companions has been investigated by several authors (e.g., Zhang *et al.* 2004; Liu & Yan 2006), clear observational evidence for such extremely high magnetic field neutron star in binary systems is still missing. According to the present study, long spin period SFXTs might provide a new prospective for detecting and studying magnetars in binary systems.

Appendix

7.5 On the height of the KHI unstable layer

In this section we expand on the approximation $h_t \sim R_M$, introduced previously in Sect. 7.1.1. As discussed by Burnard *et al.* (1983), the height h_t of the layer where matter and magnetic field coexist due to the KHI, is mostly determined by the largest wavelength unstable mode of the KHI itself. These authors suggested that

$$h_t \simeq h H_s, \tag{7.32}$$

where h is a factor of order $\sim$1, and $H_s = R_M^2\ k_b\ T(R_M)/(GM\ m_p)$ is the scale height of the magnetosheath (note that H_s is roughly of the same order as $R_M \simeq 10^{10}$ cm for $T \sim 10^8$ K). In the subsonic propeller regime, Eq. 7.32 might be a reasonable assumption due to the presence of an extended atmosphere around the magnetospheric boundary; on the contrary, it cannot be used in the subKeplerian magnetic inhibition regime, where matter flowing toward the NS is shocked very close to the magnetospheric boundary. Despite all these uncertainties, we show below that the assumption $h_t = h\ R_M$, with $h \sim 1$, gives a conservative estimate of the mass accretion rate due to the KHI. Using Eq. 7.8 and the definition $v_{conv} = \eta_{KH} v_{sh} (\rho_i/\rho_e)^{1/2}\ (1+\rho_i/\rho_e)^{-1}$, we derive the equations that define the ratio of the densities inside (ρ_i) and outside (ρ_e) the magnetosphere. These are

$$(\rho_i/\rho_e)^{1/2}(1 + \rho_i/\rho_e) = 0.3 \eta_{KH} h^{-1} R_{M10}^{3/2} P_{s3}^{-1}, \tag{7.33}$$

if $v_{sh} = v_{rot}$, and

$$(\rho_i/\rho_e)^{1/2}(1 + \rho_i/\rho_e) = 0.1 \eta_{KH} h^{-1} R_{M10}^{1/2} v_8, \tag{7.34}$$

if $v_{sh} = v_{ps}$. Equations 7.33 and 7.34 show that ρ_i/ρ_e is an increasing function of h^{-1} (for fixed values of v_8, P_{s3} and R_{M10}). Therefore, being $v_{conv} \propto (\rho_i/\rho_e)^{1/2}(1+\rho_i/\rho_e)^{-1}$ and $\dot{M}_{KH} \propto v_{conv}$, the KHI rate of plasma entry inside the magnetosphere is also an increasing function of h^{-1} (provided that $\rho_i \lesssim \rho_e$). Since the KHI unstable layer is located inside the NS magnetosphere, the maximum height attainable is $h_t = R_M$, and thus the approximation used in Sect. 7.1.1 and Sect. 7.1.2 gives a lower limit on the mass flow rate controlled by the KHI in both the subKeplerian magnetic inhibition and the subsonic propeller regime.

Note also that the above lower limit does not violate the stability condition of the quasi-static atmosphere in the subsonic propeller regime. In fact, following Ikhsanov (2001c), this atmosphere can be considered quasi-static if the relaxation time scale of the envelope is less than the drift time scale of the mass flow crossing the magnetospheric boundary. In our case matter penetration inside the NS magnetosphere in the subsonic propeller regime is mostly provided by the KHI, and the above condition translates into $\dot{M}_{KH} \lesssim (R_M/R_{co})^{3/2} \dot{M}_{capt}$, which is satisfied for a wide range of parameters (see Figs. 7.4, 7.5, and 7.6).

An upper limit to the KHI mass flow rate can be obtained by assuming $\rho_i/\rho_e = 1$ (a solution adopted, for example, by Rutledge 2001). According to Burnard *et al.* (1983), the density ρ_i can be increased until the thermal pressure inside the magnetosphere $p_i \propto \rho_i$ is comparable to the magnetic pressure $p_m = B^2(R_M)/(8\pi)$. When this limit is reached, an instability occurs on the lower surface of the unstable layer that increases h_t until $p_i < p_m$ is restored. Using the post-shocked gas temperature at R_M (see Sect. 7.1), it is shown that $\rho_i/\rho_e \sim 1$ does not violate the condition $p_i < p_m$ (at least in the subKeplerian

magnetic inhibition regime). Therefore, even though we restricted ourself to the lower limit h=1, the upper limit on $\dot{M}_{\rm KH}$ might be attainable in some instances. The KHI would then provide matter penetration inside the magnetosphere at a rate $\sim\dot{M}_{\rm capt}$, thus allowing almost all the captured matter to accrete onto the NS. A detailed calculation of KHI accretion in the subKeplerian magnetic inhibition and subsonic propeller regimes will be reported elsewhere.

7.6 Radiative losses in the supersonic propeller

As shown by Davies & Pringle (1981), the treatment of the supersonic propeller regime (see Sect. 7.1.2) is self consistent only if the energy input at the base of the atmosphere, due to the supersonic rotating NS magnetosphere, is larger than radiative losses within the atmosphere itself. The range of validity of this assumption can be determined by using the convective efficiency parameter

$$\Gamma = \mathfrak{M}_{\rm t}^2 v_{\rm t}(R) t_{\rm br}(R) R^{-1}, \tag{7.35}$$

where $\mathfrak{M}_{\rm t}$=$\rm v_t(R)/c_s(R)$ is the Mach number, $\rm v_t$ and $\rm c_s$ are the turbulent and sound velocity, and $\rm t_{br}$=2×10^{11} $\rm T^{1/2}m_p\rho^{-1}(R)$ s is the bremsstralhung cooling time. For most of the NS rotational energy dissipated at the magnetospheric radius to be convected away through the atmosphere's outer boundary, Γ should be $\gtrsim$1 across the entire envelope. Taking into account that in the supersonic propeller regime $\rm v_t\simeq c_s$, $\rm c_s\sim v_{ff}$, $\rm T\sim T_{ff}$ and ρ is given by Eq. 7.13, one finds $\Gamma\propto\rm R^{-3/2}$. Therefore the said requirement is satisfied when $\Gamma(\rm R_a)\gtrsim$1, i.e.

$$\dot{M}_{-6} \lesssim 2.2\times10^2 v_8^5 a_{10\rm d}^2. \tag{7.36}$$

For mass loss rates larger than the above limit, radiative losses are not negligible and the treatment used in Sect. 7.1.2 for the supersonic propeller regime is no longer self-consistent. We checked that the limit of Eq. 7.36 is never exceeded in the cases of interest. We note that a similar value was also derived by Ikhsanov (2002), but his limit is a factor 10 larger than ours. This might be due to the fact that Ikhsanov (2002) used $\rho_{\rm w}$ instead of $\rho_{\rm ps}(1+16/3)^{1/2}$ in the expression for the matter density at $\rm R_a$.

7.7 Radiative losses in the subsonic propeller

A similar calculation to that in Appendix 7.6 in the subsonic propeller regime shows that $\Gamma\propto\rm R^{1/2}$, and radiative losses are negligible if $\Gamma(\rm R_M)\gtrsim$1, i.e.

$$\dot{M}_{-6} \lesssim 2.8\times10^2 P_{\rm s3}^{-3} a_{10\rm d}^2 v_8 R_{\rm M10}^{5/2}(1+16R_{\rm a10}/(5R_{\rm M10}))^{-3/2}, \tag{7.37}$$

that is the same value as that in Eq. 7.23 (a somewhat different value was obtained by Ikhsanov (2001a) assuming a density $\simeq\rho_{\rm w}$ at $\rm R_M$ instead of $\rho_{\rm ps}(1+16\rm R_M/(5R_a))^{3/2}$).

Chapter 8

IGR J16479-4514: the first eclipsing supergiant fast X-ray transient?

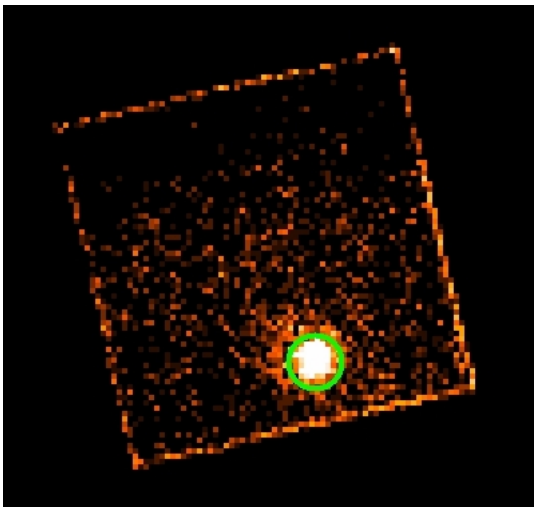

Figure 8.1: An image of the Epic-PN field of view around IGR J16479-4514. The position of the source is highlighted by using a green circle. The Epic-PN was operating in Small Window mode (see Sect. 1.5).

In this Chapter we report on the first long high sensitivity observation (∼32 ks) of the SFXT IGR J16479-4514, carried out when the source was in a low activity state. Following the discussion of Chapter 7, IGR J16479-4514 was identified as one of the most suitable SFXT to search for magnetars hosted in binary systems. In fact, this source was detected in outbursts many times, and some evidence for pulsations with a period of ∼1000 s was found (see Sect. 7.3). Furthermore, IGR J16479-4514 is known to be characterized by a persistent luminosity of $\sim 10^{34}$ erg s^{-1}, that suggests accretion at a low level might take place in this source also when it is not in outburst (Sguera *et al.* 2008; Romano *et al.* 2008a; Walter & Zurita Heras 2007). This is in agreement with the prediction of the gated accretion models described in Chapter 7.

The target of opportunity (ToO) *XMM-Newton* observation we discuss here was car-

ried out after *Swift* discovered a very bright outburst from this source on March 19 (Romano *et al.*2008bRomano Sidoli); the main goal of the ToO was to gain further inside the low level emission of IGR J16479-4514, in order to improve our knowledge of the physical mechanisms that drive this activity and investigate the possible presence of a magnetar in this source.

Surprisingly, instead of the previously known low luminosity level, the *XMM-Newton* observation caught IGR J16479-4514 in a previously undetected very low intensity level. Results from the timing, spectral and spatial analysis of the EPIC-PN data then showed that this unusual low state was caused by an episode of sudden obscuration, possibly an X-ray eclipse by the supergiant companion. So far, this remains the first hint for an X-ray eclipse revealed from an SFXT.

8.1 Data analysis and results

XMM-Newton (Jansen *et al.* 2001) observed IGR J16479-4514 between March 21 14:40:00 UT and March 22 01:30:00 UT for a total time span of ∼37 ks. The EPIC-PN and EPIC-MOS cameras were operated in the small-window and full frame mode, respectively. We processed the observation data files (ODFs) by using the standard *XMM-Newton* Science Analysis System (SAS 7.1). The total effective exposure time was ∼32 ks; the remaining observing time was discarded due to high radiation from solar activity. The EPIC-MOS data were strongly contaminated by single reflections photons from a nearby bright source (likely 4U 1642-45), and thus we report in the following on the analysis of the EPIC-PN data only. The extracted images, spectra and light curves were analyzed by using HEASOFT version 6.4.

Figure 8.2 shows the 2-10 keV EPIC-PN light curve of the observation: in the first ∼4 ks IGR J16479-4514 was caught during the decay from a higher ("A") to a lower ("B") flux state. The latter extended for most of the observation (∼28 ks). We used a bin time of 1000 s in all the light curve fits; all errors are 90% confidence level. The mean count rate during state B was 0.024±0.002, i.e., a factor ∼50 lower than the maximum count rate during state A. In order to search for spectral changes, we extracted light curves in the 2-5 keV and 5-10 keV bands. These are shown in the insert in Fig. 8.2 (first 8 ks of the observation). A fit with an exponential model plus a constant revealed a much slower decay in the soft band light curve: the e-folding time was 5400±1500 s and 910±100 s, in the 2-5 keV and 5-10 keV bands, respectively.

The energy spectra of states A and B are shown in Fig. 8.3, and were rebinned in order to have at least 20 counts per bin. Fits to these spectra were tried first by assuming an absorbed power law plus a Gaussian line at ∼6.4 keV. This model provided a good fit to the spectrum of state A (reduced χ^2=1.1) for a flatter power law index ($0.4^{+0.5}_{-0.4}$) than previously measured for the source (1.6±0.2, Sidoli *et al.* 2008)). The absorption column density was marginally larger ($1.2^{+0.6}_{-0.3}$ ×10^{23} cm^{-2} as opposed to ∼7×10^{22} cm^{-2}). During state B this simple model gave a poorer fit (reduced χ^2=1.7), a much reduced column density ($4.0^{0.6}_{-0.7}$ ×10^{22} cm^{-2}) and a power law index compatible with that of state A. The equivalent width (EW) of the Fe fluorescence line at ∼ 6.4 keV showed a striking increase from ∼ 260 eV (state A) to ∼900 eV (state B). This indicated that in state B (most of) the X-ray flux from the source was obscured along our line of sight, but kept on shining on the Fe-line emitting material. The shape of the light curve (see Fig. 8.2) and evolution of the spectrum across the state A-state B transition presented also remarkable similarities with the eclipse ingress of eclipsing X-ray sources such as OAO 1657-415 (Audley *et al.*

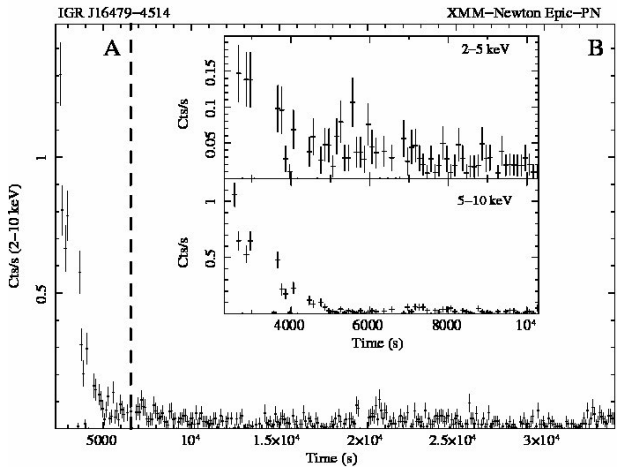

Figure 8.2: EPIC-PN light curve of IGR J16479-4514 in the 2-10 keV band. The bin time is 100 s and the start time is March 21 16:42:42UT. During the first 4 ks of the observation the source flux decayed from a higher ("A") to a lower ("B") level. The insert in the figure shows the first 8 ks of the observation in the 2-5 keV and 5-10 keV energy bands.

2006). Moreover the slower decay of the soft X-ray light curve (in turn similar to that observed in OAO 1657-415) suggested that IGR J16479-4514 is seen through an extended dust-scattering halo (see e.g., Day & Tennant 1991; Nagase *et al.* 1992).

To confirm this we analysed the radial distribution of the X-ray photons detected from IGR J16479-4514 and compared it with the point spread function (PSF) of the *XMM-Newton* telescope/EPIC-PN camera (HEW of ∼12.5"). We did this separately in the 2-5 keV and 5-10 keV bands for states A and B. The results are shown in Fig. 8.5. The radial distribution of photons from IGR J16479-4514 was compatible with the *XMM-Newton* PSF for both energy ranges during state A and for the 5-10 keV range during state B. On the contrary the 2-5 keV source photons during state B had a considerably more extended distribution than the *XMM-Newton* PSF. This behaviour is precisely the one expected from a quickly obscured source seen through a dust scattering halo: soft X-ray photon emitted when the source is unobscured are scattered along our line of sight by interstellar dust, reaching us also after X-ray source obscuration, as a results of the longer path that they follow. The dust scattering halo is most prominent at low energies (due to the energy dependence of the scattering cross section) and when the source is obscured, because contamination by direct photons from the source is virtually absent. For a halo size θ of tens of arcsec radius (see the top-right panel of Fig. 3) and the estimated source distance of 4.9 kpc (Rahoui *et al.* 2008), the longer path followed by scattered photons gives rise to a delay (see e.g., Thompson & Rothschild 2008)

$$\delta t = 5.3 d_{4.9\mathrm{kpc}} \, (\theta/\mathrm{arcsec})^2 \, x/(1-x) \sim 5300 \ s, \tag{8.1}$$

where x is the fractional distance of the halo from the source, $d_{4.9\mathrm{kpc}}$ is the source distance in unit of 4.9 kpc, and we used θ=30" and x=1/2. The typical delay is thus of few hours, in agreement with the e-folding decay time of the soft X-ray light curve in state B.

Motivated by the above findings we considered the spectral model that has been used in studies of eclipsing X-ray binaries seen through a dust-scattering halo, that is (Audley *et al.*

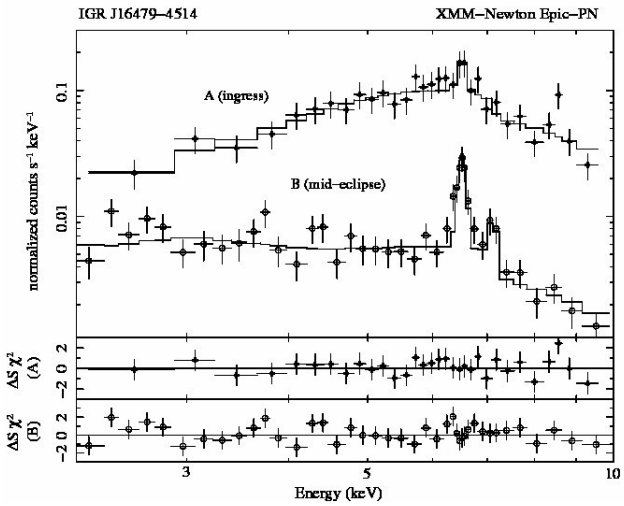

Figure 8.3: 2-10 keV spectra extracted from intervals A and B of Fig. 8.2. The best fit models and the residuals from these fits are also shown (see Sect. 8.1).

2006; Ebisawa *et al.* 1996)

$$
\begin{aligned}
I(E) \;=\; & e^{\sigma(E)N_{\rm H}}[I_{\rm s}E^{-\alpha} + e^{\sigma(E)N_{\rm Hw}}I_{\rm w}E^{-\alpha} + \\
& e^{\sigma(E)N_{\rm Hd}}I_{\rm d}E^{-\beta} + I_{\rm ln1}e^{-(E-E_{\rm ln1})^2/(2\sigma^2_{\rm ln1})} + \\
& I_{\rm ln2}e^{-(E-E_{\rm ln2})^2/(2\sigma^2_{\rm ln2})}]
\end{aligned}
\tag{8.2}
$$

Here the continuum consists of three components seen through an interstellar column density of $N_{\rm H}$: two power laws with "the same" photon index α (normalizations $I_{\rm s}$ and $I_{\rm w}$), and a third power law with photon index β=α+2 (normalization $I_{\rm d}$). The two power laws with the same photon index represent respectively, the source emission that is received directly at the earth (i.e., the direct component), and the source emission that is scattered along our line of sight by material in the immediate surroundings of the X-ray source, likely the wind from the massive companion star (we term this "wind scattered component"). The scattered component will preserve the slope of the incident spectrum, while photoelectric absorption by the wind material can in principle reduce the number of low energy photons that are scattered, thus mimicking a higher column density in the scattered component. This is why the wind scattering term in Eq. 8.2 comprises an extra absorption component ($N_{\rm Hw}$). Iron features (around $\sim$ 6.4 keV and $\sim$ 7.0 keV see Fig. 2) are represented by the Gaussians in Eq. 8.2 and arise also from reprocessing of the source radiation in the wind. The direct component is expected to dominate the X-ray emission when the source is out of eclipse. As the NS approaches the companion's limb, the source photons directly reaching us will propagate through denser and denser regions of the companion's wind, such that increased photoelectric absorption is to be expected shortly before the eclipse ingress ($N_{\rm Hd}\gtrsim N_{\rm Hw}$). The third power law component, with photon index β=α+2, originates from small angle scattering of (mainly) direct photons off interstellar dust grains along the line of sight (Day & Tennant 1991; Nagase *et al.* 1992); therefore, it should be characterized by a similar column density to that of the direct component away from eclipse. The dust scattering cross section decreases steeply for increasing photon energies, such that the spectrum of the scattered photons is softened by a factor of E^{-2}. Both the wind and dust scattered components are expected to be most

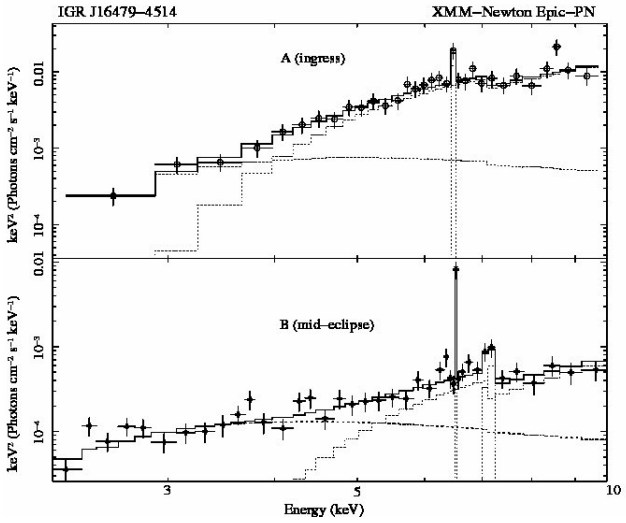

Figure 8.4: 2-10 keV unfolded spectra of Fig. 8.3. The best fit model components are displayed with dotted lines.

prominent during the eclipse, when the direct component is occulted by the companion star.

Owing to limited statistics and degeneracy in some the of spectral fit parameters, it proved impossible to disentangle the contribution from the two power laws of index α in the *XMM-Newton* spectra of IGR J16479-4514. In practice we fitted a model with only two continuum components, a single power law of slope α (with normalisation I_α and column density $N_{H,\alpha}$) and a power law of slope β (with normalisation I_β and column density $N_{H,\beta}$). The former component was taken to approximate the sum of the two α-slope power laws in Eq. 8.2, with the direct component dominating before the eclipse ingress and the wind scattered component dominating during the eclipse. The relevant model was thus

$$\begin{aligned} I(E) \;=\; & e^{\sigma(E)N_{\mathrm{H},\beta}} I_\beta E^{-\beta} + e^{\sigma(E)N_{H,\alpha}}[I_\alpha E^{-\alpha} + \\ & I_{\mathrm{ln}1} e^{-(E-E_{\mathrm{ln}1})^2/(2\sigma^2_{\mathrm{ln}1})} + \\ & I_{\mathrm{ln}2} e^{-(E-E_{\mathrm{ln}2})^2/(2\sigma^2_{\mathrm{ln}2})}]. \end{aligned} \tag{8.3}$$

We kept α fixed at 0.98, the best fit value found by Romano *et al.* (2008a) when the source was in outburst (and thus away from an X-ray eclipse); consequently we fixed also β=2.98. The best fit models are shown in Fig. 8.3, and the corresponding parameters are given in Table 8.1. In Fig. 8.4 we plot also the unfolded spectra. While in state A, a power law component with slope α plus a Gaussian line at $\sim$ 6.5 keV (EW of $\sim$ 190 eV) provided a reasonably good fit also for a fixed value of $\alpha \sim 0.98$ (χ^2/d.o.f.=33/28). However, adding the dust scattered component significantly improved the fit (χ^2/d.o.f.=20.4/26). In state A the relatively high source flux and small EW of the iron fluorescence line testifies that (most of) the emission is likely due to the direct component. In order to investigate this, we also accumulated spectra during the first 1.5 ks and last 2.5 ks of state A (not shown in Fig. 8.3). These two spectra were reasonably fit (χ^2/d.o.f.=18.6/16, 13.3/9) by assuming an absorbed powerlaw with fixed photon index 0.98 and an absorption column density of $30^{8}_{-7}\times10^{22}$ cm^{-2} and $5.6^{3.8}_{-3.0}\times10^{22}$ cm^{-2}, respectively (the addition of a Gaussian line at $\sim$6.5 keV did not significantly improved any of these fits). We interpreted

Table 8.1: Best fit parameters of the spectra during states A and B. $F_{2-10\ \mathrm{keV}}$ is the absorbed flux in the 2-10 keV band, and the X-ray luminosity L_{X} is derived from this flux assuming a source distance of 4.9 kpc (Rahoui *et al.* 2008). Errors are at 90% confidence level.

FIT PARAMETERS	STATE "A"	STATE "B"
$N_{H,\alpha}$ (10^{22} cm^{-2})	35^{18}_{-13}	54^{26}_{-25}
$N_{H,\beta}$ (10^{22} cm^{-2})	9^{-9}_{6}	6^{1}_{-2}
I_{α}	$1.8^{0.4}_{-0.3}\times10^{-3}$	$1.1^{0.5}_{-0.4}\times10^{-4}$
α	0.98 (frozen)	0.98 (frozen)
I_{β}	$5^{8}_{-4}\times10^{-3}$	$8^{2}_{-3}\times10^{-4}$
β	2.98 (frozen)	2.98 (frozen)
E_{ln1} (keV)	$6.53^{0.06}_{-0.07}$	$6.51^{0.03}_{-0.02}$
I_{ln1}	$5^{3}_{-3}\times10^{-5}$	$1.8^{1.0}_{-0.4}\times10^{-5}$
EW_{ln1} (keV)	0.15	0.77
E_{ln2}	-	$7.11^{0.06}_{-0.09}$
I_{ln2}	-	$8^{7}_{-4}\times10^{-6}$
EW_{ln2} (keV)	-	0.28
χ^2/(d.o.f.)	20.4/26	36.5/33
$F_{2-10\ \mathrm{keV}}$ (10^{-13} erg cm^{-2} s^{-1})	1.0×10^{2}	7.5
L_{X} (10^{33} erg s^{-1})	29.0	2.2

the decreasing absorption column density revealed by these fits as the effect of a change in the dominating spectral component during the early ingress to the eclipse. Specifically, the direct component dominates the first part of the state A and is absorbed by the very dense companion's limb; instead, most of the X-ray emission during the last 2.5 ks of this state is likely due to the wind scattered component, which is in turn absorbed by a lower dense material, in agreement with the expectation $N_{\mathrm{Hd}} \gtrsim N_{\mathrm{Hw}}$ discussed above.

In state B, the ratio I_{α}/I_{β} is larger than the corresponding value obtained during state A, indicating a dust scattering halo whose intensity decreases slowly during the eclipse. The intensity of the power law of slope α decreased substantially, while the EW of the Fe-line at $\sim$ 6.5 keV increased to $\sim$770 eV. We also found evidence ($\sim 2\sigma$) for an additional Fe-line at $\sim$ 7.1 keV with a $\sim$300 eV EW, consistent with being the K_{β}. Owing to the poor statistics of the present observation, we were unable to investigate further the nature of this line; however, we note that the ratio between the normalizations of the K_{α} and K_{β} lines, as inferred from fits in Table 8.1, is roughly in agreement with the expected value $\sim$0.15-0.16 (see e.g., Molendi 2003; Ibarra *et al.* 2007). The most natural interpretation of this is that in state B the direct emission component is occulted along our line of sight, while the spectrum we observe is the sum of a dust scattered component, dominating at lower energies, and a wind scattered component characterised by a high absorption. The marked increase in the EW of the Fe-line at $\sim$6.5 across the state A-state B transition testifies that the region where the line is emitted is larger than the occulting body (the supergiant companion, if we are dealing with an eclipse); this provides strong evidence that the uneclipsed emission in state B at hard X-ray energies (the α-slope power law) arises mostly from photons scattered by the wind in the immediate surrounding of the source. In both states A and B the measured $N_{H,\beta}$ is consistent with the absorption column density reported by Romano *et al.* (2008a); this provides further support in favour of the β-slope power law representing the outburst emission seen through a dust scattering halo with a delay of $\gtrsim$1 hour. These findings and interpretation are in line with those that emerged from detailed studies of some persistent eclipsing HMXBs.

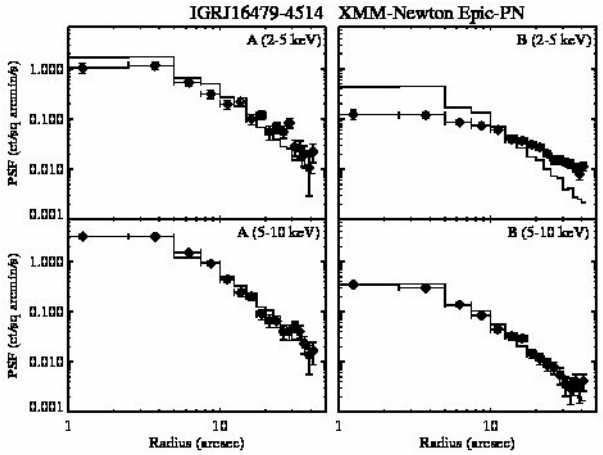

Figure 8.5: *XMM-Newton* EPIC-PN PSF as a function of the distance from the source. The upper panels are for images extracted in states A and B in the energy range 2-5 keV. Instead, the PSF in the lower panels are extracted from the same images but in the 5-10 keV energy range. For this analysis we used the XIMAGE tool (version 4.4).

We obtained also spectral fit in which α was allowed to vary as free parameters, while β=α+2. However, this did not lead to a significant improvement of any of the fits, while the best fit parameters were consistent with the ones found above.

No evidence for a coherent modulation was found in the present data up to periods of $\sim$1000 s (3σ upper limit in the 80%-90% pulse fraction[1] range).

8.2 Discussion and Conclusion

We reported on the first long ($\sim$32 ks) pointed observation of IGR J16479-4514 during a period of low X-ray emission. The decay of the light curve and the increase of the iron line EW between states A and B, likely indicated that the X-ray radiation from this source was being obscured by an occulting body. Based on the present knowledge of IGR J16479-4514, we suggested that *XMM-Newton* might have caught this source undergoing an X-ray eclipse. Obscuration by a tilted accretion disk, which is known to cause similar effects in other HMXBs (see e.g, Zane *et al.* 2004), appears a less promising possibility here. This is because the outbursts of IGR J16479-4514, and SFXT in general, have durations that are incompatible with viscous timescales in a typical accretion disc (see Sect. 7.3).

In order to interpret the source flux and spectral variations revealed by the *XMM-Newton* observation, we considered the same scenario that has been extensively discussed for eclipsing HMXBs with a dust scattering halo (see e.g., Audley *et al.* 2006; Ebisawa *et al.* 1996): during the eclipse ingress source photons reaching us directly dominated the X-ray flux we observed; while in eclipse the residual X-ray flux is due to the sum of a wind-scattered component and a dust scattering halo. Strong evidence for the wind scattered component in the case of IGR J16479-4514 comes from the marked increase of the EW of the iron fluorescence line at $\sim$ 6.5 keV. A tens of arcsec wide dust-scattering halo around IGR J16479-4514 could be directly seen in the soft X-ray *XMM-Newton* images

[1]Here for pulse fraction we mean the ratio between the pulsed emission and the total emission from the NS.

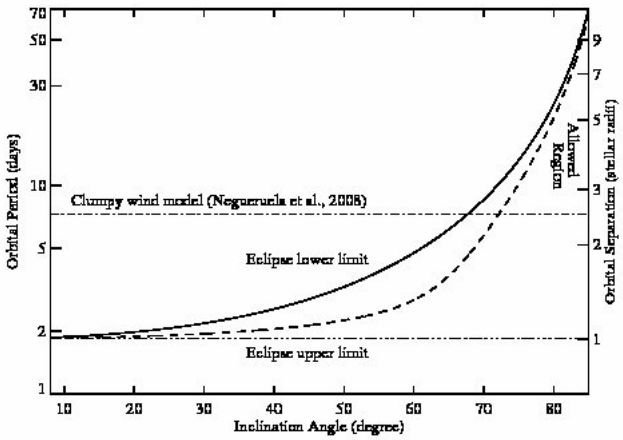

Figure 8.6: Orbital period constraints on IGR J16479-4514, as a function of the binary inclination angle. The solid line is given by Eq. 8.4 assuming an eclipse duration of 28 ks, the dashed line is for an eclipse duration of 55 ks, and the triple-dot-dashed line is for an eclipse lasting half of the binary orbital period. The dot-dashed line is the lower limit on the orbital period obtained by applying the clumpy wind model to IGR J16479-4514. According to this model, the region of allowed parameters in this plot indicates IGR J16479-4514 is a high-inclination SFXT.

accumulated during the eclipse. Moreover the residual soft X-ray decreased on a timescale of $\sim$ 1 hr after the eclipse onset, as expected for a dust scattering halo of the size seen by *XMM-Newton* at the source distance of 4.9 kpc.

We conclude that IGR J16479-4514 is the first SFXT that displayed evidence for an X-ray eclipse. In this case, some constraints on the orbital period of this system can be derived by using (Rappaport & Joss 1983)

$$R_* = a \left[\cos i^2 + \sin i^2 \sin \Theta_{\rm e}\right]^{1/2} . \tag{8.4}$$

Here i is the inclination of the orbit to the plane of the sky, $\Theta_{\rm e}$ is the eclipse half-angle, a is the binary separation, and we assume in the following a supergiant star with a mass of $\sim$30 $M_\odot$ and a radius of $R_*\sim$20 $R_\odot$. We consider circular orbits, as it is generally expected for an HMXB with a supergiant companion (Rappaport & Joss 1983). By using Kepler's law, Eq. 8.4 can be solved for the orbital period, as a function of the inclination angle, for any fixed value of the eclipse duration. This is shown in Fig. 8.6. The solid line in this figure represents the solution obtained by assuming an eclipse duration of $\sim$28 ks. This value should be regarded as a lower limit on $\Theta_{\rm e}$, since in the *XMM-Newton* observation discussed here there is no evidence for the eclipse egress. The dashed line is for an eclipse that lasts for 55 ks (chosen for comparison with the previous case), whereas the triple-dot-dashed line is for an eclipse that extends for half of the binary orbital period. The latter provides an upper limit on $\Theta_{\rm e}$. We also include in the figure, the lower limit on the orbital period that was obtained by Negueruela *et al.* (2008), by assuming the sporadic outbursting activity of SFXTs is related to accretion of clumps from the supergiant stellar wind (see Sect. 7.3). If we consider that the clumpy wind model applies to IGR J16479-4514, then the region of allowed parameter space in Fig. 8.6 suggest this source is a high inclination SFXT. From this figure we also note that, for this source, an eclipse with a

duration much longer than the ∼28 ks observed here is very unlikely: in fact the longer is the duration of the eclipse, the smaller is the allowed parameter region in Fig. 8.6. In particular, a much longer eclipse would require an unusual very high inclination angle and short orbital period that hardly reconciles with the requirements of the clumpy wind model (the NS orbit should be very close to the supergiant surface, and a persistent luminosity of $\gtrsim 10^{36}$ erg s^{-1} would be expected).

Due to its relatively high persistent luminosity ($\sim 10^{33}$-10^{34} erg s^{-1}) and the lack of a very dim quiescent state at $\sim 10^{32}$ erg s^{-1}, IGR J16479-4514 was already identified as a rather peculiar object within the SFXT class. To account for its unusual high quiescent luminosity, Sguera *et al.* (2008) suggested this source might have a smaller orbital radius than other known SFXTs: this would imply that the NS is close enough to its supergiant companion that accretion takes place at a significant rate also during quiescence.

At present, it is not clear whether eclipses should be expected also in other SFXTs. However, we note that, if other SFXTs display X-ray eclipses, their maximum luminosity swing might not be due to genuine changes in the mass accretion rate, impacting on the application of several SFXT models (Bozzo *et al.* 2008; Negueruela *et al.* 2008). Further observations of IGR J16479-4514, as well as other SFXTs in quiescence, will improve our knowledge of the low level emission of these sources, and will help clarifying this issue.

Future Prospects

In this thesis we analyzed several aspects of low and high mass X-ray binaries hosting neutron stars both from the observational and theoretical points of view. We used observations carried out with present generation X-ray telescopes in order to gain insight on the accretion processes taking place in these systems. Moreover, we developed further several aspects of the theory of these objects.

In the first part of this thesis we concentrated on low mass X-ray binaries. In this context, one of the most interesting problem is that of the magnetic threading of the accretion disk. In Chapter 2 we presented some evidence that current models are unable to interpret the slow QPOs observed from accreting X-ray pulsars and require a more general and self-consistent treatment. We are currently working on a revised version of the threaded disk model that will be presented in a forthcoming publication. Thanks to the wide range of applicability of the magnetically threaded disk model, we expect that this could find its application in a variety of conditions ranging from the pre-main sequence evolution of stars to disk accreting magnetic white dwarfs and neutron stars.

Regarding the triple nature of the binary 4U 2129+47 (see Chapter 5), a number of *XMM-Newton* observations have been recently carried out, and we expect that these will confirm our results and provide incontrovertible evidence that this system is part of a hierarchical triple. As we speculated in Chapter 5, a third body in a wide orbit also around other low mass X-ray binaries, might potentially explain the problem of their positive orbital period derivatives, and thus provide a new interesting solution for the discrepancy between the observations of these low mass X-ray binaries and the expectations of their standard evolutionary scenario.

Recently, I became interested in type I X-ray bursts from low mass X-ray binaries, and in Chapter 6 I presented my first work on this topic. As I discussed in the conclusion of the relevant Chapter, many theoretical aspects of type I X-ray bursts are still poorly understood. I intend to continue working in this field and improve my knowledge on thermonuclear bursts.

In the second part of the thesis, we focused on high mass X-ray binaries. In particular, we concentrated on supergiant fast X-ray transients, a recently-discovered subclass of supergiant X-ray binaries, which we suggested might host magnetars. As we discussed in Chapter 7, supergiant fast X-ray transients may provide the very first opportunity to detect and study magnetars in binary systems. In the near future I plan to carry out the first systematic search for binary systems that host accreting magnetars, and study the evolution and emission properties of such peculiar objects. To this aim we have already submitted proposals to the *RXTE*, *XMM-Newton*, *Chandra*, and *Suzaku* time allocation committees, asking for observations of supergiant fast X-ray transient sources. In particular, with our proposals we aim at obtaining the first high sensitivity observations of several quiescent SFXTs. The long exposure times requested will allow a detailed study of the activity of these sources at very low X-ray flux levels. As we discussed in Chapter 7, this holds the potential to discriminate between different models developed to interpret the behavior of these sources and will thus help clarifying the nature of the compact object hosted in them.

Bibliography

Alpar, M.A. & Shaham, J. (1985). Nature, 316, 239. ADS. [46]

Angelini, L., Stella, L., Parmar, A.N. (1989). ApJ, 346, 906. ADS. [43, 54]

Arnaud, K.A. (1996). Astronomical Data Analysis Software and Systems. A.S.P. Conference Series, 101, 17 . ADS. [94, 95]

Arons, J., Lea, S. M. (1980). ApJ, 2035, 1016 . ADS. [80]

Arons, J., Burnard, D., Klein, R.I., McKee, C.F., Pudritz, R.E., Lea, S.M. (1984). High Energy Transients in Astrophysics, ed. S. E. Woosley. New York:AIP, 215 . ADS. [57, 78]

Audley, M.D., Nagase, F., Mitsuda, K., Angelini, L., Kelley, R.L. (2006). MNRAS, 367, 1147 . ADS. [138, 139, 143]

Baade, W. & Zwicky, F. (1934). Phys. Rev. A, 46, 76 . ADS [1]

Balbus, S.A., Hawley, J.F. (1981). ApJ, 376, 214 . ADS. [18]

Barthelmy, S.D. et al (2008). GCN Circular, 7985. [99]

Bamba, A., Yokogawa, J., Ueno, M., Koyama, K., Yamauchi, S. (2001). PASJ, 53, 1179 . ADS. [128]

Barnard, R., Trudolyubov, S., Kolb, U.C., Haswell, C.A., Osborne, J.P., Priedhorsky, W.H. (2007). A&A, 469, 875 . ADS. [91]

Barret, D. (2001). AdSpR, 28, 307 . ADS. [8]

Bhattacharya, D. (2002). JAA, 23, 67 . ADS. [6]

Belian, R.D., Conner, J.P., Evans, W.D. (1976). ApJ, 206, 135 . ADS. [21]

Berghoefer, T.W., Schmitt, J.H.M.M., Danner, R., Cassinelli, J.P. (1997). A&A, 322, 167 . ADS. [128, 129]

Bildsten, L. Chakrabarty, D., Chiu, J., Finger, M. H., Koh, D. T., Nelson, R. W., Prince, T. A., Rubin, B. C., Scott, D. M., Stollberg, M., Vaughan, B.A., Wilson, C.A., Wilson, R.B. (1997). ApJS, 113, 367 . ADS. [54, 57, 74]

Bisnovatyi-Kogan, G.S. & Fridman, A.M. (1970). Soviet Ast., 13, 566 . ADS. [28]

Bohm-Vitense, E. (1992). Introduction to stellar astrophysics, Cambridge University press . ADS. [96]

Bondi, H. (1952). MNRAS, 112, 195 . ADS. [19, 115]

Boroson, B., O'Brien, K., Horne, K., Kallman, T., Still, M., Boyd, P.T., Quaintrell, H., Vrtilek, S.D. (2000). ApJ, 545, 399 . ADS. [43, 53]

Bozzo, E., Falanga, M., Stella, L. (2008). ApJ, 683, 1031 . ADS. [145]

Brown, E.F., Bildsten, L., Rutledge, R.E. (1998). ApJ, 504, L95 . ADS. [97]

Brown, E.F. (2000). ApJ, 531, 988 . ADS. [107]

Burderi, L., King, A.R., Wynn, G.A. (1996). ApJ, 457, 348 . ADS. [82]

Burderi, L., Possenti, A., Colpi, M., Di Salvo, T., D'amico, N.(1999). ApJ, 519, 285 . ADS. [82]

Burderi, L., Di Salvo, T., Robba, N.R., La Barbera, A., Guainazzi, M. (2000). ApJ, 530, 429 . ADS. [43, 54]

Burderi, L., Possenti, A., D'Antona, F., Di Salvo, T., Burgay, M., Stella, L., Menna, M.T., Iaria, R., Campana, S., d'Amico, N. (2001). ApJ, 560, L71 . ADS. [86]

Burderi, L., Di Salvo, T., Lavagetto, G., Menna, M.T., Papitto, A., Riggio, A., Iaria, R., D'Antona, F., Robba, N.R., Stella, L. (2007). ApJ, 657, 961 . ADS. [82]

Burnard, D.J., Arons, J., Lea, S.M. (1983). ApJ, 266, 175 . ADS. [117, 118, 135]

Burrows, D.N., Hill, J.E., Nousek, J.A., Kennea, J.A., Wells, A., Osborne, J.P., Abbey, A.F., Beardmore, A., Mukerjee, K., Short, A.D.T., et al. (2005). Space Sci. Rev., 120, 165 . ADS. [100]

Campana S., Colpi, M., Mereghetti, S., Stella, L., Tavani, M. (1998). A&A Rev., 8, 279 . ADS. [82, 98, 123]

Campana S. & Stella, L. (2000). ApJ, 541, 849 . ADS. [71, 85]

Campana, S., Gastaldello, F., Stella, L., Israel, G.L., Colpi, M., Pizzolato, F., Orlandini, M., Dal Fiume, D. (2001). ApJ, 561, 924 . ADS. [43, 54, 60]

Cash W. (1979). ApJ, 228, 939 . ADS. [95]

Cassinelli, J.P., Waldron, W.L., Sanders, W.T., Harnden, F.R., Rosner, R., Vaiana, G.S. (1981). ApJ, 250, 677 . ADS. [128, 129]

Chakrabarty, D., Bildsten, L., Grunsfeld, J.M., Koh, D.T., Prince, T.A., Vaughan, B.A., Finger, M.H., Scott, D.M., Wilson, R.B. (1997a). ApJ, 474, 414 . ADS. [57, 75]

Chakrabarty, D., Bildsten, L., Finger, M.H., Grunsfeld, J.M., Koh, D.T., Nelson, R.W., Prince, T.A., Vaughan, B.A., Wilson, R.B. (1997b). ApJ, 481L, 101 . ADS. [75, 78]

Chakrabarty, D. & Roche, P. (1997). ApJ, 489, 254 . ADS. [43, 54, 74]

Chakrabarty, D. (1998). ApJ, 492, 342 . ADS. [43]

Chenevez, J., Falanga, M., Brandt, S., Farinelli, R., Frontera, F., Goldwurm, A., in't Zand, J.J.M., Kuulkers, E., Lund, N. (2006). A&A, 449, L5 . ADS. [22]

Chenevez, J., Falanga, M., Kuulkers, E., Walter, R., Bildsten, L., Brandt, S., Lund, N., Oosterbroek, T., Zurita Heras, J. (2007). A&A, 469, L27 . ADS. [22, 112]

Chevalier, C., Ilovaisky, S.A., Motch, C., Pakull, M., Mouchet, M. (1989). A&A217, 108 . ADS. [89, 95]

Choi, C.S., Nagase, F., Makino, F., Dotani, T., Min, K.W. (1994). ApJ, 422, 799 . ADS. [53]

Colpi, M., Geppert, U., Page, D., Possenti, A. (2001). ApJ, 548, L175 . ADS. [29, 97]

Cominsky, L., Jernigan, J.G., Ossmann, W., Doty, J., Lewin, W.H.G., van Paradus, J. (1980). ApJ, 242, 1102 . ADS. [23]

Cook, G.B., Shapiro, S.L., Teukolski, S.A. (1994a). ApJ, 424, 823 . ADS. [82]

Cook, G.B., Shapiro, S.L., Teukolski, S.A. (1994b). ApJ, 432, L117 . ADS. [82]

Corbet, R.H.D. (1986). MNRAS, 220, 1047 . ADS. [11]

Corbet, R.H.D. (1996). ApJ, 457, L31 . ADS. [123]

Corbet, R., Barbier, L., Barthelmy, S., Cummings, J., Fenimore, E., Gehrels, N., Hullinger, D., Krimm, H., Markwardt, C., Palmer, D., et al. (2006). Astr. Tel., 779

. ADS. [130]

Cottam, J., Sako, M., Kahn, S.M., Paerels, F., Liedahl, D.A. (2001). ApJ, 557, 101 . ADS. [7]

Cowley, A.P., Schmidtke, P.C. (1990). ApJ, 99, 678 . ADS. [89, 90]

Cowley, A.P., Schmidtke, P.C. Hutchings, J.B., Crampton, D. (1993). AJ, 125, 2163 . ADS [7]

Cox, N.L.J., Kaper, L., Foing, B.H., Ehrenfreund, P. (2005). A&A, 438, 187 . ADS. [55]

Cumming, A. & Bildsten, L. (2000). ApJ, 544, 453 . ADS. [106]

Cumming, A. & Macbeth, J. (2004). ApJ, 603, L37 . ADS. [102, 111, 112]

Cumming, A., Macbeth, J., in 't Zand, J.J.M., Page, D. (2006). ApJ, 646, 429 . ADS. [108]

Dal Fiume, D., Orlandini, M., Cusumano, G., del Sordo, S., Feroci, M., Frontera, F., Oosterbroek, T., Palazzi, E., Parmar, A.N., Santangelo, A., Segreto, A. (1998). A&A, 329 L41 . ADS. [43, 53]

Davidsen, A., Malina, R., Bowyer, S. (1977). ApJ, 211, 866 . ADS. [74]

Davies, R.E., Fabian, A.C., Pringle, J.E. (1979). MNRAS, 186, 779 . ADS. [119]

Davies, R.E. & Pringle, J.E. (1981). MNRAS, 196, 209 . ADS. [115, 119, 120, 123, 132, 136]

Day, C.S.R. & Tennant, A.F. (1991). MNRAS, 251, 76 . ADS. [139, 140]

Degenaar, N. & Wijnands, R. (2008). Astr. Tel., 1572 . ADS. [99]

Deutsch, E.W., Margon, B., Wachter, S., Anderson, S.F. (1996). ApJ, 471, 979 . ADS. [89]

Dessart, L. & Owocki, S.P. (2003). A&A, 406, L1 . ADS. [129]

Di Salvo, T. & Burderi, L. (2003). A&A, 397, 723 . ADS. [82]

Dotani, T., Kii, T., Nagase, F., Makishima, K., Ohashi, T., Sakao, T., Koyama, K., Tuohy, I. R. (1989). PASJ, 41, 427 . ADS. [57]

Dubus, G., Giebels, B. (2008). Astr. Tel., 1715 . ADS. [30]

Duncan, R.C. & Thompson, C. (1992). ApJ, 392, L9 . ADS. [28]

Ebisawa, K., Day, C.S.R., Kallman, T.R., Nagase, F., Kotani, T., Kawashima, K., Kitamoto, S., Woo, J.W. (1996). PASJ, 48, 425 . ADS. [140, 143]

Eggleton, P.P. (1983). ApJ, 268, 368 . ADS [16]

Eksi, K.Y., Hernquist, L., Narayan, R. (2005). ApJ, 623, 41 . ADS. [61]

Elsner, R.F. & Lamb, F.K. (1977). ApJ, 215, 897 . ADS. [115]

Ergma, E. & Sarna, M.J. (2003). A&A, 399, 237 . ADS. [86, 87]

Erkut, M.H., Alpar, M.A. (2004). ApJ, 617, 461 . ADS. [51]

Falanga, M., Kuiper, L., Poutanen, J., Bonning, E.W., Hermsen, W., di Salvo, T., Goldoni, P., Goldwurm, A., Shaw, S.E., Stella, L. (2005). A&A, 444, 15 . ADS. [82]

Falanga, M., Poutanen, J., Bonning, E.W. et al. (2007). A&A, 464, 1069 . ADS. [104]

Falanga, M., Chenevez, J., Cumming, A., Kuulkers, E., Trap, G., Goldwurm, A. (2008). A&A, 484, 43 . ADS. [22, 102, 104]

Fender, R., Gallo, E., Jonker, P. (2004). Nucl. Phys. B, 132, 346 . ADS. [8]

Fiocchi, M., Bazzano, A., Ubertini, P., Jean, P. (2006). ApJ, 651, 416 . ADS. [8]

Forman, W., Jones, C., Cominsky, L., Julien, P., Murray, S., Peters, G., Tananbaum, H.,

Giacconi, R. (1978). ApJ, 38, 357 . ADS. [88]

Fujimoto, M.Y., Sztajno, M., Lewin, W.H.G., van Paradijs, J., (1987). ApJ, 319, 902 . ADS. [104, 106, 110]

Kaluzny, J. (1988). Acta Astronomica, 38, 207 . ADS. [89]

Finger, M.H., Wilson, R.B., Harmon, B.A. (1996). ApJ, 459, 288 . ADS. [43, 55]

Frank, J., King, A., Raine, D. (2002) Accretion Power in Astrophysics, Cambridge University press, Ed. R.F. Carswell, D.N.C. Lin & J.E. Pringle . ADS. [57, 58, 62, 115, 132]

Fritz, S., Kreykenbohm, I., Wilms, J., Staubert, R., Bayazit, F., Pottschmidt, K., Rodriguez, J., Santangelo, A. (2006). A&A, 458, 885 . ADS. [43, 55]

Galloway, D. K., Cumming, A., Kuulkers, E., et al. (2004). ApJ, 601, 466 . ADS. [104, 106, 110, 111]

Galloway, D.K., Muno, M.P., Hartman, J.M., Psaltis, D., Chakrabarty, D. (2006). in press, astro-ph/0608259 . ADS. [104]

Galloway, D.K. & Cumming, A. (2006b). ApJ, 652, 559 . ADS. [108, 113]

Garcia, M.R. & Grindlay, J.E. (1987). ApJ, 313, L59 . ADS. [88]

Garcia, M.R., Bailyn, C.D., Grindlay, J.E., Molnar, L.A. (1989). ApJ, 341, L75 . ADS. [90, 96]

Garcia, M., Grindlay, J., Bailyn, C. (1992). IAU Circ., 5578, 2 . ADS. [90]

Garcia, M.R. (1994). ApJ, 435, 407 . ADS. [90]

Garcia, M.R., Callanan, P.J. (1999). AJ, 118, 1390 . ADS. [90]

Gavriil, F.P., Kaspi, V.M., Woods, P.M. (2002). Nature, 419, 142 . ADS. [133]

Ghosh, P., Pethick, C.J., Lamb, F.K. (1977). ApJ, 217, 578 . ADS. [37, 38]

Ghosh, P., Lamb, F.K. (1978). ApJ, 223, L83 . ADS. [37]

Ghosh, P., Lamb, F.K. (1979a). ApJ, 232, 259 . ADS. [37, 38, 39, 40, 51, 57]

Ghosh, P. & Lamb, F.K. (1979). ApJ, 234, 296 . ADS. [37, 38, 40, 42, 51, 57, 58]

Ghosh, P., Lamb, F.K. (1992). X-ray binaries and recycled pulsars, Ed. E. van den Heuvel and S.A. Rappaport, Kluwer Academic Publishers, Boston, p. 487 . ADS. [50, 51]

Ghosh, P. (1995). Compact stars in binaries, Ed. J. van Paradijs, E.P.J. van den Heuvel, E. Kuulkers, Kluwer Academic Publishers, Dordrecht, p.57 . ADS. [50, 51]

Giacconi, R., Gursky, H., Kellogg, E., Schreirer, E., Tananbaum, H. (1971). ApJ, 167, L67 . ADS. [12, 13]

Gierliski, M. & Done, C. (2002). MNRAS, 331, 141 . ADS. [8]

González-Riestra, R., Oosterbroek, T., Kuulkers, E., Orr, A., Parmar, A. N. (2004). A&A, 420, 589 . ADS. [128]

Götz, D., Falanga, M., Senziani, F., De Luca, A., Schanne, S., von Kienlin, A. (2007). ApJ, 655, L101 . ADS. [128]

Grebenev S.A. & Sunyaev, R.A., (2005). AstL., 31, 672 . ADS. [128]

Grebenev S.A. & Sunyaev, R.A., (2005). AstL., 33, 149 . ADS. [129]

Grindlay, J., Gursky, H., Schnopper, H., Parsignault, D.R., Heise, J., Brinkman, A.C., Schrijver, J. (1975). ApJ, 205, 127 . ADS. [21]

Haensel, P. & Zdunik, J.L. (1990). A&A, 227, 431 . ADS. [107]

Haensel, P. & Zdunik, J.L. (2008). A&A, 480, 459 . ADS. [107, 110]

Halpern, J.P., Gotthelf, E.V., Helfand, D.J., Gezari, S., Wegner, G. A. (2004). Astr. Tel., 289 . ADS. [128]

Harding, A.K. & Leventhal, M. (1992). Nature, 357, 388 . ADS. [116, 117]

Harding, A.K. (1994). AIPC, 308, 429 . ADS. [12]

Hasinger, G. & van der Klis, M. (1989). A&A, 225, 79 . ADS. [8, 101]

Heger, A., Cumming, A., Galloway, D.K., Woosley, S.E. (2007). ApJ, 671, L141 . ADS. [104]

Heinz, S., Nowak, M.A. (2001). MNRAS, 320, 249 . ADS. [96]

Hellier, C. & Mason, K.O. (1989). MNRAS, 239, 715 . ADS. [7]

Henrichs, H. F. (1983). Accretion-driven stellar X-ray sources, Cambridge University Press. p. 393-429 . ADS. [133]

van den Heuvel, E.P.J. & Rappaport, S. (1987). Physics of Be stars, Cambridge, UK, p. 291 . ADS. [127]

van den Heuvel, E.P.J. (2005). Formation and Evolution of Neutron Stars in Binary Systems, Springer, Dordrecht, The Netherlands, 2005, p.191 . ADS. [11]

Hewish, A., Bell, S.J., Pilkington, J.D., Scott, P.F., Collins, R.A (1968). newblock Nature, 217, 709 . ADS. [2]

Heyl, J.S. & Kulkarni, S.R. (1998). ApJ, 506, L61 . ADS. [133]

Hoyle, R. & Fowler, W.A. (1965). Quasi-Stellar Sources and Gravitational Collapse, ed. I. Robinson, A. Schild, E. L. Shucking (Chicago : Univ. Chicago Press), 17 . ADS. [108]

Horne, K., Verbunt, F., Schneider, D.P. (1986). MNRAS, 218, 63 . ADS. [88]

Howe, S.K., Primini, F.A., Bautz, M.W., Lang, F.L., Levine, A.M., Lewin, W.H.G. (1983). ApJ, 272, 678 . ADS. [43, 54]

Ibarra, A., Matt, G., Guainazzi, M., Kuulkers, E., Jimnez-Bailn, E., Rodriguez, J., Nicastro, F., Walter, R. (2007). A&A, 465, 501 . ADS. [142]

Ikhsanov, N.R. & Pustil'nik, L.A. (1996). A&A, 312, 338 . ADS. [118]

Ikhsanov, N.R. (2001a). A&A, 368, L5 . ADS. [136]

Ikhsanov, N.R., Larionov, V.M., Beskrovnaya, N.G. (2001b). A&A, 372, 227 . ADS. [118]

Ikhsanov, N.R. (2001c). A&A, 375, 944 . ADS. [135]

Ikhsanov, N.R. (2002). A&A, 381, L61 . ADS. [136]

Ikhsanov, N.R. (2007). MNRAS, 375, 698 . ADS. [132]

Illarionov, A.F. & Sunyaev, R.A. (1975). A&A, 39, 185 . ADS. [58, 60, 82, 83, 86, 115, 116]

in 't Zand, J.J.M., Baykal, A., Strohmayer, T.E. (1998). ApJ, 496, 386 . ADS. [43, 55]

in't Zand, J.J.M., Cornelisse, R., Cumming, A. (2004). A&A, 426, 257 . ADS. [22]

in 't Zand, J.J.M., van der Sluys, M.V., Verbunt, F., Pols, O.R. (2005). A&A, 441, 675 . ADS. [22, 102, 112]

in't Zand, J.J.M. (2005). A&A, 441, L1 . ADS. [128, 129, 131]

Jansen, F., Lumb, D., Altieri, B., Clavel, J., Ehle, M., Erd, C., Gabriel, C., Guainazzi, M., Gondoin, P., Much, R., Munoz, R., Santos, M., Schartel, N., Texier, D., Vacanti, G. (2001). A&A, 365, L1 . ADS. [90, 138]

Jahoda, K., Swank, J.H., Giles, A.B., Stark, M.J., Strohmayer, T., Zhang, W., Morgan, E.H.(1996). SPIE, 2808, 59 . ADS. [100]

Jetzer, P., Strassle, M. Straumann, N. (1998). New Astr., 3, 619 . ADS. [59, 60]

Jonker, P.G., van der Klis, M. (2001). ApJ, 553, 43 . ADS. [7]

Kaluzienski, L. J.; Holt, S. S.; Boldt, E. A.; Serlemitsos, P. J. (1976). ApJ, 208, 71 . ADS. [5]

Kaplan, D. & Chakrabarty, D. (2008). Astr. Tel., 1630 . ADS [100]

Kaur, R., Paul, B., Kumar, B., Sagar, R. (2008). ApJ, 676, 1184 . ADS. [49, 50, 54]

Kennea, J.A. & Campana, S. (2006). Astr. Tel., 818 . ADS. [128]

King, A.R., Pringle, J.E., Livio, M. (2007). MNRAS, 376, 1740 . ADS. [44]

van der Klis, M. (1989). ARA&A, 27, 517 . ADS. [8]

van der Klis, M. (1995). X-Ray Binaries, p. 252 . ADS. [8, 9, 46]

van der Klis, M. (2004). A review of rapid X-ray variability in X-ray binaries . ADS [46]

Klochkov, D., Shakura, N., Postnov, K., Staubert, R., Wilms, J., Ketsaris, N. (2006). arXiv:astro-ph/0609276 . ADS. [53]

Krauss, M.I., Schulz, N.S., Chakrabarty, D., Juett, A.M., Cottam, J. (2007). ApJ, 660, 605 . ADS. [49, 50, 54]

Krolik, J.H., Hawley, J.F., Hirose, S. (2005). ApJ, 622, 1008 . ADS. [78]

Kuulkers, E., Homan, J., van der Klis, M., et al. (2002). A&A, 382, 947 . ADS. [104]

Kuulkers, E., den Hartog, P.R., in't Zand, J.J.M., Verbunt, F.W.M., Harris, W.E., Cocchi, M. (2003). A&A, 399, 663 . ADS. [104, 105, 108]

Kuulkers, E. (2004). Nucl. Phys. B, 132, 466 . ADS. [22]

Lai, D. (1999). ApJ, 524, 1030 . ADS. [57, 58, 77]

Lamb F.K. & Pethick C.J. (1974). Astrophysics and Gravitation. Proc. 16th Solvay Congress, p. 135 . ADS. [37, 38, 60, 82]

Lamb, F.K., Shibazaki, N., Alpar, M.A., Shaham, J. (1985). Nature, 317, 681 . ADS. [46]

Lewin, W.H.G.L., van Paradijs, J. Taam, R. (1993). Space Sci. Rev., 62, 223 . ADS. [22, 104]

Lewin, W.H.G.L., van Paradijs, J. Taam, R. (1995). X-ray binaries, p. 175 . ADS. [4, 22, 24, 25]

Leyder, J.-C., Walter, R., Lazos, M., Masetti, N., Produit, N. (2007). A&A, 465, L35 . ADS. [129]

Li, X.-D. & Wang, Z.-R. (1996). A&A, 307, L5 . ADS. [51]

Li, X.-D. & Wang, Z.-R. (1999). ApJ, 513, 845 . ADS. [51]

Li, J., Wickramasinghe, D.T., Rudinger, G. (1996). MNRAS, 469, 765 . ADS. [51]

Li, J. & Wickramasinghe, D.T. (1997). MNRAS, 286, L25 . ADS. [51]

Linares, M., Soleri, P., Curran, P., Wijnands, R., Degenaar, N., van der Klis, M., Starling, R., Markwardt, C. (2008). Astr. Tel., 1618 . ADS. [99, 101]

Linares, M. et al. (2008b). MNRAS, submitted, arXiv:astro-ph/0608259 . ADS. [110, 112]

Liu, Q.Z., van Paradijs, J., van den Heuvel, E.P.J. (2001). A&A, 368, 1021 . ADS. [4, 10]

Lewin, W.H.G., Ricker, G.R., McClintock, J.E. (1971). ApJ, 169, L17 . ADS. [74]

Li, X.-D. & van den Heuvel, E.P.J. (1999). ApJ, 513, L45 . ADS. [30, 133]

Lipunov, V.M. (1992). Astrophysics of Neutron Stars, Springer-Verlag . ADS. [116]

Liu, Q.Z. & Yan, J.Z. (2006). AdSpR, 38, 2906 . ADS. [132, 134]

Lovelace, R.V.E., Romanova, M.M., Bisnovatyi-Kogan, G.S. (1995). MNRAS, 275, 244 . ADS. [37, 57, 78]

Lutovinov, A., Revnivtsev, M., Gilfanov, M., Shtykovskiy, P., Molkov, S., Sunyaev, R. (2005). A&A, 444, 821 . ADS. [128, 130]

Mangano, V., Israel, G. L., Stella, L. (2004). A&A, 419, 1045 . ADS. [93]

Masetti, N., Pretorius, M.L., Palazzi, E., Bassani, L., Bazzano, A., Bird, A.J., Charles, P.A., Dean, A.J., Malizia, A., Nkundabakura, P., et al. (2006). A&A, 449, 1139 . ADS. [128]

Makishima, K., Ohashi, T., Sakao, T., Dotani, T., Inoue, H., Koyama, H., Makino, F., Mitsuda, K., Nagase, F., Thomas, H.D., Turner, M.J.L., Kii, T., Tawara, Y.K. (1988). Nature, 333, 746 . ADS. [75]

Makishima, K., Mihara, T., Nagase, F., Murakami, T. (1992). Frontiers of X-ray Astronomy, ed. Y. Tanaka & K. Koyama, Frontiers Science Series, Universal Academy Press, Tokyo, p. 23 . ADS. [55, 57]

Maraschi L. & Cavaliere A. (1977). X-ray binaries and compact objects, p. 127 . ADS. [21]

Markwardt, C.B., Cummings, J., Krimm, H. (2008). Astr. Tel., 1569 . ADS. [99, 101]

Markwardt, C.B., Cummings, J., Krimm, H. (2008b). Astr. Tel., 1616 . ADS. [99]

Mazets, E.P., Golentskii, S.V., Ilinskii, V.N., Aptekar, R.L., Guryan, Iu. A. (1979). Nature, 282, 587 . ADS. [27]

McClintock, J.E., Remillard, R.A., Margon, B. (1981). ApJ, 243, 900 . ADS. [88, 90]

McClintock, J.E., London, R.A., Bond, H.E., Grauer, A.D. (1982). ApJ, 258, 245 . ADS. [88, 89, 90]

Middleditch, J., Mason, K.O., Nelson, J.E., White, N.E. (1981). ApJ, 369, 490 . ADS. [75]

Molendi, S., Bianchi, S., Matt, G. (2003). MNRAS, 343, L1 . ADS. [142]

Molkov, S., Revnivtsev, M., Lutovinov, A., Sunyaev, R.A. (2005). A&A, 434, 1069 . ADS. [22, 104]

Moon, D. & Eikenberry, S.S. (2001). ApJ, 549, L225 . ADS. [43, 54]

Mori, K. & Ruderman, M.A. (2003). ApJ, 592, L75 . ADS. [116, 132]

Nagase, F. (1989). PASJ, 41, 1 . ADS. [57]

Nagase, F., Corbet, R.H.D., Day, C.S.R., Inoue, H., Takeshima, T., Yoshida, K., Mihara, T. (1992). ApJ, 396, 147 . ADS. [139, 140]

Nagase, F. (1994). AIPC, 308, 567 . ADS. [12]

Negueruela, I. & Okazaki, A.T. (2001). A&A, 369, 108 . ADS. [54]

Negueruela, I., Torrejon, J.M., Reig, P., Ribo, M., Smith, D.M. (2008). A population explosion. AIP Conference Proceedings 1100, p. 252 . ADS. [129, 131, 133, 144, 145]

Nespoli, E., Fabregat, J., Mennickent, R. (2007). Astr. Tel., 983 . ADS [128]

Nowak, M.A., Heinz, S., Begelman, M.C. (2002). ApJ, 573, 778 . ADS. [90]

Papitto, A., Menna, M.T., Burderi, L., Di Salvo, T., D'Antona, F., Robba, N.R. (2005). ApJ, 621, L113 . ADS. [93]

Parmar, A.N., White, N.E., Stella, L. (1989). ApJ, 338, 373 . ADS. [43]

Parmar, A.N., Smale, A.P., Verbunt, F., Corbet, R.H.D. (1991). ApJ, 366, 253 . ADS. [93]

Parmar, A.N., Oosterbroek, T., Dal Fiume, D., Orlandini, M., Santangelo, A., Segreto, A., del Sordo, S. (1999). A&A, 350, L5 . ADS. [43, 53]

Parmar, A.N., Oosterbroek, T., Del Sordo, S., Segreto, A., Santangelo, A., Dal Fiume, D., Orlandini, M. (2000). A&A, 356, 175 . ADS. [96]

Patel, S.K., Zurita, J., Del Santo, M., Finger, M., Kouveliotou, C., Eichler, D., Gogus, E., Ubertini, P., Walter, R., Woods, P., et al. (2007). ApJ, 657, 994 . ADS. [132]

Peng, F., Brown, E. F., Truran, J.W. (2007). ApJ, 654, 1022 . ADS. [107, 113]

Perna, R., Bozzo, E., Stella, L. (2006). ApJ, 639, 363 . ADS. [117]

Petterson, J.A. (1975). ApJ, 201, L61 . ADS. [53]

Pietsch, W., Steinle, H., Gottwald, M., Graser, U. (1986). A&A, 157, 23 . ADS. [89]

Podsiadlowski, P., Rappaport, S., Pfahl, E.D. (2002). ApJ, 565, 1107 . ADS. [82]

Prinja, R.K., Massa, D., Searle, S.C. (2005). A&A, 430, L41 . ADS. [129]

Psaltis, D. & Chakrabarty, D. (1999). ApJ, 521, 332 . ADS. [82]

Pringle, J.E. & Rees, M.J. (1972). A&A, 21, 1 . ADS. [58]

Pringle, J.E. (1981). ARA&A, 19, 137 . ADS. [16, 17, 18]

Rahoui, F., Chaty, S., Lagage, P.-O., Pantin, E. (2008). A&A, 484, 801 . ADS. [129, 139, 142]

Raichur, H. & Paul, B. (2008). in press, astro-ph/0806.0949 . ADS. [49, 50]

Rappaport, S., Markert, T., Li, F.K., Clark, G.W., Jernigan, J.G., McClintock, J.E. (1977). ApJ, 217, L29 . ADS. [75]

Rappaport, S. (1981). X-ray astronomy. Cambridge: KNUDSEN, 1981, p.123 . ADS. [11]

Rappaport, S.A. & Joss, P.C. (1983). Accretion-driven stellar X-ray sources, p.1 . ADS. [144]

Romano, P., Sidoli, L., Mangano, V., Vercellone, S., Kennea, J.A., Cusumano, G., Krimm, H.A., Burrows, D.N., Gehrels, N.(2008a). ApJ, 680, L137 . ADS. [137, 141, 142]

Romano, P., Sidoli, L., Mangano, V., Kennea, J.A., Burrows, D.N., Krimm, H., Gehrels, N., Vercellone, S., Cusumano, G., Paizis, A. (2008b). Astr. Tel., 1435 . ADS. [138]

Romanova, M.M., Ustyugova, G.V., Koldoba, A.V., Lovelace, R.V.E. (2002). ApJ, 578, 420 . ADS. [37]

Romanova, M.M., Ustyugova, G.V., Koldoba, A.V., Wick, J.V., Lovelace, R.V.E. (2003). ApJ, 595, 1009 . ADS. [37, 51]

Romanova, M.M., Ustyugova, G. V., Koldoba, A.V., Lovelace, R.V.E. (2004). ApJ, 616, 151 . ADS. [37, 60]

Romanova, M.M., Ustyugova, G.V., Koldoba, A.V., Lovelace, R.V.E. (2005). ApJ, 635, L165 . ADS. [82]

Rothschild, R.E., Blanco, P.R., Gruber, D.E., Heindl, W.A., MacDonald, D.R., Marsden, D.C., Pelling, M.R., Wayne, L.R., Hink, P.L. (1998). ApJ, 496, 538 . ADS. [100]

Rutledge, E.R. (2001). ApJ, 553, 796 . ADS. [116, 132, 135]

Sakamoto, T. et al. (2008). GCN circular, 8034 . ADS. [99]

Sguera, V., Barlow, E.J., Bird, A.J., Clark, D.J., Dean, A.J., Hill, A.B., Moran, L., Shaw,

S.E., Willis, D.R., Bazzano, A., et al. (2005). A&A, 444, 221 . ADS. [128]

Sguera, V., Bazzano, A., Bird, A.J., Dean, A.J., Ubertini, P., Barlow, E.J., Bassani, L., Clark, D.J., Hill, A.B., Malizia, A., et al. (2006). ApJ, 646, 452 . ADS. [128]

Sguera, V., Bird, A.J., Dean, A.J., Bazzano, A., Ubertini, P., Landi, R., Malizia, A., Barlow, E.J., Clark, D.J., Hill, A.B., Molina, M. et al. (2007). A&A, 462, 695 . ADS. [128]

Sguera, V., Bassani, L., Landi, R., Bazzano, A., Bird, A.J., Dean, A.J., Malizia, A., Masetti, N., Ubertini, P. (2008). A&A, 487, 619. ADS. [137, 145]

Scharlemann, E.T. (1978). ApJ, 219, 617 . ADS. [37]

Shakura, N.I. & Sunyaev, R.A. (1973). A&A, 24, 337 . ADS. [17, 41, 79]

Shapiro, S.L. Lightman, A.P. (1976). ApJ, 204, 555 . ADS. [20]

Shinoda, K., Kii, T., Mitsuda, K., Nagase, F., Tanaka, Y., Makishima, K., Shibazaki, N. (1990). PASJ, 42, L27 . ADS. [43]

Sidoli, L., Vercellone, S., Mereghetti, S., Tavani, M. (2005). A&A, 429, L47 . ADS. [128]

Sidoli, L., Romano, P., Mereghetti, S., Paizis, A., Vercellone, S., Mangano, V., Gtz, D. (2007). A&A, 476, 1307 . ADS. [128, 129]

Sidoli, L., Romano, P., Mangano, V., Pellizzoni, A., Kennea, J.A., Cusumano, G., Vercellone, S., Paizis, A., Burrows, D.N., Gehrels, N. (2008). newblock in press, astro-ph/0805.1808 . ADS. [138]

Smith, D.M. (2004). Astr. Tel., 338 . ADS. [130]

Smith, D.M., Heindl, W.A., Markwardt, C.B., Swank, J.H., Negueruela, I., Harrison, T.E., Huss, L. (2006). ApJ, 638, 974 . ADS. [128]

Soong, Y. & Swank, J.H. (1989). X Ray Binaries, p. 617 . ADS. [43, 54]

Spruit, H.C., Taam, R.E. (1993). ApJ, 402, 593 . ADS. [61, 79]

Starling, R. & Evans, P. (2008). Astr. Tel., 1621 . ADS. [99]

Steele, I.A., Negueruela, I., Coe, M.J., Roche, P. (1998). MNRAS, 297, L5 . ADS. [55]

Stella, L. & Rosner, R. (1984). ApJ, 277, 312 . ADS. [79]

Stella, L., White, N.E., Rosner, R. (1986). ApJ, 308, 669 . ADS. [115, 116, 126, 127, 132]

Stella, L., White, N.E., Priedhorsky, W. (1987). ApJ, 315, 49 . ADS. [5]

Stella, L., Campana S., Colpi, M., Mereghetti, L., Tavani (1994). ApJ, 423, L47 . ADS. [71, 97]

Strohmayer, T.E., Zhang, W., Swank, J.H., Smale, A., Titarchuk, L., Day, C., Lee, U. (1996). ApJ, 469, 9 . ADS. [8]

Strohmayer, T.E., Zhang, W., Swank, J.H. (1997). ApJ, 487, L77 . ADS. [81]

Strohmayer, T.E. & Bildsten, L. (2006). Compact stellar X-ray sources, ed. W. H. G. Lewin & M. van der Klis, Cambridge University Press . ADS. [22, 112]

Strohmayer, T.E., Markwardt, C.B. Swank, J.H. (2008). Astr. Tel., 1635 . ADS. [99]

Sunyaev, R.A., Grebenev, S.A., Lutovinov, A.A., Rodriguez, J., Mereghetti, S., Gotz, D., Courvoisier, T. (2003). Astr. Tel.190 . ADS. [129]

Swank, J. & Markwardt, C. (2001). ASP Conf. Ser. 251, New Century of X-ray Astronomy, ed. H. Inoue & H. Kunieda, San Francisco, p. 94 . ADS. [101]

Taam, R.E. (1985). Annu. Rev. Nucl. Part. Sci., Vol. 35, p. 1 . ADS. [24]

Taam, R.E., King, A.R., Ritter, H. (2000). ApJ, 541, 329 . ADS. [82]

Takeshima, T., Dotani, T., Mitsuda, K., Naga, F. (1991). PASJ, 43, L43 . ADS. [43, 54]

Tamura, K., Hiroshi, T., Kitamoto, S., Hayashida, K., Nagase, F. (1992). ApJ, 389, 676 . ADS. [43, 54]

Tauris, T.M. & Savonije, G.J. (1999). A&A, 350, 928 . ADS. [16, 82, 86, 87]

Tauris, T.M. & van den Heuvel, E.P.J. (2006). Formation and evolution of compact stellar X-ray sources, ed. W. Lewin & M. van der Klis, Cambridge, UK, p. 623 . ADS. [127]

Thompson, T.W.J. & Rothschild, R.E. (2008). in press, astro-ph/0806.2859 . ADS. [139]

Thorstensen, J., Charles, P., Bowyer, S., Briel, U.G., Doxsey, R.E., Griffiths, R.E., Schwartz, D.A. (1979). ApJ, 233, L57 . ADS. [88, 90]

Thorstensen, J.R., Brownsberger, K.R., Mook, D.E., et al. (1988). ApJ, 334, 430 . ADS. [89, 95]

Tomsick, J.A., Lingenfelter, R., Corbel, S., Goldwurm, A., Kaaret, P. (2004). Astr. Tel., 224 . ADS. [130]

Tomsick, J.A., Chaty, S., Rodriguez, J., Foschini, L., Walter, R., Kaaret, P. (2006). ApJ, 647, 1309 . ADS. [128]

Toropina, O.D., Romanova, M.M., Toropin, Y.M., Lovelace, R.V.E. (2001). ApJ, 561, 964 . ADS. [116, 117, 118, 132]

Toropina, O.D., Romanova, M.M., Lovelace, R.V.E. (2006). MNRAS, 371, 569 . ADS. [116, 117]

Truemper, J., Pietsch, W., Reppin, C., Voges, W., Staubert, R., Kendziorra, E. (1978). ApJ, 219, 105 . ADS. [14]

Ulmer, M.P., Shulman, S., Yentis, D., Evans, W.D., McNutt, D., Meekins, J., Wood, K., Byram, E.T., Chubb, T.A., Friedman, H. (1980). ApJ, 235, L159. ADS. [88]

Ustyugova, G.V., Koldoba, A.V., Romanova, M.M., Lovelace, R.V.E. (2006). ApJ, 646, 304 . ADS. [37, 82, 87]

Verbunt, F. (1993). A&A Rev., 31, 93 . ADS. [96]

Vietri, M. (2008). Foundations of high-energy astrophysics, Chicago University press, pp. 325. [18, 42, 53]

Wallace, R.K. & Woosley, S.E. (1981). ApJ, 45, 389 . ADS. [106]

Walter, R., Zurita Heras, J., Bassani, L., Bazzano, A., Bodaghee, A., Dean, A., Dubath, P., Parmar, A.N., Renaud, M., Ubertini, P.(2006). A&A, 453, 133 . ADS. [128, 130]

Walter, R. & Zurita Heras, J. A. (2007). A&A, 476, 335 . ADS. [128, 129, 133, 137]

Wang Y.M. & Robertson J.A. (1984). A&A, 139, 93 . ADS. [80]

Wang Y.M. & Robertson J.A. (1985). A&A, 151, 361 . ADS. [62, 79, 82]

Wang, Y.M. (1987). A&A, 183, 257 . ADS. [38, 39, 41, 42, 50, 51, 53, 57]

Wang, Y.M. (1995). ApJ, 449, L153 . ADS. [38, 39, 41, 44, 51, 57]

Wang, Y.-M. (1996). ApJ, 465, L111 . ADS. [42, 50]

Wang, Y.-M. (1997). ApJ, 487, L85 . ADS. [51]

Weaver, T.A., Zimmerman, G.B., Woosley, S.E. (1978). ApJ, 225, 1021 . ADS. [83]

Wenzel, W. (1983). Information Bulletin on Variable Stars, 2452, 1 . ADS. [89, 95]

White, N.E., Holt, S.S. (1982). ApJ, 257, 318 . ADS. [5, 7]

White, N.E. (1988). Nature, 333, 708 . ADS. [57]

White, N. E., Nagase, F., Parmar, A. N. (1995). X-ray Binaries, ed. Lewin, W.H.G., Van

Paradijs J., van den Heuvel, E.P.J., Cambridge University Press . ADS. [96]

Wijnands, R. (2005). Pulsars New Research. NY: Nova Science Publishers, p. 53 . ADS. [82]

Wilson, R.B., Scott, D.M., Finger, M.H. (1997). AIP Conf. Proc., 410, 739 . ADS. [53]

Wilson, C.A., Finger, M.H., Coe, M.J., Laycock, S., Fabregat, J. (2002). ApJ, 570, 287 . ADS. [54]

Woo, J.W., Clark, G.W., Levine A.M., Corbet, R.H.D., Nagase, F. (1996). ApJ, 467, 811 . ADS. [43, 54]

Woods, P.M. & Thompson, C. (2006). Compact stellar X-ray sources, ed. W. Lewin & M. van der Klis, Cambridge, UK, p. 547 . ADS. [29, 133]

Woosley, S.E., Taam, R.E. (1976). Nature, 263, 101 . ADS. [21]

Woosley, S.E., Heger, A., Cumming, A. et al. (2004). ApJS, 151, 75 . ADS. [107, 109, 110, 111, 112]

Zane, S., Turolla, R., Stella, L., Treves, A. (2001). ApJ, 560, 384 . ADS. [133]

Zane, S., Ramsay, G., Jimenez-Garate, M.A., Willem den Herder, J., Hailey, C.J. (2004). MNRAS, 350, 506 . ADS. [53, 143]

Zavlin, V.E., Pavlov, G.G., Shibanov, Y.A. (1996). A&A, 315,141 . ADS. [95]

Zeldovich, Ya.B., Guseynov, O.H. (1966). ApJ, 144, 840 . ADS. [13]

Zhang, F., Li, X.-D. Wang, Z.-R. (2004). CHJAA, 4, 320 . ADS. [132, 134]

Zurita Heras, J.A. Walter, R. (2004). Astr. Tel., 336 . ADS. [130]

Zurita Heras, J.A., Chaty, S., Rodriguez, J. (2007). Astr. Tel., 1035 . ADS. [128, 131]